UC Irvine

UC Irvine Electronic Theses and Dissertations

Title

Non-precious metal (non-PGM) based catalysts for the electroreduction of CO2 to value-added products

Permalink

https://escholarship.org/uc/item/304572sc

Author

Delafontaine, Laurent

Publication Date

2022

Supplemental Material

https://escholarship.org/uc/item/304572sc#supplemental

Peer reviewed|Thesis/dissertation

eScholarship.org Powered by the California Digital Library
University of California

UNIVERSITY OF CALIFORNIA,
IRVINE

Non-precious metal (non-PGM) based catalysts for the electroreduction of CO_2 to value-added products

DISSERTATION

submitted in partial satisfaction of the requirements
for the degree of

DOCTOR OF PHILOSOPHY

in Chemical and Biochemical Engineering

by

Laurent Delafontaine

Dissertation Committee:
Chancellor's Professor Plamen Atanassov, Chair
Associate Professor Rachel Martin
Assistant Professor Iryna Zenyuk

2022

Section 1: Figure 1 © 2020 ChemSusChem

Section 2: Chapters 1, and 2 © 2022 ChemElectroChem

Section 3: Chapters 2, and 3 © 2021 Journal of Catalysis

Section 3: Chapters 4, and 5 © 2022 ACS Energy Letters

All other materials © 2022 Laurent Delafontaine

Table of Contents

List of Figures

Section 1

Section 2

Section 3

Section 4

List of Tables

Acknowledgements

I would like to express my deepest appreciation to my committee chair, Professor Plamen Atanassov for his scientific and personal guidance throughout my PhD. Especially recently, his encouragement and reassurance were invaluable to me in navigating the personal challenges I was facing. His scientific guidance allowed me to become an ethical scientist with a great attention to detail. As he said: that the purpose of a PhD is to be able to stand on your own two feet as a scientist and the purpose of a dissertation is to be defended; I believe that I can stand on my own two feet now as a scientist and defend the dissertation below.

I thank ChemSusChem, ChemElectroChem, Journal of Catalysis, and ACS Energy Letters for permission to include copyrighted research articles in this work. Figure 1 from section 1 of this thesis/dissertation is a reprint of the material as it appears in (Delafontaine, L., T. Asset and P. Atanassov (2020). "Metal–nitrogen–carbon electrocatalysts for CO2 reduction towards syngas generation." ChemSusChem 13(7): 1688-1698.), used with permission from ChemSusChem. The co-authors listed in this publication are Tristan Asset, and Plamen Atanassov. Chapters 1, and 2 of section 2 of this thesis/dissertation is a reprint of the material as it appears in (Delafontaine, L., E. Murphy, S. Guo, Y. Liu, T. Asset, Y. Huang, J. Chen, I. V. Zenyuk, X. Pan and P. Atanassov (2022). "Synergistic Electrocatalytic Syngas Production from Carbon Dioxide by Bi-Metallic Atomically Dispersed Catalysts." ChemElectroChem 9(17): e202200647.), used with permission from ChemSusChem. The co-authors listed in this publication are Eamonn Murphy (contributed equally), Shengyuan Guo, Yuanchao Liu, Tristan Asset, Ying Huang, Jiazhe Chen, Iryna Zenyuk, Xiaoqing Pan, and Plamen Atanassov. Chapters 2, and 3 of section 3 of this thesis/dissertation is a reprint of the material as it appears in (Ozden, S., L. Delafontaine, T. Asset, S. Guo, K. A. Filsinger, R. D. Priestley, P. Atanassov, and C. B. Arnold (2021). "Graphene-based catalyst for CO2 reduction: The critical role of solvents in materials design." Journal of Catalysis 404: 512-517.) used with permission from

Journal of Catalysis. The co-authors listed in this publication are Sehmus Ozden (contributed equally), Tristan Asset, Shengyuan Guo, Kai Filsinger, Rodney Priestley, Plamen Atanassov, and Craig Arnold. Chapters 4, and 5 of section 3 of this thesis/dissertation is a reprint of the material as it appears in (Ferri, M., et al. (2022). "Steering Cu-Based CO2RR Electrocatalysts' Selectivity: Effect of Hydroxyapatite Acid/Base Moieties in Promoting Formate Production." ACS Energy Letters 7(7): 2304-2310.) used with permission from ACS Energy Letters. The co-authors listed in this publication are Laurent Delafontaine (contributed equally), Michele Ferri (contributed equally), Shengyuan Guo, Tristan Asset, Pierangela Cristiani, Sebastiano Campisi, Antonella Gervasini, and Plamen Atanassov.

Vita
Laurent Delafontaine

2011-2015 B.S. in Chemical Engineering, Tulane University

2015-2016 M.S. in Chemical Engineering, Tulane University

2016-2017 Field Engineer, Halliburton Energy Services, Inc.

2018-2022 PhD in Chemical and Biochemical Engineering, University of California, Irvine

FIELD OF STUDY

Technical and practical engineering/electrochemical aspects for the development of non-precious metal (non-PGM) based catalysts for the electroreduction of CO_2 to value-added products. The development of heterogeneous carbon-based electrocatalysts for CO_2 reduction is explored.

PUBLICATIONS/PATENTS

1. Article accepted for publishing: Delafontaine, L., Murphy, E., Guo, S., Liu, Y., Asset, T., Pan, X., Atanassov, P. (2022). Synergistic electrocatalytic syngas production from carbon dioxide by bi-metallic atomically dispersed catalysts. ChemElectroChem.

2. Article published: Ferri, M., Delafontaine, L., Guo, S., Asset, T., Cristiani, P., Campisi, S., Gervasini, A., & Atanassov, P. (2022). Steering Cu-Based CO2RR Electrocatalysts' Selectivity: Effect of Hydroxyapatite Acid/Base Moieties in Promoting Formate Production. In ACS Energy Letters (pp. 2304–2310). American Chemical Society (ACS).

3. Manuscript being drafted: Delafontaine, L., Cosenza, A., Murphy, E., Guo, S., Liu, Y., Chen, J., Atanassov, P. (2022). Highly Efficient and Selective CO2 Electroreduction to CO on Novel Metal-Nitrogen-Carbon (M-N-C) Catalyst.

4. Article published: Ozden, S., Delafontaine, L., Asset, T., Guo, S., Filsinger, K. A., Priestley, R. D., Atanassov, P., & Arnold, C. B. (2021). Graphene-based catalyst for CO2 reduction: The critical role of solvents in materials design. In Journal of Catalysis (Vol. 404, pp. 512–517).

5. Article published: Delafontaine, L., Asset, T., & Atanassov, P. (2020). Metal–Nitrogen–Carbon Electrocatalysts for CO 2 Reduction towards Syngas Generation. ChemSusChem, 13(7), 1688–1698. https://doi.org/10.1002/cssc.201903281.

6. Provisional Patent for novel metal-nitrogen-carbon synthesis (2022).

Abstract of the Dissertation

Non-precious metal (non-PGM) based catalysts for the electroreduction of CO_2 to value-added products

by

Laurent Delafontaine

Doctor of Philosophy in Chemical and Biomolecular Engineering

University of California, Irvine, 2022

Chancellor's Professor Plamen Atanassov, Chair

Non-precious group metal electrocatalysts are explored for CO_2 reduction. Carbon-based metal-nitrogen-carbon (M-N-C) catalysts are investigated and tested via a handmade microfluidic flow cell. Copper-based catalysts are also explored for the reduction of CO_2 as so far as how the solvent and acidic/basic moiety dopant content may influence the observed performance. The M-N-C catalysts are explored based on the sacrificial support method (SSM) which was developed by the Atanassov Lab in 2008. A bifunctional bi-metallic M-N-C is developed and studied for syngas production. Finally, a novel synthesis method for M-N-C catalysts is presented which is a one-pot synthesis that produces catalysts with comparable or improved activity for CO_2 reduction compared to the state-of-the-art and SSM catalysts. This novel synthesis may be tailored for a range of electrocatalytic applications. As such, it is an industry disrupting technology due to its requiring no harsh solvents of any kind as well its industrial scalability. The materials characterization is explored using standard analytic methods such as transmission electron microscopy (TEM), and X-Ray Diffraction (XRD). The elemental mapping of the catalysts is explored via energy dispersive X-ray spectroscopy (EDS). X-ray Photoelectron spectroscopy (XPS) is used for assessing the surface chemical changes of the catalysts. Scanning electron microscopy (SEM), combined with BET adsorption studies, Raman spectroscopy, and studies of the metal coordination sphere(s) using XANES/NEXAFS are also employed. The electrochemical characterization is carried out using voltametric techniques: linear sweep voltammetry (LSV), cyclic voltammetry (CV), potentiostatic electrochemical impedance spectroscopy (PEIS), and chronoamperometry (CA). The gas-

phase product distribution is explored via gas chromatography and the liquid-phase product distribution is assessed by ^{1}H NMR. The material/electrochemical techniques are used in tandem to suggest possible electrocatalytic mechanism and reasons for the observed activity/selectivity. The catalyst development is approached from one of two perspectives: either i.) to gain theoretical and fundamental physical insight to the heterogeneous electrocatalytic process itself or ii.) to assess the possibility for the catalysts to be explored for industrial applications. Addressing the second point, the ease of manufacturability as well as the robustness of the developed catalysts are considered. Finally, a novel Ni-N-C catalyst is developed which shows unmatched selectivity for CO production at both high overpotential and low overpotential. Conventionally and before this catalyst, Ni-N-C was only able to achieve high selectivity at high overpotential. The novel Ni-N-C synthesized here shows > 85 % faradaic efficiency for CO formation (FE_{CO}) at -0.3 V vs. RHE and > 99 % FE_{CO} at -1.1 V vs. RHE.

Section 1: Introduction

Part I: Background for Electrochemical CO_2RR

Atmospheric CO_2 concentrations have drastically increased from 250 ppm at the beginning of the industrial revolution to greater than 390 ppm. [1] The fact that CO_2 is both a stable molecule, with a long lifetime in the atmosphere of 30 to 90 years, and a potent greenhouse gas has exacerbated global warming into a planetary crisis. For this reason, there has been much research into different technologies to mitigate anthropogenic CO_2 emissions. These efforts can be separated broadly into two categories: carbon capture and storage technologies (CCS) and carbon capture and utilization technologies (CCU)[87]. The United States and Europe are spearheading the global CCU/CCS efforts which in 2020 captured 40 Mt of CO_2 and saw a 33 % increase in CCS facilities. [2] Although CCU investment has consistently been less than 0.5% of global investment in clean energy technologies, there is growing interest and expectations for that number to increase. Among CCU technologies, the electrochemical CO_2 reduction reaction (CO_2RR) has become an increasingly popular area of research. This is due to the fact that it may be performed under ambient conditions without extreme thermal/mechanical energy input and the products of CO_2RR can be immediately used for the production of fuels/value-added chemicals. [3, 4]

CO_2 is a stable fully oxidized molecule that requires substantial energy input to be reduced into desirable products of carbon monoxide (CO), formate ($HCOO^-$), syngas, or more reduced C_1, and C_{2+} products. The single electron reduction of CO_2 to CO_2^- has a high thermodynamic potential of E^0 = -1.90 V vs. standard hydrogen electrode (SHE). [4] Because it is energetically expensive to proceed through this anionic intermediate with an unfavorable bent molecular configuration, CO_2RR usually proceeds through separate more stable intermediates. The standard electrode potentials are summarized in table 1 below while the common mechanistic pathway(s) to these final product(s) are listed in figure 1. Each mechanistic step in figure 1 has an associated overpotential which means a more negative cathodic potential is required for CO_2RR. Furthermore, the overpotential conventionally has three contributions: an activation overpotential due to kinetic activations (η_{act}), ohmic overpotential due to ohmic resistances (η_{ohm}), and a mass transport related overpotential (η_{mt}). [5, 6]

$$E = E^0 + \eta_{act} + \eta_{ohm} + \eta_{mt}$$

These all contribute to an increased operating cell voltage summarized in figure 2 from Martin et al. [4] Furthermore, E^0 is a Nernstian cell voltage which is based off the Gibbs free energy ($\Delta G = \Delta H - T\Delta S$, $E^0 = -\frac{\Delta G}{nF}$, where n = the # of electrons transferred per mole of product and F is Faraday's constant). All the cathodic products listed in table 1 (with the exception of formate), when coupled to the anodic OER, are overall endothermic and require an additional entropic overpotential to achieve the thermoneutral voltage (E^n, $E^n = -\frac{\Delta H}{nF}$). This is important from an industrial design perspective as a lower operating voltage may be sustained at higher operating temperature for those endothermic reactions with the exception of formate whose thermoneutral and standard cell potential are similar (e.g., for CO_2 reduction to CO at 25° C and standard conditions, the reversible cell voltage is 1.33 V vs. 0.97 V at 800° C).

Products	**E (V) (RHE)**	$\boldsymbol{E(V)(SHE)}$, **pH = 8.23**	$\boldsymbol{E^0(V)}$	$\boldsymbol{E^n(V)}$	$\boldsymbol{E^0}$-$\boldsymbol{E^n}$**(mV)**
CO	-0.107	-0.59	-1.33	-1.47	140
H_2	0.00	-0.48	-1.23	-1.48	250
HCOOH	-0.197	-0.68	-1.32	-1.32	0
CH_4	+0.173	-0.31	-1.06	-1.15	94
C_2H_4	+0.073	-0.41	-1.16	-1.22	60
O_2	+1.23	+0.74	-	-	-

Table 1: Products for CO2RR half-reactions. All reduction reactions are coupled to OER (last reaction) and the pH is taken as the average of the pH measurement before and after the electrochemical experiment. E0 represents the Nernstian standard potential while En represents the thermoneutral standard potential.

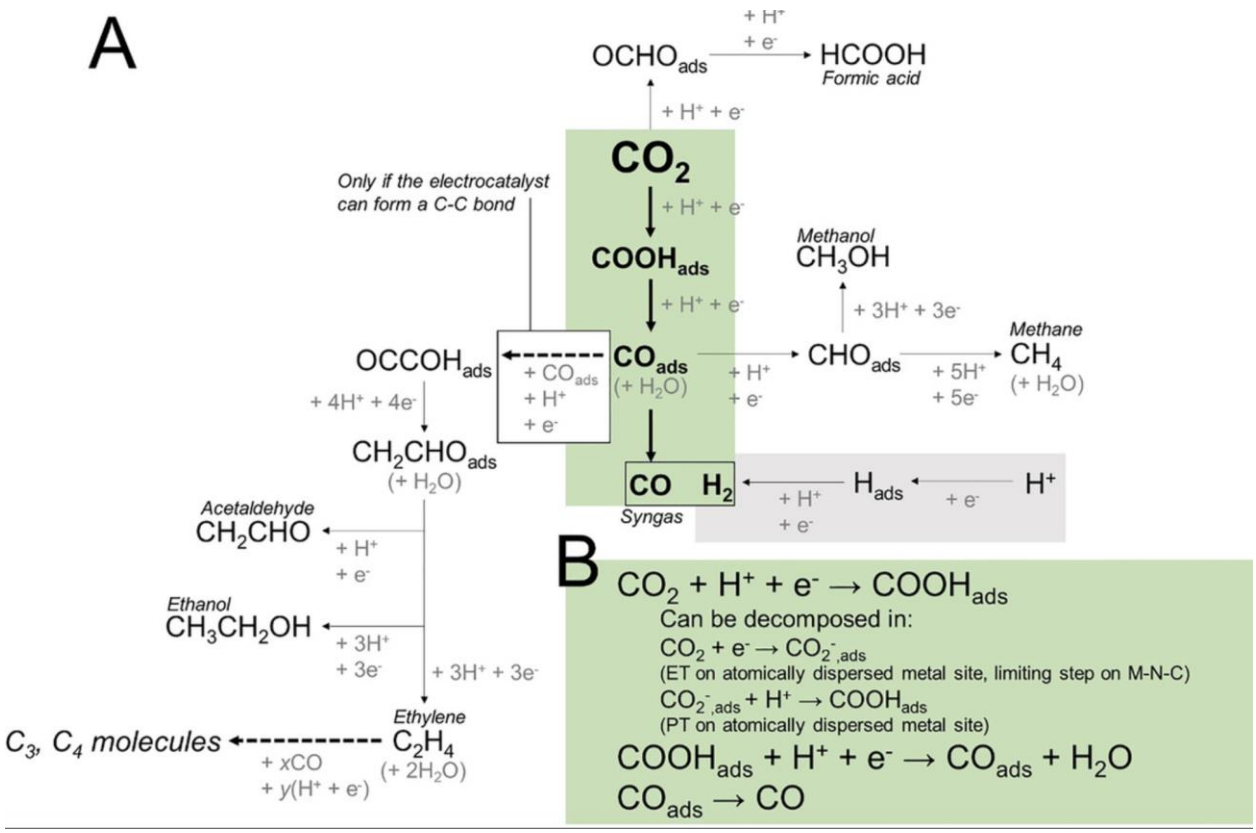

Figure 1: Schematic for the CO2RR mechanism. From Delafontaine et al. [1] Part A overviews the reaction mechanism to different products. Part B focuses on CO2 reduction to CO on atomically dispersed metal active site centers in M-N-C catalysts (ET: electron transfer, PT: proton transfer, COOHads: carbon-bound intermediate, OCHOads, CHOads: oxygen-bound intermediates.

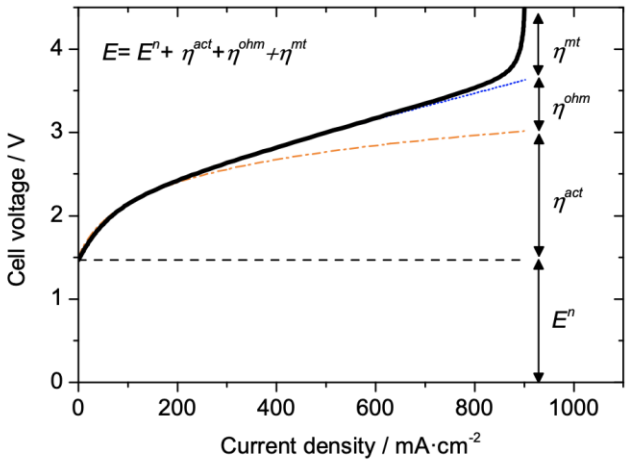

Figure 2: Theoretical Voltammogram for CO2 Reduction. From Martín et al. [4] Theoretical voltammogram showing cell voltage (V) vs. current density for CO producing electrolyzer with CO2 reduction to CO at cathode and oxygen evolution reaction (OER) at anode.

Part II: Narrowing down CO_2RR fundamentals as they apply to our current studies including catalyst syntheses

The ohmic overpotential are energetic losses caused by ions moving through the electrolyte and electrons through the electrode during the electrochemical reduction of CO_2. The activation overpotential are inefficiencies due to overcoming a reaction energy barrier which depends on the adsorption/desorption of reaction intermediates. The ohmic and especially activation overpotential are both highly dependent on the cathode material or the choice in electrocatalyst. This is experimentally realizable by the onset potential for generation of a specified product. The difference between this experimental onset potential ($E_{exp,onset}$) and the standard electrode potential (E^0) is the observed experimental overpotential (η_{exp}) using the electrochemical cell ($\eta_{exp} = E_{exp,onset} - E^0$). It should be noted that the cathodic overpotential is being studied here and it is desired to optimize the cathode by catalyst design, and reaction engineering. Additionally, this onset potential is often system dependent and usually presents a strong pH dependence. For this reason, if a potential vs. RHE reference electrode is applied but the local cathode pH is higher than the pH in the vicinity of the RHE reference electrode, then the actual applied potential at the cathode will be reduced by a factor of -0.059 * ($pH_{cathode}$ – $pH_{reference\ electrode}$) according to the pH dependence of the standard hydrogen electrode (Figure 3). By way of example, if the pH in the vicinity of the reference electrode for 0 V vs. RHE applied potential is 8 ($pH_{reference\ electrode}$ = 8) and the local cathode pH is 10 ($pH_{cathode}$ = 10), then the actual working electrode potential will be -0.118 V vs. RHE. Hence, accurate calculation of an onset potential is only as good as the ability to estimate the local cathode pH. The anode will also have an associated overpotential for OER and may be further optimized beyond what is considered here.

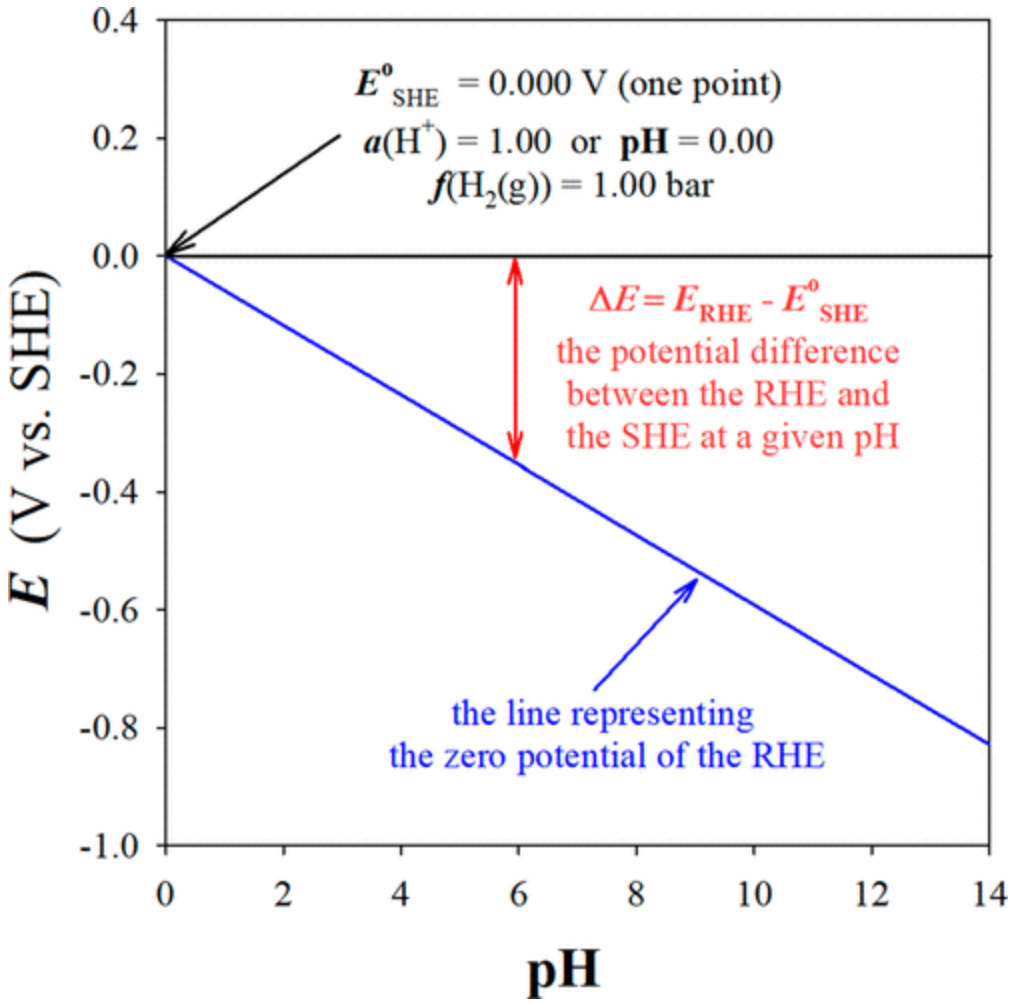

Figure 3: Reference Electrode Potential vs. pH. From Jerkiewicz et al. [7] Plot of E versus pH for the H+(aq)/H2(g) redox couple for f(H2) = 1.00 bar and T = 298.15 K.

The first part of the preliminary results will test different commercial catalysts to assess their role in CO_2RR. This serves to compare to literature in order to validate our current setup for evaluation of gas diffusion electrodes (GDE). The key difference between the GDE and aqueous-based CO_2RR is that in the GDE, CO_2 diffuses from the gas phase and meets the triple phase boundary (TPB) without the need of first dissolving in the aqueous phase.

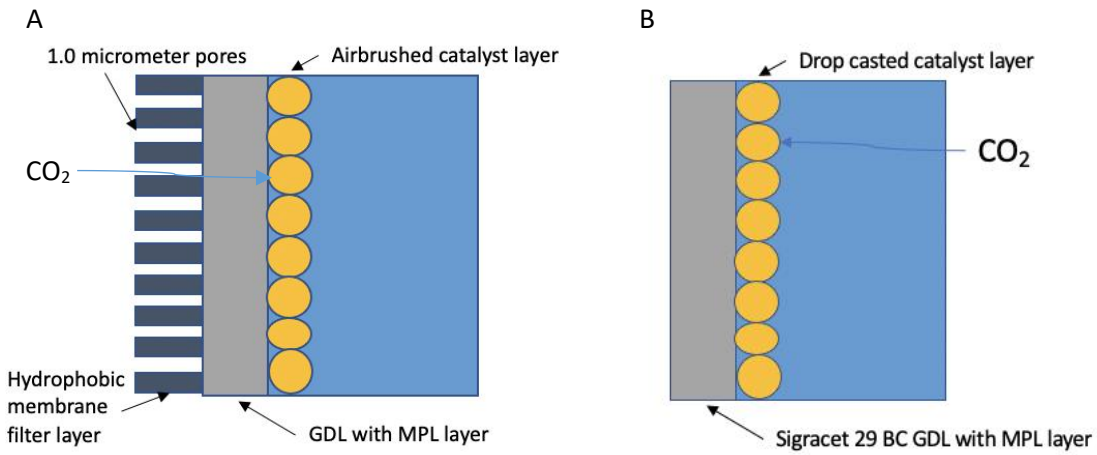

Figure 4: A) GDE-based system for evaluating CO2RR catalysts vs. aqueous-based system in aqueous-based system in B.

In the GDE system (figure 4 A), the membrane filter layer is a STERLITECH® laminated 1 micrometer porous PTFE membrane filter which is hot-pressed at 200 F and 0.5 kN/cm^2 for 10 min to a Sigracet 29 BC GDL layer. The catalyst ink, which is a mixture of DI water, IPA/EtOH, ionic binder (either Nafion® or sustainion ionomer solution), and catalyst powder is airbrushed by hand on the GDL layer. The GDE has its mass taken before and after and the difference is the mass of catalyst deposited on the GDE. In the aqueous-based system, the CO_2 must first be dissolved in the aqueous phase and then diffuse to the catalyst layer (CL). This is the common system employed using H-cells to study M-N-C and other catalysts' performance for CO_2RR[82].

The flow cell design for evaluating GDE is as follows. The distance between the cathode and anode is just large enough to accommodate the gas/liquid tubing ID plus the thickness of two O-Rings under compression. The gas sampling strategy is to fill a 5.115 mL gas-tight vial which has one 20-gauge needle connected to the gas tubing outlet from our cell and one 20-gauge exit needle to purge the gas vial and prevent over-pressurization. The gas and liquid tubing are 1/16" by 0.040" (OD" by ID") and the 20-gauge needle OD matches the tubing ID for a gas-tight seal. The reference electrode is placed in an external beaker connected to the recirculating electrolyte so that it is not in between the current flowing between cathode and anode. There are 8 bolts which hold the anode side cap, liquid flow chamber, and gas flow chamber together and ensure no electrolyte leakage (Figure 1). The GDL is a 5 cm^2 square piece of Sigracet 29 BC carbon paper hot pressed to a STERLITECH laminated PTFE 1.0-micron pore size membrane filter. The wetted area of carbon paper is 1 cm^2 and is facing the liquid chamber with the PTFE filter facing the gas chamber. Electrolyte is recirculated using a peristaltic pump at 26.1 mL/min and 10 sccm of inlet gas is fed to the gas chamber inlet.

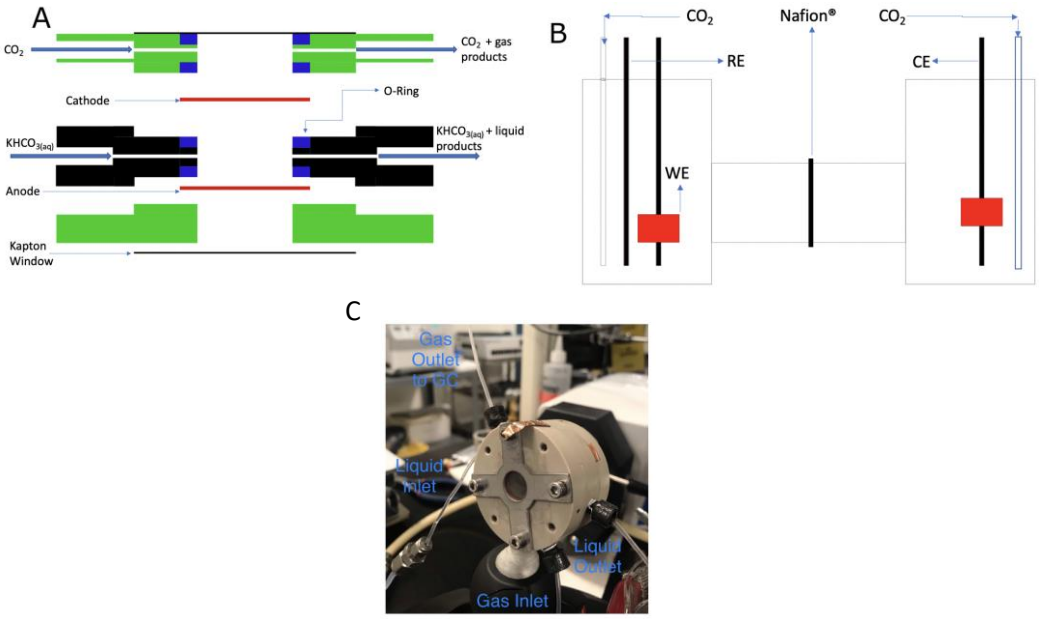

Figure 5: Schematic of flow cell (A) and H-Cell (B); flow cell (C).

There is always a significant rate-enhancement when switching from a traditional H-cell to a GDE assembly. This is due to the fact that the CO_2 gas-phase reactant remains in the gas phase and diffuses to the catalytic layer. In opposition to this, when an H-cell is used, CO_2 must first dissolve into an aqueous electrolyte and then diffuse in the bulk liquid phase to the catalytic layer. There is an intrinsic penalty or reduction in the concentration of CO_2 at the catalyst surface when using an H-cell which is given by the solubility of CO_2 in aqueous electrolyte.

To test this fact, we used commercial Sn nanopowder catalyst and evaluated the formate production by ^{1}H NMR to compare the H-cell and GDE performance. As shown in figure 6, at lower overpotential, the GDE at 3 h shows a greater than 13-fold increase in formate production and a greater than 30-fold increase in formate production when the 30-minute experiment is extrapolated to 3 hours to account for catalyst deactivation during the 3 h GDE experiment.

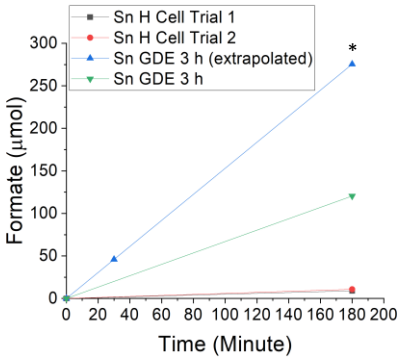

Figure 6: Micromoles of formate produced versus electrolysis time (minutes) for GDE and H-Cell (catalyst = Sn). Cathodic Loading = 1.5 mg/cm2; Anodic Pt Loading = 4.25 mg/cm2. For GDE experiments, potential = -0.88 V versus RHE. For H-Cell experiments, potential = -0.94 versus RHE. * = data point collected at t = 30 min extrapolated to 3 h.

Four commercial catalyst standards are chosen to represent four groups depending on their expected products in the CO_2/H_2O co-electrolysis process as follows: (1) CO-selective, (2) H_2-selective, (3) formate-selective, (4) C_1+C_2 – selective. The CO selective monometallic group contains Au, Ag, and Zn and is represented by our catalyst standard of unsupported Ag nanoparticles[94,120,121]. These have particle size < 100 nm and have a 99.5 % (trace metal basis) purity. The H_2 selective group includes Fe, Ni, and Pt and is represented by Pt 20 wt.% on graphitized carbon. This catalyst also serves as our anode for electrochemical experiments comparing commercial catalysts. Finally, it is replaced with bare carbon GDL for a totally non-PGM system. The formate selective catalysts are Sn, In, Pb and are represented by Sn nanopowder with particle size <150 nm and ≥ 99 % purity[122,123]. Cu nanopowder is reported to have a particle size of 25 nm and is our benchmark catalyst for the production of more highly reduced multi-carbon products as well as CO and formate[124,125].

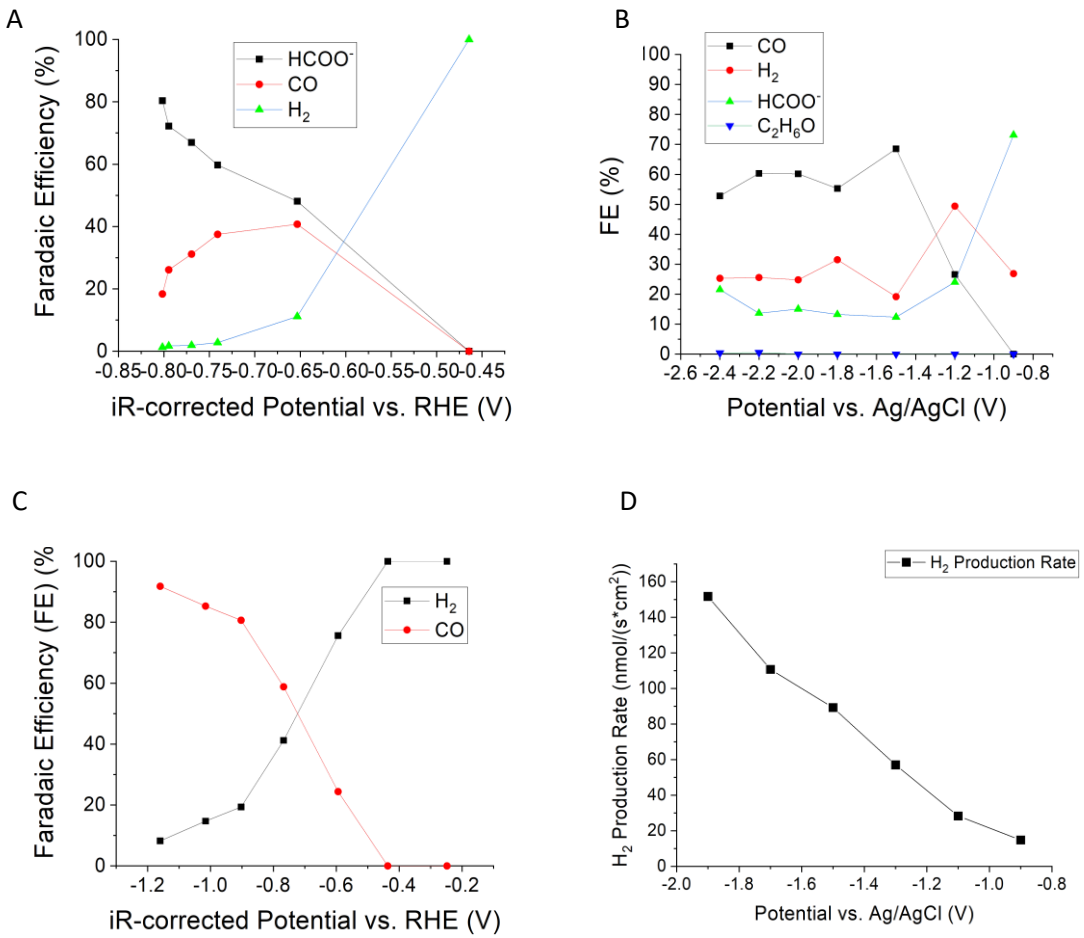

Figure 7: Results for commercial catalyst standards. Results for A) Sn nanopowder, B) Cu nanopowder, C) Ag nanopowder, D) Pt nanopowder. Cathode catalyst loading is 1.5 mg/cm2geo and anode catalyst loading is 4.25 mg/cm2. The iR-corrected potential is taken by obtaining the electrolyte resistance (Rohm) from PEIS data.

The results for the commercial catalysts confirm the expected experimental trends observed elsewhere in literature. Pt nanoparticles show a monotonically increasing HER at increasingly cathodic potentials with absence of CO_2RR products. Sn nanopowder has a high selectivity for $HCOO^-$ production, a moderate selectivity for CO, and a minor selectivity for HER. Importantly, the benchmark CO-producing catalyst Ag nanoparticles shows a high selectivity for CO consistent with literature. For comparison, our results for CO mirror closely the results from Jiang et al[127] in figure 8 for *Air-Ag* without H_2 treatment. These results for Ag catalysts may be compared to M-N-C catalysts for product selectivity for CO.

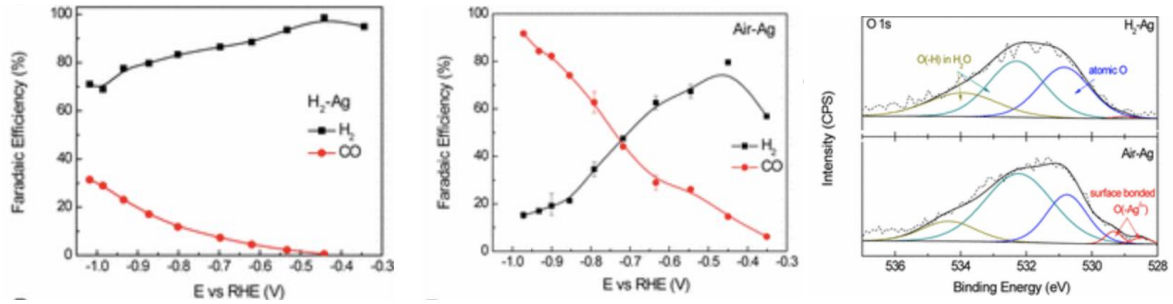

Figure 8. Data from Jiang et al.[127]: Left and center is Faradaic efficiency versus RHE for H_2-Ag and Air-Ag, respectively. Figure on right is deconvolution of O 1s region of the XPS spectra for H_2-Ag (with H_2 treatment) and Air-Ag (without H_2 treatment).

It should be noted that the analysis for commercial copper nanoparticle standard was performed without the ability to detect methane/ethylene. This catalyst is reported elsewhere by Garcia et al[126] who investigated CO_2RR product selectivity on Cu nanoparticles from 25-80 nm in average diameter as being highly selective for ethylene. As reported previously[96], certain single crystallographic compositions such as a high presence of (100) facets can dramatically influence the CO_2RR products on copper by enhancing C_2 product formation. Furthermore, it has been uncovered that high concentration of (111) facets leads to selectivity to C_1 hydrocarbon formation (e.g., CH_4) while (100) facets lead to more efficient C-C coupling and higher production of ethylene[40,41,43,96]. The strategy is to seek to increase the abundance of weakly coordinated copper sites to improve their reactivity for CO_2RR which has been investigated via electropolishing, sputtering, anodization, and electrodeposition[41,128]

The synthesis method (e.g., the solvent choice in Cu nanoparticle synthesis) or the choice of template for an atomically dispersed M-N-C catalyst has major implications in terms of the resulting electrocatalytic activity. The benefit of carbon-based catalysts vs. metal-based catalysts is they have increased abundance which dramatically reduces their employment in industrial devices. However, carbon-based as well as atomically tailored metal-based catalysts often require long syntheses which have substantial batch-to-batch variability. These industrial limitations often impede their large scale deployment.

What follows is a brief synopsis of the various catalyst-dependent facets/factors influencing CO_2 reduction selectivity/activity. The industrial scalability is importantly highlighted for the different syntheses. Depending on the catalyst employed, the CO_2RR mechanism shown in figure 1 leads to a variety of different products. These include CO, H_2 from the competing hydrogen evolution reaction (HER), formate, and C_1/C_2 aldehydes/alcohols[66, 82]. The selectivity to different products is highly dependent on the binding energy of the various reaction intermediates to the cathode catalyst. On metals such as platinum and iron, the HER is favored strongly over CO_2RR. Gold and silver are known to be selective for CO production. An alternative pathway in the top of figure 1 leads to formic acid production on metals such as tin. Copper is unique in its ability to catalyze the reduction of CO_2 to more highly reduced C_1, and C_2 hydrocarbons and alcohols. Silver (Ag) and gold (Au) based electrocatalysts are attractive because they are highly selective for CO production. However, these are precious metal catalysts which are expensive and increasingly scarce. Therefore, it is desired to find non-precious-metal

group (PGM) catalysts which are inexpensive and made from naturally abundant organic precursor chemicals. A promising alternative to non-PGM catalysts are the family of metal-nitrogen-carbon and nitrogen-carbon electrocatalysts. These are produced with trace amounts of more abundant metallic precursor elements. Unlike Cu-based catalysts which suffer from poor selectivity by producing a variety of products, M-N-C catalysts excel in producing CO and H_2 with high production rates and energy efficiencies. M-N-C catalysts, only recently studied in the 1970s as porphyrins and phthalocyanines, have now garnered research interest for their electrochemical performance as ORR catalysts. Recently, they have also shown grown great promise as CO_2RR catalysts and are currently being investigated as potential candidates for the nitrogen reduction reaction (NRR). Much of the literature in M-N-C catalysts, however, have been obtained in aqueous-based systems which have insufficient production rates to be considered for industrialization. Herein, a series of mono- and bi-metallic M-N-C catalysts are investigated with the aim to evaluate their industrial feasibility for reducing CO_2 to value-added products. The various physical and chemical properties of these catalysts are studied and specifically they are correlated with their selectivity to the desired products of CO/H_2. The M-N-C catalysts are studied as they are the non-PGM based catalysts most ready to replace expensive silver and gold-based catalysts for the production of mixtures of CO/H_2 or syngas. The reduction of CO_2 to syngas or CO is primed for industrialization because these products can be produced with both high faradaic efficiency and a high overall conversion rate. Furthermore, CO_2 reduction to syngas can be coupled to a subsequent gas phase-catalytic Fischer-Tropsch process for production of synthetic fuels. [7]

However, other catalysts exhibit other interesting capabilities. As mentioned before, Cu-based catalysts are unique in their ability to catalyze the reduction of CO_2 to more highly reduced C_1 and C_2 hydrocarbons and alcohols. For this reason, we also study commercially purchased Cu nanoparticles by incorporating it into a GDE. We further study electrodeposited copper on GDE samples to evaluate their potential application in CO_2RR. The electrodeposited copper samples have an advantage over other powder-based catalysts as they do not require a binder. Using bulk catalysts (plates, discs, rods) suffers from the fact that they have low ECSA values and hence overall production rates. Nanoparticle catalysts benefit from the fact that they can minimize precious metal usage and maximize ECSA leading to much higher geometric current densities than their bulk counterparts. The nanoparticle catalysts, however, require an ionic binder such as Nafion® which introduces an extra electronic resistance and impedes their long-term stability. [8] The electrodeposited samples bypass this problem and often have high porosity which also leads to a high specific surface area. The drawbacks of these types of catalysts are that their morphologies are often hard to predict and there is often a large variability in the surface electrode structure. These were investigated to study powder-based and solid-based catalysts for completeness. Finally, the role of solvent in Cu nanoparticle synthesis as well as the role of altered acidic/basic surface moieties via Cu doping with hydroxyapatite (HAP) were separately investigated. [9, 10] There are several figures of merit to analyze in order to compare the various catalysts' performances including the onset potential for product generation as mentioned previously.

Along with the onset potential for product generation, we also consider the faradaic efficiency for generation of species i (FE_i) in evaluating the cathode candidates for CO_2RR.

$$FE_i(\%) = \frac{n_i m_i F}{Q} \times 100$$

n_i = moles of e^- transferred per mole product, m_i = moles of product generated, Q = total charge transferred, and F = Faraday's constant

We also study the current density normalized to geometric surface area of the GDE surface which is reported in (mA/cm^2*s) for different potentials. The geometric current density can be used along with the faradaic efficiency to the desired product to assess the overall CO_2RR performance to improve the design of catalyst(s). The electrochemically active surface area (ECSA), active site density (SD), and turnover frequency (TOF) for the catalysts we synthesize are all important metrics to consider. These are discussed in order to study the intrinsic vs. extrinsic catalytic selectivity for CO_2RR over hydrogen evolution (HER). The various experimental methods for assessing SD, and TOF for M-N-C catalysts is presented. The double-layer capacitance (D-L capacitance) measured in Farads or milliFarads/cm^2 is studied and compared to BET (Brunauer, Emmett and Teller) surface area in order to gain a semi-quantitative comparison between M-N-C catalysts of different surface areas. CO cryosorption is an example of a more quantitative method of assessing SD for M-N-C catalysts. [11]

As mentioned previously, M-N-C catalysts are prime candidates for further development for electrocatalytic CO_2 reduction. These metal-nitrogen-doped carbon electrocatalysts are considered the most active platinum group metal-free benchmark catalysts for energy conversion (e.g., fuel cell/CO_2 electroreduction/N_2 electroreduction) and are synthesized by various means. They are generally produced by pyrolytic means and offer atomically dispersed metal active sites with high atom utilization resulting in high electrocatalytic activity. The synthesis proceeds through one of three major categories of synthesis protocols: either through soft-template approach[12-16], hard-templating with silica[17-23], sacrificial polymer approach [24-26], or through a combination of the methods above such as by the combined sacrificial polymer and sacrificial metal organic framework (MOF) approach [26].

Use of MOFs such as Zn-based ZIF-8 as pyrolytic precursors is a powerful soft-templating approach to synthesizing M-N-C catalysts. Utilizing ZIF-8, an optimized Fe-N-C was synthesized by soft-template method in 2011 which achieved an impressive 0.9 W cm^{-2}_{geo} in an H_2/O_2 polymer electrolyte membrane fuel cell (PEMFC).[27] The silica hard-templating approach discussed more below has been refined for over a decade which has yielded arguably the top M-N-C candidate for replacing platinum-group metal electrocatalysts. A third method is the sacrificial polymer approach which utilizes nitrogen-doped polymers (e.g., polyaniline, and polypyrrole) as dual nitrogen/carbon source which upon polymerization in the presence of a metallic salt, and pyrolytic treatment followed by acid washing yields a highly active M-N-C catalyst[24]. These methods each offer different routes to a highly efficient electrocatalyst however they each also have substantial synthetic limitations which impede their large-scale commercialization.

These challenges can be simplified to three main obstacles: (i). use of the hard-template approach or the sacrificial polymer approach requires an acid or basic solvent wash step (usually in harsh hydrofluoric acid or caustic KOH) which increases the synthesis time substantially and requires the

disposal of large quantities of acids/bases which increases the overall cost of the process, (ii). the syntheses produce catalysts with modest active site density (SD) which impedes their overall catalytic throughput, and (iii). the intermediate acid-wash step to produce the state-of-the-art M-N-C catalysts before the final pyrolysis complicates the process by requiring a hands-on transferring of the step for acid-wash and back to the pyrolysis chamber which limits its industrial scale-up. Furthermore, the environmental remediation of large quantities of harsh solvents used for removing the template is far more involved and less environmentally benign than remediation of gaseous acid streams.

By way of example, the state-of-the-art catalyst identified by Chen et al [17] this year and [28] in 2020 are produced by hard-templating with silica. This method was developed by the Atanassov lab in 2008 [29] and has since been commercialized by Pajarito Powder© due to the high electrocatalytic activity of the catalysts produced by this synthesis technique. This approach initially necessitated a metal macrocycle (e.g., metal porphyrin), but has since been simplified to utilize simple metallic salts, and common nitrogen/carbon precursors mixed in optimum ratios with silica particles of varying particle size/surface areas[30, 31]. The proper ratio of silica precursor(s) and their respective particle sizes have a substantial impact on the final pore size distribution and eventually lead to a hierarchical porosity with beneficial electrocatalytic properties. This precursor mixture is subjected to a first pyrolysis in inert or reductive atmosphere(s) followed by an acid washing step in highly concentrated (25 wt.%) hydrofluoric acid (HF) to generate a high degree of mesoporosity through the hard templating effect. The silica templating production of M-N-C catalysts by Pajarito Powder has been shown to produce less M-N_x (a chemical moiety integral to its electrocatalytic activity) than laboratory batches from University of New Mexico (UNM) where the technique was developed[28]. This is evidence of the limitations in the industrial scale-up of this synthesis technique. To date and to the best of the author's knowledge, no silica hard-template synthesis of M-N-C catalysts has been accomplished that completely avoids the utilization of harsh acids/bases while also not relying on the utilization of metal macrocycles.

The new synthesis uses no harsh acid or bases. Previous syntheses have required the utilization of and disposal of huge quantities of toxic HF. The current invention is a much safer synthesis and much less expensive as one of the largest costs in commercialization of previous M-N-C syntheses has been HF disposal which this synthesis completely avoids. The previous syntheses have required long synthesis times up to 10-14 days while the current synthesis can be accomplished in 1 day.

For CO_2 reduction, the resulting catalyst (e.g., Ni-N-C) shows unparalleled selectivity and high electrocatalytic activity. A faradaic efficiency for CO formation of greater than 99 % is achieved at high overpotential (E_{cath}= -1.1 V vs. RHE) while the competing M-N-C catalysts show a maximum CO faradaic efficiency at *ca.* -0.7 V vs. RHE and increasing H_2 selectivity (unwanted byproduct) at more negative potentials [5, 12, 32, 33].

Section 2: Bimetallic M-N-C Catalysts for Syngas Generation

Chapter 1: Bi-metallic M-N-C (M = Fe, Mo) Catalysts for CO_2 Reduction

The production of syngas by traditional processes such as steam methane reforming is energetically intensive and produces a large amount of CO_2 emissions. In contrast, the electrochemical CO_2 reduction reaction (CO_2RR) enables the carbon neutral production of syngas at ambient conditions. Among non-precious metal catalysts, metal-nitrogen-carbon electrocatalysts are inexpensive and highly selective towards syngas production. This study examined the selectivity of mono- and bi-metallic (M-N-C, M = Fe, Mo or FeMo) electrocatalysts towards syngas production. The ratio of the CO:H_2 in the syngas was tuned by modifying the ratio of metallic precursors in the bi-metallic FeMo-N-C catalysts, tailoring the catalysts' selectivity towards the CO_2RR or the hydrogen evolution reaction (HER). The catalyst synthesis temperature(s) are considered as they influence the catalyst morphology and activity. Further, the dependence of the ratio of CO:H_2 in the syngas as a function of the potential is explored for the different bi-metallic catalysts. This work showed that by tailoring both the ratio of Fe:Mo in the bi-metallic catalyst and optimizing the reductive potential, a CO:H_2 ratio between 0.25 to 5 was achievable. This study demonstrated a novel approach in which the ratio of the product syngas composition can be tailored in a single reaction, without the need for further downstream processing to reach a desired composition.

Introduction

Electrochemical CO_2 reduction is a promising method to mitigate anthropogenic CO_2 emissions while simultaneously producing value-added chemicals. One of the most feasible methods for industrial applications is the implementation of an H_2O/CO_2 co-electrolysis process where the target products are H_2 and CO. Synthesis gas (syngas) is generally a mixture of CO, H_2, CO_2, and smaller amounts of CH_4 and other gases.[34] The market value for syngas is low compared to other possible products from CO_2 reduction (e.g., market value for syngas = 0.06 \$ kg^{-1}; market value for CO = 0.6 \$ kg^{-1} and for *n*-propanol = 1.43 \$ kg^{-1}).[5, 35, 36] However, the product stream from a CO_2 electrolyzer producing CO and H_2 may be used with minimal processing/purification in a subsequent step producing higher value products (e.g., for production of C_x (x >= 1) compounds through the Fischer-Tropsch process, for catalytic methanation of syngas, or for biological or fermentation-based processes producing high-value alcohols).[5, 35-38] The primary catalysts which are conventionally used in a H_2O/CO_2 co-electrolysis process are Ag and Au-based catalysts. These catalysts have the highest selectivity for CO but are prohibitively expensive for large scale use.[39-41] Therefore, earth-abundant non-precious metal catalysts are increasingly developed as cathode materials for CO_2 conversion processes.

Among non-precious metal catalysts explored, atomically dispersed, transition metal-nitrogen-carbon (M-N-C) catalysts have proven to be highly selective for CO_2 reduction.[12, 42] Metal-free N-C catalysts also show substantial selectivity for CO_2 reduction with lower activity compared to their metal counterparts.[32] While Fe-containing M-N-C catalysts are known to catalyze the reduction of CO_2 to CO at

low overpotential, Mo-containing M-N-C catalysts have active Mo-N_x centers which may catalyze the competing HER reaction.[7, 12, 32, 42, 43] The active sites of M-N-C catalysts are diverse and complex, containing both nitrogen coordinated metal sites (M-N_x), and a variety of metal-free (N-C) sites whose participation in the CO_2RR vs. HER is highly dependent on the specific N-moiety and the surrounding chemical environment.[7, 12, 42] Fe-N-C catalysts are highly selective for CO formation at low overpotential (E > -0.50 V_{RHE}), while the Ni-N-C catalyst boasts the lowest Tafel slope for CO_2 reduction to CO and generally the highest overall CO production rates at higher overpotential (E < -0.75 V_{RHE}).[44] Generally, mono-metallic M-N-C catalysts which have substantial selectivity to CO (e.g., M-N-C catalysts where M = Fe, Ni, Mn, Cr, and to a lesser extent Co) have a potential-dependent faradaic efficiency for CO formation.[7, 45] As more reductive potentials are applied, the faradaic efficiency (FE) for CO formation will reach a maximum (e.g., > 90 % for Fe and Ni-containing M-N-C) and then decrease as HER activity increases.[45] This offers a dynamic control over the syngas or CO:H_2 product ratio by changing the applied reductive potential. The selectivity of several M-N-C catalysts for syngas generation are summarized in Table S1. The ability to selectively tailor the ratio of CO:H_2 in the produced syngas in a single reaction enables a desired syngas compostion (to fit a desired application) to be realized without the need for further downstream mixing or processing.

One approach to selectively tailor the ratio of CO:H_2 in syngas from the CO_2RR was presented by Huan et al.[33] In this work, they demonstrated that a structure-selectivity relationship could be used to tailor the syngas composition. Using a Fe-N-C catalyst, they found that atomically dispersed Fe-N_4 sites are highly selective for CO production, reaching a FE_{CO} over 90% at low overpotentials. In contrast, it was shown that over Fe-based nanoparticles, proton reduction to H_2 dominates. Therefore, by selectively tailoring the amount of atomically dispersed Fe-N_4 sites to Fe-nanoparticles the ratio of CO:H_2 could be tuned between 0 - 4.

This study offers a unique pathway to selectively tailor the syngas compostion. By controlling the synthesis of an atomically dispersed mono- and bi-metallic Fe, Mo and FeMo-N-C catalysts, in which the Fe-N_x sites selectively reduce CO_2 to CO, while the Mo-N_x sites reduce H^+ to H_2. Over mono-metallic Fe-N-C, a FE_{CO} greater than 90% could be achieved. Similarly, over Mo-N-C, a FE_{H2} of greater than 90% was achieved. By synthesizing a bi-metallic FeMo-N-C catalyst and tailoring the ratio of the Fe-N_x to Mo-N_x sites, the product ratio of CO:H_2 is easily tuned. Furthermore, by simultaneously utilizing the potential dependence on product selectivity, a tunable CO:H_2 ratio between 0.25 – 5 was realized. These results demonstrate a novel approach to selectively tailor the syngas over a wide range of compositions in a single reaction.

Results and Discussion

Synthesis/Characterization of Atomically Dispersed Metal-Nitrogen-Carbon (M-N-C) Catalysts

Atomically dispersed mono- and bi-metallic M-N-C samples were synthesized using the previously established sacrificial support method (SSM).[30] Briefly, the SSM involves solution phase mixing and mechanical integration of a carbon-nitrogen containing source, nicarbazine, with a hard silica template, and metal salt precursors. The precursor mixture was then pyrolyzed in a reductive 7% H_2 atmosphere, followed by a hydrofluoric acid wash which removed the silica template. A second pyrolysis under a

reductive 10% NH_3 atmosphere was performed which removes any fluorinated species, increases the graphitization content, etches micropores, and thereby enhances the catalytic activity.[17] The synthesis temperature was adjusted for the bi-metallic FeMo-N-C samples to preserve atomically dispersed metallic sites. Atomically dispersed M-N_x active sites provide for the highest atom use efficiency and allow for a selectivity study without the influence from a separate metallic phase.[46] When a high temperature of 975 ˚C or 950 ˚C was used in either the 1st or 2nd pyrolysis for the FeMo-N-C samples, the presence of a metallic nanoparticle phase was observed by X-ray diffraction (XRD) shown in Fig. 1a and observed by scanning transmission electron microscopy (STEM) (Figure S1). The larger high contrast spots (Fig. S1) correspond to alloyed nanoparticles of Fe/Mo metal, which are only observed at higher pyrolysis temperatures for the bi-metallic samples. This effect is not observed for the mono-metallic (Fe/Mo-N-C) catalysts, which maintain atomically dispersed sites at the higher pyrolysis tempeatures (Figures S2 a & b). The notation used throughout this study for the synthesis temperature(s) in ˚C for mono- and bi-metallic M-N-C catalysts is written as M-N-C (X/Y), where X = the first pyrolysis temperature, while Y = the second pyrolysis temperature (e.g., FeMo-N-C (975/950) is first treated at 975 ˚C and then 950 ˚C). If no temperature is specified, then a pyrolysis temperature of 650 ˚C was used for both pyrolysis steps.

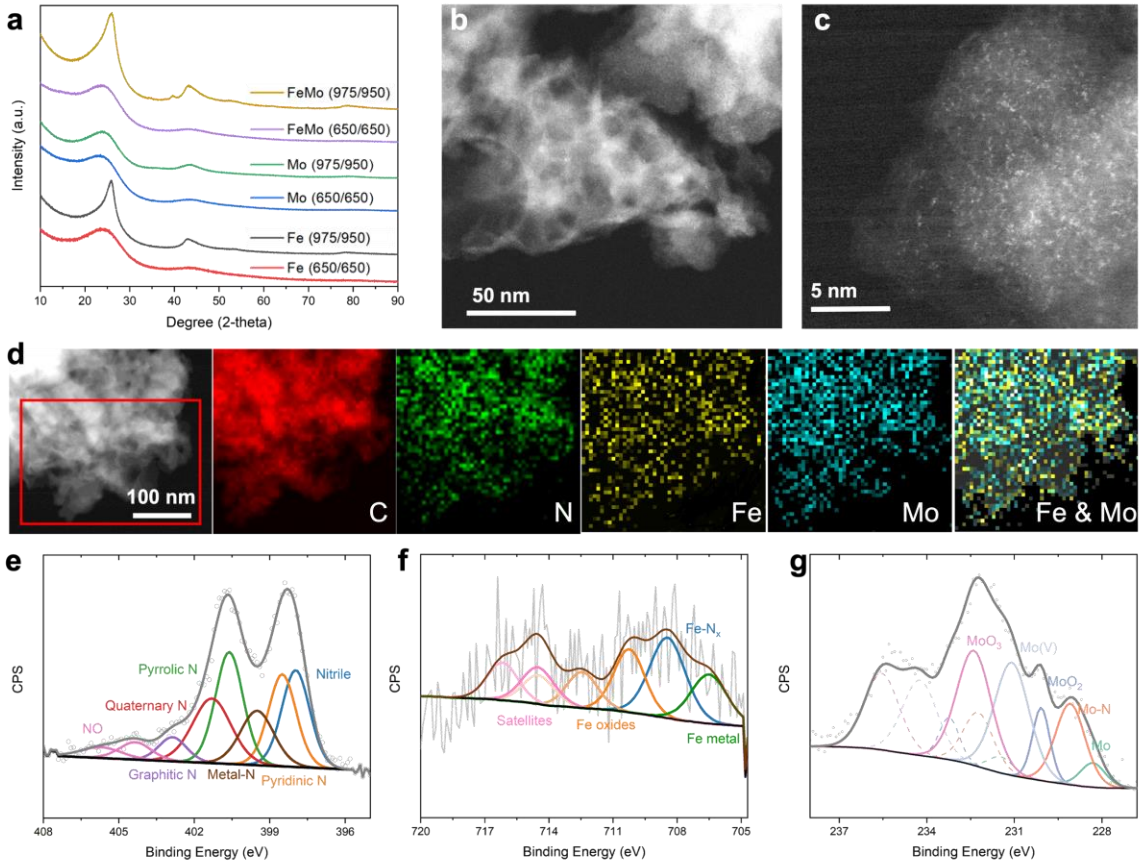

2. 1: Figure 1: Physical Characterization of Catalysts. (a) XRD patterns for the Fe-N-C, Mo-N-C, and FeMo-N-C catalysts at high and low pyrolysis temperature(s). (b) Low magnification AC-HAADF STEM image of

the FeMo-N-C (650/650) catalyst. (c) High magnification AC-HAADF STEM image of FeMo-N-C (650/650); atomically dispersed Fe and Mo sites are indicated by the high contrast points. (d) AC-HAADF image and corresponding elemental mapping of FeMo-N-C (650/650). XPS spectra of the FeMo-N-C (650/650) catalyst (e) N 1s spectra, indicating the presence of M-Nx moieties. (f) Fe 2p spectra showing the formation of Fe-Nx sites. (g) Mo 3d spectra showing the formation of Mo-Nx sites.

The XRD spectra for the mono- and bi-metallic catalysts synthesized at both the high and low pyrolysis temperatures are shown in Fig. 1a (and Fig. S3 a & b). The mono-metallic Fe/Mo-N-C catalysts and bi-metallic FeMo-N-C synthesized at the lower temperature of 650 ˚C show only the characteristic (002) and (100) peaks for mixed graphitic/amorphous carbon, which suggests that no metallic crystalline phases are present. While the FeMo-N-C pyrolyzed at the higher temperatures (975/950) shows the presence of a metallic crystalline phase at 2θ ~ 39 ˚. The asymmetric peak shape suggests the presence of carbon lattice defects while the increased width of the (002) peak suggests microcrystallites separate from graphitic carbon.[31, 47] The low mag aberration corrected high angle annular dark field (AC-HAADF) image of the FeMo-N-C catalyst in Fig. 1b shows the well defined hierarchical porous structure characteristic of the etched silica template (as confirmed through SEM and BET in Fig. S4 and Fig. S5, respectivley). The high mag AC-HAADF image in Fig. 1c shows distinct bright spots indicating atomically dispersed Fe and Mo sites. Elemental mapping from energy dispersive X-ray spectroscopy (EDS) in Fig. 1d shows the presence and homogenous distribution of C, N, Fe and Mo thoughout the catalyst. The percent atomic concentration (at.%) as obtained by XPS is summarized for the mono- and bi-metallic samples in Table S2 and is found to be a function of the pyrolysis temperature. The C and N at.% was 94.7 % and 2.5 % respectively, for the samples synthesized at the high temperatures (975/950), regardless of the metal dopant(s). The C at. % decreased to 85.1 % and N at. % increased to 9.8 % for the lower pyrolysis temperature FeMo-N-C(650/650) samples. The deconvoluted N 1s X-ray photoelectron spectroscopy (XPS) spectra in Fig. 1e reveals the presence of several N-moieties, assigned to be pyridinic (398 eV), pyrrolic (401 eV), quaternary (401.5 eV) and graphitic N (403 eV). Furthermore, the formation of nitrogen coordinated metal sites, M-N_x (399.5 eV) is observed. Likewise, the Fe 2p spectra (Fig. 1f) shows the presence of N-coordinated Fe-Nx sites. The Mo 3d spectra further reveals the formation of N-coordinated Mo-N_x sites. Investigation of the X-Ray Absorption Near Edge Structure (XANES) and EXAFS is also evidence of atomically dispersed metallic Fe or Mo in a carbon matrix (Figure S6). The absorption in the Mo-K edge and Fe-K edge shows absorbances for M-N_x coordination and lacks the additional absorbance bands seen for the representative metallic foils. This suggests that a key active site involved in the CO_2RR vs. HER mechanisms are metal-coordinated nitrogen sites (M-N_x) and that it is not an issue of a metallic phase promoting HER as discussed in the synthesis section. Additionally, XPS analysis shows variations in precursor Fe:Mo does not significantly alter the total percentage of M-N_x sites which suggests that the ratio of Fe-N_x to Mo-N_x has a larger influence on the selectivity.

The N 1s (XPS) spectra show that the relative proportions of N-moieties do not depend on the metallic precursor ratio of iron to molybdenum. The four samples with varying precursor ratios of Fe:Mo from 0.25:1 to 1:0.25 show remarkably similar percentages of N-moieties. The N 1s spectra show a high proportion of low binding energy nitrogen moieties such as pyridinic nitrogen and metal-coordinated

nitrogen (i.e., Fe-N_x or Mo-N_x) versus higher binding energy nitrogen moieties which is indicative of favorable catalytic activity. The total metal atom content of atomically dispersed catalysts is difficult to assess and usually underestimated by XPS, so inductively coupled plasma mass spectroscopy (ICP-MS) was utilized to assess the total metal atom percentage (Table S3).

Additionally, according to an opinion article by Artyushkova, the ratio of N 1s low binding energy (BE) to high BE moieties was considered as another metric to standardize.[48] A high ratio of low BE N-moieties less than 400 eV to high BE above 400 eV has been shown to be beneficial for the oxygen reduction reaction (ORR). Similarly, a high concentration of pyridinic nitrogen species has been shown to promote CO_2 reduction, hypothesized to be through offering an abundance of chemisorption sites.[49, 50] For the CO-specific catalysts, the series of FeMo-N-C catalysts shows an increase in this ratio compared to the mono- and bi-metallic catalysts synthesized at higher temperatures (975/950), which suggests a more favorable local chemical environment for CO_2 reduction (Table S4).

The Raman spectra of graphitic carbon shows a characteristic E_{2g} vibrational mode at ~1581 cm^{-1}(G-band) while disordered carbon shows a peak at ~1350 cm^{-1}(D-band). There is a decreasing I_d/I_g ratio, which represents the ratio of D-band to G-band Raman peaks, with an increase in pyrolysis temperature (Fig. S7). This reveals an increase in the relative graphitization at the higher pyrolysis temperature(s), which is known to be autocatalyzed by the presence of iron at high temperatures. Evidence of local graphitization can be seen by annular bright-field (ABF-STEM) imaging in Fig. S8, via the presence of graphitic sheets which are observed for pyrolysis temperatures of 950 ˚C and above. The level of graphitization can have a substantial impact on catalyst morphology and reactivity.[31, 48] Therefore, it is an important metric to standardize for when assessing the influence of precursor metallic ratio on catalytic activity.

Previous studies have shown that atomically dispersed M-N_x sites are often located in the micropores of carbon supports.[51, 52] Furthermore, prior investigation has also shown porosity to be a controlling factor in the CO_2 reduction activity on metal-free N-C active sites.[53] A bimodal pore size distribution with meso/microporosity (a characteristic feature of catalysts synthesized using the SSM) is observed here (Fig. S5) which has been shown to have beneficial electrocatalytic properties.[54] The pyrolysis temperature also will greatly influence the overall surface area and electrochemically active surface area. An increase in the electrochemical surface area (ECSA) will lead to a higher overall reaction rate. In order to study the correlation between the Brunauer-Emmett-Teller (BET) surface area and the electrochemically active surface area, the double layer (D-L) capacitance values are plotted against the BET surface area values. A positive correlation is seen between the higher synthesis temperatures and

noteable increases in BET surface area, as well as D-L capacitance (Figure S9), which results in an increase in the geometric current density (Figure S10).

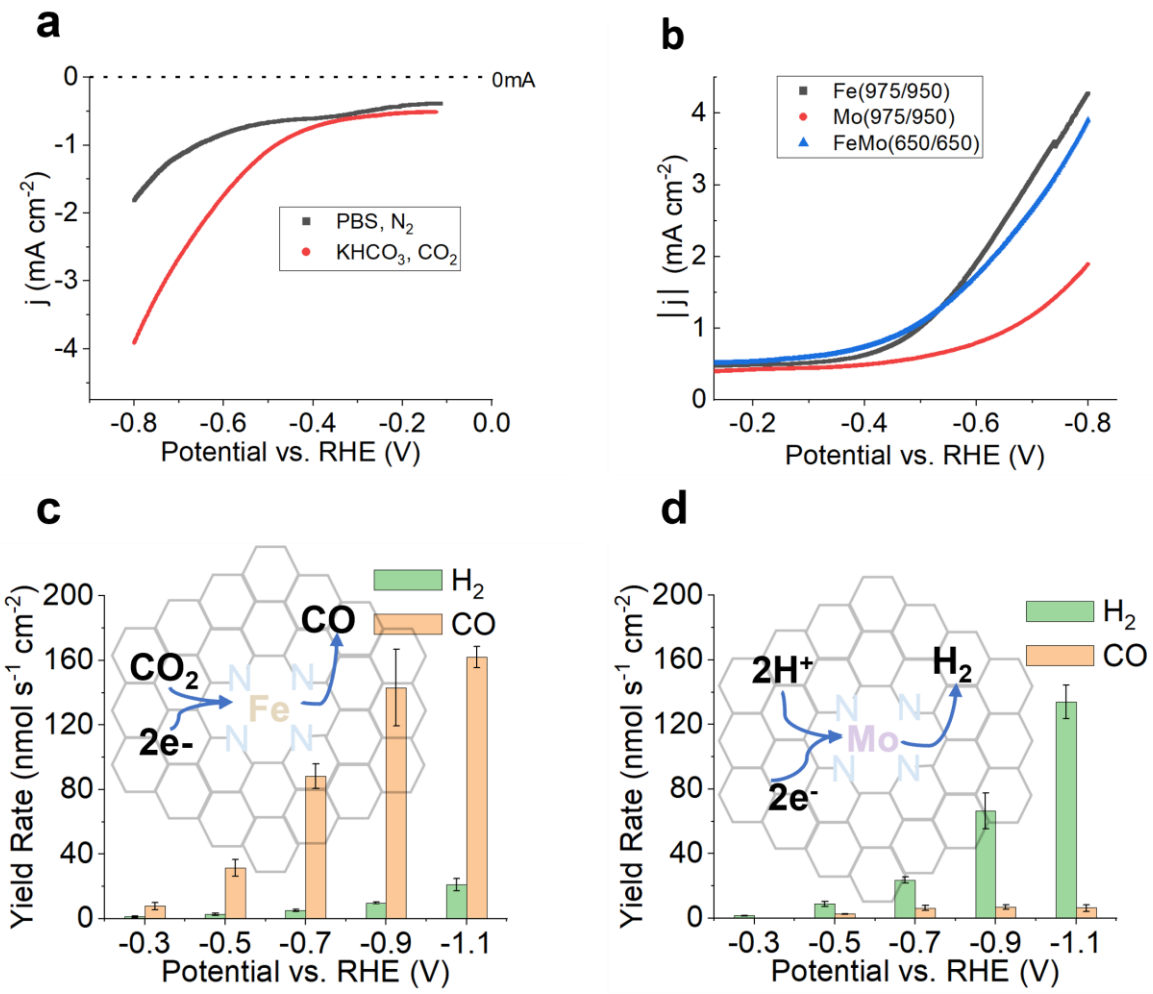

2. 2 : Figure 2: (a) LSV curves (scan rate of 1 mV/s) in N_2-saturated 0.1 M PBS (K_2HPO4/KH_2PO_4) solution and CO2-saturated 0.1 M $KHCO_3$ solution using 0.3 mg cm_{geo}^{-2} catalyst loading for FeMo-N-C (650/650). (b) Current density in CO_2-saturated 0.1 M $KHCO_3$ using 0.3 mg cm_{geo}^{-2} catalyst loading for mono- and bi-metallic samples. CO_2RR yield rates (nmol s^{-1} cm^{-2}) for (c) Fe-N-C and (d) Mo-N-C, using a flow cell system.

Electrochemical Performance of Mono- and Bi-metallic M-N-C Catalysts

After obtaining a full physical characterization of the catalysts, It was hypothesized, given that Fe-N-C is highly selective for CO formation while Mo-N-C catalysts have high HER activity, that altering the ratio of iron to molybdenum in the catalyst could be utilized as a tunable parameter for varying syngas composition.

Firstly, the aqueous-phase CO_2RR vs. HER activity was investigated for the mono- and bi-metallic M-N-C samples. Linear sweep voltammetry (LSV) was performed at a scan rate of 1 mV s^{-1} between 0.0

and -0.8 V_{RHE} (e.g., sweeping from 0.0 V to -0.8 V vs. RHE in the cathodic direction). Figure 2a shows the differences in current response between the samples in the presence or absence of CO_2. A substantial increase in the current density for the FeMo-N-C under CO_2-saturated *vs.* CO_2-absent conditions is evidence of its activity for the CO_2RR.

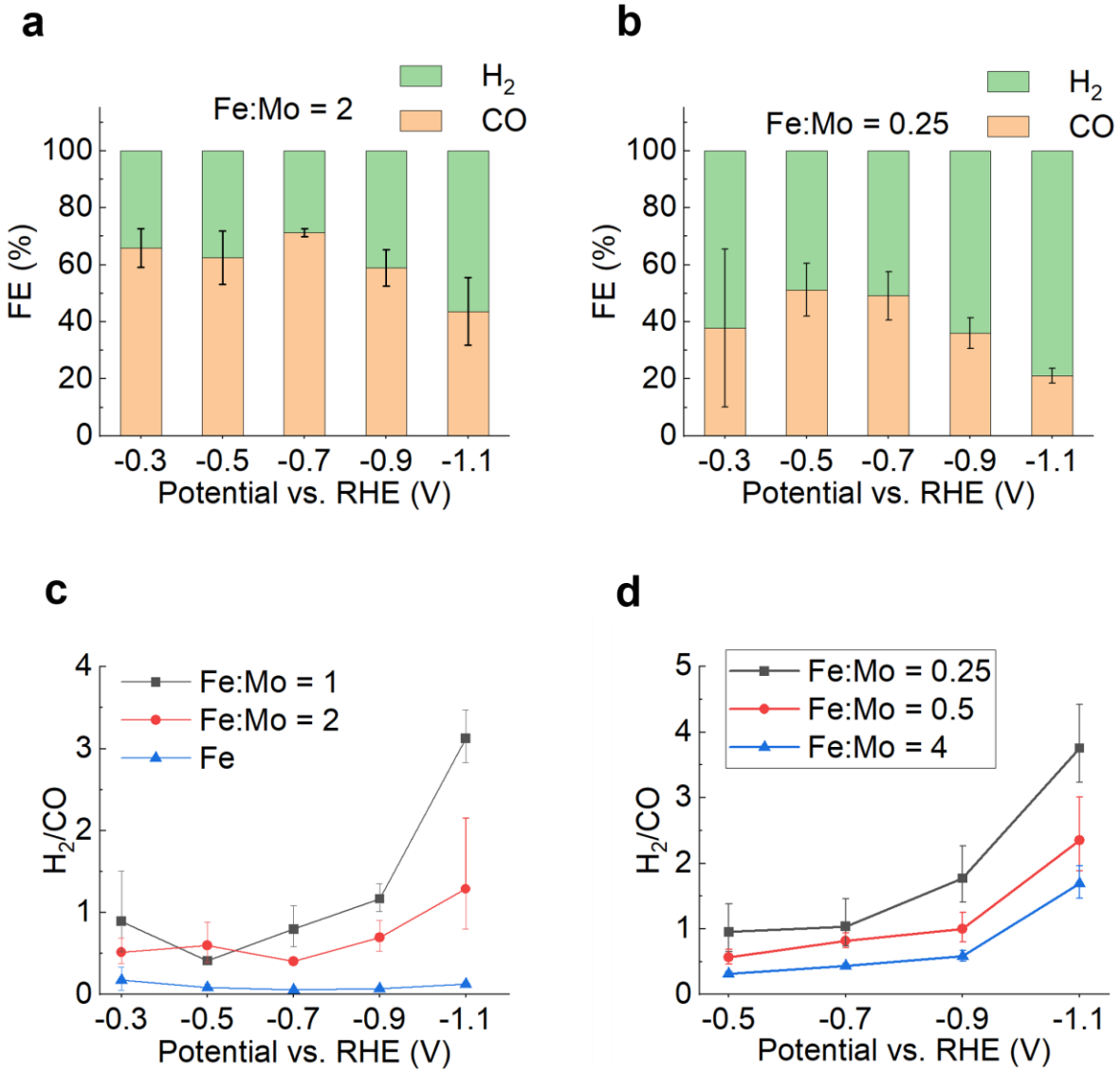

2. 3: Figure 3: Faradaic efficiency (%) for FeMo-N-C (650/650) where the ratio of (a) Fe:Mo = 1:0.5 and (b) Fe:Mo = 0.25:1, using a catalyst loading of 1.0 mg/cm2. (c) and (d) The syngas ratio (H2/CO) vs. cathodic potential for different molar precursor ratios of Fe:Mo and Fe-N-C.

Comparison between LSVs performed in the presence (red curve) and absence (black curve) of CO_2 show substantial CO_2RR activity for Fe-N-C (975/950) and FeMo-N-C (650/650). By contrast, Mo-N-C

(975/950) shows comparable activity for CO_2-saturated and CO_2-absent conditions (Figure S11) suggesting slight activity for the CO_2RR but that the catalyst is mostly selective for the HER. Further, Fe-N-C (975/950) shows an earlier onset potential for the CO_2RR than the HER, confirming its high selectivity towards the CO_2RR. While Fe-N-C has been studied extensively for CO_2 reduction[7, 55], there is a lack of electrocatalytic performance data and material characterization for Mo-N-C which is found here to be highly selective for HER over CO_2 reduction.

It is well-known that the overall activity of aqueous-phase CO_2 electroreduction in a standard two compartment H-cell is limited by the limited solubility of CO_2. To address the limited solubility of CO_2 in aqueous electrolytes, gas diffusion electrode (GDE)-based systems are often employed. The switch from aqueous-phase CO_2 reduction to GDE systems brings with it a whole range of new engineering parameters to optimize such as the inlet pressure, CO_2 purity, humidity, and mass transport within the catalyst pores.[44, 56, 57]. For example, pressurized CO_2 electrolysis has been proposed to allow for an easier integration into dowstream processes such as Fischer-Tropsch syntheses at the expense of reduced electrolyte conductivity and higher cell voltages.[57] This narrow pressure range and additional problems such as CO_2 crossover, reduced long term stability, and carbonate formation are additional hurdles to commercialization of the technology.[58-60] GDE setups bypass the solubility challenge which aqueous-based systems face through the creation of a triple-phase boundary which allows for higher conversion rates that are more feasible for industrial applications.[5, 44, 61] For this reason, a custom-built GDE flow cell system was employed to examine the catalyst selectivity for the CO_2RR vs. HER (Figure S12). A simplified electrochemical cell was employed in order to reduce the process parameter space so that a few key parameters could be independently studied. The electrochemical setup showed relative stability for 3 h. After 3 h, liquid that bypassed the PTFE layer of the cathode was observed in the gas chamber which resulted in a significantly reduced FE_{co}, most likely due to reduced CO_2 transport to the catalyst layer (Figure S13). The process parameters were examined for the new FeMo-N-C materials within the range where the electrochemical cell showed stable performance. The material composition, applied reductive potential, catalyst loading, and electrolyte type/concentration were systematically investigated as engineering controls to influence the product distribution.

The ratio of atomically dispersed Fe to Mo atoms in the catalyst was used as a parameter to influence the final ratio of CO to H_2 in the product gas. Accordingly, the molar precursor ratio of iron to molybdenum was varied in the FeMo-N-C (650/650) catalyst series to observe the compositional changes in the produced syngas. The yield rate and faradaic efficiency for CO/H_2 for the bi-metallic samples show there is a positive correlation between the ratio of iron to molybdenum and the faradaic efficiency (%) for CO. An increase in the iron to molybdenum molar precursor ratio results in the generation of more Fe-N_x sites and therefore an increase in selectivity for CO_2 reduction *vs.* HER. The expected selectivity for the CO_2RR to CO (Fe-N-C) and the HER (Mo-N-C) for the mono-metallic samples was confirmed. Fe-N-C in Fig. 2c is highly selective for CO generation and achieves a FE_{CO} between 84 % to 94 % over the potential window from -0.3 V to -1.1 V vs. RHE ($FE_{CO,\ max}$=94.4 % at -0.7 V). This selectivity of the Fe-N-C catalyst surpasses that of Ag nanoparticles, known to be selective for CO production (Fig. S14). By contrast, in Mo-N-C (975/950), Fig. 2d shows a high selectivity for the HER over the CO_2RR over the entire potential window from -0.3 V to -1.1 V_{RHE}. The increased selectivity for H_2 over CO for Mo-N-C is higher than other M-N-C catalysts known to have a reduced faradaic efficiency for CO formation such as Co-N-C studied by

Pan et al.[62] For the series of bi-metallic FeMo-N-C catalysts, we see a mixed selectivity for CO_2RR/HER which is intermediate between Fe-N-C and Mo-N-C. The onset potential for CO generation for the iron-containing M-N-C catalysts is near the thermodynamic minimum while for the Mo-N-C catalyst, the onset potential for CO generation is between *ca.* -0.3 to -0.5 V_{RHE} and FE_{CO} reaches a maximum of only *ca.* 22 % between -0.5 V and -0.7 V_{RHE} (Figure S15).

In terms of CO_2RR to CO activity, the bimetallic FeMo-N-C (650/650) with a ratio of Fe:Mo = 1 reaches a maximum CO partial current density of -7.1 mA cm^{-2} at -0.9 V_{RHE}. While, as expected, the mono-metallic Fe-N-C (975/950) was the most CO-selective catalyst for FE_{CO} (Fig. 2c) and boasted the largest CO partial current density of -31.3 +/- 1.3 mA cm-2 at a potential of -1.1V_{RHE} (Fig. S16) with a corresponding FE_{CO} = 88.6 %. The large difference in the maximum CO partial current densities between the catalysts synthesized at different temperatures is likely a result of changes in the catalyst morphology which results in Fe-N-C (975/950) having a higher BET surface area and double-layer capacitance than the FeMo-N-C (650/650) series of catalysts (Figures S9 and S17). These morphological changes are due to the limiting synthesis conditions required to maintain atomic dispersion in the bi-metallic samples, which is necessary for investigating the selectivity changes for CO:H_2 resulting from changes in the quantity of Fe-N_x and Mo-N_x sites.

By comparing Fig. 3a and Fig. 3b, it is observed when the ratio of iron to molybdenum is varied there is a marked shift in the selectivity from the CO_2RR to HER at both low and high overpotentials. Figure 3 shows several interesting trends when the ratio of iron to molybdenum is varied. As expected, when the ratio of iron to molybdenum is increased (generating more Fe-N_x sites), the catalyst becomes more selective for the CO_2RR, resulting in decreased (H_2:CO) syngas compositions. ICP-MS was used to confirm that changing the Fe molar precusor ratio of Fe:Mo, results in corresponding changes in the molar ratio of Fe:Mo in the final catalyst, (e.g., for a precursor molar ratio of Fe:Mo = 0.25 and 4, the final atomic weight percentage ratio of Fe:Mo was determined to be 0.28 and 0.97, respectively (Table S3)). When the molar precursor ratio of Fe:Mo is 0.25, creating significantly more Mo-N_x sites, the $j_{CO,\,max}$ = -5.3 mA cm_{geo}^{-2} (FE_{co} = 36.1 % at -0.9 V_{RHE}). When this ratio is increased to 4.0, creating significantly more Fe-N_x sites, the maximum CO partial current density and FE_{CO} increases to $j_{CO,\,max}$ = -12.3 mA cm_{geo}^{-2} (FE_{co} = 63.2 % at -0.9 V_{RHE}). Fig. 3c and Fig. 3d show that the syngas ratio is relatively independent of potential and depends primarily on the ratio of Fe:Mo until *ca.* -0.9 V_{RHE}. Once the potential is made more negative than -0.9 V_{RHE}, the syngas ratio depends on both the potential and the ratio of Fe:Mo as is also observed in Fig. S18, where the largest shifts in H_2/CO are seen for the most cathodic potentials investigated (*e.g.*, -0.9 V_{RHE} and -1.1 V_{RHE}). By utilizing the changes in the ratio of Fe:Mo and altering the reductive potential, it was shown

(Fig. 3d) that the H_2:CO ratio could be tuned between 0.2 – 4 (resulting in a corresponding CO:H_2 ratio of 0.25 – 5).

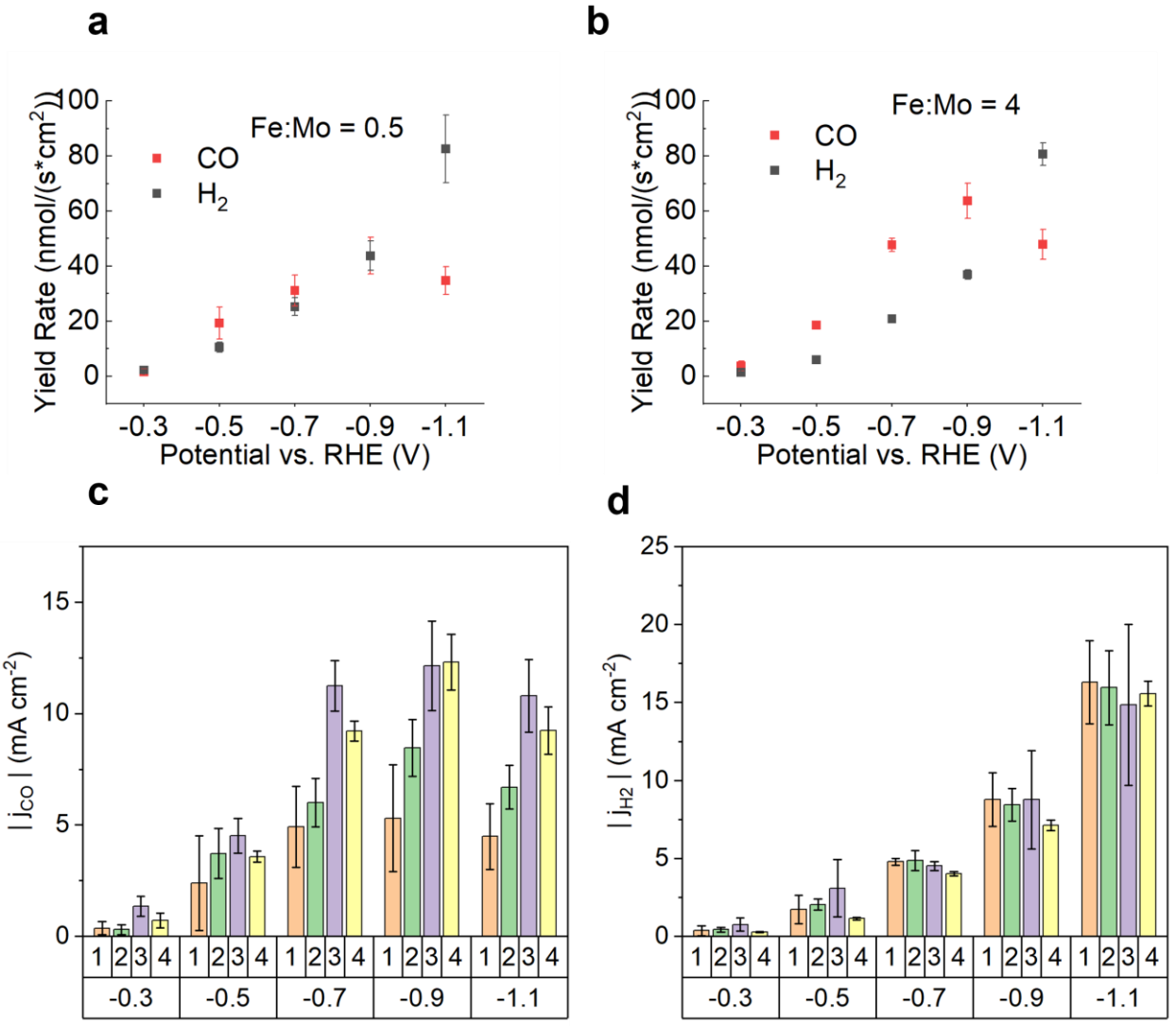

2. 4: Figure 4. Electrochemical performance of the bi-metallic FeMo-N-C samples. Yield Rate (nmol s-1 cmgeo-2) for (a) Fe: Mo = 0.5:1 and (b) Fe: Mo = 1:0.2. The magnitude of the (c) CO partial current density and (d) H2 partial current density (V vs. RHE). Samples labeled 1, 2, 3, 4 correspond to a ratio of Fe:Mo = 0.25, 0.5, 2, 4, respectively.

Importantly, the partial current density for the HER (j_{H2}) is much less sensitive to variations in the ratio of iron to molybdenum ($j_{H2,\,max}$ = *ca.* -15 mA cm^{-2} for all FeMo-N-C (650/650) samples) as can be seen when comparing Fig. 4c and Fig. 4d. The partial current density for the HER (j_{H2}) (Fig. 4d) increases monotonically as the potential is made more reductive from *ca.* -0.5 mA cm^{-2} at -0.3 V_{RHE} to *ca.* -15 mA cm^{-2} at -1.1 V_{RHE} regardless of the precursor Fe:Mo ratio. Variations in the Fe:Mo precursor ratio does not result in a significant change in j_{H2}. It was observed that during the catalyst synthesis, molybdenum has a much higher retention in the final sample (Table S3): varying the metallic precursor ratio causes a more

significant weight percent (wt.%) change for iron than for molybdenum (e.g., increasing precursor Fe:Mo from 0.25 to 4.0 results in a much larger relative increase in iron (from 0.40 to 1.46 wt.% Fe) than a relative decrease for Molybdenum (from 1.46 to 0.99 wt.% Mo)). This suggests, that for reducing the final Mo at.% (Mo-N_x sites), larger reductions in the molar Mo precursor ratio need to be considered to achieve the corresponding change in the molar Mo at.% in the final material. The different final atomic metal wt.% sensitivity to precursor ratio has significant implications in terms of the CO_2RR activity of the resulting catalysts (Fig. 4a and Fig. 4b). By changing the Fe:Mo precursor ratio from 0.5 to 4, a large increase in the yield rate of CO (as more Fe-N_x sites are present) is seen when comparing Fig. 4a and Fig. 4b. In contrast, the yield rate of H_2 remains almost unchanged despite changes in the Fe:Mo precursor ratio. This supports the ICP-MS observation that changes in the final Mo wt.% are less sensitive to changes in the Fe:Mo precursor ratio (e.g., a large quantity of Mo-N_x sites remain even for large Fe/Mo precursor ratios). A similar trend is seen for samples with other Fe:Mo ratios shown in Fig. 4c and Fig. S19. The corresponding j_{CO} and j_{H2} partial current densities for the FeMo-N-C catalysts at Fe:Mo ratios of 0.25, 0.5, 2 and 4 are shown in Fig. 4 c & d.

The trends for faradaic efficiency (Fig. 3) and partial current density (Fig. 4) for the FeMo-N-C (650/650) samples demonstrate that the syngas composition can be tuned through either changes in the ratio of Fe:Mo, and/or changes in the reductive potential.

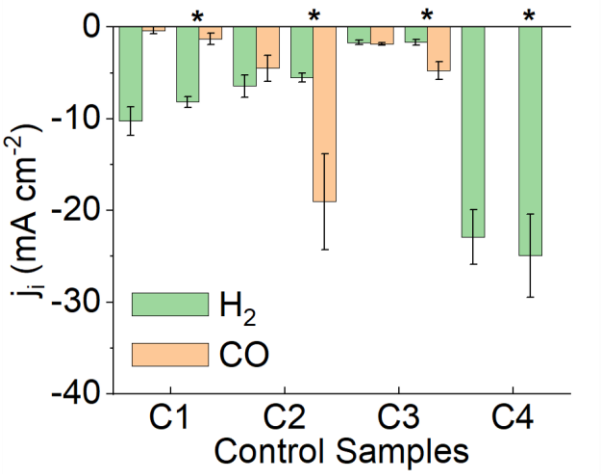

2. 5: Figure 5. Partial current density for H_2 or CO, under several control experiments, using the FeMo-N-C (650/650) (Fe:Mo = 1:0.5). Low catalyst loading (no asterisk) is 0.1 mg cm_{geo}^{-2} while high catalyst loading (asterisk *) is 1.0 mg cm_{geo}^{-2}. Control 1 (C1): N_2 inlet, 0.5 M $KHCO_3$(aq); Control 2 (C2): CO_2 inlet, 0.5 M $KHCO_3$(aq); Control 3 (C3): CO2 inlet, 0.1 M $KHCO_3$ (aq); Control 4 (C4): N_2 inlet, 0.5 M potassium phosphate buffer (PBS) (pH =7.5) (aq).

In addition to factors intrinsic to the catalyst composition which influences selectivity/reactivity, the reaction conditions were also investigated to uncover their role in syngas selectivity. Several control experiments were conducted to assess the influence of reaction conditions on CO_2RR *vs.* HER activity (Fig. 5). These controls investigate the role of the catalyst loading, electrolyte type/concentration, and inlet feed composition on CO_2 reduction vs. HER activity. To confirm the CO_2 supplied from the gas feed is the

main contributor to the observed CO_2RR products, a control was conducted using a N_2 gas feed in a 0.5M $KHCO_3$ electrolyte. It is known that in the absence of gas phase CO_2, some CO_2 can be supplied through the $KHCO_3$ electrolyte resulting in limited CO production. The role of bicarbonate in supplying CO_2 to the cathode is highly important for many different systems.[63] Some groups have even used highly concentrated bicarbonate electrolytes as CO_2 sources for formate production to avoid the need for a pure CO_2 feed stream.[64, 65]. Control 1 shows that even in the absence of a gaseous CO_2 feed, there is still CO formation from CO_2 supplied by the electrolyte. A trace amount of CO is even produced (-0.19 mA cm_{geo}^{-2} at -1.38 V_{RHE}) using bare Sigracet 29 BC carbon GDL, 100 % CO_2 feed, and 0.5M $KHCO_3$ but no CO is detected for potentials less cathodic than -1.38 V_{RHE} (Fig. S20). This is evidence that the bare carbon paper itself is sufficient for trace CO_2 reduction given a sufficiently high overpotential. Control experiment 2 shows that the catalyst loading can have a significant effect on the CO_2RR/HER selectivity. When the catalyst loading is increased from 0.1 to 1.0 mg/cm^2 (denoted by an *), there is an increase in the CO partial current density and resultant increase in the FE_{CO} from 40.4 % to 76.3 %. The effect of the catalyst loading on the syngas selectivity is rooted in changes in the morphology of the catalytic layer, the active site accessibility, and the mass transfer limitations for the HER and CO_2RR. Previous studies have shown that even the method of deposition (e.g.,dip coating, brush painting, drop casting, or spray coating) of the catalyst layer can result in significant morphology changes which influence catalyst selectivity.[66] The catalyst layer thickness will also increase with increased loading which will alter the potential drop across that layer and the resulting selectivity. Both the catalyst layer thickness and the change in morphology with respect to catalyst loading may ultimately have a significant effect on the observed selectivity.[66-68] The third control experiment is evidence that the electrolyte concentration plays a significant role on the observed CO_2RR/HER activity, where the high concentration 0.5M $KHCO_3$ electrolyte showed significantly higher CO and H_2 partial current densities (at both high and low catalyst loadings) than the 0.1M $KHCO_3$ electrolyte. This is likely due to a decrease in the ohmic resistance and an increase in the electrolyte buffering capacity at higher bicarbonate concentrations. There does not appear to be a statistically significant effect on the selectivity by changing the electrolyte concentration alone which seems to point to the fact that the change in the electrolyte conductivity has a greater effect than its buffering capacity on influencing the overall activity. Control 4 confirms the source of CO to be largely from the CO_2 feed gas with a small contribution from the $KHCO_3$ electrolyte. By eliminating both the CO_2 gas feed and CO_2 containing $KHCO_3$ electrolyte and utilizing a N_2 gas feed with a phosphate buffer solution (PBS), no CO was detected during the electrolysis which is evidence that the CO originates from the cathodic reaction.

Conclusions

In summary, a novel approach to tailor the CO:H_2 composition of syngas produced through the electrochemical CO_2RR was demonstrated by selectively tuning the ratio of atomically dispersed Fe-N_x and Mo-N_x sites in a bi-metallic FeMo-N-C catalyst. It was demonstrated that the ratio of Fe:Mo in the catalyst could be altered with minimal effect on the catalyst's local chemical environment, such as degree of graphitization, N-moiety content, and morphological characteristics. This enabled changes in the CO:H_2 ratio to be attributed to changes in the quantities of Fe-N_x and Mo-N_x sites, rather than to physical changes in the cataysts. Among the series of bimetallic FeMo-N-C catalysts, the catalyst with the highest Fe:Mo ratio of 1:0.25 shows the highest CO production rate and faradaic efficiency. The catalyst with the lowest Fe:Mo ratio of 0.25:1 shows the lowest FE_{CO} and j_{CO}. The possibility for a dynamic control of the syngas

composition was shown by changing the reductive potential. As demonstrated for the FeMo-N-C catalyst, a reductive potential between -0.5 to -0.7 V_{RHE} yielded CO as the major product, while operating at more reductive potentials yielded H_2 as the major product. By employing changes in the quantity of Fe-N_x to Mo-N_x sites and changes in the applied reductive potential, syngas ratios of CO:H_2 between 0.25 – 5 were obtained. The unique approach shown here provides a pathway to selectively tailor the ratio of CO:H_2 in syngas, produced in a single reaction, which eliminates the need for downstream mixing to achieve a desired composition.

Methods

Synthesis of atomically dispersed Fe/Mo/FeMo-N-C

The series of Fe, Mo and FeMo-N-C catalysts utilized in this work were synthesized following the sacrifical support method. For a typical synthesis (taking FeMo-N-C as an example), 6.25 g nicarbazin; 0.6 g iron nitrate nonahydrate; 0.26 g ammonium molybdate tetrahydrate (The amount of metallic precursor is calculated such that the total number of metal atoms in each catalyst is the same); 1.25 g LM-150; 1.25 g OX-50 and 0.5 g stöber spheres were dispersed in water, sonciated for 30 min and dried at 45 ˚C under constant stirring. The resulting powder is ball-milled at 45 Hz for 1 hour, and then is pyrolyzed under 7 % H_2 for 45 min at 650 ˚C. The powder is ball-milled again and etched with 40 wt. % HF for 4 days. The mixture is washed until pH $\geq$ 5. After drying, the powder undergoes a second pyrolysis for 30 min at 650 ˚C under a 10 % NH_3 followed by a final ball-milling step.

For the mono-metallic Fe-N-C and Mo-N-C, the synthesis is identical with only the pyrolysis temperatures being changed to 975 ˚C in the first pyrolysis and 950 ˚C in the second.

For comparison, unsupported Ag nanoparticles were purchased having particle size < 100 nm and a 99.5 % (trace metal basis) purity.

Physical Characterization

The formation of atomically dispersed metal sites and catalyst strcuture were analyzed by aberration-corrected scanning transmission electron microscopy and energy dispersive X-ray spectroscopy (EDS) using a JEOL ARM300CF at an accelerating voltage of 300 kV. The surface morphology of the catalyts was visualized by scanning electron microscopy using a FEI Magellan 400 XHR SEM. The surface chemical structure, valence state and composition was analyzed using X-ray photoelectron spectroscopy performed on a Kratos AXIS Supra spectrometer with a monochromatic Al Kα source (The raw N 1s and Mo 3d spectra are given in Fig. S21 and S22, respectivley). The crystalline structure of the catalysts was analyzed by powder X-ray diffraction using a Rigaku Powder X-ray diffractometer. Inductively coupled plasma mass spectrometry was used to quantify the metallic content of the catalysts. N_2 physisorption was performed on a Micromeritics 3Flex Analyzer at 77K. The surface area and pore size distribution were calculated using the Brunauer-Emmett-Teller method and non-local density functional theory model (NLDFT), respectively. Raman spectra were recorded on a InVia, Renishaw Corp., UK system.

XANES/EXAFS

XAS data was collected at the 10-BM beamline of the Advanced Photon Source (APS) at Argonne National Laboratory. The sample was first mixed with some binder and pressed as a pellet. The pellet was then sealed with Kapton tapes in the holder. Measurement was conducted at the Fe K edge and Mo K edge in transmission mode. The data was processed and modeled using the Demeter XAS software package.[69]

The EXAFS amplitude reduction factor S02 was determined based on the fitting of a standard reference material.

Preparation of the working electrode

A GDE was fabricated by hot pressing a Sterlitech PTFE membrane filter to a Sigracet 29 BC GDL carbon paper. For a 1.0 mg/cm^2 loading, the catalyst ink was made by sonicating 900 μL IPA, 100 μL DI water, 10 mg catalyst powder, and 60 μL 5 wt. % nafion ionmor solution (in lower aliphatic alcohols). The ink was spray coated onto a heated carbon paper for the cathode and the anode was bare carbon paper bonded to PTFE. Unsupported Ag nanoparticles (particle size < 100 nm) were purchased from Sigma-Aldrich which have a 99.5 % (trace metal basis) purity and were used in the same ink formulation for Ag-based cathode.

Electrochemical CO_2 Reduction

The electrocatalytic activity was evaluated using a custom-built gas diffusion electrode flow cell (Figure S21) in a three-electrode configuration. Connection to the counter/working electrode was made via alligator clips attached to conductive Cu tape attached to the electrode and isolated from the ionic/electrolyte path. The distance between counter electrode (anode) and working electrode (cathode) was 0.6 cm and was separated by a liquid electrolyte which was recirculated using an anolog variable speed pump (Core Palmer Masterflex, Model No: SK-07555-00). The liquid electrolyte flow rate was measured to be 26.1 +/- 1.1 mL min^{-1}. The CO_2 was Research grade 4.8 purchased from Praxair (99.998%) with < 0.1 ppm CO and < 2 ppm THC (as CH_4). The pure CO_2 gas stream was fed directly to the inlet of the gas chamber of the flow cell at a rate of 10 sccm by means of an Alicat 0-50 sccm mass flow controller. A 5-channel EC-Lab VSP-300 potentiostat was used for electrochemical measurements. Constant potential electrolysis (CPE) was performed across the potential range from -0.3 V vs. RHE to -1.1 V vs. RHE. Each potential was applied for 30 minutes and the current response was measured. Perturbations in current density are due to mechanical disturbance of the cell in removing gas sampling vials for GC analysis. Three gas sampling vials are removed per potential over the thirty minute CA experiment (Figure S23). The reference electrode was a Gaskatel^{TM} reversible hydrogen electrode (RHE) used to apply the selected cathode potential in potassium bicarbonate or phospate buffer solution (PBS) based electrolyte. The

faradaic efficiency for the product(s) detected was calculated based on the charge transferred to obtain the selected product divided by the total charge transferred to obtain all products.

$$FE_i = \frac{N_i n_i F}{\sum N_i n_i F}$$

Where, N_i represents the number of moles of product detected by either GC or ^{1}H NMR, n_i represents the number of moles of e^- transferred per mole of product produced (*e.g.*, 2 for CO and H_2), and F is Faraday's contant (F = 96485 C mol^{-1} of electrons).

Product detection

The gaseous products generated during CO_2 reduction electrolysis were sampled and injected into a dual-column gas chromatograph to detect CO/H_2 along with any possible CH_4 or hydrocarbons. Three 5 mL PTFE/red rubber septa sealed gas vials were collected over the course of every 30 minute chronoamperometry measurement and each were used for separate direct injections into a dual parallel column Agilent 7890B Gas Chromatography unit. Each gas sampling vial was purged with the flow cell effluent by means of an exit needle inserted into the vial to allow the composition of the gas vial to equilibrate with the gas chamber composition. An Agilent HP-MOLESIEVE column connected to a thermal conductivity detector (TCD) using Helium carrier gas was used to quantify CO while the carrier gas was switched to N_2 using the same HP-MOLESIEVE column and TCD detector for H_2 detection. A GS-CarbonPlot column connected to a flame ionization detector was used to screen for any hydrocarbon production. ^{1}H NMR was performed to confirm the absence of any liquid products.

Chapter 2: Supporting Data: Bi-metallic M-N-C (M = Fe, Mo) Catalysts for CO2 Reduction

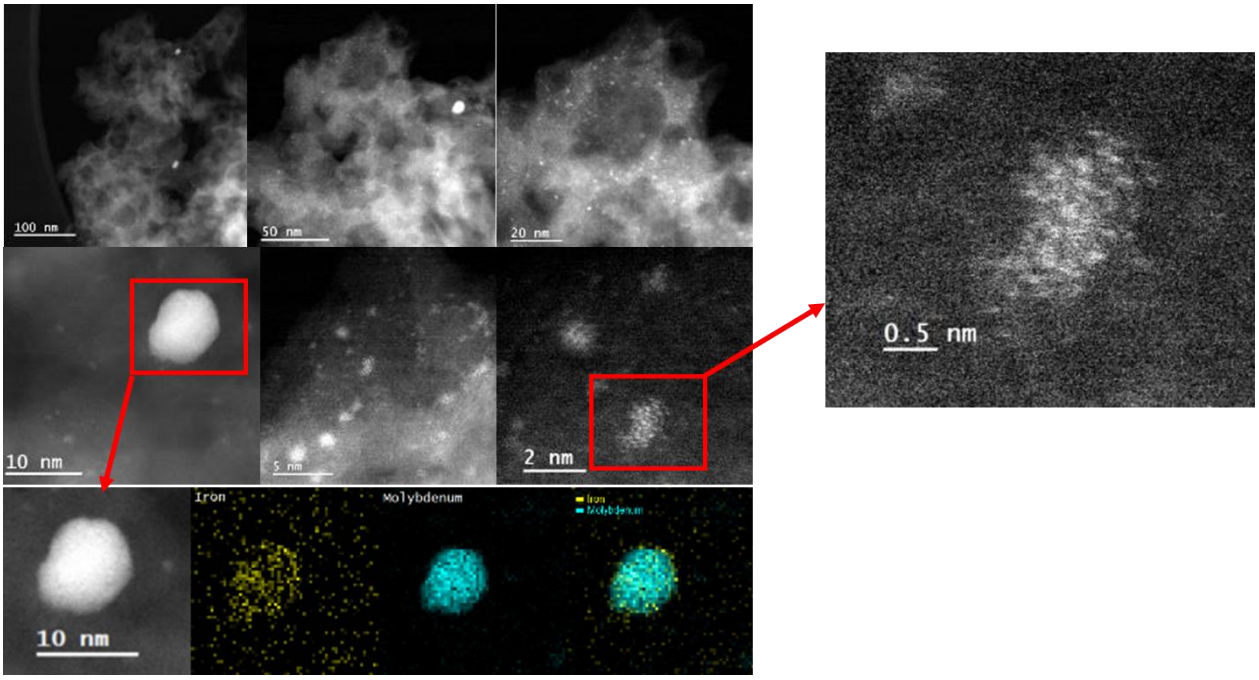

2. S 1: Figure S1: Low & high magnification AC-HAADF STEM images and corresponding EDS mapping of the FeMo-N-C (975/950) catalysts. The high contrasts spots indicate the presence of alloyed Fe/Mo nanoclusters and nanoparticles formed at the higher pyrolysis temperatures.

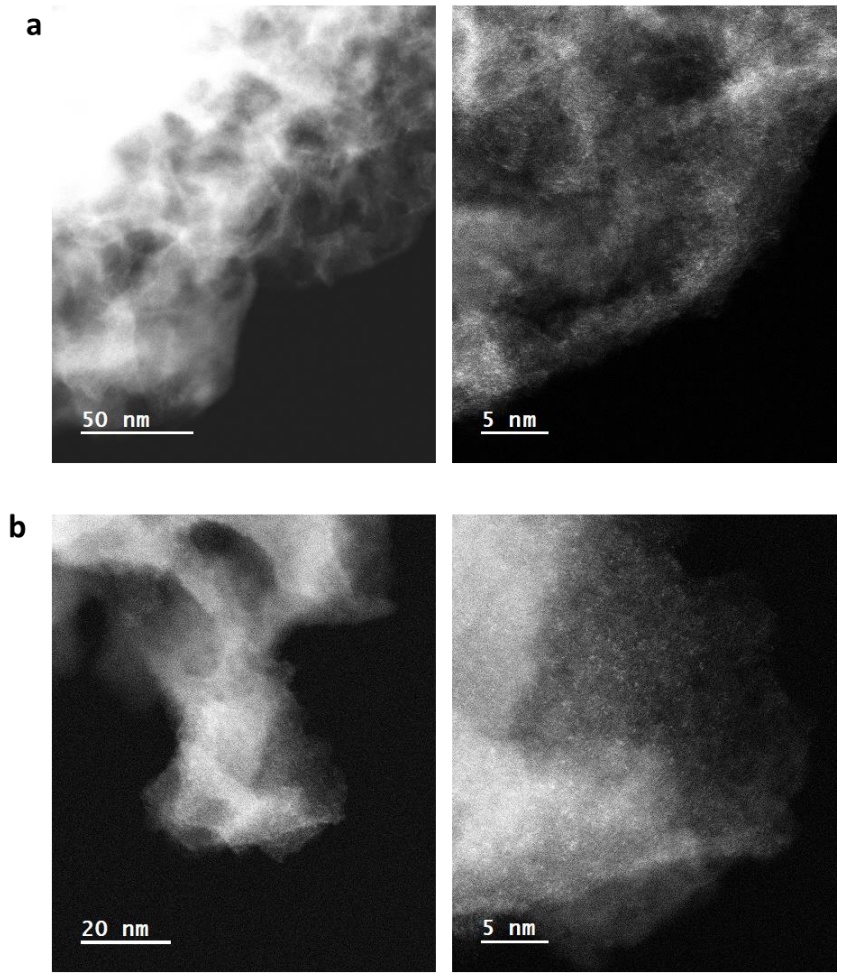

2. S 2: Figure S2: Low & high magnification AC-HAADF STEM images of the Fe-N-C (975/950) and (b) Mo-N-C (975/950) catalysts. The high contrast spots in the high magnification images are atomically dispersed Fe and Mo sites.

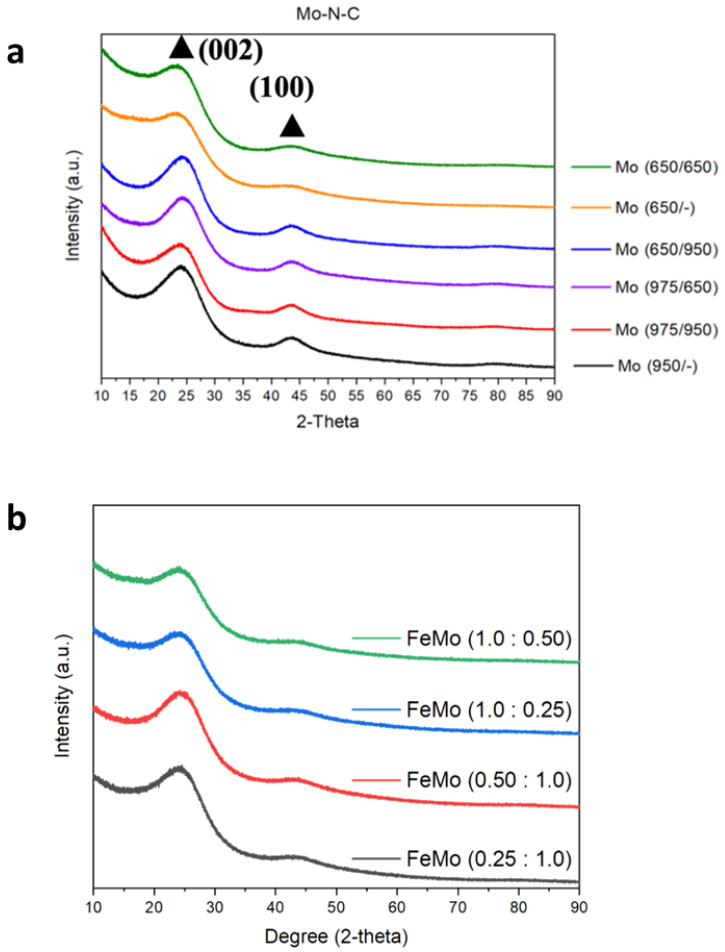

2. S 3: Figure S3: XRD patterns for (a) Mo-N-C at different synthesis temperatures and for (b) The bi-metallic FeMo-N-C catalysts at varying Fe:Mo ratios.

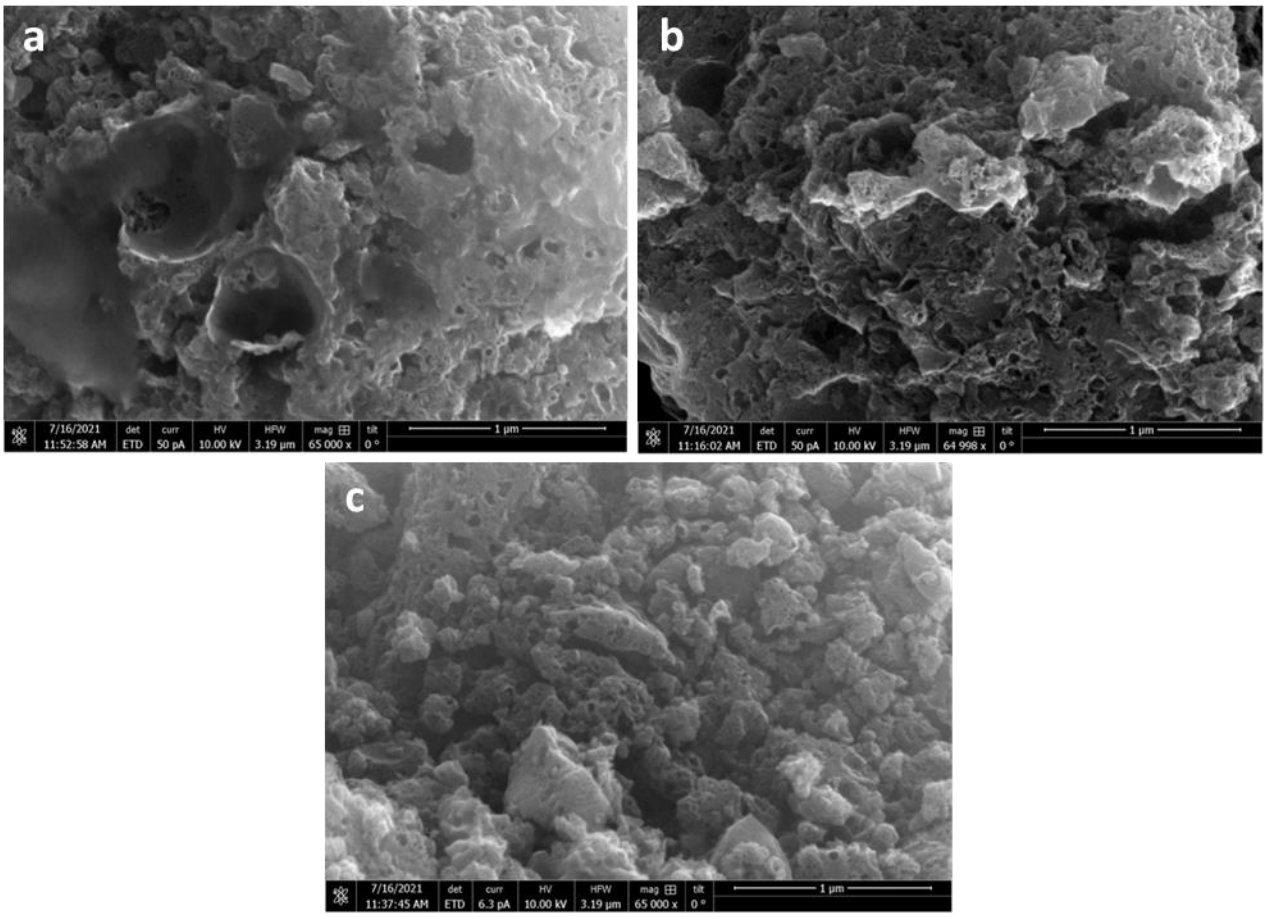

2. S 4: Figure S4: SEM images for (a) Mo-N-C (b) Fe-N-C and (c) FeMo-N-C showing the hierarchical porous structure obtained from the SSM method.

Catalyst	Surface Area (m^2/g)
Fe-N-C (975/950)	959.3
Mo-N-C (975/950)	522.4
FeMo-N-C (650/650)	591.6

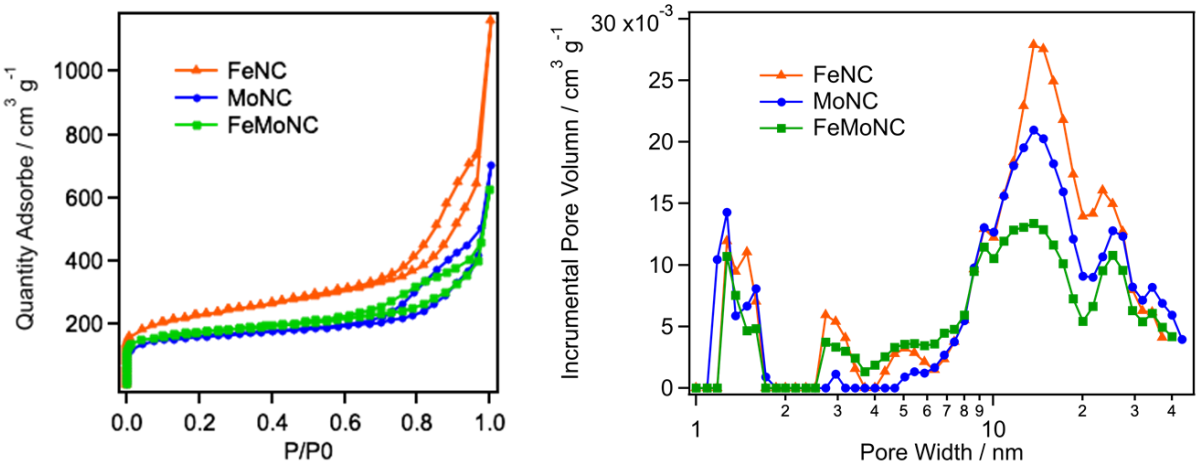

2. S 5: Figure S5: N2 physisorption of the Fe/Mo/FeMo-N-C catalysts with the corresponding BET surface area and pore size distribution.

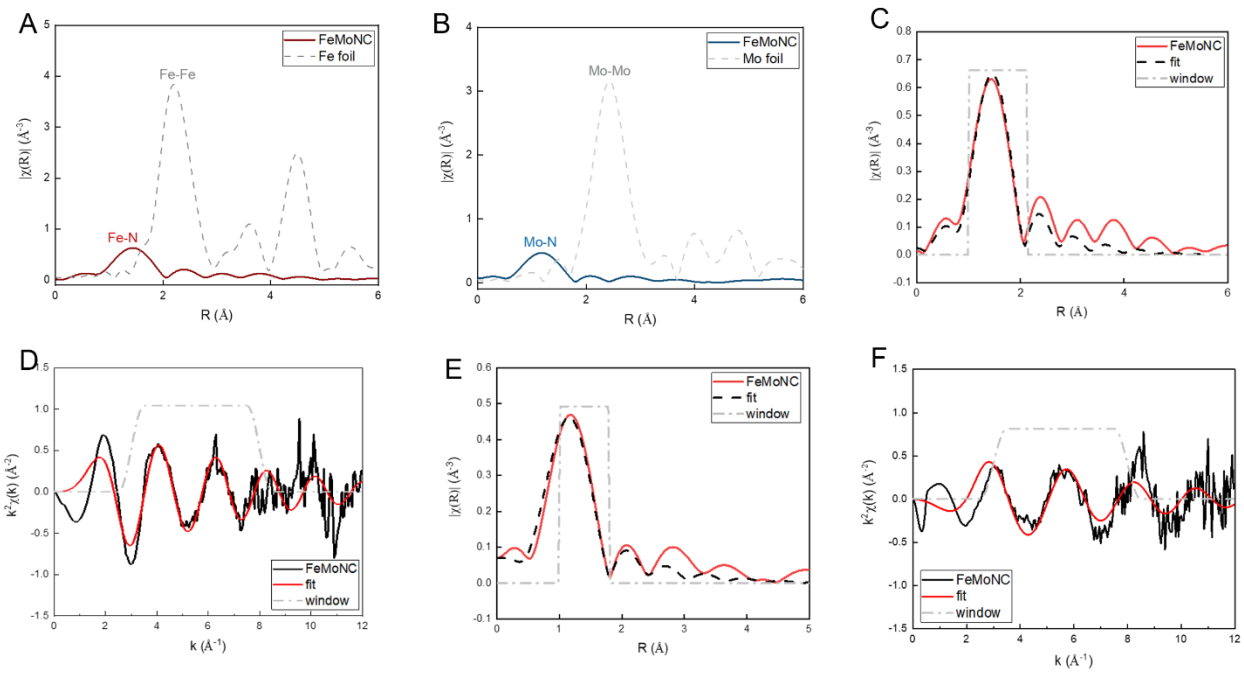

2. S 6: Figure S6: Fe K-absorption edge of the FeMo-N-C and representative Fe foil (top) and Mo K-absorption edge of the FeMo-N-C and representative Mo foil (bottom).

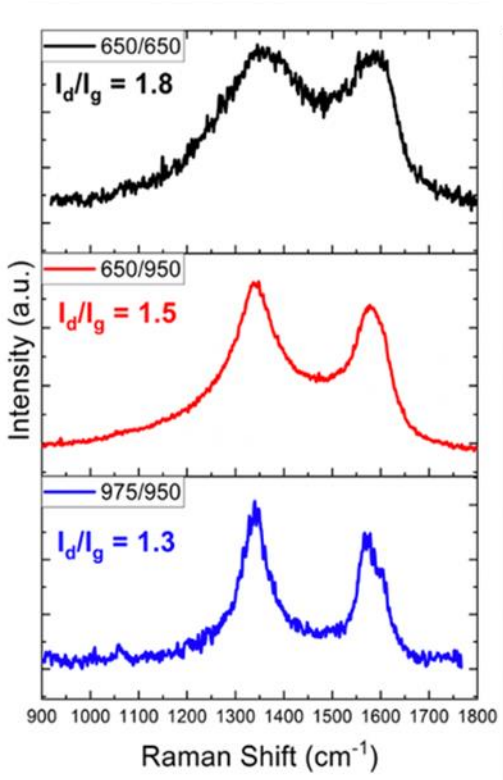

2. S 7: Figure S7: (A) Raman spectra of the FeMo-N-C catalyst at different pyrolysis temperatures, with the corresponding D/G ratio.

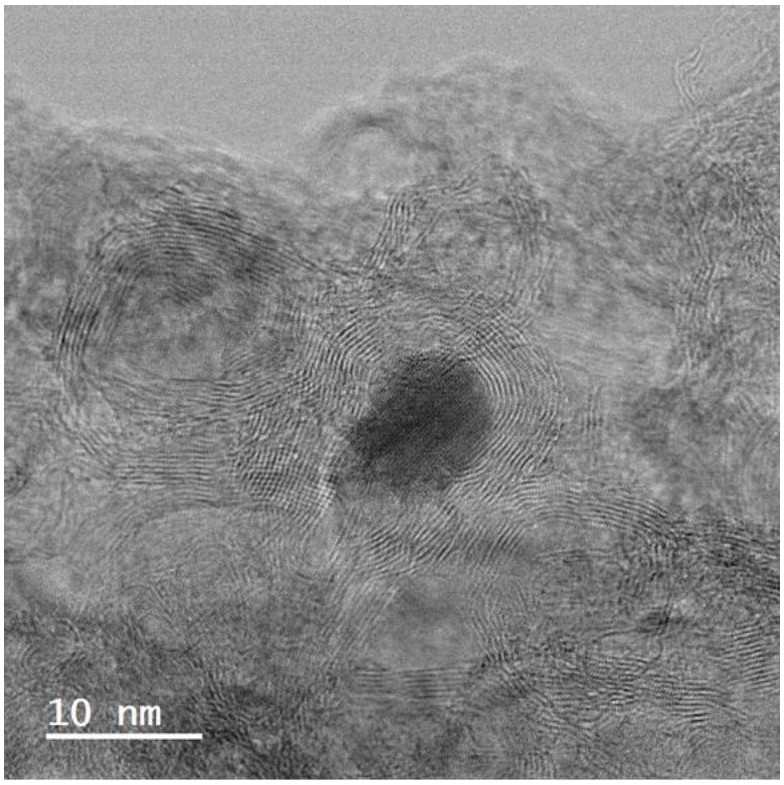

2. S 8: Figure S8: Annular bright-field STEM image of FeMo-N-C (975/950), demonstrating the autocatalyzed graphitization by an iron nanoparticle at high temperatures. Resulting graphitic sheets can be observed.

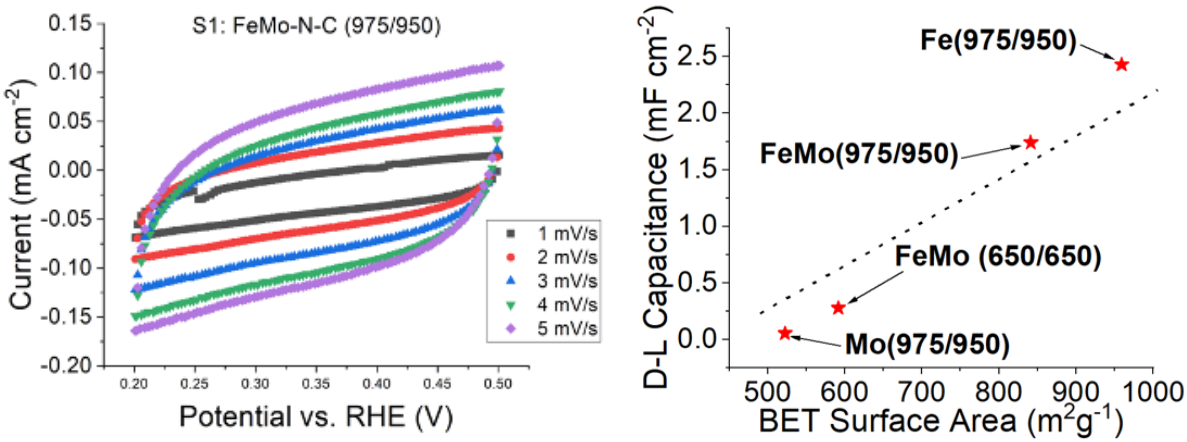

2. S 9: Figure S9: D-L capacitance (mF cm^{-2}) plotted vs. BET surface area (m^2 g^{-1}). Catalyst loading = 0.5 mg cm^{-2}, 0.2 to 0.5 V_{RHE}.

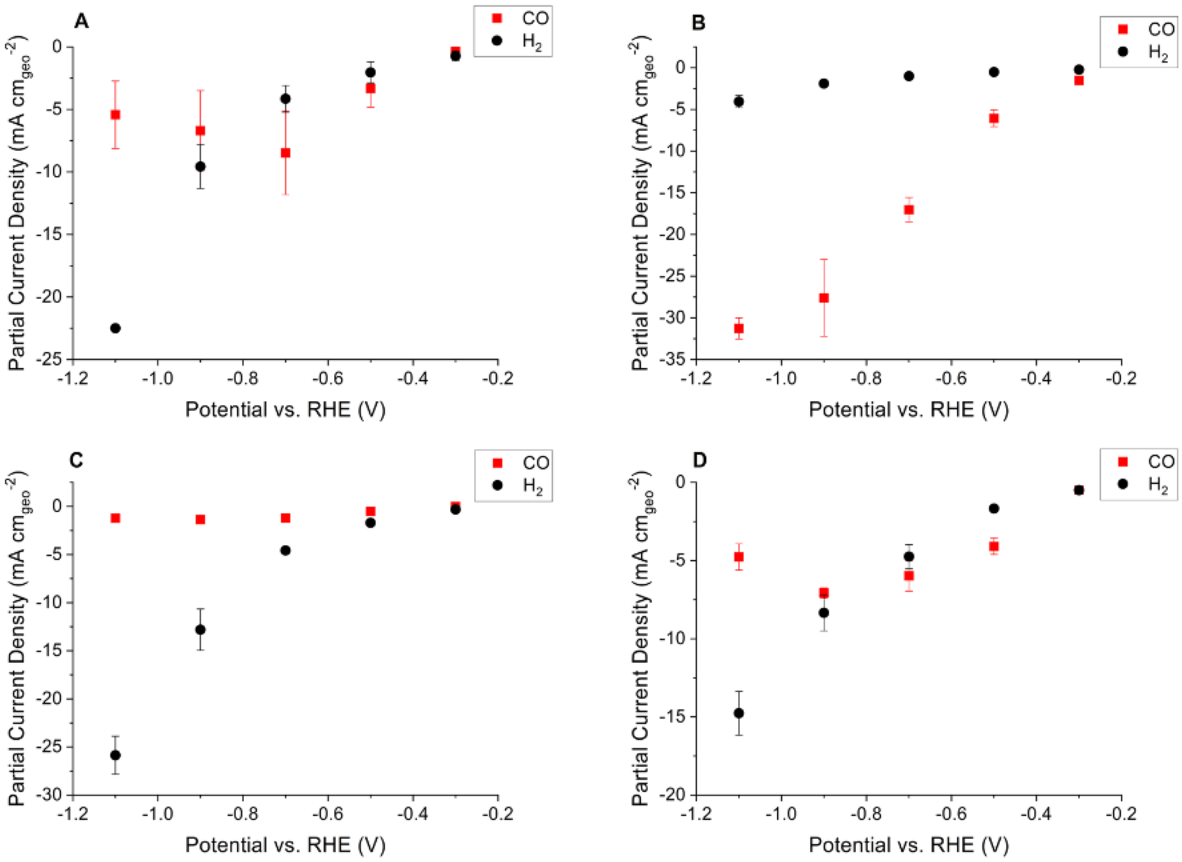

2. S 10: Figure S10: (A) FeMo-N-C (975/950); (B) Fe-N-C (975/950); (C) Mo-N-C (975/950); (D) FeMo-N-C (650/650) with Fe: Mo = 1:1; catalyst loading = 1.0 mg/cm2, 100 % CO2 feed, 0.5M KHCO3(aq)

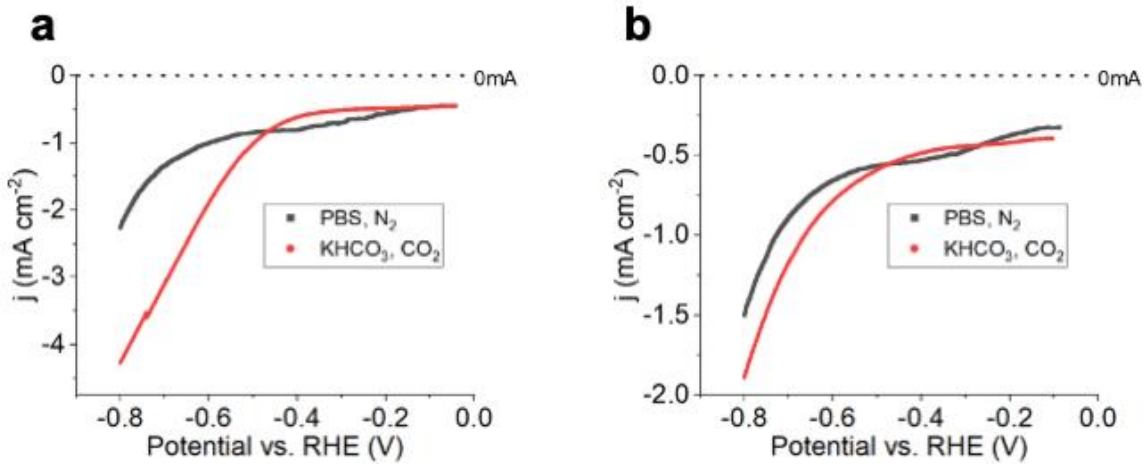

2. S 11: Figure S11: LSV curves in N2-saturated 0.1 M PBS (K2HPO4/KH2PO4) solution and CO2-saturated 0.1 M KHCO3 solution using 0.3 mg cmgeo-2 catalyst loading for (A) Fe-N-C (975/950) and (B) Mo-N-C (975/950). The scan is in the cathodic direction at 1 mV/s.

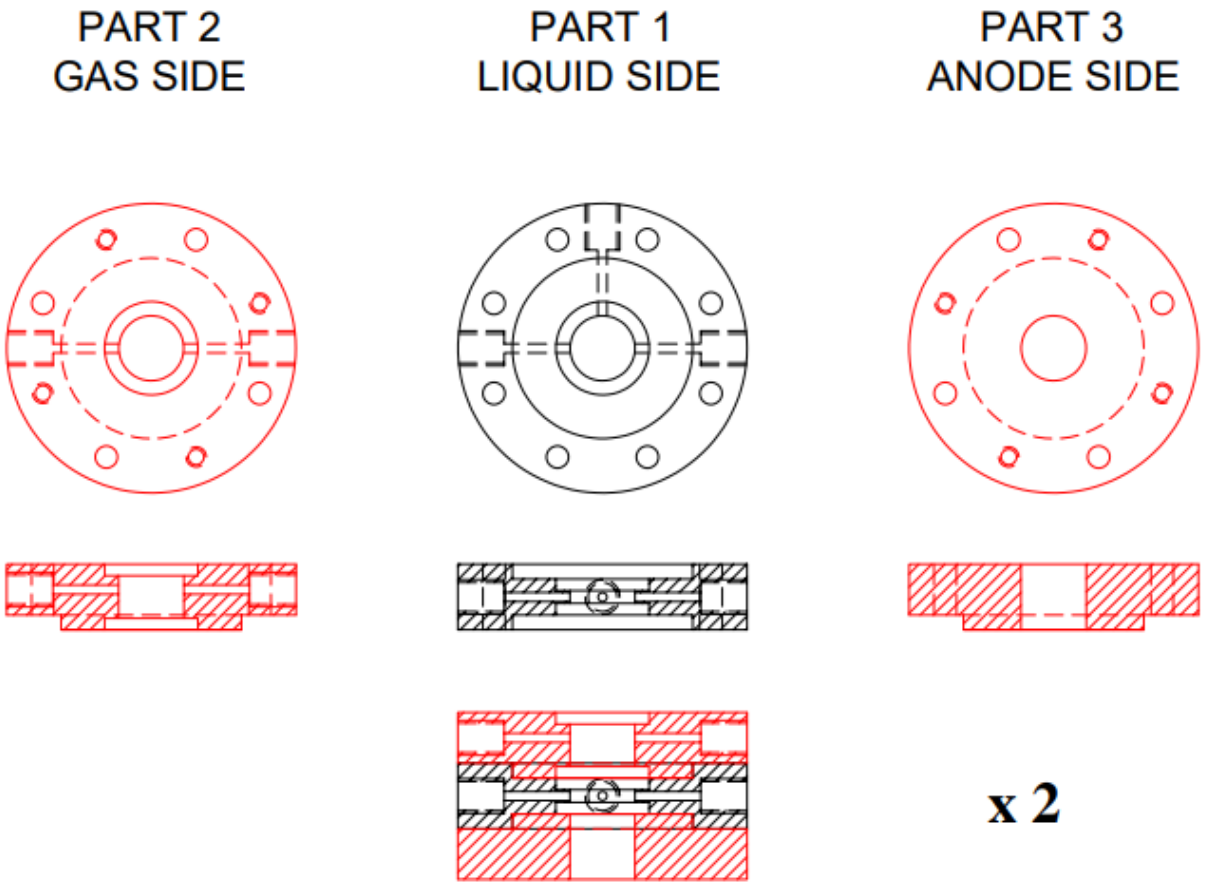

2. S 12: Figure S12: Flow Cell Diagram.

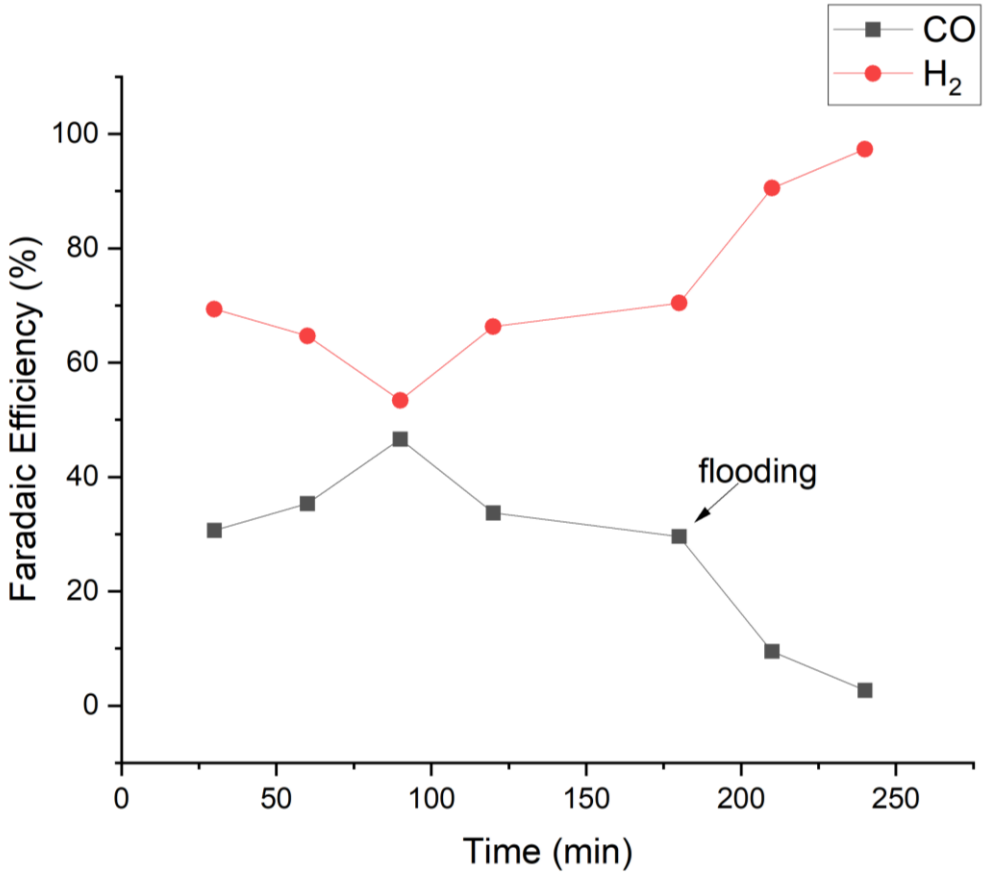

2. S 13: Figure S13: Stability towards CO_2RR vs. HER reaction. Faradaic efficiency (%) plotted for CO and H_2 formation plotted for CPE over 4 h for FeMo-N-C (where Fe/Mo = 0.25). The catalyst loading is 1.05 mg cm $^{-2}$.

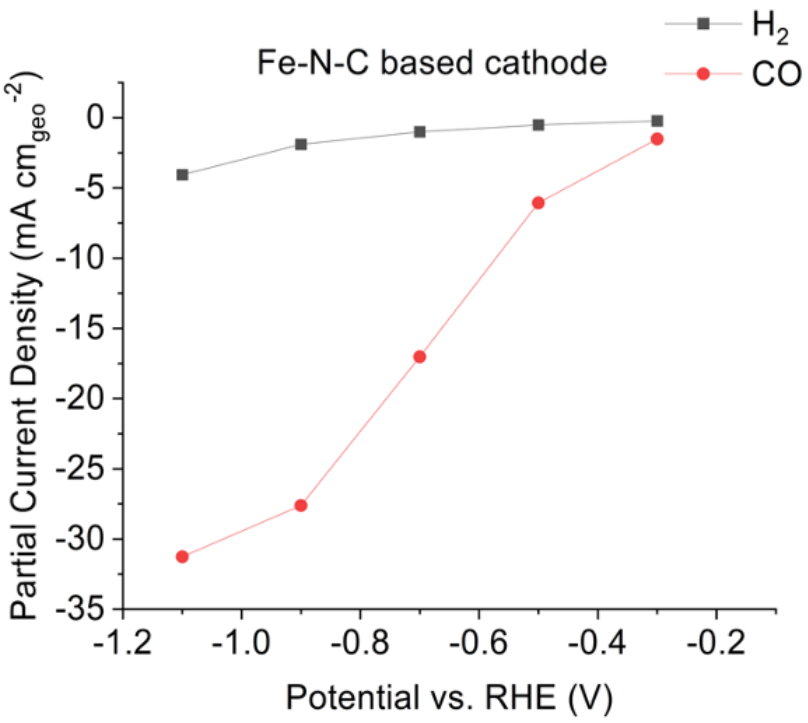
Fe-N-C based cathode
H2
CO
Partial Current Density (mA cm-2geo)
0
-5
-10
-15
-20
-25
-30
-35
-1.2
-1.0
-0.8
-0.6
-0.4
-0.2
Potential vs. RHE (V)

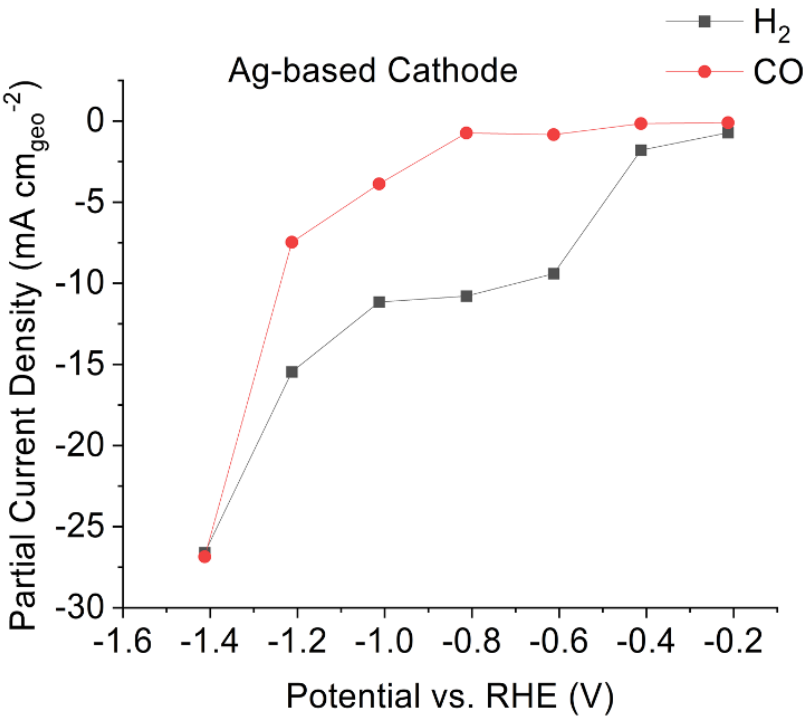

2. S 14: Figure S14: Comparison of geometric partial current densities with flow cell for Ag-based and Fe-N-C-based cathodes at 1.0 mg cm_{geo}^{-2} catalyst loading in 100 % CO_2 feed and 0.5 M $KHCO_3$ electrolyte.

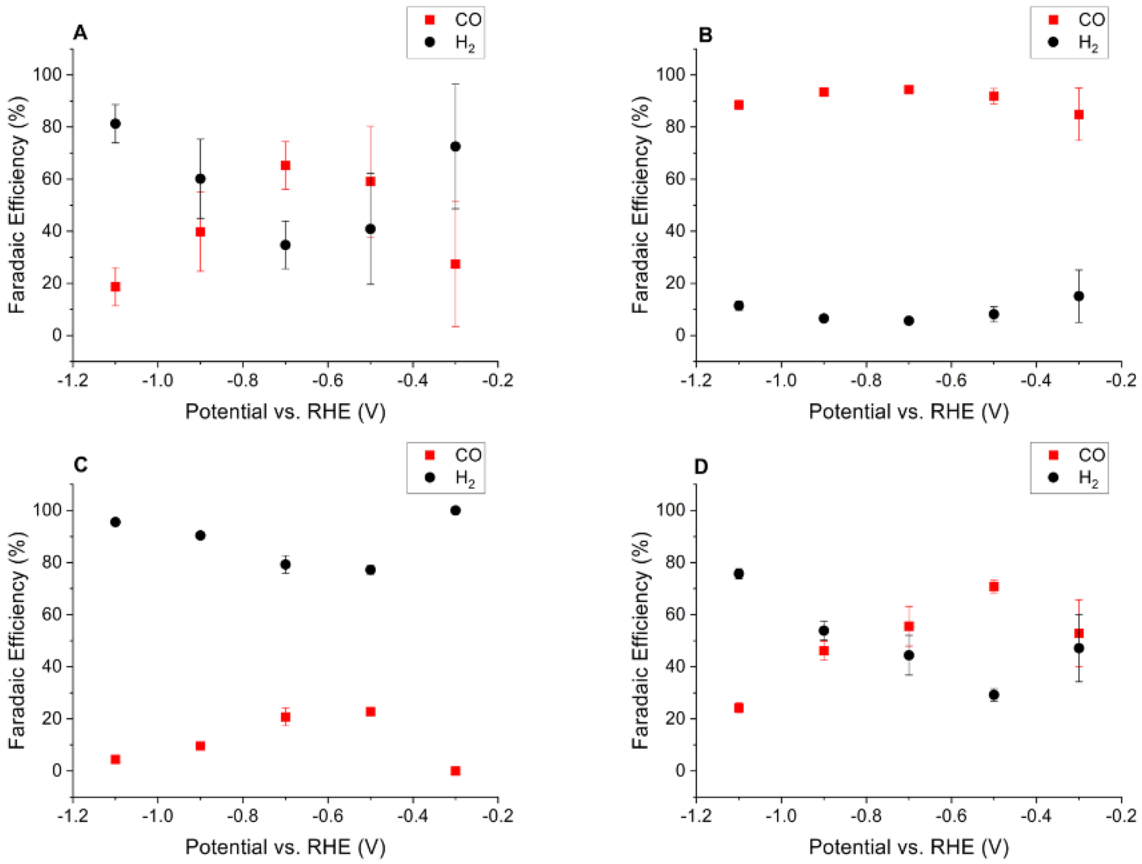

2. S 15: Figure S15: (A) FeMo-N-C (975/950); (B) Fe-N-C (975/950); (C) Mo-N-C (975/950); (D) FeMo-N-C (650/650); catalyst loading = 1.0 mg cm^{-2}, 100 % CO_2 feed, 0.5 M $KHCO_3$ (aq).

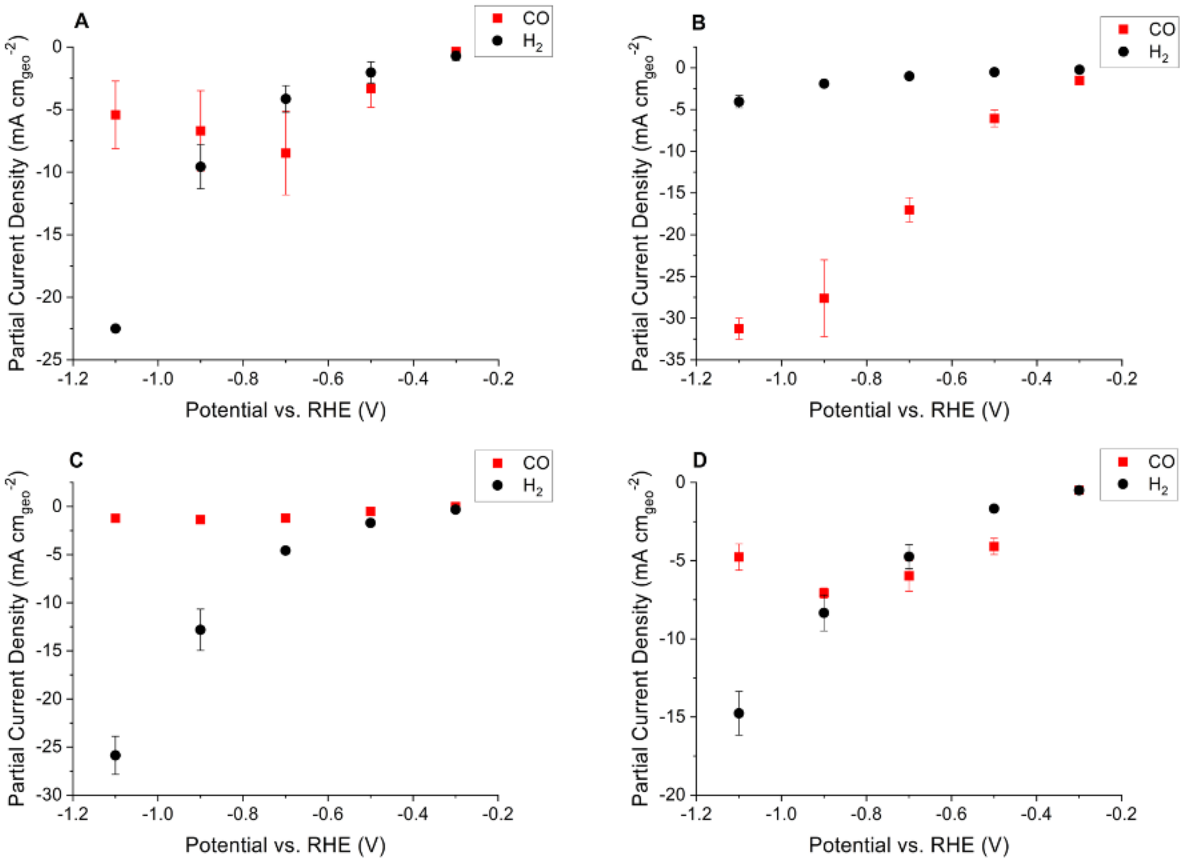

2. S 16: Figure S16: Product analysis from -0.3 V to -1.1 V vs. RHE for (A) FeMo-N-C (975/950); (B) Fe-N-C (975/950); (C) Mo-N-C (975/950); (D) FeMo-N-C (650/650); catalyst loading = 1.0 mg cm^{-2}, 100 % CO_2 feed, 0.5 M $KHCO_3$(aq).

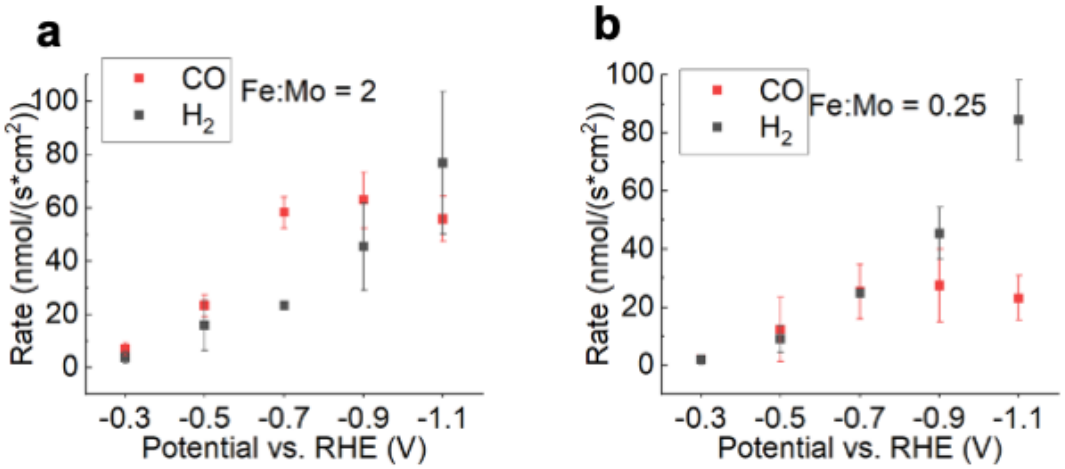

2. S 17: Figure S17: Yield Rate (nmol s^{-1} cm_{geo}^{-2}) for (A) FeMo-N-C for Fe: Mo = 2 and (B) Fe: Mo = 0.25.

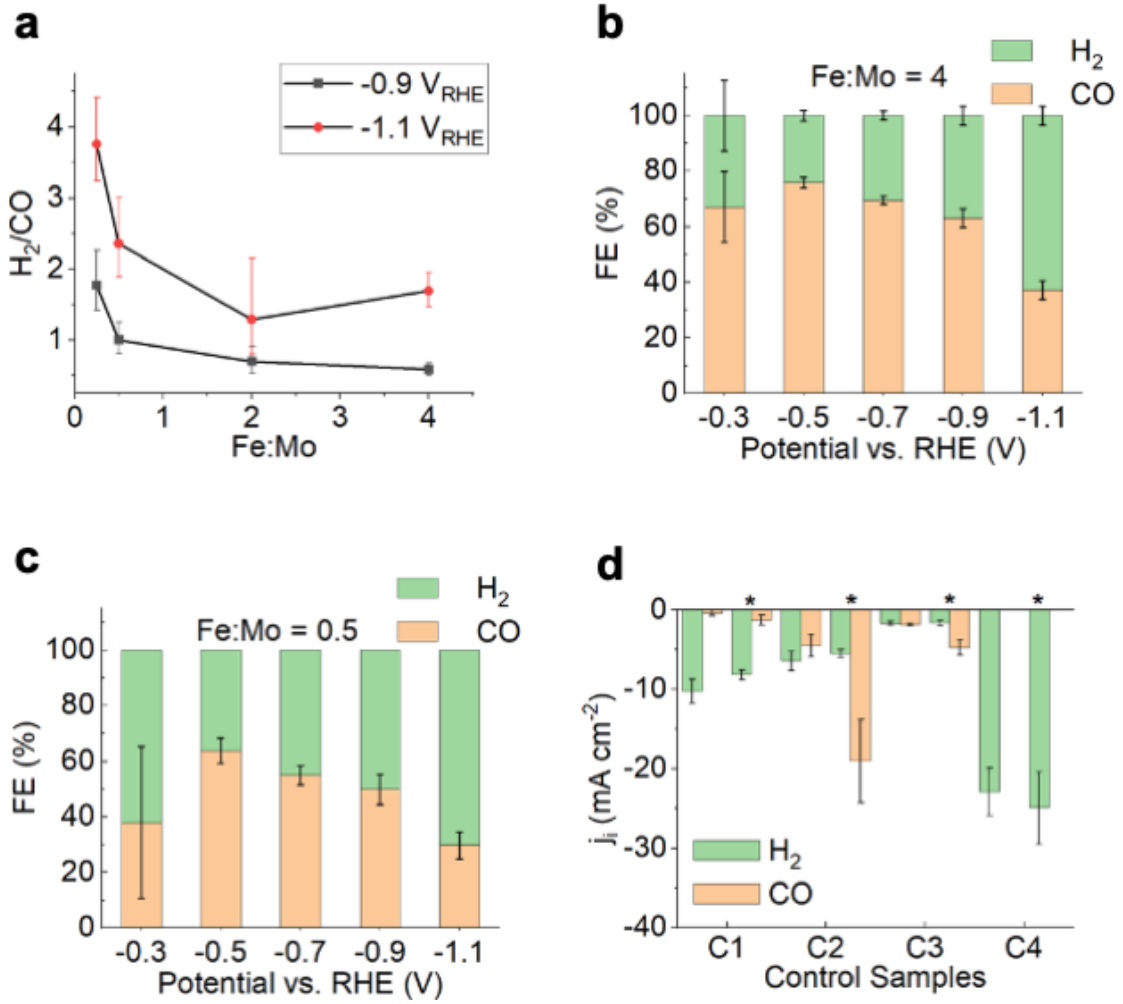

2. S 18: Figure S18: (A) H_2/CO syngas ratio versus metal precursor ratio (Fe:Mo) at -0.9 and -1.1 V vs. RHE. (B and C) Faradaic efficiency (%) for FeMo-N-C (650/650) where Fe: Mo = (B) 1:0.25; (C) 0.5:1 using 1.0 mg cm^{-2}, 100 % CO_2 inlet, 0.5 M $KHCO_3$ (aq) electrolyte. (D) Partial current density for species i (H_2 or CO) for Control Samples using FeMo-N-C (650/650) (Fe /Mo = 1:0.5). Low catalyst loading (no asterisk (*)) is 0.1 mg cm_{geo}^{-2} while high catalyst loading (asterisk (*)) is 1.0 mg cm_{geo}^{-2}. C1: N_2 inlet, 0.5 M $KHCO_3$(aq); C2: CO_2 inlet, 0.5 M $KHCO_3$(aq); C3: CO_2 inlet, 0.1 M $KHCO_3$(aq); C4: N_2 inlet, 0.5 M potassium phosphate buffer (PBS) (pH =7.5) (aq).

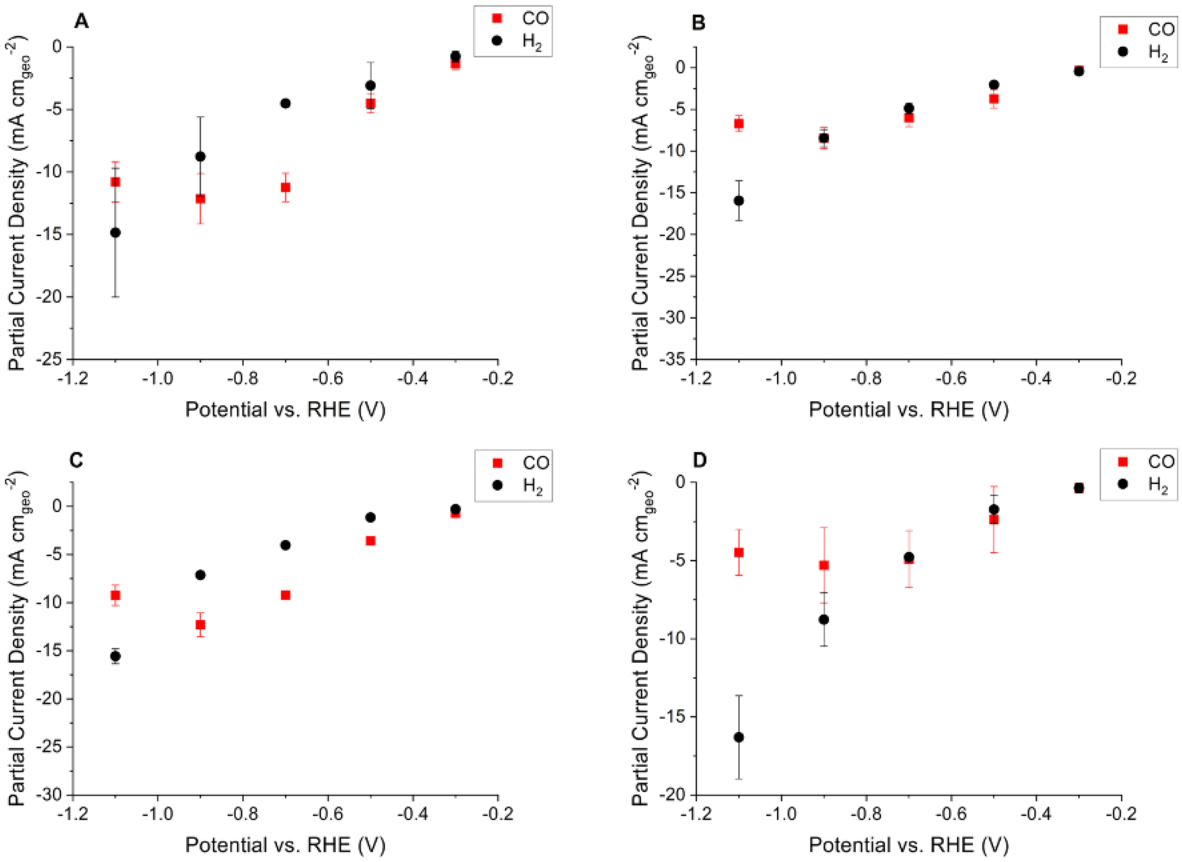

2. S 19: Figure S19: FeMo-N-C (650/650) with precursor molar Fe: Mo ratio of (A) 1:0.5, (B) 0.5:1, (C) 1:0.25; (D) 0.25:1. Catalyst loading = 1.0 mg cm^{-2}, 100 % CO_2 feed, 0.5 M $KHCO_3$(aq).

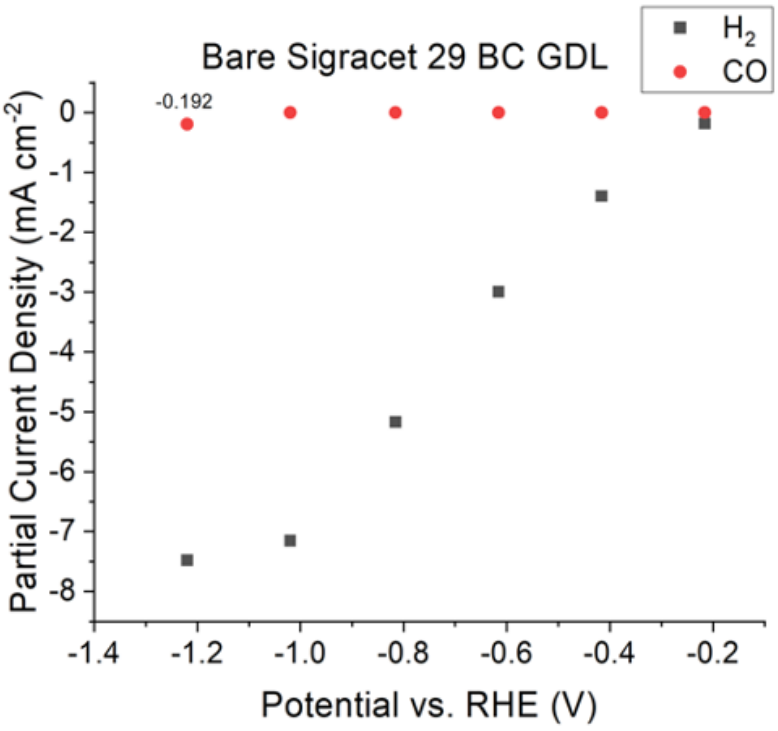

2. S 20: Figure S20: Partial current density for CO_2RR vs. HER products at -0.9 V_{RHE} on bare GDL using 100 % CO_2 inlet, and 0.5 M $KHCO_3$.

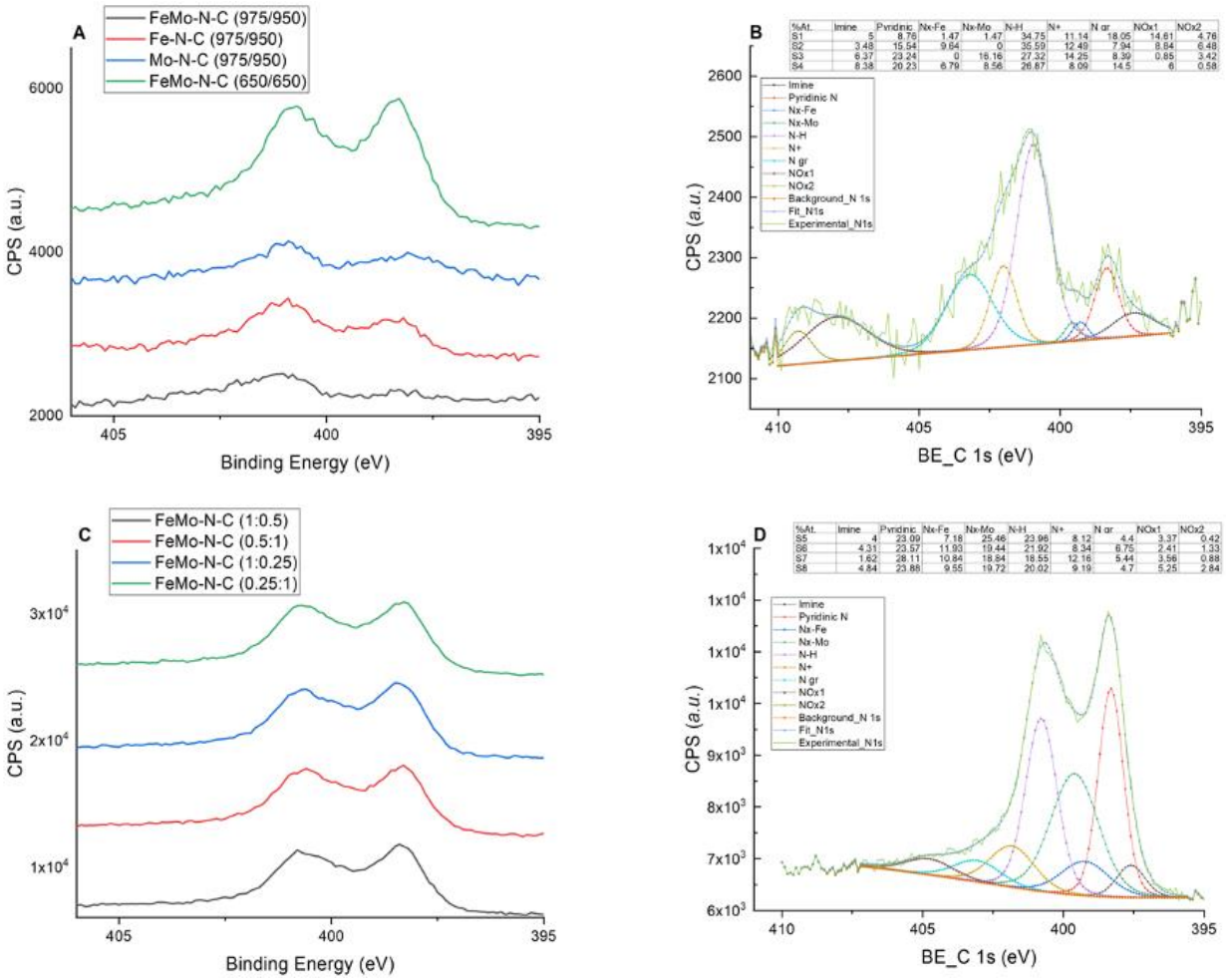

2. S 21: Figure S21: High-resolution N 1s XPS spectra (S1: FeMo-N-C (975/950); S2: Fe-N-C (975/950); S3: Mo-N-C (975/950); S4: FeMo-N-C (650/650); FeMo-N-C (650/650) where Fe:Mo molar precursor ratio = 1:0.5 (S5), 0.5:1 (S6), 1:0.25 (S7), and 0.25:1 (S8)) with component fitting and relative % of nitrogen moieties showing sample spectra for S1 (Fig 2B) and S5 (Fig 2D).

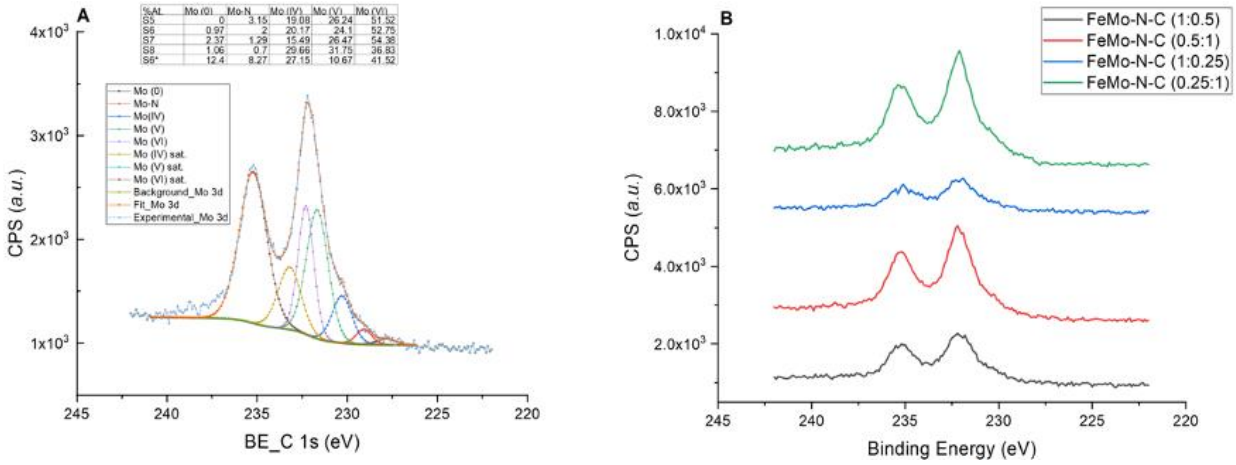

2. S 22: Figure S22: High-resolution Mo 3d XPS spectra with component fitting and relative % of Mo moieties showing sample spectra for FeMo-N-C (0.5:1) (S6) where (S6*) denotes post-electrolysis sample.

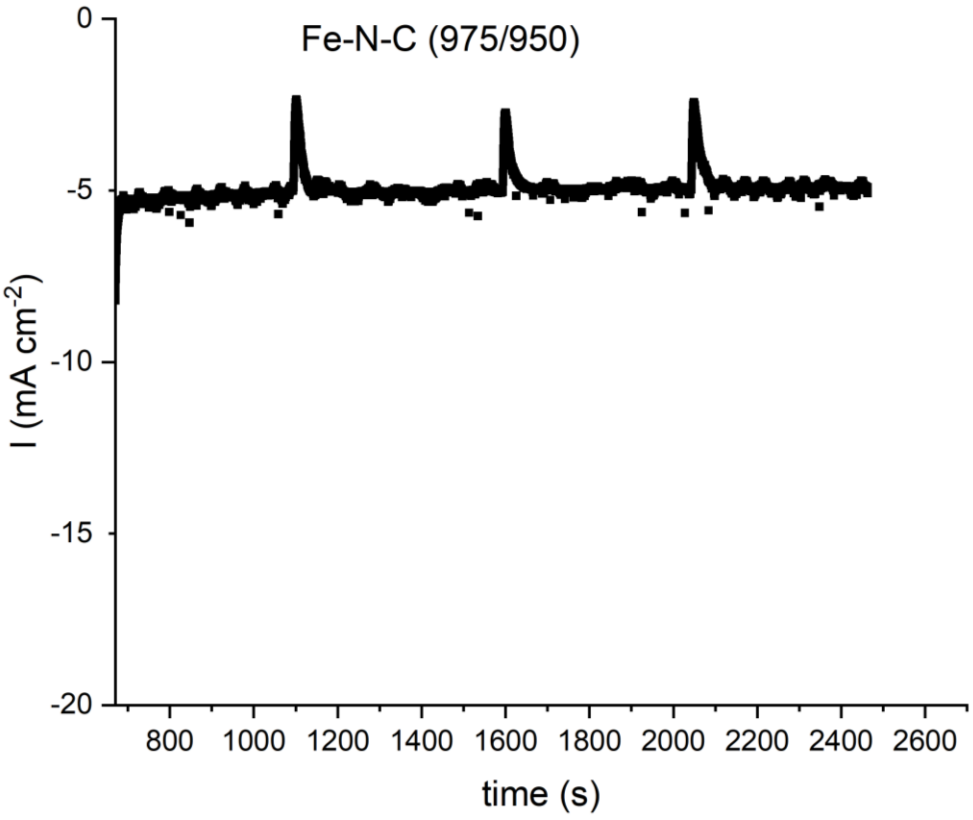

2. S 23: Figure S23: Sample chronoamperometry (CA) curve at -0.3 V vs. RHE for constant potential electrolysis (CPE).

Catalysts	*Synthesis Method*	*Electrolyte*	*Potential and absolute current density ($\|j_{CO}\|$) for syngas (CO:H_2 = 1:2)*	*Reference*
Ni-N-C	Carbon + aniline, metal nitrate ($NiCl_2$), Pyrolysis (× 2) 900°C for 1 h in N_2 atmosphere	1 M $KHCO_3$ (flow-cell)	*ca.* – 1.7 V *vs.* RHE *ca.* 160 mA cm_{geo}^{-2}	Möller *et al.*[44]
Mn-N-C Fe-N-C Co-N-C	Urea, citric acid, metal nitrate. Pyrolysis (Pyr × 1): 550°C for 2h + 900°C for 1h in Ar atmosphere	0.1 M $KHCO_3$ (static electrolyte)	*ca.* – 0.9 V vs. RHE *ca.* 1.2 mA cm_{geo}^{-2} *ca.* – 0.8 V vs. RHE *ca.* 3 mA cm_{geo}^{-2} *ca.* – 0.45 and – 0.85 V vs. RHE *ca.* 0.5 and 5 mA cm_{geo}^{-2}	Pan *et al.* [62]
Mn-N-C Fe-N-C Ni-N-C	1. 4,4'-dipyridyl hydrate, EtOH, $CoCl_26H_2O$ + $CuCl_22H_2O$. Pyr (× 1): 500°C, 2h, Ar = N-C. 2. N-C + MCl_x solution, Pyr (× 1): 900°C for 2h in Ar, 1 h in H_2	0.1 M $KHCO_3$ (static electrolyte)	*ca.* – 0.47 and – 0.65 V vs. RHE *ca.* 1.5 and 3.3 mA cm_{geo}^{-2} *ca.*– 0.72 V vs. RHE *ca.* 5 mA cm_{geo}^{-2} *ca.*– 0.47 V vs. RHE *ca.* 0.5 mA cm_{geo}^{-2}	Ju *et al.* [70]
Ni-N-GS (graphene spheres)	Electrospinning of Polyacrylonitrile, polypyrrolidone, $Ni(NO_3)_26H_2O$, dicyandiamide solution in dimethyl formaldehyde. Pyr (× 1): 750°C for 1h in 5% H_2 95 % Ar atmosphere.	0.1 M $KHCO_3$ (static electrolyte) 1 M $KHCO_3$ (flow-cell)	*ca.* – 0.60 V vs. RHE *ca.* 1.5 mA cm_{geo}^{-2} *ca.* – 0.45 V vs. RHE *ca.* 15 mA cm_{geo}^{-2}	Jiang *et al.*[61]
Fe-N-C	Metal organic framework (ZIF-8), ferrous acetate, phenanthroline.	0.5 M $NaHCO_3$ (static electrolyte)	*ca.* – 0.92 V vs. RHE $\|j_{CO}\|$ *not reported*	Huan *et al.* [33]

	Pyr (× 2): 1050°C for 1 h in Ar 950°C for 5 mn in NH_3			
Co-N-C	$Zn(NO_3)_26H_2O$, 2-methylimidazole, $Co(NO_3)_39H_2O$, methanol Pyr (× 1): 1100°C for 1h in Ar atmosphere	0.1 M $KHCO_3$ (static electrolyte)	*ca.* – 0.4 and – 0.8 V vs. RHE *ca.* 0.2 and 1.8 mA cm_{geo}^{-2}	Pan *et al.* [71]
Fe-N-C	Melamine, formaldehyde soln. (37 wt.%), iron chloride, Pyr (× 1) 950°C for 1 h in N_2	0.1 M $KHCO_3$ (H-cell)	*ca.* -0.90 V vs. RHE *ca.* 1.3 mA mg^{-1}	Zhao *et al.*[72]
Ni-N-C	PANI-derived carbon, $Ni(CN)_4^{2-}$ metallic precursor. Pyr (× 1) 1000°C	0.1 M $KHCO_3$ (H-cell)	*ca.* -0.60 V, -1.0 V, -1.1 V vs. RHE; $\|j_{CO}\|$ = 0.4, 4.8, 3.3 mA cm_{geo}^{-2} for H_2/CO of 0.8, 1.1, and 6.3, respectively.	Wang *et al.*[73]
FeMo-N-C (molar precursor Fe /Mo = 0.25)	SSM with nicarbazin, silica, Stöber spheres, iron metallic salt, molybdenum metallic salt	0.5 M $KHCO_3$ (Flow-cell)	-0.3 and -0.9 V vs. RHE 0.4 and 5.3 mA cm_{geo}^{-2}	*This work*
FeMo-N-C (molar precursor Fe /Mo = 4.0)			-1.1 V vs. RHE 9.3 mA cm_{geo}^{-2}	
FeMo-N-C (molar precursor Fe /Mo = 2.0)			-1.1 V vs. RHE 10.8 mA cm_{geo}^{-2} for H_2/CO = 1.28	

Table 2: Table S1: Literature summary for M-N-C catalysts for syngas generation.

Sample	%At. Conc. Oxygen	%At. Conc. Carbon	%At. Conc. Nitrogen	%At. Conc. Molybdenum	%At. Conc. Iron
FeMo-N-C (975/950)	1.49	96.67	1.62	0.2	0.02
Fe-N-C (975/950)	1.61	95.12	3.25	0	0.02
Mo-N-C (975/950)	2.56	94.23	2.72	0.49	0
FeMo-N-C (650/650)	2.3	83.3	14.19	0.2	0.01
FeMo-N-C (1:0.5)	5.53	85.93	8.36	0.16	0.04
FeMo-N-C (0.5:1)	5.71	85.32	8.69	0.26	0.03
FeMo-N-C (1:0.25)	5.54	85.45	8.74	0.1	0.17
FeMo-N-C (0.25:1)	5.33	85.37	8.96	0.29	0.04

Table 3: Table S2: %At. Conc. as obtained by high-resolution X-Ray photoelectron spectroscopy for mono- and bi-metallic MNC samples.

Sample	Molar Precursor ratio Fe: Mo	Fe (ppb) ICP-MS	Mo (ppb) ICP-MS	Fe wt.%	Mo wt.%	Total Metal Atomic Wt. %	Mass % Ratio Fe/ Mo (ICP-MS)
FeMo (0.25)	0.25	43.95	159.16	0.4	1.46	1.86	0.28
FeMo (0.5)	0.5	56.84	161.81	0.44	1.25	1.69	0.35
FeMo (2)	2	100.81	82.13	0.81	0.66	1.46	1.23
FeMo (4)	4	110.47	114	0.96	0.99	1.95	0.97
Mo		0	231.6	0	2.2	2.12	
Fe		52.86	0	0.44	0	0.44	

Table 4: Table S3: ICP-MS of Fe-N-C, Mo-N-C and FeMo-N-C electrocatalysts.

Sample	Low BE range/ High BE range	$FE_{co,max}$
1	0.238	65.3 +/- 9.1 % at -0.7 V vs. RHE
2	0.448	94.4 +/- 1.1 % at -0.7 V vs. RHE
3	0.837	22.8 +/- 1.6 % at -0.5 V vs. RHE
4	0.804	70.8 +/- 2.4 % at -0.5 V vs. RHE
5	1.107	71.3 +/- 1.3 % at -0.7 V vs. RHE
6	1.015	63.8 +/- 4.5 % at -0.5 V vs. RHE
7	1.047	75.8 +/- 1.8 % at -0.5 V vs. RHE
8	0.994	51.2 +/- 9.2 % at -0.5 V vs. RHE

Table 5: Table S4: Correlation between the ratio of all XPS peaks lower than 400 eV to that above 400 eV for N 1s spectra for sample catalysts (S1: FeMo-N-C (975/950); S2: Fe-N-C (975/950); S3: Mo-N-C (975/950); S4: FeMo-N-C (650/650); FeMo-N-C (650/650) where Fe:Mo molar precursor ratio = 1:0.5 (S5), 0.5:1 (S6), 1:0.25 (S7), and 0.25:1 (S8)).

	Fe K edge
N_N	3.4±0.7
r_{Fe-N}	2.00±0.05
	Mo K edge
N_N	1.5±0.3
r_{Mo-N}	1.74±0.02

σ^2 are set to 0.003

Table 6: Table S5: Fitting results for the Fe-N/Mo-N distances (bond length: Å).

Section 3: Copper-Based Catalysts (Cu-based catalysts) for CO2 Reduction

Chapter 1: Overview/Introduction to Cu-based Catalysts for CO_2 Reduction

Copper is unique in its ability to reduce CO_2 beyond CO to further reduced C1, C2, and even trace amounts of C3 products. [74, 75] However, copper-based catalysts often suffer from poor product selectivity and usually do not have a high conversion rate to hydrocarbons. Li et al recently studied modified Cu electrodes by reducing µm-thick Cu2O and found improved CO2R current density and selectivity for CO/HCOOH compared to polycrystalline Cu at the expense of a lower faradaic efficiency for hydrocarbon (CH_4/C_2H_4) formation. [74] Hori et al studied a series of copper single-crystal electrodes and found the selectivity towards C1 vs. C2 products (e.g., CH_4 vs. C_2H_4) was tunable based on the catalysts' crystallographic structure. [76] They found Cu (111) mainly yields CH_4 while Cu (100) yields C_2H_4. Zhong et al furthered this crystallographic-activity study as their group synthesized stepped Cu (110) and Cu (100) copper hydroxide/oxides derived Cu catalysts which yielded impressively high faradaic efficiencies for C2 products as high as 82%. [75]

In addition to obtaining favorable crystallographic open facets for CO_2 reduction on Cu-based catalysts, the subsurface oxygen content, particle size, coordination environment, and structure and density of both total grain boundaries (GBs) and randomly-oriented GBs are all critical factors influencing the electrocatalytic performance. [77, 78] While*CO is strongly bound on Ag and Au catalysts, Cu offers intermediate binding strength of *CO with an absence of underpotential deposited hydrogen leading to the ability for C-C coupling and more highly reduced products. [74, 77] Complementary techniques such as temperature-programmed desorption of CO (CO-TPD) and transmission electron microscopy-based automated crystal orientation mapping (TEM-ACOM) reveals the association of stronger CO-binding sites with increased occurrence of randomly oriented GBs. Kanan et al have shown that the presence of random GBs is associated with increased occurrence of C-C coupling and high selectivity for the electroreduction of CO to C2 oxygenates (e.g., ethanol and acetate) in alkaline KOH. [79, 80]

Research into highly dense Cu nanowires has yielded additional insights into the explicit role of GBs in promoting or hindering CO/CO2 electroreduction. [81, 82] Ma et al studied Cu nanowires produced by electrically reducing CuO nanowires on Cu mesh (ECR method) vs. nanowires produced by thermal annealing (HR method) in H_2 between (150 – 300) °C. [82]The L/D (length over diameter) of nanowires is found to be a function of the synthesis method of nanowires. Additionally, the catalysts produced by thermal annealing (HR) are found to be less active for CO_2R compared to those produced electrochemically. By contrast, the ECR Cu nanowires have high CO_2R activity and are selective for CO production in the low overpotential region (E > -0.5 V vs. RHE), and C2 species (ethane, ethylene, and ethanol) in the high overpotential region (E < -0.5 V vs. RHE). The role of GBs in promoting or hindering CO_2R is still being investigated. Williamson-Hall analysis of XRD patterns is instructive for correlating lattice strain to occurrence of differently oriented GBs and resulting CO_2R activity. Additionally, GB-induced increases in CO_2R activity may be due to increased presence of undercoordinated Cu sites. Koper et al examined CO and CO_2 reduction activity on different Cu crystallographic orientations as a function of pH for Cu (111) and Cu (100). They found a favorable formation of ethylene on Cu (100) and it was suggested that this occurred through pH-independent electron transfer to form $*C_2O_2^-$

intermediate. [83] Enhancement of CO_2R activity may be ascribed to increased open Cu (100) as well as Cu(110) facets in the vicinity of random GBs which would agree with previous studies. [78, 84]

In addition to the importance of a high number of Cu rich defect sites with coordination number lower than the bulk coordination number, the macroscopic morphology of the gas diffusion electrode (GDE) is critically important. In order to investigate how the macroscopic morphology of Cu electrodes may influence the electrocatalytic performance, several different electrodeposited Cu samples were investigated. Electrodeposition has been used effectively by several groups to avoid the use of an ionic binder for CO_2R. [85-88] We evaluated how the GDE performance of an electrodeposited sample is influenced by the deposition time and charge. Clearly, if the deposition charge is too high, the GDE attribute of enhanced CO_2 diffusion to active site and product diffusion away is hampered. As deposition charge increases, the performance of the resultant foam starts to approach that of a foil electrode as CO_2 diffusion to the CL and product diffusion away from the CL are dramatically reduced. A summary of the plating solution, deposition charge, and major products for different GDE samples is shown in table 7.

GDE Sample	Plating Solution	Deposition Charge (C/cm^2)	Major Product(g)
GDE A_1	0.2 M $CuSO_4$, 1.5 M H_2SO_4	20.270	H_2
GDE A_2	0.2 M $CuSO_4$, 1.5 M H_2SO_4	0.656	H_2
GDE A_3	0.2 M $CuSO_4$, 1.5 M H_2SO_4	2.105	H_2
GDE B	0.1 M $CuSO_4$, 0.1 M $ZnSO_4$, 1.5 M H_2SO_4	0.321	H_2

Table 7: Plating Solutions, deposition charge C/cm2, and major observed product(s). GDE A3 was presoaked in concentrated HNO3 for 1 hour before electrodeposition.

The electrochemical selectivity of the electrodeposited samples is shown in figure 9 as well as the relationship between deposition charge and H_2 production rate. Concerning the deposition charge,

we can see a sharp decrease in the H_2 production rate as the deposition charge increases from 0.3 to 2.1 C/cm^2 and then a more gradual decrease as the deposition increases by another order of magnitude to 20.3 C/cm^2. The H_2 production rate reaches 109.7 nmol/(s*cm^2) for a deposition charge of 0.3 C/cm^2 which compares well to the H_2-benchmark Pt cathode (Pt cathode at -1.219 V_{RHE}, which produces 151.7 nmol H_2/(s*cm^2)). The CO_2RR selectivity of the electrodeposited copper on GDE samples is low. This is most likely due to surface inhomogeneities and less than optimal crystallographic structure for CO_2RR (e.g., low proportion of undercoordinated highly reactive Cu facets). Additionally, it is much harder to obtain a good electrodeposition on carbon GDE vs. electropolished copper foil. Also the electrolyte employed was 0.5 M $KHCO_3$ which has been shown to allow for increased HER compared to more alkaline electrolytes for electrodeposited samples. [85]For this reason, according to Hoang et al who used HNO_3 treatment as well as Cu sputtering on carbon GDL to pretreat the surface for electrodeposition (choosing the latter so as not to cause GDL flooding which can be avoided with our GDL/PTFE combined GDE), we pretreated GDE A_3 by soaking in concentrated HNO_3 for 1 hour prior to electrodeposition. [85]

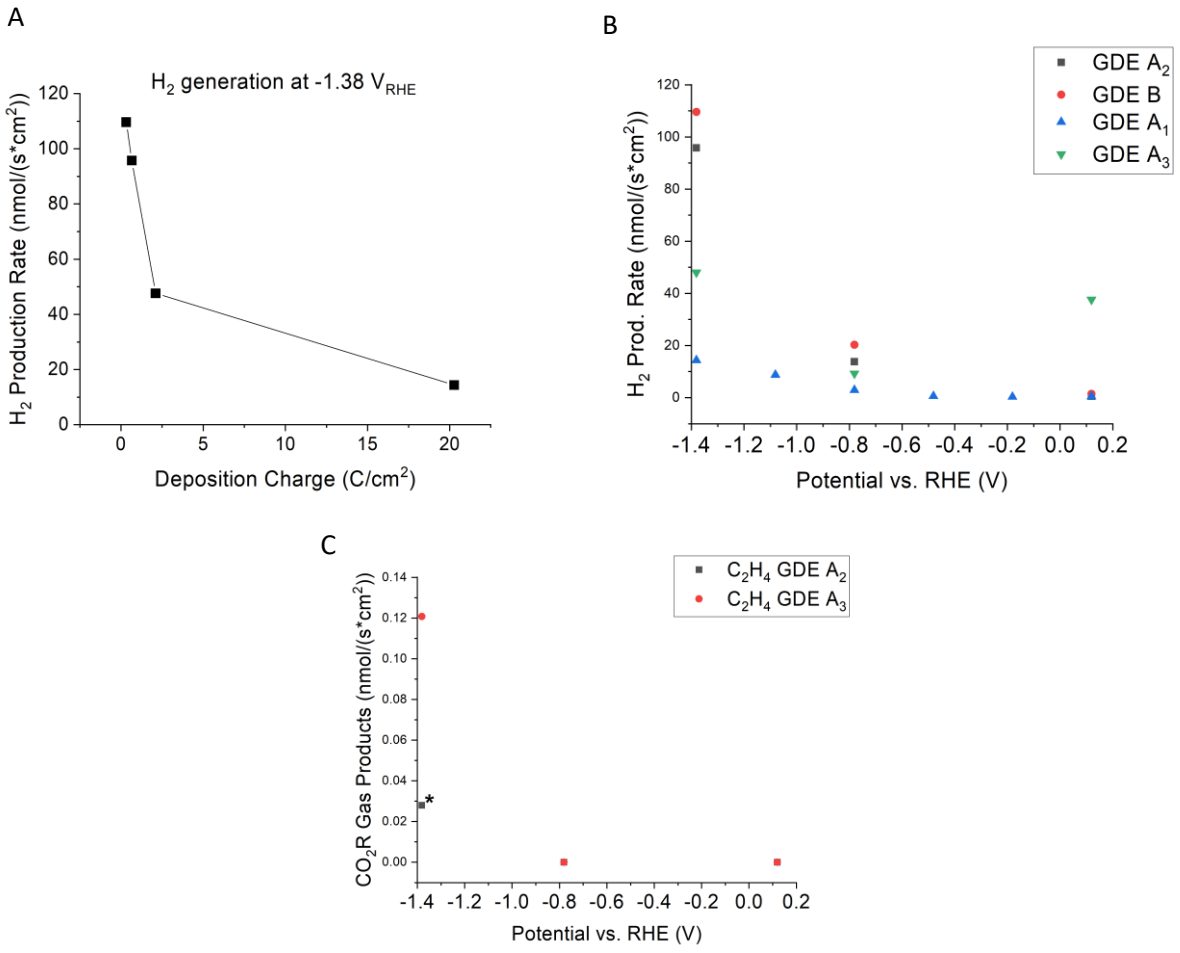

Figure 3.1. 1: (A & B) H2 production rates using deposition solution as in table 7 and two-electrode setup at -1 V vs. open-circuit voltage. C). CO2R gas products. * in picture means ethylene detected for GDE A2 was broad peak possibly due to GC column contamination.

Although the faradaic efficiency for CO_2RR products is low (FE_{C2H4} = 0.25%), it is interesting that ethylene was detected with the absence of CO. The only other CO_2RR product was formate for the electrodeposited GDE samples (7.78 and 8.36 nmol/(s*cm^2) for GDE A_2 and GDE B at -1.38 V_{RHE}, respectively). Additionally, presoaking the GDE in HNO_3 caused a noticeable increase in C_2H_4 production detected by a sharp well-resolved peak on the GC-FID detector. The increased occurrence of CO_2R for pretreated GDL at lower deposition current presents a guiding parameter for engineering GDE for CO_2R.

Chapter 2: Graphene-based catalyst for CO2 reduction: The critical role of solvents in materials design

In addition to the morphological attributes influencing CO_2R on electrodeposited samples, the interlayer spacing of reduced graphene oxide layers supporting Cu nanoparticles in powder-based Cu catalysts may substantially alter the catalytic performance. As the field was lacking a systematic analysis of the specific effect for different solvents in Cu nanoparticle syntheses, we explored the role of five common solvent classes in affecting CO_2R activity. The role of water, ethanol (EtOH), ethylene glycol (EG), Dimethylformamide (DMF), and γ-Butyrolactone (GBL) on the synthesis of reduced graphene oxide (rGO)-copper nanoparticles (Cu NP) electrocatalysts used in CO_2 reduction reactions (CO_2R) was investigated.

As these solvents have different sizes and contain different terminal groups (hydroxyl, carbonyl, and amine), we have observed the variation of surface area, porosity, nanoparticle yield, defect density and CO_2R activities. We have shown that the selected solvents influence the morphology, porosity, surface area, defect density of the rGO-CuNP composite samples. In addition, the solvent affects the yield of CuNP and properties of rGO, especially the interlayer d spacing. Finally, we demonstrate how the selected solvent affects the properties of rGO-supported CuNP for CO_2R activity.

Result and discussion

Physical properties of rGO-CuNP such as defect density morphology, d-spacing, surface area, porosity and yield of nanoparticles strongly depend on the selection of the solvent for their synthesis because each precursor/solvent combination will exhibit a different solid–liquid interface interaction and corresponding growth rate of CuNP. [89-91]

The defect density and d-spacing can be determined from powder X-ray diffraction (XRD) (Fig. 3.2. 1a) studies of prepared rGO-CuNP. The characteristic diffraction peaks of CuNP at 43.2°, 50.65°, and 74.1° can be assigned to 〈1 1 1〉, 〈2 0 0〉, and 〈2 2 0〉 planes of fcc structure of Cu (Fig. 3.2. 1a). Other diffraction peaks positions at 33.04° and 61.34° correspond to 〈1 1 0〉 and 〈2 2 0〉 planes of CuO and Cu2O respectively (Fig. 3.2. 1a). All these diffraction peaks have been observed with different peak intensities in all solvent media used for the synthesis of rGO-CuNP. The interlayer spacing of non-oxidized graphite is 0.34 nm, which is equal to the van der Waals thickness of a single layer of carbon atoms. [92] The interlayer d-spacing of as-processed rGO in different solvents is greater than non-oxidized graphite due to the intrusion of solvent molecules between rGO nanosheets. The XRD spectra of rGO yields a d-spacing of 1.1, 1.3, 1.7, 2.0 and 2.2 nm in water, GBL, EG, EtOH and DMF, respectively. Recently, some reports have showed that interlayer spacing of GO is affected by the size and functional groups of solvents. [93, 94] Oxygen-containing solvents are strongly interacting with the hydroxyl, epoxy

and carboxylic acid functionalities on the surface of GO. Therefore, the expansion of interlayer spacing of GO is affected by the adsorption and the size of solvent molecules which is consistent with the data observed in our study. [93]

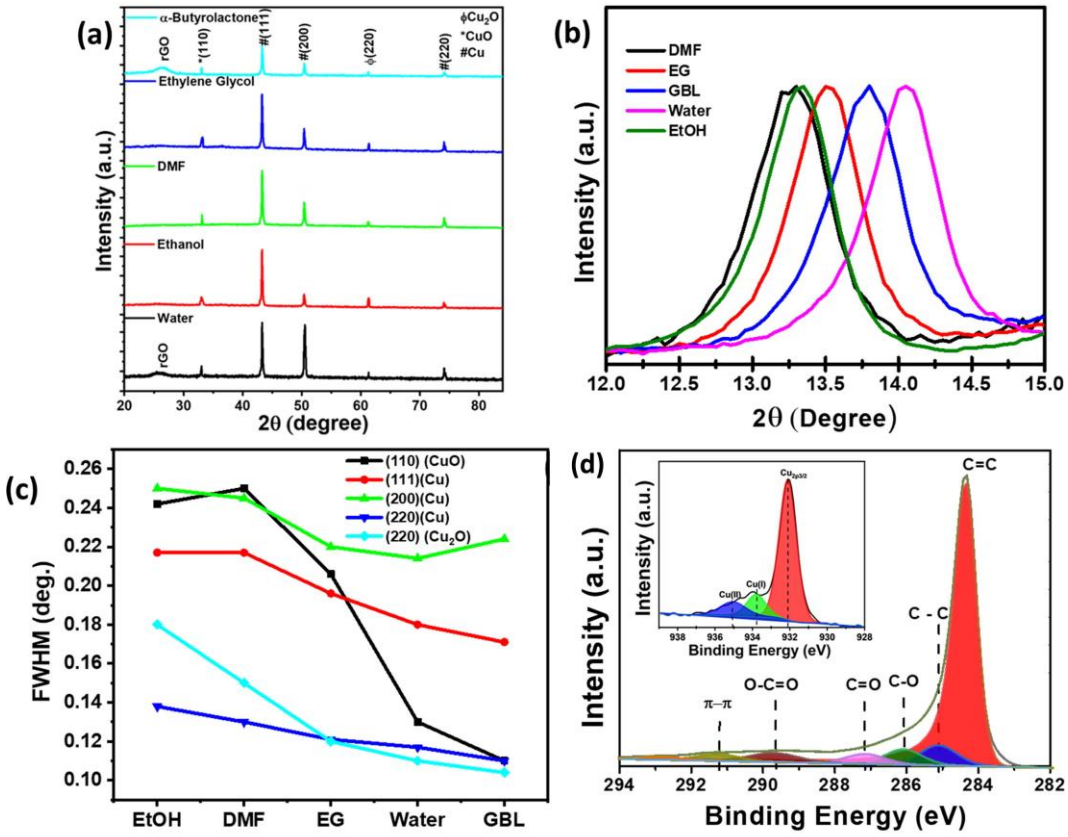

Figure 3.2. 1: (a) X-ray diffraction (XRD) spectra of GO-CuNP grown in various solvents. (b) normalized XRD peak of GO corresponded to (0 0 1) plane and determine the interlayer spacing of GO in different solvents (c) the effect of solvents on full width half maximum (FWHM) of CuNP in the solvent dependent synthesis of rGO-CuNP (d) C1s and Cu2p XPS spectra of GO-CuNP grown in DMF.

The full width at half maximum (FWHM) of the CuNP diffraction peaks in various solvent media is shown for the different solvents. The FWHM is inversely related to the disorder in the crystal structure such as point defects, line defects, interstitial defects, and grain boundaries. Thus the defect density of CuNP exhibits the following trend, EtOH > DMF > EG > water > GBL. All samples are grown at the same temperature and time and the only differences is the solvent media, which strongly affects the mass transfer due to the strength of the solvent and Cu+2 intermolecular interactions. When Cu+2 ions are reduced on the surface of growing rGO, the desolvation process determines the growth rate. According to the defect density shown in Fig. 3.2. 1c, we can infer that the desolvation rate is greatest in ethanol and decreases from DMF to EG to water to GBL and thus ethanol has the weakest solvent-Cu+2 molecular interaction.

A detailed microscopic characterization has been performed to understand the morphology and structure of rGO-CuNP nanostructures synthesized in different solvent media. Scanning Electron Microscopy (SEM) reveals the effect of solvent on the morphology of CuNP and the yield of CuNP on the surface of rGO. Fig. 3.1. 3 shows that CuNP are uniformly distributed and well-dispersed on the graphene layers. The morphology of CuNP is similar in all solvents we have used except water. The synthesis in water media results in spherical, elliptic, wire, and jointed structural morphologies of CuNP. In addition, the SEM shows porosity differences among the rGO-CuNP structures. As seen in Fig. 3.2. 2, the assembly of rGO-CuNP is more porous with the synthesis in ethanol, DMF, and GBL, in which rGO-layers are better dispersed with intercalated CuNP compared to the rGO-CuNP synthesized in water and EG where rGO-layers stack more densely. Fig. 3.2. 2f-j shows the backscattered electron (BSE) SEM images, which clearly indicates the placement and morphology of CuNP on the surface and between rGO layers. In addition, it demonstrates that graphene produced in this manner is highly defective and this would be expected to increase the active site density and hence improve the catalytic activity of the material. [95, 96] It can clearly be seen that there is CuNP size variation between samples. The size of CuNP synthesized in DMF are smaller than the rest of samples. Dynamic Light Scattering (DLS) is also used to measure the average hydrodynamic size distributions to corroborate the size of CuNP in the used solvents (Figure 3.2. S1a). The mean hydrodynamic diameters of CuNP synthesized in DMF are smaller compared to the rest, which is also observed in SEM images. The size distribution of CuNP strongly depend on the selection of the solvent for their synthesis because of the differences between solid–liquid interface interaction. Here, homogenous dissolution of $CuCl_4$ in solvent leads the better dispersion on the surface of rGO and thus fast nucleation occurs, and anisotropic growth leads to the formation of smaller CuNP.

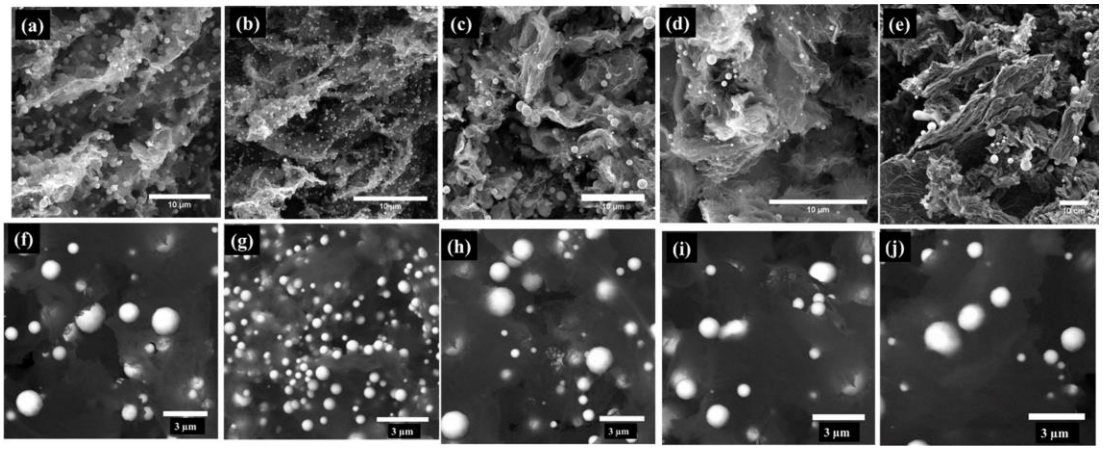

Figure 3.2. 2: Scanning electron microscope (SEM) characterization of solvent dependent synthesis of rGO-CuNP. (a) Ethanol, (b) DMF, (c) Ethylene Glycol, (d) γ-Butyrolactone (e) water. (f-j) backscattered electron (BSE) SEM images of solvent dependent synthesis of rGO-CuNP. (f) Ethanol, (g) DMF, (h) Ethylene Glycol, (i) γ-Butyrolactone (j) water.

The porosity and surface area of the samples are further characterized by Brunauer-Emmett-Teller (BET) measurements (Figure 3.2. S1). Nitrogen adsorption–desorption isotherms and pore size distributions are measured at 77 K in powder form. The BET specific surface area is calculated from the nitrogen adsorption isotherms. The surface area of rGO-CuNP electrocatalysts synthesized in DMF, EtOH, GBL, water and EG are 522.8, 317.5, 298.2, 117.8 and 68.1 m2/g, respectively. The pore size of rGO-CuNP structures is DMF > EtOH > GBL > EG > water. Such nanoscale porosity comes mostly from defects and interlayer d-spacing of GO. [97] As shown in figure 3.2.S2, the defect density of rGO is estimated by the ratio of D-band and G-band, which are related to sp3 and sp2 carbon, respectively. [95, 96] The intensity ratio of the D-band and G-band of rGO-CuNP synthesized in different solvents is relatively close to each other. Thus, the differences in the porosity levels are due to the interlayer d-spacing of rGO layers. This result is consistent with the SEM analysis where EG and water derived samples produce a more densely packed morphology as compared to DMF, EtOH and GBL samples.

Understanding the competition between hydrogen evolution and CO_2R is of fundamental importance to increase the faradaic efficiency for electrocatalytic CO_2 reduction. rGO-CuNP samples synthesized in different solvents are first investigated by cyclic voltammetry in neutral electrolyte saturated with N_2 for understanding their hydrogen evolution reactions (HER) reactivity before being tested in neutral electrolyte saturated with CO_2 for investigation of their CO_2R activity (Fig. 3.2. 3). The electrocatalysts synthesized in EtOH, DMF, and EG exhibit a high current at – 1.0 V vs. RHE (∼35 mA cm^{-2}) and a significant current difference between the CO_2-saturated experiment and the N_2-saturated experiment, hence suggesting a selectivity toward CO_2R compared to HER. The materials with the highest selectivity toward CO_2R are those exhibiting the higher surface area and defect density of CuNP. The electrocatalysts with the highest selectivity toward CO_2R are those exhibiting the higher surface area and defect density of CuNP. The electrochemical stability of the electrocatalysts is also investigated, by performing a 2 h chronoamperometry at – 0.55 V vs. RHE (Figure 3.2. S3). The electrocatalyst synthesized in EtOH shows an increase in activity (Figure 3.2. S5) while the overall activity is maintained in the low potential range (up to – 0.7 V vs. RHE) for the electrocatalysts synthesized in DMF and EG.

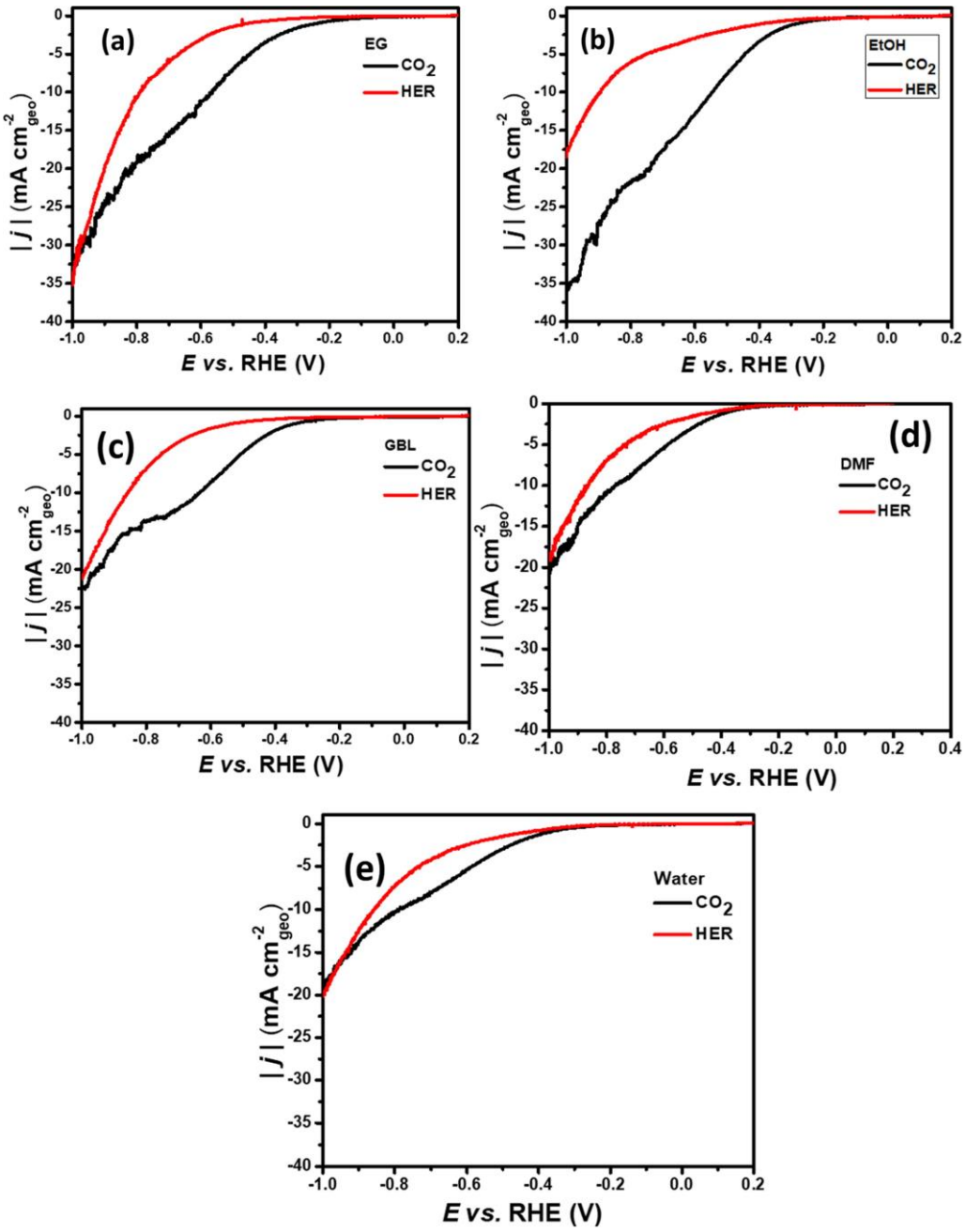

Figure 3.2. 3: Electrocatalytic activity for the CO2 reduction reaction (CO2RR) and hydrogen evolution reaction (HER) of the G-CuNP electrocatalysts synthesized in (a)Ethylene glycol, (b) ethanol, (c) γ-Butyrolactone, (d) Dimethylformamide, (e) water. All the experiments were performed at 20 mV s−1, in a 0.1 M phosphate buffer (pH = 7.5) saturated with N2 or CO2.

Energy efficiency is one of the major considerations for reducing CO_2 by electrochemical methods. Thus, to further investigate the solvent effects, Faradaic efficiency of each rGO-CuNP electrocatalyst and generated products as a result of CO_2 reduction are calculated. To determine the

selectivity of each catalyst, gaseous and liquid products generated as a result of CO_2 reduction are analyzed by gas chromatography (GC) and NMR to calculate the overall Faradaic efficiency for CO_2 reduction. The products generated with the highest efficiencies are CO, formate, and H_2. The efficiency of rGO-CuNP electrocatalysis produced using DMF, EtOH, GBL, water and EG are generated roughly similar products. The formation of high ratio CO could indicate either a lack of reactivity or that the surface binds CO too strongly and prevents its further reaction to additionally reduced products, poisoning the catalyst surface and favoring H_2 formation. The highest Faradaic efficiency of CO generation, 28.4% is obtained with the rGO-CuNP synthesized in DMF (-1.38 V). Faradaic efficiency of CO generation is ~ 15% for the rGO-CNP synthesized in EG and GBL while it is 20% and 22% for the rGO-CNP synthesized in EtOH, and water respectively at the −1.38 V. The other generated product with the highest efficiency is formate (HCOO−) with the ~ 19.5% efficiency at −1.38 V when DMF used as a solvent. The faradic efficiency for HCOO− generation was ~ 17%, ~14.5%, ~15.3%, ~13.1% for the electrocatalyst produced in EG, EtOH, water and GBL, respectively. The reduction of CO2 produces multiple carbon-based products depending on the nature of the electrocatalyst. This process comprises multiple proton/electron transfers in which a large number of intermediates and energy barriers are involved. Here, the faradic efficiency is affected by surface area, the defect density, porosity, and size of the rGO-CuNP since the highest faradic efficiency for both CO and HCOO− obtained with the electrocatalyst synthesized in DMF that has the highest surface area, larger porosity, defect density of rGO-CuNP with the smaller CuNP.

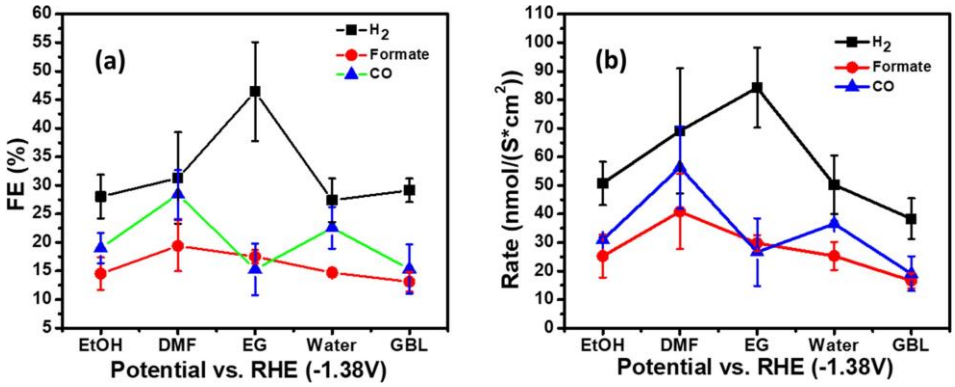

Figure 3.2. 4: (a)Faradaic efficiency and (b) Production rate for the formate and CO generated with CO2 reduction reaction with the rGO-CuNP electrocatalyst manufactured in different solvents.

In terms of CO_2R selectivity, there is a shift to formate and CO formation at the most cathodic potential tested (-1.381 V vs. RHE) for all electrocatalysts. However, the production rate is varying depending on the catalyst synthesized in a specific solvent that is most likely caused by differences in the surface area, the interlayer spacing between rGO and the properties of the CuNP. Here, the production rate of formate and CO is 41.4 nmol/S*cm2 and 56.5 nmol/S*cm2, respectively when using an rGO-CuNP electrocatalyst fabricated in DMF solvent (Fig. 3.2. 4b). The production rate of formate is 30.5, 25.4, 16.5, 25.3 nmol/S*cm2 obtained by rGO-CuNP electrocatalyst synthesized in EG, EtOH, GBL and water respectively. Furthermore, the production rate of CO is 27.3, 31.1, 19.2, and 36.5 nmol/S*cm^2 obtained by rGO-CuNP electrocatalyst synthesized in EG, EtOH, GBL and water respectively. Here, defects play the role on overall charge state of the electrocatalyst, thus increasing the density and

activity of potential active sites, which accelerate the transfer of electrons and reduce the formation energy of key intermediates. In addition, higher porosity and surface area is another critical factor for reducing CO2 to low-hydrocarbon products. Such porosity and high surface area improve the adsorption of CO_2 and intermediates on the surface of rGO-CuNP. The adsorbed CO and intermediates accept both electrons and protons simultaneously and therefore, low-hydrocarbon products occur. In addition to introducing defect sites and exposing reactive Cu facets, a short interparticle distance between Cu nanoparticles has been shown to promote the re-adsorption of CO intermediates and their further reduction to hydrocarbons. [77, 98, 99]We find only trace amounts of hydrocarbons which reaches a maximum of ca. 1 nmol/S*cm2 of ethylene corresponding to a faradaic efficiency for ethylene of 5 % using GBL solvent. The formation of high ratio CO could indicate either a lack of reactivity or that the surface binds CO too strongly and prevents its further reaction to additionally reduced products, poisoning the catalyst surface and favoring H_2 formation. [77]

Experimental section:

The rGO-CuNP catalysts were synthesized in different solvents using the hydrothermal method as shown in Fig. 1. 0.4 g $CuCl_2 \cdot 2H_2O$ and 0.2 g graphene oxide (GO) with 10 µL Hydrazine hydrate (50–60%) were dispersed in 5 ml water, ethanol (EtOH), ethylene glycol (EG), Dimethylformamide (DMF), γ-Butyrolactone (GBL) and placed in a 50 ml Teflon vial and autoclaved at 180 °C for 12 h. Then the rGO-CuNP composite structures were freeze-dried and crushed into a powder. 4 µL of an ink composed of 6.28 mg of electrocatalyst, 1290 µL of MilliQ H_2O (R = 18.2 MΩ), 43.1 µL of 5 wt.% Nafion (Sigma Aldrich) & 667 µL of IPA was deposited onto a 2 mm diameter glassy carbon disc. The ink was dried in an oven at 40 °C resulting in a 100 µg cm^{-2} catalyst loading on the glassy carbon electrode substrate.

LSV electrochemical experiments were performed in a 3-electrode cell, with an Ag/AgCl reference electrode and a Pt wire as the counter electrode (at pH = 7.5). The experiments were performed in a 0.1 M phosphate buffer solution (pH = 7.5) saturated with CO2. To assess their stability, the activity for the CO_2R was studied before and after t = 2 h of operation in a CO2-saturated electrolyte at – 1.215 V vs. RHE. Flow cell experiments were conducted in the same microfluidic flow cell used in chapter 2 (2. S 12: Figure S12: Flow Cell Diagram.) in a three-electrode configuration vs. reversible hydrogen electrode (RHE).

The chemical composition is measured by scanning electron microscopy (SEM) (FEI Quanta 200 FEG ESEM). X-ray diffraction (XRD) characterization was analyzed using the Bruker D8 Discover X-Ray Diffractometer. Raman spectroscopy analysis was collected using a Horiba Raman spectrometer with a 532 nm wavelength laser. X-ray photoelectron spectroscopy (XPS) characterization was carried out using Thermo Fisher K-Alpha + X-ray Photoelectron Spectrometer (XPS/UPS). Nitrogen adsorption–desorption isotherms and pore size distributions of the aerogels were measured at 77 K in powder form by Brunauer-Emmett-Teller (BET).

Chapter 3: Supplementary Figures for Graphene-based catalyst for CO2 reduction

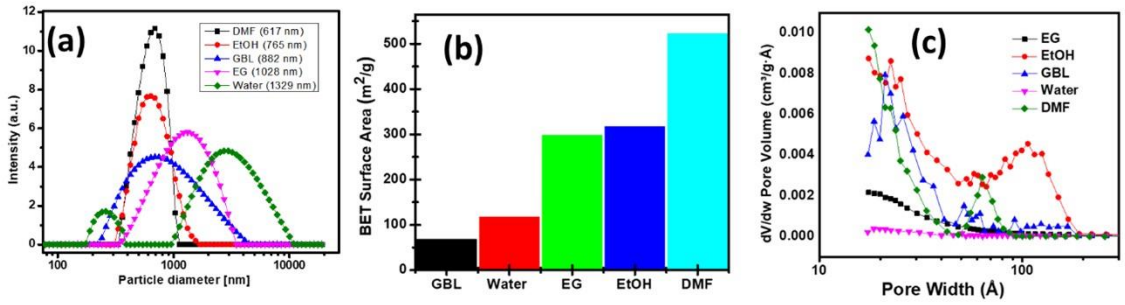

Figure 3.3. 1: (a) Dynamic Light Scattering (DLS), (b) BET surface area and (bc) pore-size distribution of rGO-CuNP in different solvents.

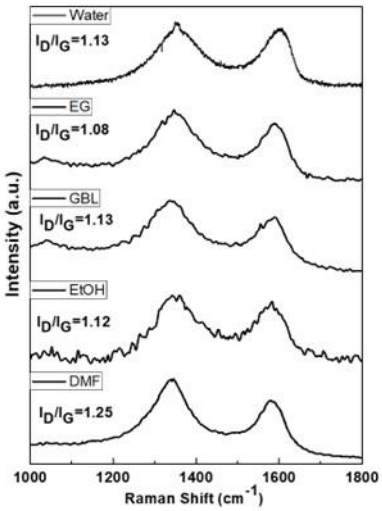

Figure 3.3. 2: Raman spectra of rGO-CuNP synthesized in different solvents.

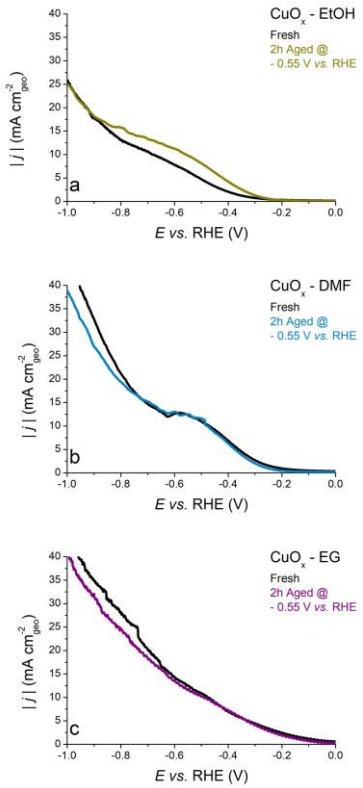

Figure 3.3. 3: Electrocatalytic performances of the different electrocatalysts in a CO2 saturated 0.1 M phosphate buffer solution (pH = 7.5) at 20 mV s-1 before (fresh) and after 2h at – 0.55 V vs. RHE in a CO2 saturated 0.1 M phosphate buffer solution (pH = 7.5).

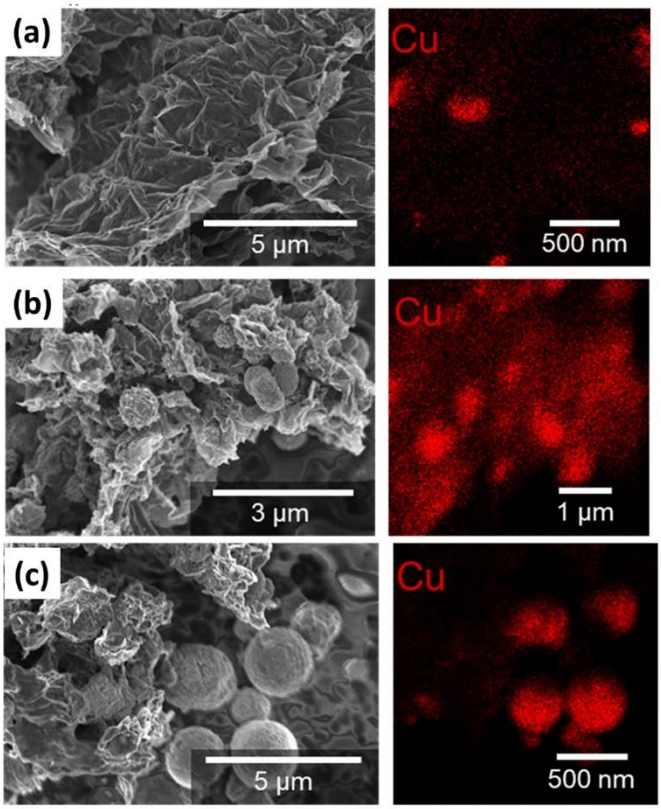

Figure 3.3. 4: SEM and energy dispersive X-ray (EDAX) mapping of the electrocatalysts growth in (c) EtOH, (d) DMF, and (e) EG after 2h electrocatalytic activity of CO2 reduction at – 0.55 V vs. RHE in a CO2 saturated 0.1 M phosphate buffer solution (pH = 7.5).

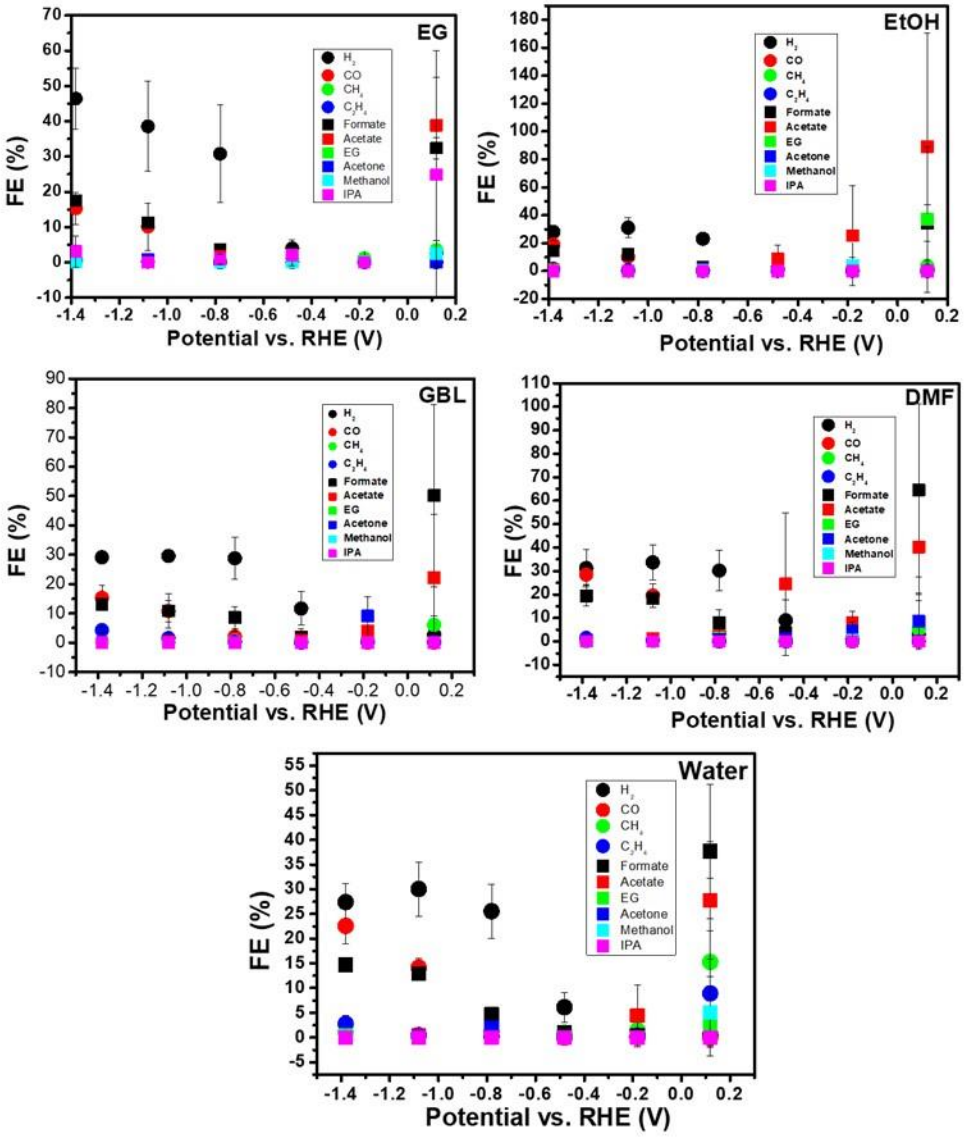

Figure 3.3. 5: Faradaic efficiency for the products generated with CO2RR with the rGO-CuNP samples manufactured in (a) Ethylene Glycol, (b) Ethanol, (c) γ-Butyrolactone (d) Dimethylformamide, and (e) water.

Chapter 4: Steering Cu-based CO_2R Electrocatalysts' Selectivity by Hydroxyapatite (HAP) Doping

The doping of electrocatalysts for the enhancement of the CO_2R is an attractive method to lower the overpotential of key intermediate mechanistic steps in the process. The involvement of soluble organic promoters to act as cocatalysts in the CO_2R process branches away from strictly heterogeneous electrocatalysis to involve homogeneous catalysis as well. Vasilyev et al categorized the involvement of soluble organic promoters in the CO_2R process into 3 categories: i.) redox shuttles which transfer electrons from the electrode to CO_2 that are regenerable and hence serve as "real" electrocatalysts, ii.) hydride transfer agents which may transfer hydrogen to adsorbed CO_2 to form hydrogenated products (e.g., formate), iii.) ionic compounds which may coat the electrode surface and change the energy of key reaction intermediates. [100] An example of a redox shuttle mechanism is the double Schiff base N,N'-bis(2-hydroxy-1-naphthaldehyde)-m-phenylenediimine (NMPD) where NMPD decreases the overpotential for CO_2 reduction by *ca.* 700 mV for selective production of oxalic acid. [101] Inorganic hydride transfer agents such as boranes and borohydrides may shuttle hydrides to bound CO_2 for formate production. [102, 103] Further, ionic compounds may be used such as tetraalkylammonium salts which may adsorb to the electrode surface and change the energetics of key CO_2R intermediates. [100]

There is a significant effect of Cu nanoparticle (NP) size on the resulting product selectivity as DFT and experimental studies show. [104, 105] Cu NPs with size > 15 nm seem to be the most promising metal-based catalyst for enhanced selectivity towards high added-value compounds. Regarding metal-free catalysts, N-doped carbon structures with high surface area, controlled porosity, high conductivity and high pyridinic and pyrrolic N content offer high CO_2R activity. In addition, doping with materials exhibiting marked Lewis basicity could further enhance catalytic activities through CO_2 activation. This may occur by stabilizing CO_2 in a bent molecular configuration as breaking the CO_2 linearity usually requires a high energy input.

In the view of combining the unique features of Cu-based and N-doped carbons catalysts, commercial Cu NPs (Ø = 25 nm) were supported on three-dimensional N-doped graphene nanosheets (3D-GNS), synthesized by sacrificial support method. [106] The resulting Cu@3D-GNS should benefit from (i) optimal dispersion and stabilization of Cu NPs onto the carbonaceous support (ii) enhanced CO2 adsorption capacity and (iii) partaking of both moieties of the composite (Cu and pyridinic/pyrrolic N-sites) to the process. Moreover, due to the three-dimensional structure and controlled porosity of 3D-GNS, the time of retention should be increased which should favor multiple ETs and C-C coupling towards C_2+ products.

Seeing as hydroxyapatite (HAP) is an amphoteric molecule, the doping of Cu-based catalysts such as Cu@3D-GNS may lead to stabilization of various CO_2R intermediates. The difficulty in applying such a dopant is that HAP has poor electrical conductivity and hence is difficult to incorporate into an electrocatalyst. Recent studies have shown HAP to be a successful dopant for photocatalytic CO_2 reduction so we wondered if it could be applied for the electrocatalytic reduction of CO_2. Chong et al showed HAP decorated Pt/TiO_2 to be an efficient photocatalyst for CO_2R. [107] Additionally, Wang et al showed enhanced photocatalytic reduction of CO_2 using Ti- and F-doped HAP for efficient CH_4 production. [108] It was hypothesized that HAP may act as a CO_2 reservoir for enhancing the local

concentration of CO_2 in the vicinity of the active site. Additionally, it may reduce the overpotential for CO_2 activation by stabilizing adsorbed CO_2 in a bent as opposed to linear configuration (Figure 1).

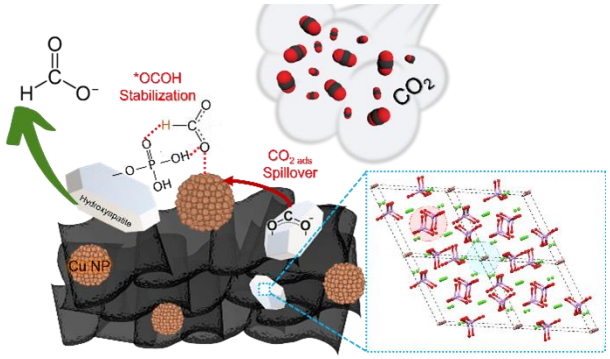

Figure 3.4. 1: Proposed mechanism of stabilization of *OCOH

Herein, we find that the presence of HAP does not significantly suppress or enhance either the HER or CO2RR. We demonstrate that an amphoteric calcium phosphate additive (Hydroxyapatite, HAP, Ca10(PO4)6(OH)2) alters the product distribution from Cu-based catalysts by steering CO2RR selectivity towards liquid oxygenated products, promoting formate production over CO.

Several parameters such as nanoparticle size[104] and shape[109] and thermal/synthetic history[110] of Cu-based catalysts have been investigated, always aiming to enhance the efficiency of the process and/or tune CO_2RR selectivity. Furthermore, active phase/support interaction have been exploited to boost Cu nanoparticle activity and selectivity towards specific products while improving conductivity and preventing aggregation of the same nanoparticles. For example, Collins et al. reported that 25 nm Cu nanoparticles were significantly more selective towards C2H4 when supported on single-wall carbon nanotubes compared to electrodeposited Cu films (FE ≈ 41% vs. ≈ 19%, E = -2.2 V vs Ag/AgCl).[111] Similarly, Sun et al. observed major increases in FE_{C2H4} when supporting 7 nm Cu nanoparticles onto N-doped graphene instead of carbon black (ca. 79% vs 6.3%, E = -1.1 V vs RHE)[112], while an outstanding performance was delivered by Cu nanoparticles on N-doped carbon nanospikes, reaching a remarkable FE ≈ 63% towards ethanol at -1.2 V vs RHE.[113] Both authors attributed such improved selectivity towards C2+ products to the presence of N moieties in the support: besides tightly anchoring Cu nanoparticles, these sites (Lewis bases) may behave as reservoir of CO_2(ads) and *H species, facilitating the overall process.

It is interesting to note that, despite the evidence that acid/base functional groups may influence catalyst CO2RR selectivity by acting on surface stabilization of intermediates, the use of acid/basic additives has rarely been investigated in this field. Recently, Xu et al. reported that the presence of phosphate groups on the surface of electrodeposited Cu electrodes increases HCOO– faradaic efficiency by a factor ca. 2.5 as compared to Cu foil. [114]

Hydroxyapatite (HAP, Ca10(PO4)6(OH)2) is a calcium phosphate characterized by marked water insolubility (Kps ≈ 4.7·10-59,[115]), thermal and chemical stability and peculiar surface properties. Indeed, HAP possesses a highly functionalized and amphoteric surface [116, 117] which in turn results in a particular

affinity towards CO_2.[118, 119] CO_2 (and eventually CO_2RR intermediates) may indeed be stabilized onto HAP acid and/or basic sites, coordinating to the surface accordingly.[117] Such coordinative ability of HAP is critical for directing the reaction pathway and determining the selectivity in CO2 reduction reaction, as recently pointed out by Wai et al., who studied carbon dioxide methanation over nickel hydroxyapatite catalysts.[120] In particular, in situ DRIFTS measurements at different temperatures proved that surface hydroxyl (*OH) and oxide (*O) groups from HAP phosphates are directly involved in the interaction with chemisorbed CO_2 to form hydrogen-carbonates (HCO3*), which then undergo further hydrogenation to be transformed into bidentate formate specie (HCOO*).

Additionally, HAP Brønsted acid sites (PO-H) could act as proton donors/acceptors, facilitating the proton transfers required by the reaction. To date, no application of HAP in electrocatalytic CO_2RR has been reported, although a few papers have implemented it in catalytic and photocatalytic applications.[107, 108, 120]

With the purpose of studying the effect introduced by acid/basic HAP functionalities on CO2RR selectivity, we first designed and synthesized a catalyst composed by Cu nanoparticles (25 nm in size) supported onto a 3D assembly of N-doped graphene nanosheets (3D-GNS, [106, 121]). Secondly, admixing with HAP has been performed and the differences in electrocatalytic performance analyzed.

The Cu-based and Cu-based HAP-admixed catalysts, hereinafter referred to as Cu/3D-GNS and Cu+HAP/3D-GNS respectively, has been synthesized starting from the individual materials and following a stepwise procedure aimed to guarantee the maximum dispersion of both Cu and HAP nanoparticles (NPs) onto 3D-GNS. Obtained electrocatalysts exhibited 20 wt.% Cu and 10 wt.% HAP loading by design (molar Cu to HAP ratio equal to ca. 30). The detailed synthetic route can be found in the Supporting Information.

The pristine support (3D-GNS) and both catalysts have been structurally and morphologically characterized by means of N2 adsorption/desorption isotherms, STEM/EDX and XPS. Figure 2 reports the main outcomes of Cu+HAP/3D-GNS characterization while additional data are available in the Supporting Information (Figures S1 to S4 and Table 1), together with the experimental and instrumental details.

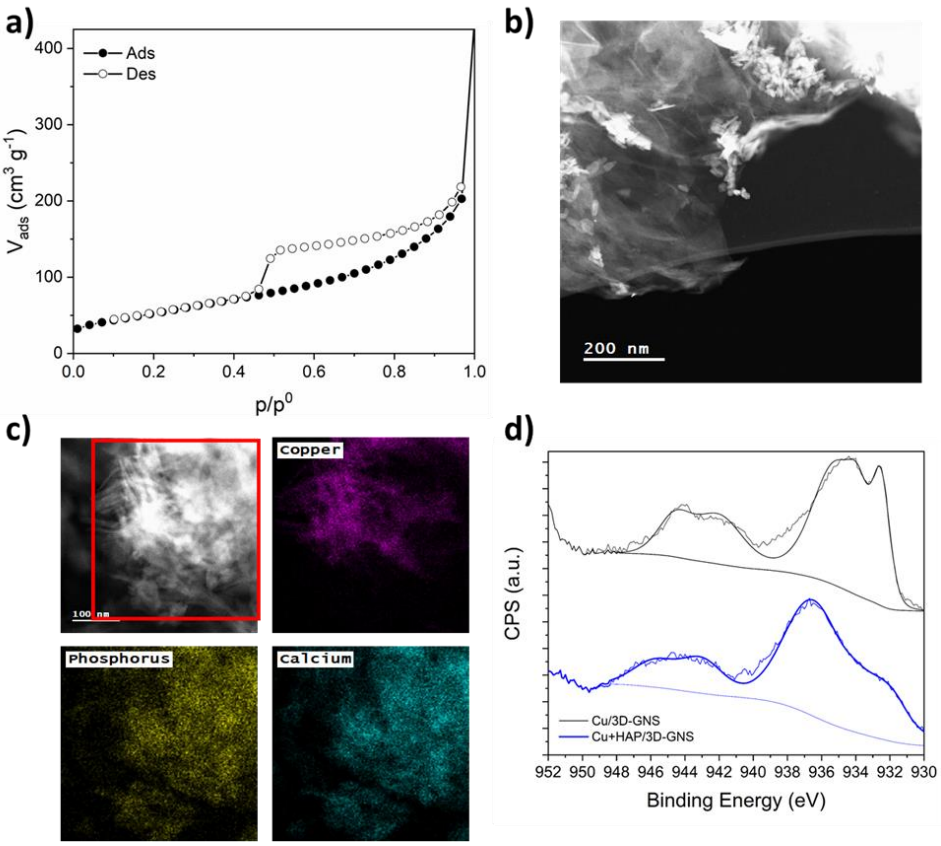

Figure 3.4. 2: Cu+HAP/3D-GNS characterization: N2 adsorption/desorption isotherm (a), STEM images (b) with correlated STEM/EDX elemental maps (c), and high-resolution XPS spectra of Cu 2p region (d).

Overall, the structural and morphological features of the support are retained upon both immobilization of the active phase (Cu NPs) and of the additive (HAP). All samples exhibit type IV N2 ads/des isotherms with H2 type hysteresis loop (Figure 2a and Figure S1), which identifies them as strictly mesoporous materials, as further confirmed by their pore size distribution (Figure S1). However, a decrease in both surface area (SA) and pore volume (V_{Pore}) is registered upon Cu NPs immobilization (Table 1), possibly caused by a partial pore obstruction by Cu NPs, which size matches that exhibited by 3D-GNS pores (Figure S1 and reference[121]).

Sample	SA[a]	V_{Pore}[b]	Elemental composition (*at.%*)					
	$m^2 g^{-1}$	$cm^3 g^{-1}$	C 1s	O 1s	N 1s	Cu 2p	Ca 2p	P 2s[c]
3D-GNS	209.17	0.214	95.97	2.98	1.25	-	-	-
Cu/3D-GNS	168.88	0.188	92.71	5.81	1.21	0.27	-	-
Cu+HAP/3D-GNS	190.74	0.187	75.20	13.52	0.57	0.27	6.46	3.99

[a] *Calculated by linear (2-parameters) BET equation;*

[b] *PSD calculated according to N_2 – DFT Model*

[c] *P quantification was performed on P 2s peak and not on P 2p one as to avoid integration errors caused by the overlapping of P 2p and Cu 3s contributions.*

Table 8: 1: Structural/Morphological and Surface Compositional Features Obtained by Means of N2 Adsorption/Desorption and XPS on the Pristine 3D-GNS Support and Both Catalysts.

STEM images (Figure 2b, Figure S2) confirm that the three-dimensional open pore structure of 3D-GNS is preserved in both catalysts, guaranteeing optimal mass diffusion of reactants and products under reaction conditions. Focusing on the Cu/3D-GNS catalyst (Figure S2), STEM images display both large Cu aggregates and small, finely dispersed Cu NPs. If the presence of large deposits may be ascribed to partial aggregation, the detection of Cu NPs with size < 25 nm may be due to a poor distribution of the commercial nanoparticles themselves. The successful admixing with HAP in Cu+HAP/3D-GNS samples is confirmed by the observation of HAP platelets all over the surface of the support (Figure S2), although for STEM images it is impossible to assess their close contact with Cu NPs. However, EDX maps display an effective overlap between Ca and P (i.e. HAP) and Cu signals (Figure 3c), thus indicating that a cooperation between the active phase and the acid/basic moieties of HAP may be expected.

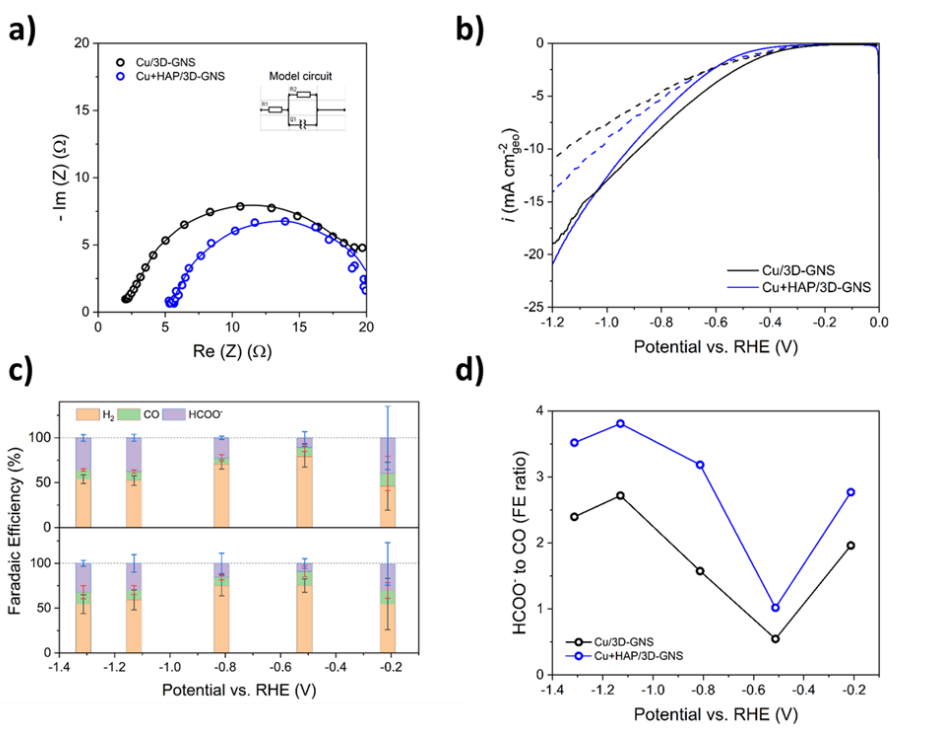

Figure 3.4. 3: Nyquist plots (a), linear sweep voltammetry (b), Faradaic efficiencies (bottom: Cu/3D-GNS; top: Cu+HAP/3D-GNS) (c), and formate-to-CO Faradaic efficiency ratios (d) of Cu/3D-GNS and Cu+HAP/3D-GNS catalysts.

XPS surveys of both pristine support and catalysts (Figure S3) provided an overview of the functional groups and surface atomic concentration at the surface; the related quantitative elemental analysis results are reported in Table 1. Each sample displays the typical contributions of its constitutive elements, namely carbon (C 1s, ca. 285 eV), oxygen (O 1s, ca. 533 eV) and nitrogen (N 1s, ca. 400 eV) for pristine 3D-GNS; additional copper (Cu 2p3/2, ca. 930 and Cu 2p1/2, ca. 960 eV) for Cu/3D-GNS; additional calcium (Ca 2p, ca. 350 eV and Ca 2s, ca. 440 eV) and phosphorus (P 2p at ca. 140 eV and P 2s at ca. 195 eV) for Cu+HAP/3D-GNS. Interestingly, at. % of Ca and P in Cu+HAP/3D-GNS are adherent to the effective HAP wt.% loading and their atomic ratio (ca. 1.62 against the stoichiometric 1.67) confirms no other calcium phosphate phases were formed upon admixing. Quantitative results obtained for pristine 3D-GNS are consistent with literature. [122] Likewise, deconvolution of high-resolution XPS spectra of C 1s and N 1s (Figure S4) revealed the predominant graphitic (sp2 C, ca. 36% of total C) and pyridinic (ca. 31% of total N) nature of 3D-GNS structure and structural moieties, respectively (Table S1).

Regarding the Cu surface atomic concentration, the values detected in Cu/3D-GNS and Cu+HAP/3D-GNS (Table 1) are ca. 10 times lower than expected by design. Possible explanations of such results could be: (i) the combination of 3D-GNS extended porous structure and moderate Cu loading, which may lead to the confinement of Cu NPs in the pores of the support; (ii) Cu NP partial aggregation and/or inhomogeneous dispersion; (iii) the fact that XPS, as a surface technique, yields an at.% quantification which may not be relatable to the volume ratio of the sample constitutive elements, especially for composite materials. The analysis of the Cu 2p3/2 region for both Cu/3D-GNS and

Cu+HAP/3D-GNS (Figure 1d) revealed the presence of modest amount of Cu species in low oxidation states (metallic copper or Cu(I), at 932.5 eV, Table S2). In any case, the HR spectra were dominated by the peaks related to Cu(II) species, namely CuO (933.8 eV, Table S2), Cu(OH)2 (935.1 eV, Table S2) and the related Cu(II) shake peaks (942-948 eV, Table S2). An additional component in the region between 936-938 eV was present exclusively in Cu+HAP/3D-GNS sample. This component might be ascribed to electron-poor Cu(II) species surrounded by electronegative groups, that in this specific case might be associated with hydroxyl and phosphate surface groups of HAP.

After characterization, inks were made from catalyst powders and gas diffusion electrodes (GDEs) were fabricated by drop-casting. Such GDEs have been tested as cathodes in a lab-scale microfluidic CO2 electrolyzer (i.e., electrochemical flow-cell, Figure S5). All the experimental details, from GDEs fabrication to electrochemical testing and products analyses, are available in the Supporting Information. Nyquist plots (Figure 3a) reveal a low uncompensated resistance of the cell. For both Cu/3D-GNS and Cu+HAP/3D-GNS GDEs, a similar R_{CT} indicates that the presence of HAP, a ceramic and thus insulating compound, does not impact on the electron transfer ability of the catalytic system.

Linear scan voltammetry (LSV) curves of both catalysts have been collected, feeding the cell either with N_2 (0.1 M PBS) or CO_2 (0.175 M $KHCO_3$) (Figure 3b), as to evaluate the magnitude of CO_2RR versus HER on the catalysts. For both Cu/3D-GNS and Cu+HAP/3D-GNS samples, a net increase of the current densities delivered at potentials lower than -0.6 V vs RHE is observed when switching from N_2 to CO_2 feeding. This confirms that, despite the unavoidable presence of parasitic HER, the catalysts exhibit CO_2RR activity. Admixing with HAP results in a slight increase of the delivered current densities under both N_2 and CO_2 feeding. Such result suggests that HAP basic moieties (i.e. surface hydroxyl *OH and oxide *O groups from phosphates[117]) might be able to foster both HER and CO2RR, acting as a reservoir/supplier of protons or CO2 molecules to the vicinal Cu NPs. However, as the ratio of the current densities delivered under different gas feeding is similar for both catalysts, HAP does not suppress and/or enhance neither HER nor CO_2RR. From these considerations, only an effect on the CO_2RR product distribution may be observed by HAP admixing.

As to shed light on the product distribution yielded by the catalysts, 30 minutes long chronoamperometric (CA) test, coupled with ex-situ determination and quantification of the reaction products, have been carried out (sample GC traces and 1H-NMR spectra available in the Supporting Information, Figure S6 and S7). The product distribution of Cu/3D-GNS and Cu+HAP/3D-GNS is reported in Figure 2c while numerical data are available in the Supporting Information (Table S3).

The relative HER and CO2RR faradaic efficiencies, plotted in Figure S8, are consistent with the LSV data, showing a predominance of HER at potentials less cathodic than -1.0 V vs RHE. Moving towards more cathodic potentials (more negative than -1.0 V vs RHE), a ca. 50% FE_{CO2RR} is reached by both catalysts, with slightly higher values for Cu+HAP/3D-GNS. Going into the details of CO_2RR selectivity, the main product for both catalysts is formate (Figure 3c), followed by CO and traces of methane and ethylene (Figure S9). Focusing at first on the Cu/3D-GNS product distribution, the low FE in ethylene, normally detected in higher amounts on large size Cu NPs, might be related to the use of 0.5 M $KHCO_3$ as electrolyte. Indeed, the CO* coupling that leads to the ethylene production pathway is favored under strongly alkaline conditions. [123] The buffering ability of concentrated $KHCO_3$, together

with the moderate current densities achieved during the test (limiting the alkalinization at the catalyst/electrolyte interphase [124]), probably concur in steering the CO_2RR process selectivity towards C1 products. On the other hand, the predominance of formate over CO and methane could be ascribed to the preferential stabilization of formate intermediates by the 3D-GNS moieties of the support. [125]

Admixing with HAP does not significantly alter the competition between CO_2RR and the parasitic HER (Figure 3c, Figure S8 and S10), as expected from LSVs. At first sight the admixing with HAP seems not to alter the product distribution either, but by calculating the ratio of formate to CO faradaic efficiencies, the effect of HAP itself on the CO2RR reaction pathways (Figure 3d) is revealed. Indeed, the formate to CO FE ratio of Cu+HAP/3D-GNS is shifted to higher values, indicating HAP is able to steer the selectivity towards formate (Figure 3d). This observation agrees with that observed by Xu et al. and Wai et al., respectively, for the electrochemical CO2RR on phosphate decorated Cu electrodes and the carbon dioxide methanation over nickel hydroxyapatite catalysts. [114, 120]

Running longer CA tests (up to 120 minutes) and monitoring the product distribution over time shows that both catalysts exhibit stable performance and invariant selectivity as well (Figure S11). Noticeably, throughout the whole extended reaction time, the formate to CO FE ratio remains higher for the HAP admixed catalyst (Figure S12). It is worth noting that XPS characterization of used catalysts confirmed the stability of these systems, whose surface Cu content was almost the same (at.% ca. 0.3 %) before and after testing. The decomposition of HR spectra revealed just slight differences in the relative distribution of copper species with an increase of Cu(0) and Cu(I) compared to Cu(II) observed for the HAP admixed catalyst in the post-electrolysis sample. Although usually used for samples with a lower proportion of Cu(II), the Cu LMM peak may be used to qualitatively assess the ratio of Cu(0) to Cu(I) with the Cu/3D-GNS sample showing primarily Cu(0) and the Cu+HAP/3D-GNS sample showing a mixed proportion of Cu(0) and Cu(I) species (Table S2 Figure S13 and S14).

A tentative mechanism of CO_2 reduction on Cu+HAP/3D-GNS is proposed in Figure 4. Based on the few reports available in literature about the effect of phosphate groups on CO_2 reduction mechanisms[120], it might be presumed that phosphate groups themselves promote the formation of a H_{ads} species, supplying a proton to Cu NPs upon the first electron transfer. Then, this H_{ads} might follow the typical parasitic HER route to form H_2 or favor the formation of a $HCOO_{ads}$ species, resulting in the formation of a formate ion upon the second electron transfer. Although the suppression of CO production in the presence of HAP could be explained by this tentative mechanism, other effects of HAP acid/basic moieties (e.g., preferential stabilization of formate intermediates through acid-base interactions between oxygen atoms and Ca2+ acidic sites) on the CO_2RR pathway cannot be ruled out.

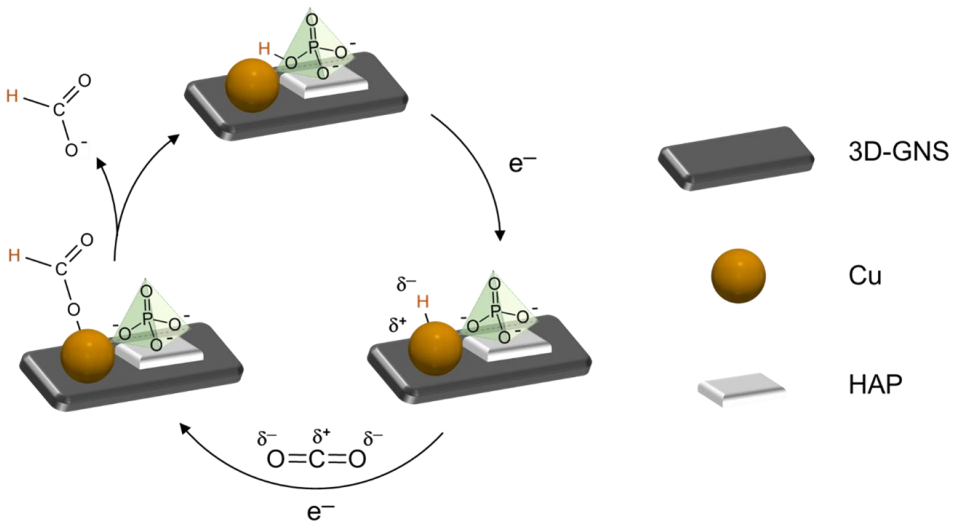

Figure 3.4. 4: Proposed mechanism for HCOO– boosted production on the HAP-admixed catalyst.

Overall, the present study indicates that the admixing of Cu-based catalysts with acid/basic additives may be a powerful strategy to bypass linear scaling relationships, which critically impact on catalysts selectivity, hampering their industrial implementation. Acid/basic moieties may indeed help in steering the CO_2RR selectivity towards specific products (in this case, formate) by means of the preferential stabilization of defined reaction intermediates. Further studies, from DFT simulations to in-situ spectroelectrochemical studies, will be aimed at disclosing the CO_2 to formate reaction pathway onto HAP admixed catalysts. With the present communication, the authors hope to stimulate further research on the effect of different acid/base (and oxo- and/or carbophilic) surface groups on CO_2RR catalysts' product selectivity, possibly paving the way to more efficient and selective electrocatalysts.

Chapter 5: Supporting Information for Steering Cu-based CO_2R Electrocatalysts' Selectivity by HAP Doping

Catalysts preparation

Synthesis of 3D-GNS support

Three-dimensional assemblies of graphene nanosheets (3D-GNS) have been synthesized according to the patented Sacrificial Support Method (SSM).[106] Briefly, graphene oxide (obtained following a modified Hummers method [126]) was exfoliated by ultrasonication (600 kJ delivered energy, 10 gGO L-1MilliQ H2O for 2 hours). Then, 20 g of EH-5 fumed silica (Cab-O-Sil, SA ≈ 400 m2 g−1) were added to the mixture and the suspension sonicated for 1 hour; the resulting solution was dried at 85°C overnight. Dry powders were ball-milled (400 RPM, 15 minutes) and then underwent a reduction treatment (800°C under a 100 sccm flow of 7% H2 in Ar flux, 1 hour). The obtained sample, now constituted by a graphene nanosheets-silica mixture (GNS-SiO2), was once again ball-milled according to the above-described procedure. Acidic etching with 25 wt.% HF (24 hours long) was subsequently

performed to leach the SiO_2 support. The leached sample was filtered and repeatedly washed with MilliQ water until reaching the neutrality of the wash water. Powders were then dried again at 85°C, overnight. Finally, the nitrogen doping of the carbonaceous structure was performed by treating the powders in presence of ammonia (850°C under a 100 sccm flow of 10% NH3 in Ar, 2 hours). Such obtained 3D-GNS powders have been stocked and used as support for both catalysts.

Synthesis of HAP NPs

HAP NPs were synthesized according the a co-precipitation route reported in literature [116], with slight modifications. Briefly, 100 mL of a 0.400 M (NH4)2HPO4 solution (> 98.0%, Sigma-Aldrich)) were placed in a three-necked round flask equipped with a mechanical stirrer. Solution pH was adjusted to ca. 9.7 (± 0.2) adding ca. 10 mL of a 28-30 wt. % NH4OH solution (Fluka). Then, under vigorous agitation (200 RPM), 100 mL of a 0.668 M Ca(NO3)2·4H2O solution (> 99.0%, Merck ACS) were added dropwise (1.65 mL min-1) at RT. Periodic additions of base were performed as to maintain a constant pH ≈ 9.7.

Upon completion of the addition, the suspension was stirred for 5 minutes and then filtered. The obtained HAP was washed with MilliQ water up to the neutrality of washing water, then dried for 16 h at 50°C under vacuum and thermally treated for 8 h at 120°C under air.

Cu NPs supporting and HAP admixing of 3D-GNS

The two-step immobilization procedure of Cu and HAP NPs onto 3D-GNS exploited the different pH_{PZC} of the individual components. Preparation of the Cu/3D-GNS catalyst: ca. 85 mg of 3D-GNS were dispersed in ca. 40 mL of isopropyl alcohol and the pH adjusted to 10 by the addition of 0.7 mL of a 0.1 M KOH aqueous solution. Separately, same procedure was applied to ca. 24 mg of commercial Cu NP (Sigma-Aldrich, CAS 7440-50-8, size = 25 nm). Both mixtures were sonicated for 30 minutes as to achieve optimal suspension. Then, Cu NPs suspension was added the 3D-GNS one and the resulting mixture was stirred at RT for 48 hours. The slurry was filtered on a 0.45 µm Nylon membrane, washed with MilliQ water and dried at 110°C for 45 minutes, thus obtaining the Cu-based Cu/3D-GNS catalyst. Preparation of the admixed Cu+HAP/3D-GNS catalyst: ca. 100 mg of Cu/3D-GNS were suspended in ca. 90 mL of MilliQ water and the pH adjusted to 7 adding 42 mL of a 0.1 M KOH aqueous solution. Separately, HAP NPs were suspended in ca. 20 mL of MilliQ water and the pH adjusted at 7 by adding 15 mL of a 0.1 M KOH solution. Both mixtures were sonicated for 45 minutes as to achieve optimal suspension. HAP suspension was then added to the Cu/3D-GNS one and the resulting mixture was stirred at RT for 48 hours. The slurry was filtered and rinsed with MilliQ water as described above. The final drying at 110°C for 3 hours yielded the Cu-based HAP-admixed Cu+HAP/3D-GNS catalyst.

Structural and morphological characterization

N2 adsorption/desorption isotherms: analyses have been performed using a Micromeritics 3Flex Analyzer. Low-pressure part of the adsorption branch of the isotherm has been linearized according to the linear 2-parameter BET equation ($0.01 < p/p0 < 0.35$) whilst the desorption branch has been interpreted by N2 – DFT model, as to determine specific surface area (Sa) and pore size distribution (PSD), respectively. STEM/EDX imaging: Aberration-corrected scanning transmission electron microscopy (AC-STEM) characterization was carried out by means of a JEOL Grand ARM300F equipped

with two spherical aberration correctors and an EDX probe. Operative voltage was set at 300 kV. XPS: measurements were carried out using an AXIS Supra instrument (Kratos Analytical), equipped with a dual anode Al/Ag monochromatic X-ray source. Data treatment, peak deconvolution and integration where performed using CasaXPS software. In particular, peak deconvolution and assignment of specific contributions in the N 1s and C 1s regions was performed following ad-hoc optimized procedures reported in literature [122].

Electrocatalytic setup and testing

GDEs fabrication

GDEs were obtained drop-casting catalyst inks on 1.5x1.5 cm Sigracet BC29 carbon paper gas diffusion layers supported by hot pressing (100°C, applied pressure ca. 6-7 tons m-2, 10 minutes) onto a STERLITECH laminated PTFE 1.0 µm pore size membrane filter. Electrocatalyst inks were prepared mixing precise amounts of catalyst, Cu/3D-GNS or Cu+HAP/3D-GNS for the cathode and commercial Pt/C (20 wt.% Pt on C, Sigma-Aldrich) for the anode, with a Nafion solution (5 wt.% solution in lower alcohols, Sigma-Aldrich) in isopropyl alcohol. The Nafion/C content of catalyst ratio of the cathode's ink was ca. 0.3. The mixtures were then sonicated for ca. 30 minutes before being drop-casted onto the GDLs. Electrode loadings by design were ca. 0.4 mg Cu cm^{-2} and 5.00 mg Pt/C cm^{-2} for cathode and anode, respectively.

Flow-cell assembly and operational parameters

An exploded view of the electrochemical microfluidic flow-cell used in this study is reported in Figure S5a along with the full experimental setup (Figure S5b). The flow-cell was assembled with fresh anode and cathode for each experiment; electric leads were provided by copper tape. In a typical experiment, 35 mL of a 0.5 KHCO3 (> 99.7%, Sigma-Aldrich) aqueous solution (pH ca. 8.1), used as electrolyte, was continuously flowed through the central compartment of the cell by means of a Masterflex L/S® peristaltic pump (flowrate of ca. 1 mL min^{-1}). The reference electrode (Ag/AgCl) was placed in the 50 mL beaker used as electrolyte reservoir during the tests (Figure S5b). CO2 (99.99% pure, Matheson) was feed to the cathode GDE through the gas chamber at a constant flowrate of 10.00 sccm by means of an Alicat MC series mass flowmeter. The mixture of unreacted CO_2 and gaseous products leaving the cell continuously purged the sampling vial. Both liquid and gas phase samples were collected at the end of each chronoamperometric run and tested according to the procedures reported in the dedicated paragraph.

Electrochemical testing

Electrochemical tests were carried out using a BioLogic model VSP300 potentiostat connected to the EC Lab software interface. Before testing CO2RR performances, each cathode underwent conditioning by means of cyclic voltammetry (CV) in the potential range from 0 V to – 1.4 V vs RHE at v_{scan} = 50 mV s-1 until stable voltametric behavior was achieved.

Potentiostatic electrochemical impedance spectroscopy (PEIS) was applied for the determination of the cell uncompensated resistance (Ru), collecting data in the range between 200 kHz and 100 mHz, at -0.5 V vs RHE; PEIS have been fitted according to a R1(R2Q2) model circuit, as reported in Figure 2a.

CO_2RR versus HER onset competition have been determined by means of linear scanning voltammetry (LSV, from 0 V to – 1.2 V vs RHE at vscan = 1 mV s-1), respectively feeding the cell with pure CO_2 (electrolyte: 0.175 M $KHCO_3$) and N_2 (electrolyte: 0.1 M PBS). The increased concentration of $KHCO_3$ was utilized so that the electrolyte ionic conductivity was constant (ca. 1560 mS/m, Surpass 3 electrokinetic analyzer conductivity probe) while the choice of PBS as electrolyte for N2-fed LSVs was dictated by the necessity to completely rule out any CO_2RR activity of the catalyst. Finally, 30 to 120 minutes long chronoamperometric (CA) scans have been performed in the potential range from – 0.2 V to – 1.4 V vs RHE as to evaluate the delivered current density (i.e., reaction rate) and product distribution.

Coupling the electrochemical information obtained from CA tests with products quantification by GC-TCD and 1H-NMR (see the following paragraph), faradaic efficiency towards detected products was calculated according to the following formula:

$$FE_{Product} = \frac{Q_{Prod}}{Q_{Tot}} = \frac{n \times F \times mol_{Product}}{I_{Tot} \times t}$$

, where Q_{Prod} and Q_{Tot} are the quantity of charge (measured in Coulombs, C) stocked in the product of interest and totally exchanged by the catalytic system, respectively. Q_{Prod} was calculated as the product of the number of electrons (moles) required for the generation of 1 mole of product (n) times the Faraday constant (F) times the quantity of the product itself ($mol_{Product}$, measured in moles). Q_{Tot} was instead calculated as the product of the total current exchanged by the system (I, measured in A) times the time of cathodic potential application in the CA scan (t, measured in seconds).

From a sake of clarity and comparison with literature, applied potential has been converted in E vs RHE and corrected by the ohmic drop using the following formula:

$$E_{RHE-IR\ Compensated} = E_{Ag/AgCl} + 0.197\ V + 0.059 \times pH - IR_u$$

, where all potentials are reported are in V, I is the current (< 0 since cathodic) delivered by the system under the applied potential in A and R_u is the uncompensated resistance (determined by PEIS) in Ω.

Analysis of CO_2RR products

Gas phase products have been identified and quantified by GC/TCD using an Agilent 7890 gas chromatograph equipped with a 19095P-MS6 HP Molsieve Column (Ø = 530 µm length = 30m). Different gas carriers, oven temperatures and flowrates have been used for the determination of different gas phase products. H_2 has been separated by the columns at 40°C using N_2 as gas carrier (flowrate = 27.7 mL min-1) while CO, CH4 and C2H4 separation method involved the same parameters but He as carrier (flowrate = 57.7 mL min-1).

Liquid phase products were detected and quantified by 1H NMR, applying the internal standard method. Briefly, 0.1 mL of D2O and 0.1 mL of 6 mM DSS (2,2-Dimethyl-2-silapentane-5-sulfonate, internal standard) were added to 0.5 mL of the sample in an NMR tube. 1H NMR spectra of the samples were then acquired using a Bruker CRYO500 MHz NMR spectrometer with a 6 sec pre-scan delay, an acquisition time of 106 s for a total number of 16 scans. The free induction decays (FIDs) were weighted by a 90-degree phase-shifted sine-bell function before Fourier transformation. The signal of water, standing around at 4.78 ppm, have been systematically suppressed using pulsed field gradients method. NMR peaks have been assigned to each CO_2RR product by comparison with NMR spectra collected on standard solution and in according to literature [127]. Quantitative evaluation of products has been carried out using the internal standard method and the peak area ratio. The applied formula was:

$$C_x = \frac{A_x}{A_{Cal}} \times \frac{N_{Cal}}{N_x} \times C_{Cal}$$

, where C is the molar concentration of the product of interest, A the peak area and N the multiplicity associated with the peak, with subscripts x and Cal indicating the product of interest and the internal standard (DSS), respectively. The DSS peak selected for the formula application was the singlet positioned at chemical shift 0 ppm, with multiplicity (N_{Cal}) equal to 9.

Supporting Figures

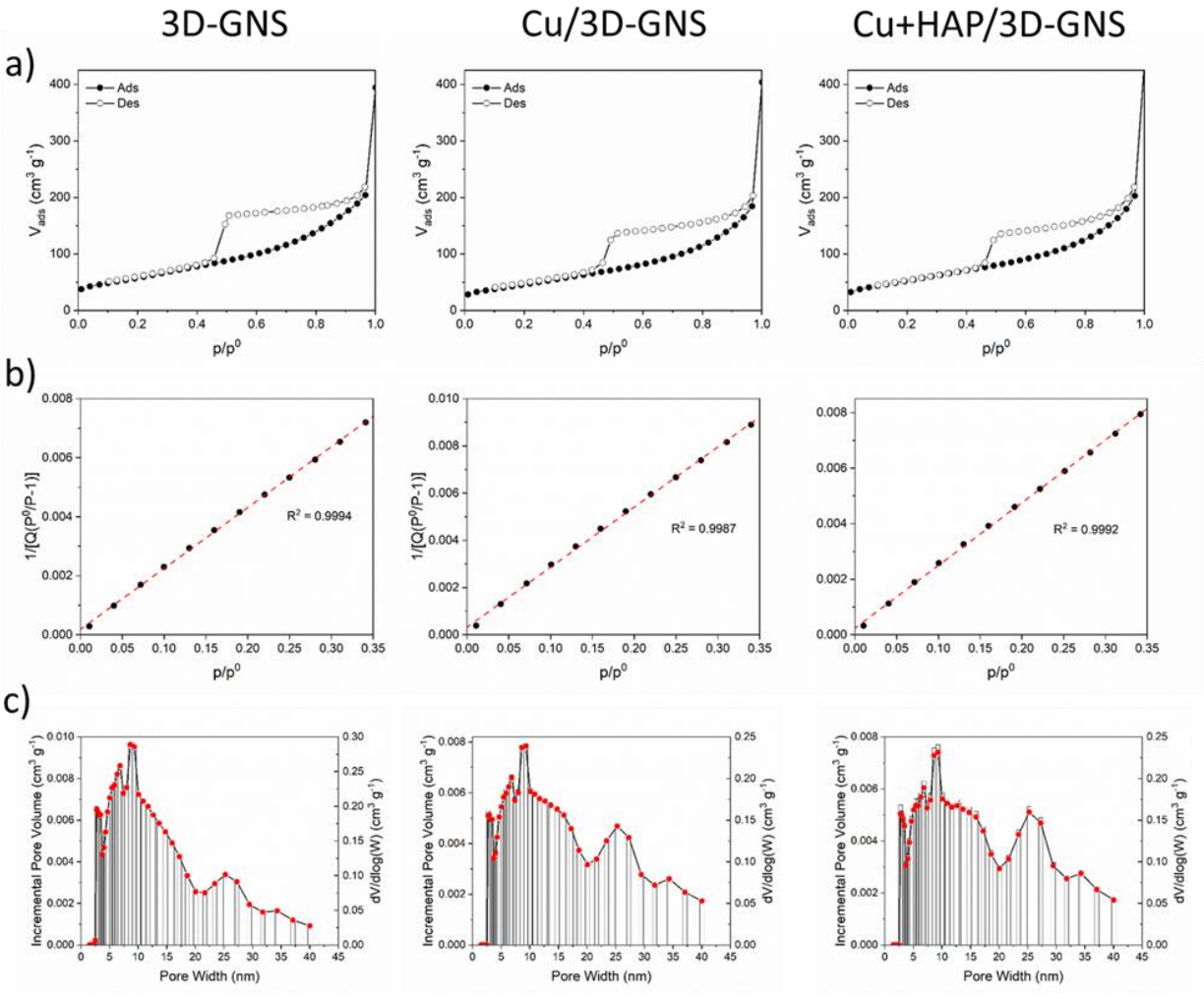

Figure 3.5. 1: Results of N2 adsorption/desorption analyses on the pristine 3D-GNS support and both catalysts. Adsorption/desorption isotherms (a), 2-parameters BET linearization (b) and pore size distribution according to the N2 – DFT model (c).

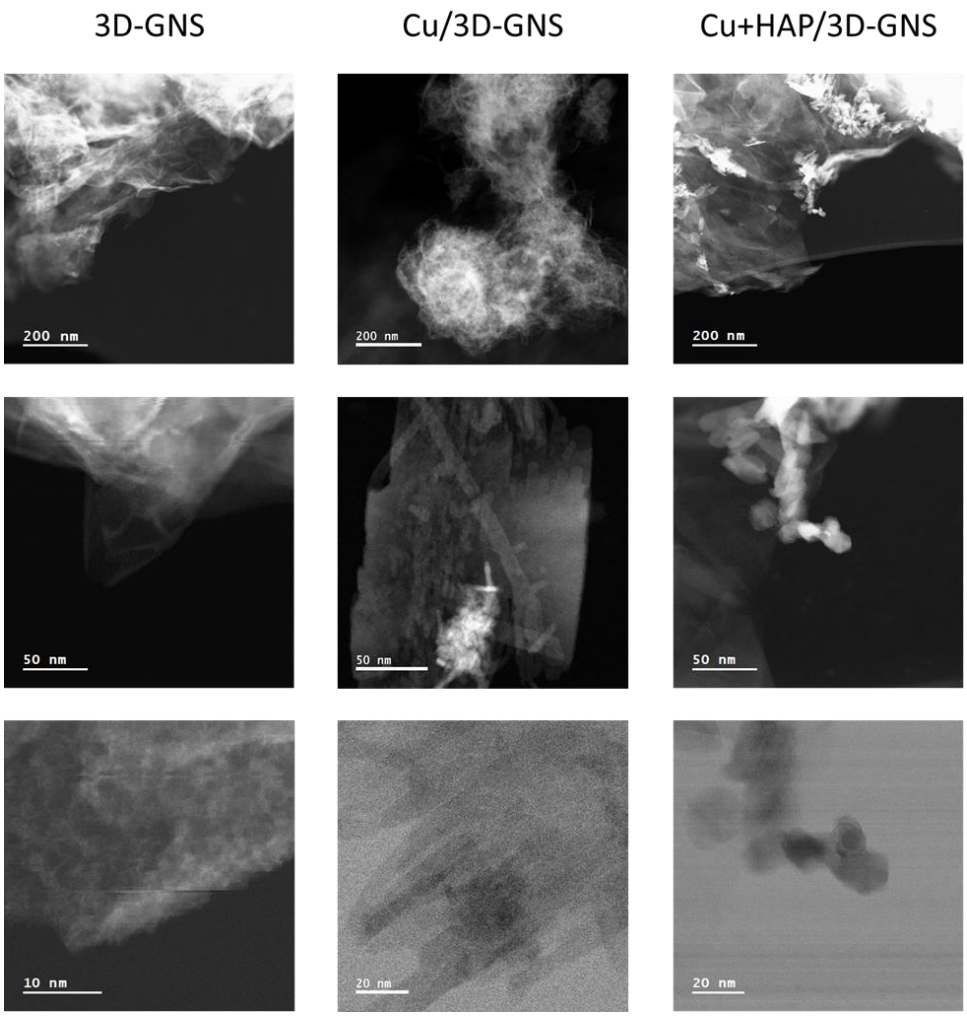

Figure 3.5. 2: Dark and bright field STEM images of the pristine support (3D-GNS) and of Cu/3D-GNS and Cu+HAP/3D-GNS catalysts at different magnification

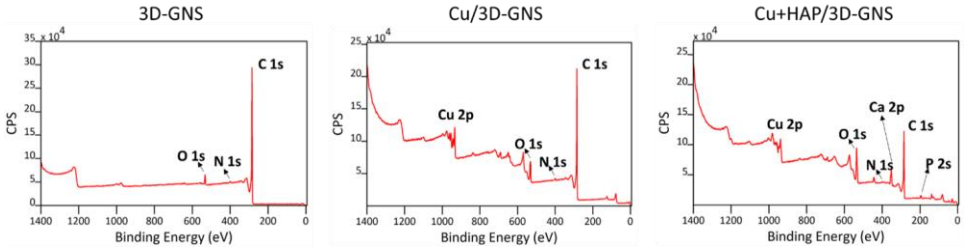

Figure 3.5. 3: XPS surveys registered on pristine 3D-GNS and both catalysts.

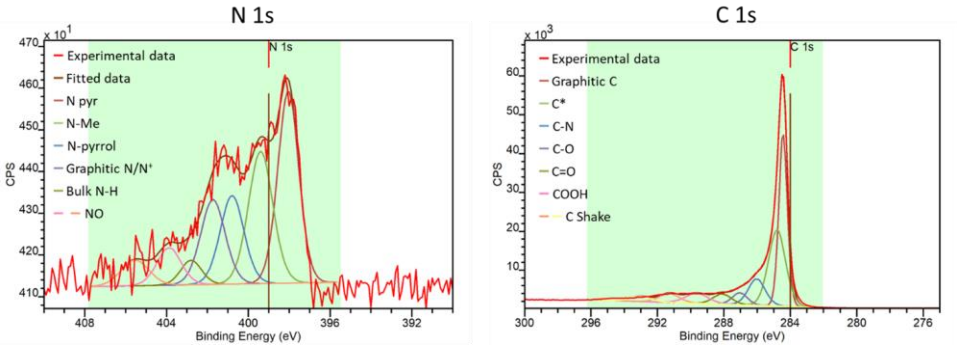

Figure 3.5. 4: High-Resolution XPS spectra of N 1s (left) and C 1s (right) regions, collected on the pristine 3D-GNS support.

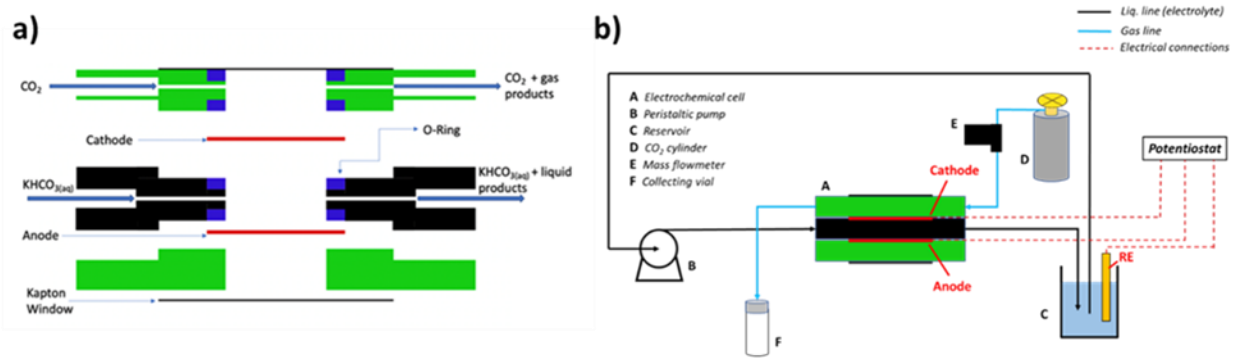

Figure 3.5. 5: Exploded view of the electrochemical flow-cell and b) complete flowsheet of the electrochemical system used to perform CO2RR tests.

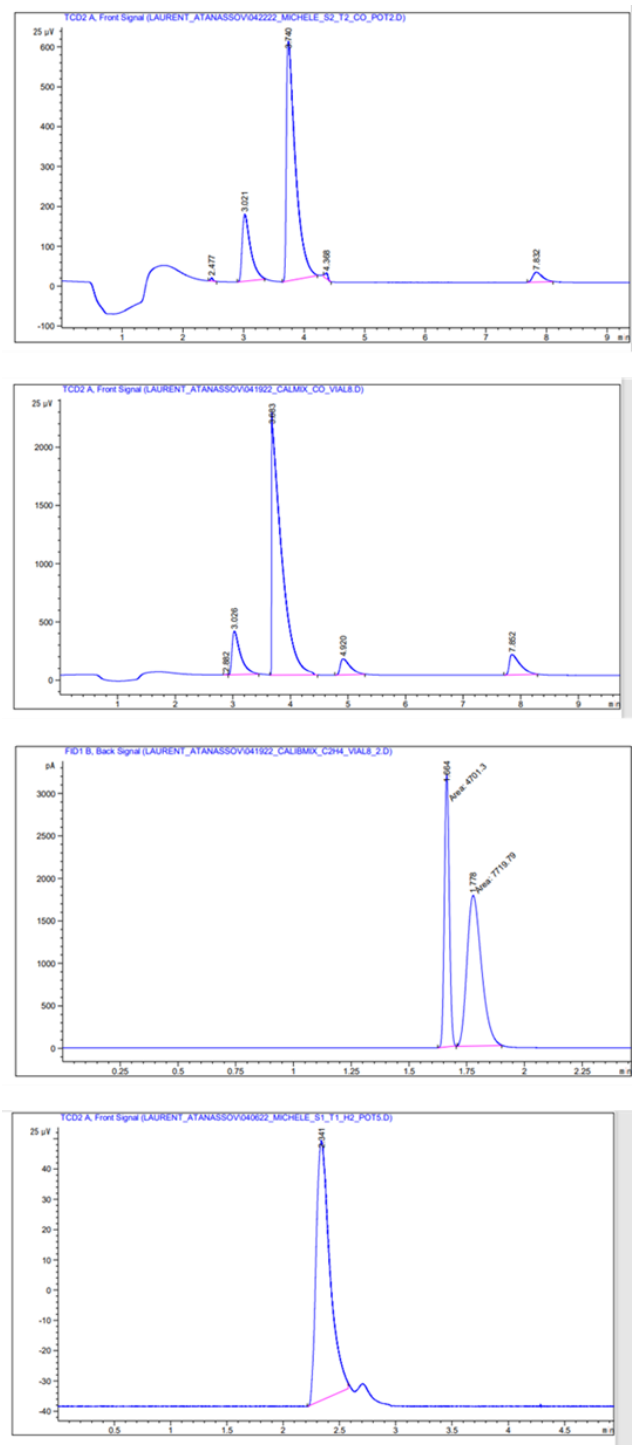

Figure 3.5. 6: Sample gas chromatograms. From top to bottom: Cu+HAP/3D-GNS, E = -1.13 V vs RHE (CO peak at 7.8 minutes corresponding to a 0.376 %V/V CO concentration); calibration mixture corresponding to a 2.993 %V/V CO concentration; calibration mixture corresponding to a 2.76 %V/V concentration of both CH4 (peak at 1.66 minutes) and C2H4 (peak at 1.75 minutes); Cu/3D-GNS at -1.31 V vs RHE (H2 peak a 2.4 minutes corresponding to a 2.318 %V/V H2 concentration).

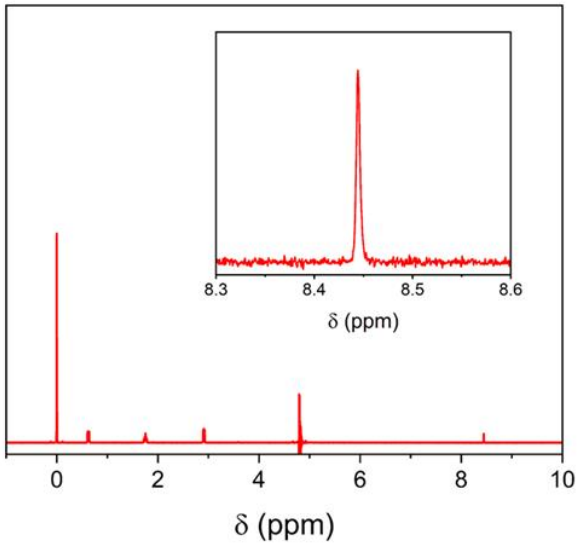

Figure 3.5. 7: Sample 1H-NMR spectrum of a formate calibration solution (ca. 0.6 mM) in aqueous 0.5 M KHCO3. Peaks at 0, 0.65, 1.75 and 2.90 ppm are assigned to the DSS internal standard. Peak at ca. 4.78 ppm is instead ascribed to water. Formate peak (ca. 8.45 ppm) is magnified in the inset.

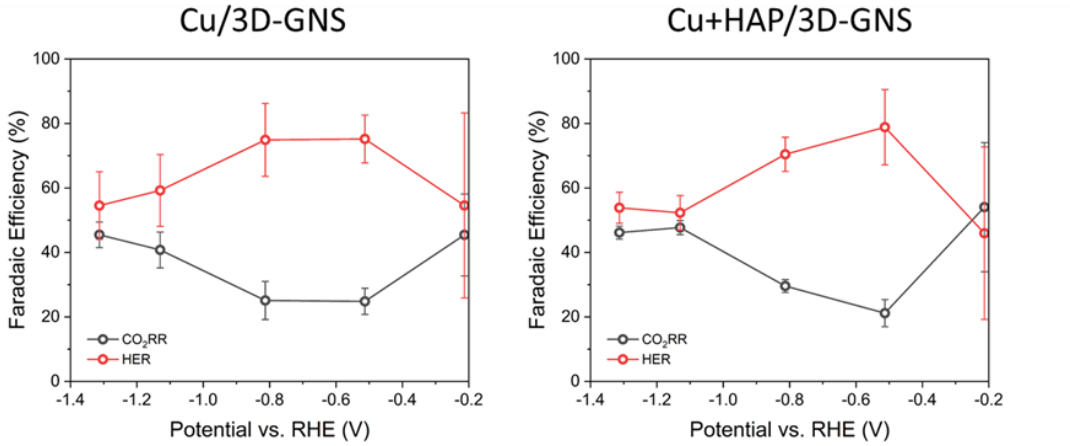

Figure 3.5. 8: HER versus CO2RR total faradaic efficiencies as determined from 30 minutes long chronoamperometric tests on the investigated catalysts.

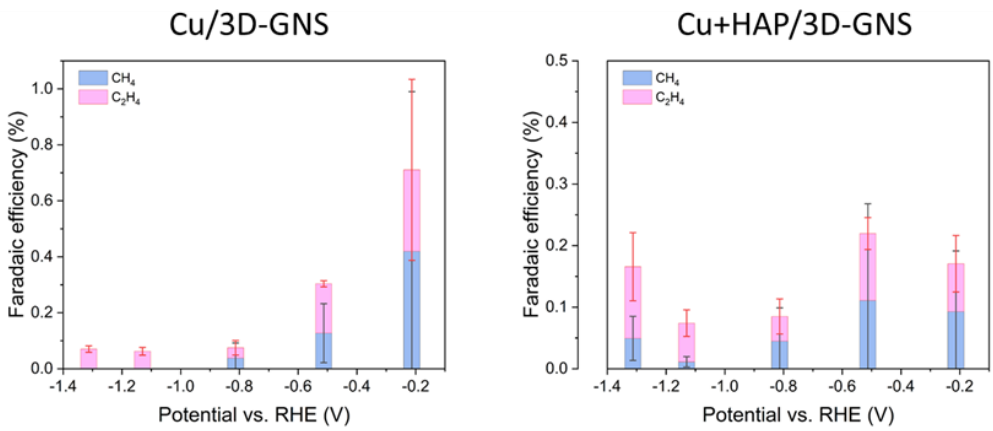

Figure 3.5. 9: Faradaic efficiencies of minor CO2RR products as determined from 30 minutes long chronoamperometric tests on the investigated catalysts.

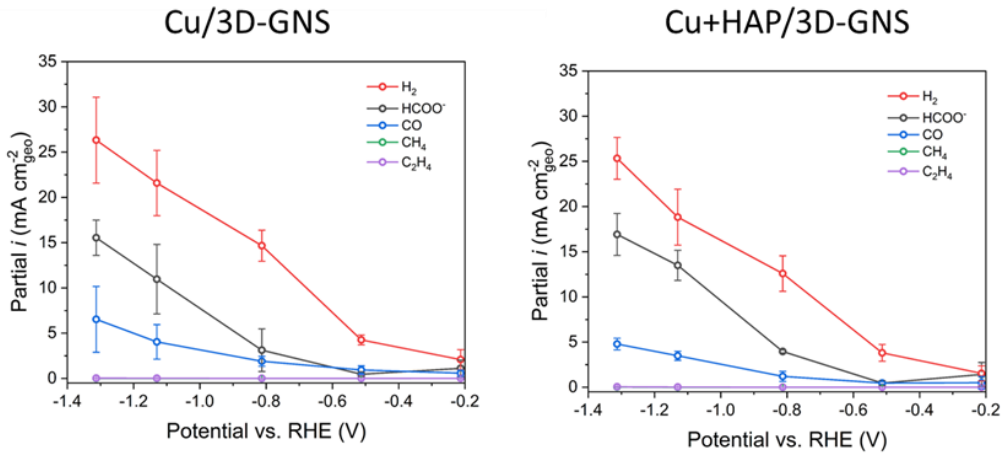

Figure 3.5. 10: Partial current densities of the electrolysis as determined from 30 minutes long chronoamperometric tests on the investigated catalysts

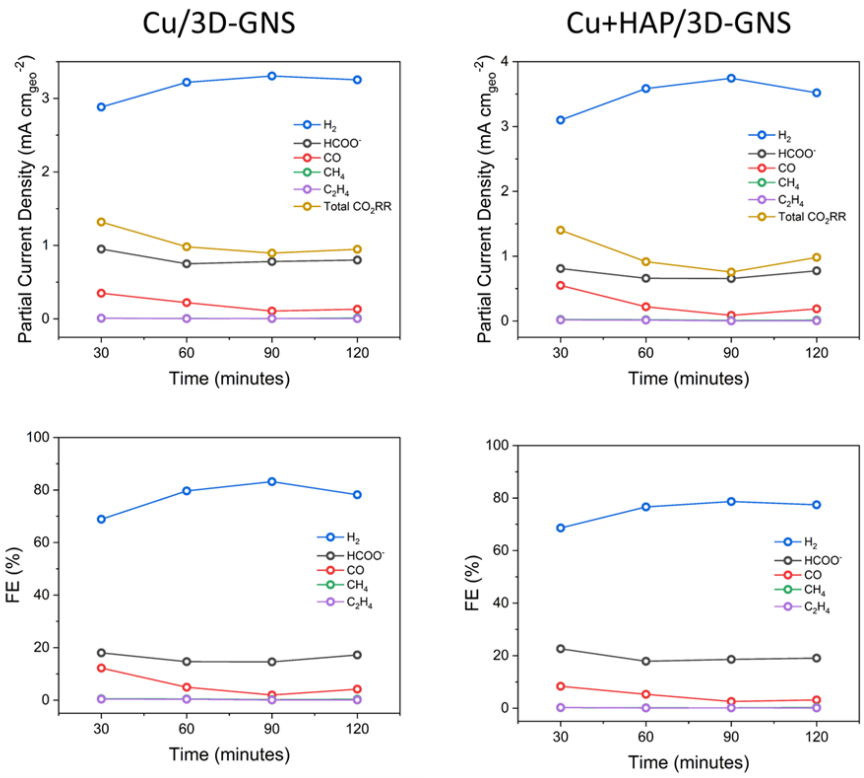

Figure 3.5. 11: Partial current densities (top) and faradaic efficiencies (bottom) versus time as determined from 120 minutes long chronoamperometric scans (E = -0.5 V vs RHE) for the investigated catalysts

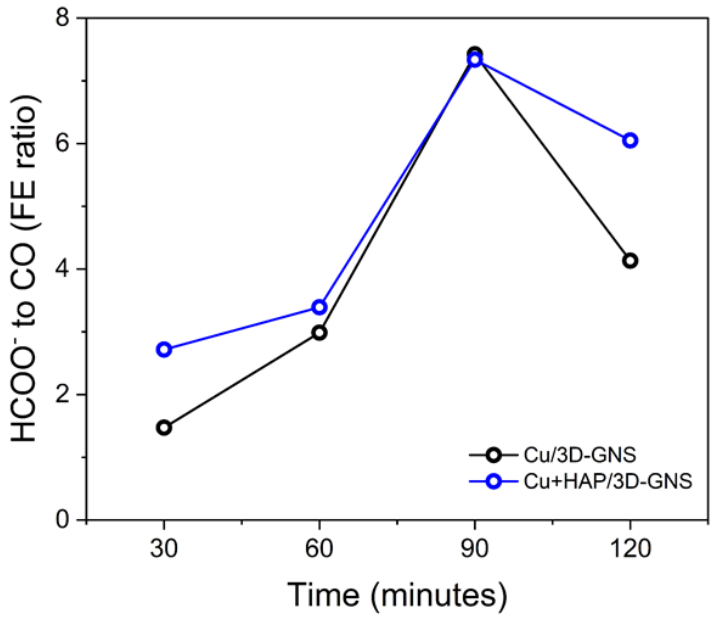

Figure 3.5. 12: Formate to CO FE ratio versus time as determined from 120 minutes long chronoamperometric scans (E = -0.5 V vs RHE) for the investigated catalysts

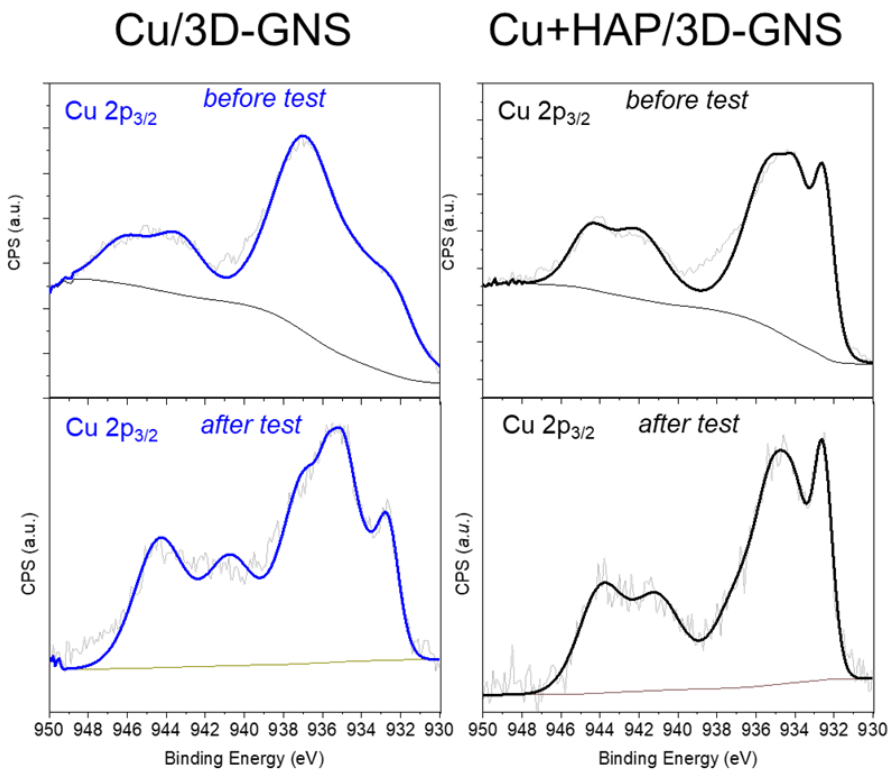

Figure 3.5. 13: Comparison of the high resolution XPS spectra, collected in the Cu 2p region for both catalysts, before and after 120 minutes long CA scans (E = -0.5 V vs RHE)

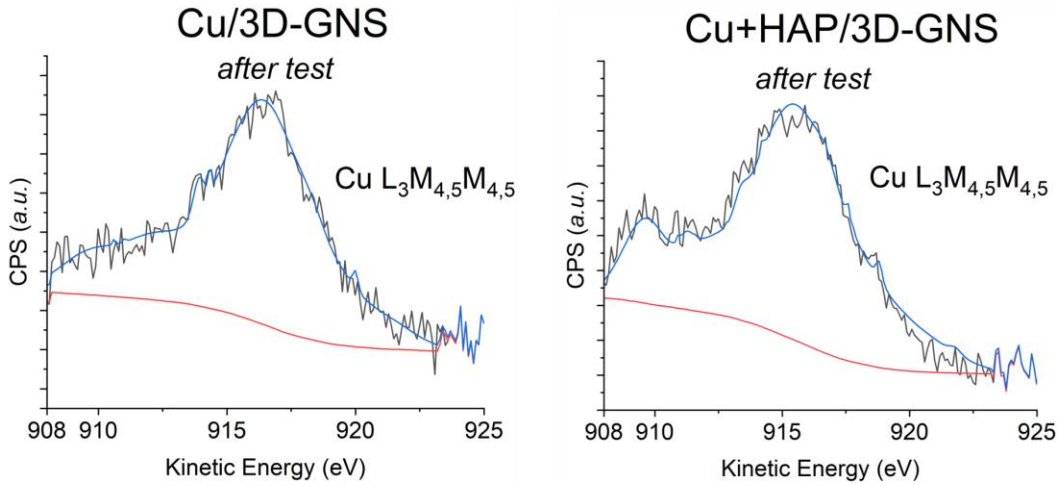

Figure 3.5. 14: Comparison of the high resolution XPS Cu $L_3M_{4,5}M_{4,5}$ for both catalysts after 120 minutes long CA scans (E = -0.5 V vs RHE).

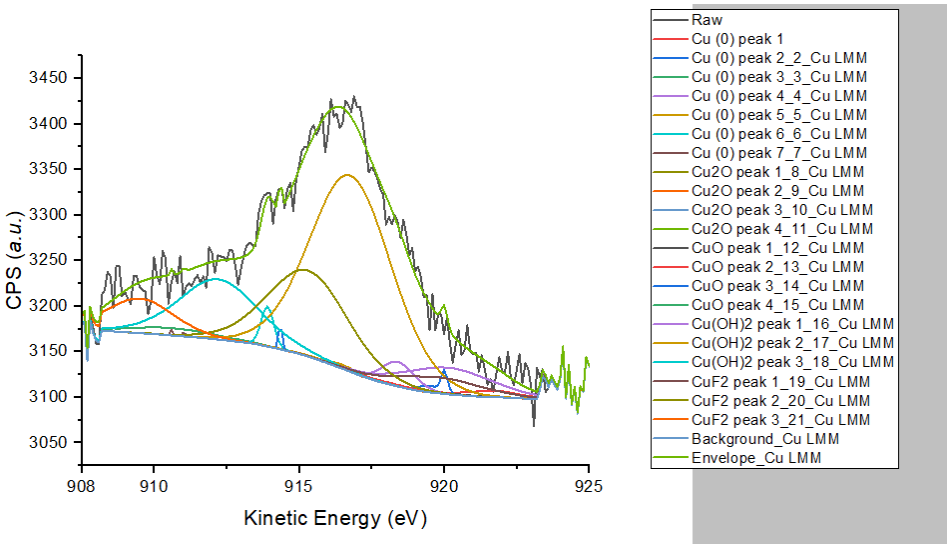

Figure 3.5. 15: Cu/3D-GNS Cu $L_3M_{4,5}M_{4,5}$ Peak deconvolution.

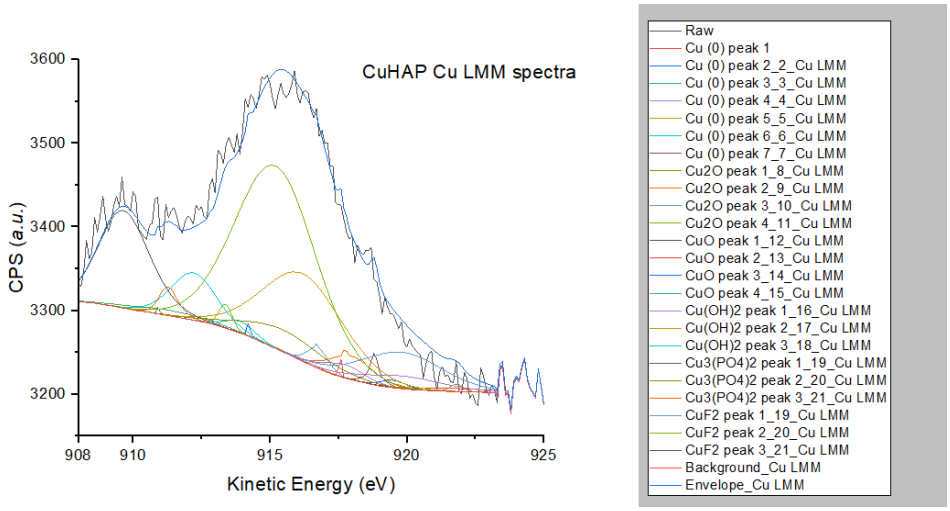

Figure 3.5. 16: Cu+HAP/3D-GNS Cu $L_3M_{4,5}M_{4,5}$ Peak deconvolution.

List of Tables

	at.% contributions (3D-GNS)						
	N pyr	*N amine*	*N-pyrrol*	*Graphitic N/N⁺*	*Bulk NH*	*NO*	
N 1s	31.21	23.15	16.33	13.47	5.85	10.02	
	(398.0 eV)	*(399.4 eV)*	*(400.8 eV)*	*(401.7 eV)*	*(402.8 eV)*	*(403.9 - 405.5 eV)*	
	Graphitic C	*sp^3 C*	*C-N*	*C-O*	*C=O*	*COOH*	*C Shake*
C 1s	35.72	31.98	10.45	5.43	4.28	5.47	6.69
	(284.4 eV)	*(284.8 eV)*	*(286.0 eV)*	*(287.0 eV)*	*(288.1 eV)*	*(289.6 eV)*	*(291.3 – 293.0 eV)*

Table 9: S1: Contribution of different N-moieties and different C bonding obtained from deconvolution of the High-Resolution N 1s and C 1s spectra of 3D-GNS reported in Figure S4.

	Cu (0 or I)	CuO	$Cu(OH)_2$	Cu(II) in an electron-poor local environment	Cu(II) shake 1	Cu(II) shake 2
Cu/3D-GNS	932.5	933.8	935.1	-	942	944.6
Before test	(15.4%)	(6.8%)	(48.2%)		(19.9%)	(9.7%)
Cu/3D-GNS	932.5	933.9	935.1	936.8	941	943.9
After test	(15.7%)	(13.2%)	(20.5%)	(16.4%)	(15.9%)	(18.1%)
Cu+HAP/3D-GNS	932.4	933.8	934.9	935.8-938.5	945	947.8
Before test	(3.7%)	(7.8%)	(5.6%)	(61.6%)	(12.4%)	(8.9%)
Cu+HAP/3D-GNS	932.6	933.8	934.9	935.8-936.8	941	944.3
After test	(7.9%)	(9.3%)	(9.8%)	(34%)	(17.7%)	(21.3%)

Table 10: S2: XPS data of the Cu 2p region of fresh and used electrocatalysts.

E vs RHE (IR corrected)	FE_{H2}		FE_{CO}		FEC_{H4}		FE_{C2H4}		FE_{HCOO-}	
V	%		%		%		%		%	
-0.213	54.6	± 28.7	15.1	± 8.7	0.4	± 0.6	0.3	± 0.3	29.6	± 23.8
-0.513	75.2	± 7.4	15.8	± 6.1	0.1	± 0.1	0.2	± 0.01	8.7	± 5.4
-0.813	74.9	± 11.3	9.7	± 3.0	0.03	± 0.05	0.04	± 0.03	15.3	± 11.5
-1.13	59.2	± 11.1	10.9	± 5.0	0	-	0.06	± 0.01	29.8	± 9.9
-1.313	54.5	± 10.5	13.4	± 7.2	0	-	0.07	± 0.01	32.0	± 3.4

E vs RHE (IR corrected)	FE_{H2}		FE_{CO}		FEC_{H4}		FE_{C2H4}		FE_{HCOO-}	
V	%		%		%		%		%	
-0.213	46.0	± 26.7	14.3	± 19.1	0.09	± 0.1	0.08	± 0.05	39.6	± 35.2
-0.513	78.8	± 11.7	10.4	± 4.6	0.1	± 0.2	0.1	± 0.03	10.6	± 7.1
-0.813	70.4	± 5.3	7.0	± 3.6	0.04	± 0.05	0.04	± 0.03	22.4	± 1.7
-1.13	52.3	± 5.4	9.9	± 2.1	0.01	± 0.008	0.06	± 0.02	37.7	± 3.9
-1.313	53.8	± 4.8	10.2	± 1.4	0.05	± 0.04	0.1	± 0.06	35.8	± 3.8

Table 11: S3: Faradaic efficiency registered on Cu/3D-GNS (upper table) and Cu+HAP/3D-GNS (lower table), as determined from 30 minutes long chronoamperometric tests.

Section 4: Novel synthesis method for M-N-C Catalysts by dynamic template removal

Chapter 1: Acid-free process intensification for the synthesis of non-precious metal-nitrogen-carbon electrocatalysts for oxygen reduction reaction

While the focus of the bulk of this dissertation has been on the development of non-PGM, specifically carbon-based metal-nitrogen-carbon catalysts, for CO_2 reduction reaction, the catalysts developed in this section also show promise for application in oxygen reduction reaction (ORR). The utilization of non-PGM based catalysts for ORR is at a much later stage of development than for CO_2R as the impetus towards their development have been larger. For example, as mentioned previously, the company Pajarito Powder, has developed the SSM to produce carbon-based catalysts for ORR application in fuel cells either as direct catalysts or as active catalyst supports. [128] The need to move away from Pt-based materials for fuel cell catalysts has a wide impetus in moving towards sustainable MEA production for economical fuel-cell electric vehicles. To illustrate the advancement in non-PGM based electrocatalyst research for application in fuel cells, DAIHATSU has developed the first non-PGM direct hydrazine fuel cell system which powers a 100% Pt-free zero-emission vehicle based on NiZn catalysts from Serov and Atanassov et al. [129] The catalysts utilized in this system are also industrially scalable as they are produced from mechanochemical instead of solvothermal mixing. For the same reason, the novel synthesis method presented herein avoids the use of harsh solvents and achieves an extremely active and stable ORR M-N-C catalyst. This chapter is devoted to the application of the novel M-N-C catalysts for ORR, while chapter 2 delves into greater detail into the mechanism for their formation, as well as their application for CO_2R.

The cathodic electrochemical reaction, oxygen reduction reaction (ORR), is sluggish and the state of the art electrocatalyst that is required, platinum [130], is expensive, scarce, and characterized by price volatility [131]. The ORR mechanism in aqueous solutions involves several elementary steps and can occur through a direct four-electron pathway ($4e^-$ transfer) with reduction of O_2 to H_2O or through a two-electron pathway ($2e^-$ transfer) with formation of H_2O_2. Hydrogen peroxide can be further reduced leading to the flow of two additional electrons ($2x2e^-$ transfer) [132]. The direct total reduction is more efficient and does not involve the production of H_2O_2, which is a reactive and corrosive compound that can have a negative impact on electrocatalyst durability [133]. Non-precious transition metal-nitrogen-carbon electrocatalysts are the most promising alternative to platinum-based catalysts for ORR. Carbon has the purpose of conducting electrons and to provide a high surface area porous structure with increased reactant/product transport. The transition metal, present as a single atom defect site in a layer of graphitic carbon (or at the edge of or bridging two graphitic sheets), is considered to be the dominant active site. Nitrogen is able to coordinate the transition metal atom and link it to the carbonaceous structure, while providing an electron withdrawing effect and enhance the catalytic activity of the metal center. [134] From a historical point of view, the development of those materials started around 1960 when it was discovered that cobalt phthalocyanine is active towards ORR. [135] It is a macrocyclic, organic compound with four nitrogen atoms coordinating a single cobalt atom. Since those molecules lack durability in acidic electrolyte, it was found that heat treatment at high temperature (400-1000°C) can be an effective way to increase their stability and activity. Later it was shown that atomically dispersed active sites can be obtained through pyrolysis from diverse sources of carbon and nitrogen atoms in the presence of

transition metal salts. [136] Those electrocatalysts show a plurality of possible active sites, depending on how the transition metal is coordinated by nitrogen atoms. Generally, they are located as defects on graphitic planes and their general formula is M-N_x, where x represents the number of nitrogen atoms coordinating the metal atom. Several types of coordination are possible and each of them show a different binding energy to the reactant with consequent different activity. [137, 138] M-N_4, showing an optimal binding energy for O_2, is believed to be the main electrocatalytic site for ORR. [139, 140] Metal-free N-C moieties that are present in those materials are also believed to contribute to the electrocatalytic activity; in particular an increasing content of pyridinic nitrogen is beneficial for ORR while graphitic nitrogen can facilitate the adsorption of oxygen molecules. [139, 141, 142] There are different approaches for the synthesis of those electrocatalysts that share some aspects in common, such as mixing of precursors, pyrolysis and acid washing. [143, 144] Compounds with high N:C atomic ratio such as nicarbazin and melamine are desirable to incorporate the highest possible number of nitrogen atoms in the carbon structure which increases the density of active sites. Pyrolysis is the key to obtain the final structure of the electrocatalyst with atomically dispersed active sites as it provides the energy to recombine the chemical bonds. It is a thermochemical decomposition of reactants in anoxic conditions with temperatures in the range 700-1100°C. High temperatures (usually greater than 900 °C) are needed to allow for the onset of graphitization of the carbon matrix and the insertion of atomically dispersed metal atom sites. [145] Variables such as the ramp rate, final temperature, and gas composition can be optimized to finely tune the final structure of the material [146]; in particular, previous studies show a ramp rate of about 10°C min^{-1} leads to optimal pore size for ORR while the final temperature must be selected accurately in order to avoid agglomeration of metal particles and excessive graphitization. [145] The presence of ammonia in the pyrolysis atmosphere leads to an increased activity since it results in a greater specific surface area, compared to the use of inert gases, although it does not influence the nature of nitrogen moieties and the entity of nitrogen doping. [147]

Acid washing is the successive step for the removal of acid soluble metal containing compounds such as metal/metal oxide nanoparticles that are not strongly bonded to the carbon structure. Since they do not contribute to the electrocatalytic activity, they represent an inert mass that is generally removed through HCl or H_2SO_4 acid solutions. [148, 149] Finally a second pyrolysis step is important since it can improve the morphology of the porous structure and the configuration of nitrogen, which boosts the catalytic activity. [150] In this work the focus is on the sacrificial support method (SSM), developed by Atanassov's group at University of New Mexico [151], based on the mixing of silica particles together with the precursors through ball milling, solvent evaporation or wet impregnation before pyrolysis. [22, 152, 153] This approach allows to negatively replicate the tridimensional porous structure of silica and to obtain an electrocatalyst with controlled porosity and atomically dispersed active sites. [154] Finally, a treatment with HF aqueous solution (5-25% wt) or alkaline KOH aqueous solution is necessary for the removal of the silica template maintaining at the same time the morphology of the electrocatalyst. [128] Increasing the amount of metal salt does not allow to atomically disperse all the transition metal atoms since there is a limit amount that can be incorporated as single atom, that is why the masses of precursors are other variables to be optimized. [155] This method is the only one that has been developed in the industrial world by Pajarito Powder company for the synthesis of non-noble metal catalysts, since it allows both high stability and activity. [128] However there are some problems to be solved such as the huge amount of liquid acid waste

that is produced (HF aqueous solution), that requires downstream processes for its treatment and represents a danger for human beings and the environment. This poses the question of the sustainability of the whole process. This study explores, for the first time, a sustainable and environmentally friendly variation of the traditional sacrificial support method, based on the addition of Teflon powder to the mass of precursors before pyrolysis without further acid washing. In such a way, the use of HF is totally avoided, with increased safety for the operators and increased ease of environmental remediation of the waste products. The idea comes from previous works in the fields of supercapacitors and carbon capture for the synthesis of carbonaceous porous structures based on the use of silica templates. [156-158] The use of polytetrafluoroethylene allowed the production of carbon materials with enhanced surface area and microporosity, leading to a complete removal of silica during heat treatment through in situ decomposition of Teflon with chain mechanism and formation of minimal amount of gaseous HF, that is able to rapidly react with silicon producing gaseous silicon tetrafluoride (SiF_4). The PTFE/silicon mass ratio and pyrolysis time are key variables to determine the final morphology of the material. In particular, reducing the amount of Teflon at constant mass of silica and increasing pyrolysis time leads to decreased surface area and pore volume. [157] This approach drastically reduces the synthesis time since no further steps of acid washing are necessary which simultaneously avoids the treatment of huge amounts of liquid waste. Thus, this new synthesis approach can be labelled green and sustainable and can be classified under the umbrella of "process intensification" (PI). By definition, PI observes the conceptual design principles for a safe chemical process according to an inherent safety process (safety-by-design) which i. avoids the use of extra chemicals or solvents; ii. avoids extra pumps or vessels; iii. reduces holdups and number of unit of operations; iv. refers to a inherent continuous process control. [159, 160]

A set of four mono-metallic electrocatalysts (Fe_{AD}-N-C^{AF}, Co-N-C^{AF}, Mn-N-C^{AF}, Ni-N-C^{AF}) were synthesized through the dynamic template removal method with the addition of Teflon to the mass of precursors before pyrolysis, characterized by physical-chemical methods (SEM, XPS, Raman Spectroscopy, XRD, STEM/EDS and BET) and tested for ORR in acidic, neutral and alkaline electrolytes. Nicarbazin was selected as the source of carbon and nitrogen atoms, along with hydrated nitrate salts, which were used to simultaneously provide nitrogen and transition metal atoms. RRDE tests show that activities comparable to state-of-the-art non-precious electrocatalysts are achievable and further improvements are possible. In detail, halfwave potentials of 0.73 V vs RHE in 0.1 M $HClO_4$ and 0.81 V vs RHE in 0.1 M KOH were obtained through the iron-based material with $4e^-$ pathway for ORR and excellent stability. This study paves the road towards a novel and sustainable acid-free process for the synthesis of those materials which can be explored with different optimization routes.

2. Materials and methods

2.1 Chemicals

Nickel(II) nitrate hexahydrate (purity ≥ 98.5%), manganese(II) nitrate tetrahydrate (purity ≥ 97.0%), iron(III) nitrate nonahydrate (purity ≥ 98.0%), cobalt(II) nitrate hexahydrate (purity ≥ 98.0%), polytetrafluoroethylene powder (1 µm particle size), Nafion perfluorinated resin solution 5 wt. % and nicarbazin were purchased from Sigma-Aldrich (USA). LM-150 fumed silica (surface area ~ 150 $m^2 g^{-1}$) was purchased from Cabot (USA). Aerosil OX 50 (surface area ~ 50 $m^2 g^{-1}$), Aerosil 90 (surface area ~ 90 $m^2 g^{-1}$) and Aerosil 200 (surface area ~ 200 $m^2 g^{-1}$) were purchased from Evonik (USA). Stöber's spheres (320 nm

average diameter) were synthesized by Stöber's method [37]. Potassium hydroxide (purity ≥ 85.0%), sodium chloride (purity ≥ 99.5%), isopropanol (IPA, purity ≥ 99.9%) and hydrochloric acid (36.5 to 38 % w/w) were purchased from Fisher Chemical (USA). Perchloric acid 70% was purchased from Merck Millipore (USA) and ethyl alcohol was purchased from Gold Shield Distributors. Aluminum oxide polishing solution (5 µm) was purchased from Allied High Tech Products (USA). Nitrogen 6.0 was purchased from Linde (USA), oxygen 5.0 was purchased from Praxair (USA) and ammonia (9.9 mole %, nitrogen: balance) was purchased from Airgas (USA). Deionized ultrapure water (DIW) was obtained using a Millipore Milli-Q system (product water conductivity at 25 °C = 0.056 µS cm^{-1}).

2.2 Electrocatalyst synthesis

In the synthesis of Fe_{AD}-N-C^{AF}, Co-N-C^{AF}, Mn-N-C^{AF}, Ni-N-C^{AF} four different types of silica particles (Stober spheres, Aerosil 90, Aerosil 200, LM-150 fumed silica) were used simultaneously for each electrocatalyst; the contemporaneous use of multiple varieties of silica with different surface area and porosity allows to obtain a hierarchical pore size distribution that is beneficial for the electrochemical reactions. In particular the most active sites sit mainly in micropores, mesopores facilitate the accessibility of gas or ions to the active sites and macropores enhance mass transport of reactants and products [6]. In the synthesis of the iron-based electrocatalyst, 6.25 g of nicarbazin, 1.19 g of iron nitrate nonahydrate, 1.25 g of LM-150 fumed silica, 0.5 g of Stöber's spheres, 0.94 g of Aerosil 90 and 0.31 g of Aerosil 200 were dispersed in deionized water, sonicated for 30 min and mixed at 45°C under constant stirring overnight (Cole-Parmer Stuart Stirring Hot Plate). To completely dry the precursors, a successive step in the oven at 60°C and ambient pressure was realized. After grinding with mortar and pestle, a calculated amount of Teflon particles based on the wt. % of silica according to the following equation was added to the powder.

$$m_t(mg) = \frac{\left(mass\ of\ powder\ obtained\ after\ drying\ (mg)\right) * \frac{wt\ \%\ SiO_2}{100}}{\frac{0.09\ mg\ silica}{mg\ Teflon}} \quad (1)$$

The mixture was then split equally in three agate ball mill jars (volume 100 ml each) with 32 agate balls (10 balls with 10.28 mm diameter, 22 balls with 6.26 mm diameter) in each jar and subject to ball-milling (PQ-N04 Planetary Ball Mill) at 10 Hz for 1 hr. Since it was evident that Teflon powder tends to stick to the walls, every 15 min the jars were opened and the powder was mixed manually. The reactants were loaded into a weigh boat and subject to pyrolysis under 100 % N_2 atmosphere in a quartz tube, heating from room temperature to 900°C with a ramp rate of 5 °C min^{-1} and a 180 min hold at 900°C. A Thermcraft controller was used to regulate the temperature while MKS mass flow controller allowed to adjust the flow rate of nitrogen to 100 ml min^{-1}. The obtained powder was subject to ball-milling again at the same conditions described above and it is denoted as Fe-N-C-Postpyr1 in this study. Then, Fe-N-C-Postpyr1 was pyrolyzed for the second time under 10 mole % NH_3 and 90 mole % N_2 atmosphere with a ramp rate of 10°C min^{-1} and 30 min hold at 950°C to obtain Fe_{AD}-N-C^{AF}. A similar procedure was used to synthesize all the other materials and the mass proportions of the precursors are summarized in Tab. 1, where each raw is representative of an electrocatalyst and the amounts are normalized with respect to 1 gr of hydrated nitrate salt. The mass ratios were selected so that each electrocatalyst shows the same amount of

transition metal atoms per unit total mass of precursors, to have a consistent comparison of performances.

SAMPLE	Me SOURCE	C,N SOURCE	SILICA TEMPLATE			
	Hydrated nitrate salt	Nicarbazin $C_{19}H_{18}N_6O_6$	LM-150 (SA ~ 150m^2/g)	Stöber spheres	Aerosil 90 (SA ~ 90 m^2/g)	Aerosil 200 (SA ~ 200 m^2/g)
Fe_{AD}-N-C^{AF}	1 g $Fe(NO_3)_3 \cdot 9H_2O$	5.25 g	1.05 g	0.42 g	0.78 g	0.26 g
Ni-N-C^{AF}	1 g $Ni(NO_3)_2 \cdot 6H_2O$	7.26 g	1.45 g	0.58 g	1.09 g	0.36 g
Co-N-C^{AF}	1 g $Co(NO_3)_2 \cdot 6H_20$	7.26 g	1.45 g	0.58 g	1.09 g	0.36 g
Mn-N-C^{AF}	1 g $Mn(NO_3)_2 \cdot 4H_2O$	8.45 g	1.69 g	0.68 g	1.27 g	0.42 g

Table 12: Table 1. Precursors and mass ratios for the synthesis of M-N-C electrocatalysts.

A fraction of Fe_{AD}-N-C^{AF} was also washed with hydrochloric acid aqueous solution at 80°C for 8 hr under constant stirring and centrifuged (Hermle Z366 centrifuge) through 6 cycles of 5 min each at 9200 rpm with intermediate deionized water rinsing between each cycle. The suspension was finally filtered under vacuum using a Nylon membrane (GVS Filter Technology, disk diam. 47 mm NY 0.22 µm) and washed with deionized water until the pH was neutral. The sample was then dried in the oven at ambient pressure and 55°C overnight. The acid solution was prepared by mixing 4.35 ml of hydrochloric acid (36.5 to 38 % w/w) with 95.65 ml of deionized water. The notation used in this study for the acid-washed catalyst is Fe-N-C-AW. Another fraction of Fe_{AD}-N-C^{AF} powder was subjected to a third ball-milling step at the same conditions described above and is denoted as Fe_{AD}-N-C^{AF}-BM.

2.3 Physical-chemical characterization

Scanning electron microscopy (SEM) was conducted using a FEI Magellan 400 XHR SEM to visualize the surface morphology of the electrocatalysts. Current (50 pA – 0.80 nA) and voltage (18 kV - 20 kV) were adjusted for each catalyst in order to focus and both TLD and ETD detectors were used depending on the case. X-Ray photoelectron spectroscopy (XPS) on a Kratos AXIS Supra spectrometer with a monochromatic Al Kα source (1486.6 eV) at 15 mA anode current allowed to determine the atomic composition and chemical structure of the surface. Survey spectra were obtained in the range 0 to 1400 eV, detailed N_{1s} spectra in the range 390 to 415 eV, C_{1s} spectra in the range 270 to 300 eV and F_{1s} spectra in the range 675 to 695 eV. The calibration was performed respect to a value of the C_{1s} binding energy equal to 284.5 eV. To quantify the elemental composition Casa XPS is the software that was used, selecting a linear

background for N1s, C1s, F1s regions and a Shirley background for transition metal regions. Peak fitting was realized using a 70%/30% Gaussian/Lorentzian line shape. X-ray diffraction analysis was realized using a Rigaku Powder X-ray diffractometer with Cu (K radiation 0.15418 nm) run at 40 kV and 30 mA with a Nickel K-beta filter, a step size of 0.03° and 2θ varying from 20° to 85°, in order to understand the crystalline structure of the materials. Phase identification was conducted through the software PDXL and ICDD database. Raman spectra were obtained through inVia, Renishaw Corp., UK system with a 633 nm laser to quantify the degree of disorder of carbon. The morphology and single atom sites of the catalyst was analyzed by aberration-corrected scanning transmission electron microscopy using a JOEL ARM-200F at an accelerating voltage of 200 kV. The elemental distribution of the electrocatalyst was analyzed by energy dispersive X-Ray spectroscopy using a FEI Talos F200X at an accelerating voltage of 200 kV, equipped with superX 4 SSD EDX detectors. N_2 physisorption was realized on a Micromeritics 3Flex Analyzer at a temperature of 77K. The surface area and the distribution of the pore dimensions were calculated using the Brunauer-Emmett-Teller (BET) method and Barrett-Joyner-Halenda (BJH) method, respectively.

2.4 Electrochemical measurements

The electrochemical tests were conducted with a three-electrode system (Pine research instrument), a potentiostat (BioLogic VSP-300), a rotating ring-disk electrode (Pine research instrument, glassy carbon disk 0.247 cm^2 geometric area, Pt ring), a rotation rate control unit (Pine research instrument), carbon rod as counter electrode, HydroFlex hydrogen reference electrode (Gaskatel) and a Teflon cell (200 ml). Before any test, the working electrode and the ring were cleaned by wiping with ethanol and sonicating in ethanol for 10 minutes. Aluminum oxide (5 µm) solution was also used to polish the working electrode. The Teflon cell was cleaned by rinsing 5 times with deionized water at ambient temperature and by filling 1 time with deionized water bringing it to the boil through microwaves. For ORR, the activity of the electrocatalysts was investigated in 0.1 M KOH (pH=13), 0.1 M $HClO_4$ (pH=1), 0.5 M NaCl (pH=7) and 2 M NaCl (pH=7) aqueous solutions saturated by bubbling O_2 or N_2. For each electrocatalyst the ink was prepared by mixing 3.94 mg of powder with 255.2 µl of DIW, 255.2 µl of IPA and 21.3 µl of Nafion perfluorinated resin solution 5 wt. %. Platinum on graphitized carbon (Pt/C, 20 wt.%) is used as a benchmark; the ink is based on 2.5 mg of Pt/C powder, 1619.4 µl of DIW, 1619.4 µl of IPA and 135.0 µl of Nafion perfluorinated resin solution 5 wt. %. The suspensions were then sonicated for 30 min at ambient temperature. 20 µl of ink were deposited onto the glassy carbon disk and dried at ambient conditions in such a way that electrocatalyst loadings of 600 µg cm^{-2} for PGM-free electrocatalysts and 60 µg cm^{-2} for Pt/C were obtained. The electrolytic solution was bubbled with N_2 for 15 min before any test in order to purge any other gas. Electrochemical impedence spectroscopy (EIS) was performed without rotation of the disk to evaluate the ohmic resistance of the solution, by setting the potential of the working electrode at 0.45 V vs RHE, the sinus amplitude at 10 mV and by varying the frequency in the range 1.0 Hz - 1.0 MHz. The solution resistance can be evaluated by extrapolating the real axis value at the high frequency intercept and it is useful for iR compensation. Prior to kinetic measurements, cyclic voltammetry (CV) in the potential range 0.05 – 1.23 V vs RHE with a scan rate of 500 mV s^{-1} was conducted for 100 cycles in order to activate and clean the surface of the electrocatalyst; this procedure was sufficient to obtain a stable response. Another CV under N_2 is collected at 1600 rpm at a scan rate of 5 mV s^{-1} in the potential window 0.1 – 1.05 V vs RHE to evaluate the capacitive current that was then removed

from the current due to the electrocatalytic reaction. The electrolyte was saturated with O_2 for 15 min and a final CV at 1600 rpm was collected at a scan rate of 5 mV s^{-1} between 0.1 – 1.05 V vs RHE, fixing the potential of the ring at 1.1 V vs RHE to collect the current due to H_2O_2 oxidation; the anodic sweep was used to extract kinetic data. Each test was repeated twice. An electrocatalyst loading study in the range 50 µg cm^{-2} - 900 µg cm^{-2} was conducted using Fe_{AD}-N-C^{AF}-BM catalyst in 0.1 M $HClO_4$ electrolyte for ORR, by preparing inks at different concentrations and by executing RRDE tests at the same conditions described above; each test was repeated twice. Accelerated durability testing was conducted on Fe_{AD}-N-C^{AF}-BM electrocatalyst with a loading of 700 µg cm^{-2} in N_2 saturated 0.1 M $HClO_4$ by cycling the potential between 0.60 and 1.00 V at 50 mV s^{-1}; the activity for ORR was evaluated through RRDE polarization curves at 1600 rpm in O_2 saturated electrolyte before and after 5,000 and 10,000 cycles.

3. Results and discussion

3.1 Structure and morphology

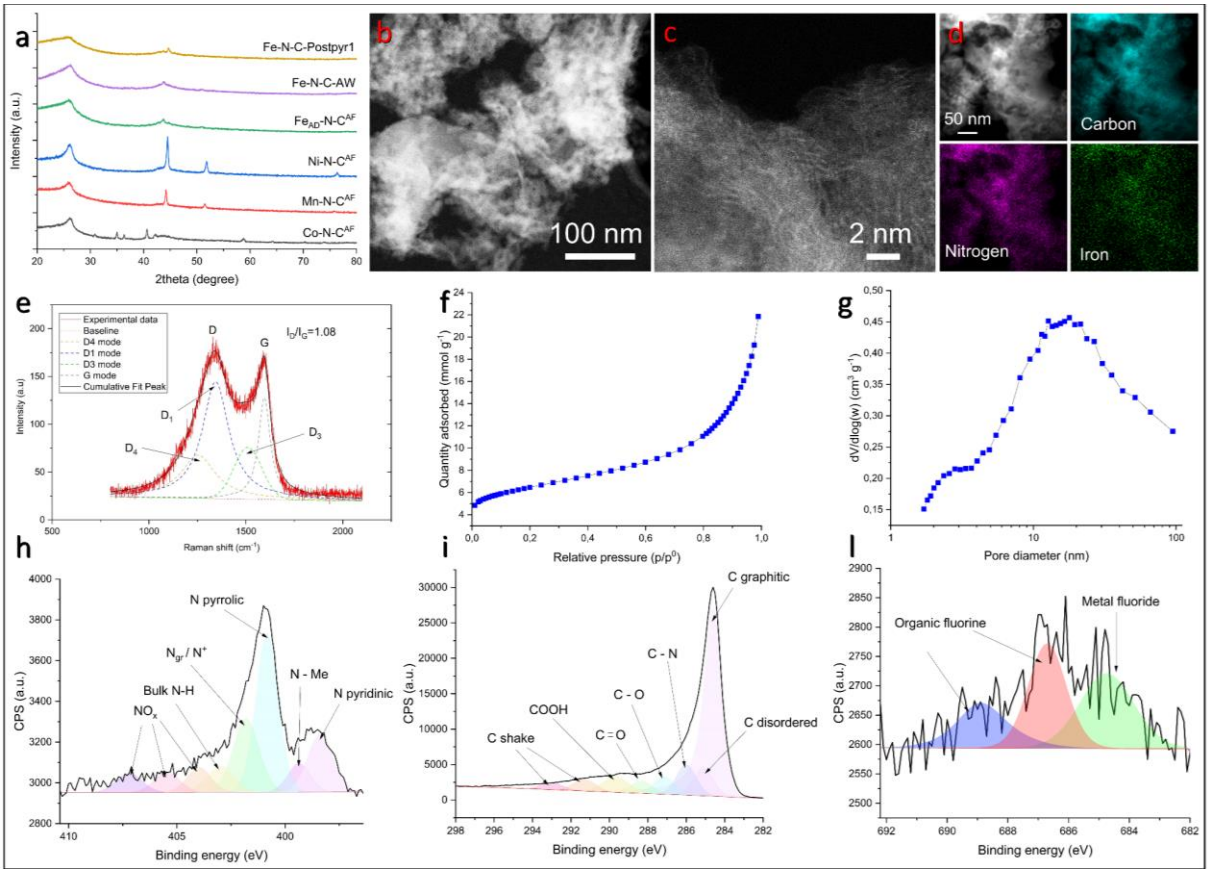

Figure 4.1. 1: Figure 1. Chemical-physical characterization. (a) XRD patterns of Co-N-CAF, Mn-N-CAF, Ni-N-CAF, FeAD-N-CAF, Fe-N-C-AW and Fe-N-C-Postpyr1. (b) Low magnification AC-HAADF STEM image of FeAD-N-CAF. (c) Atomic resolution AC-HAADF STEM image of FeAD-N-CAF, bright spots indicate atomically dispersed Fe sites. (d) AC-HAADF STEM image and corresponding EDS mapping of the FeAD-N-CAF catalyst. (e) Raman spectrum of FeAD-N-CAF. (f) N2 adsorption isotherm and (g) corresponding pore size distribution of FeAD-N-CAF. (h-l) High-resolution N1s, C1s and F1s spectra respectively of FeAD-N-CAF.

The crystalline structure of the materials was analyzed through XRD and the patterns are shown in **Fig. 1 a**. All the electrocatalysts show diffraction peaks at about 26° and 44° that can be both ascribed to graphitic carbon, respectively related to the (002) and (100) planes. The sharpness of the peak at 26° is decreasing following the order Ni-N-C^{AF} > Co-N-C^{AF} > Mn-N-C^{AF} > Fe_{AD}-N-C^{AF}, underlining that a different number of graphene layers is stacked in the carbonaceous structure among the different materials. It is known that the presence of transition metals can catalyze graphitization of carbon during heat treatment [161] as evident in **Fig. S1 e-f** and Ni demonstrates higher catalytic property in this sense. Fe_{AD}-N-C^{AF} shows a broader peak at 26°, highlighting the presence of increased long-range disorder and lattice defects in the graphitic structure. The presence of nanoparticles is evident for all the materials, because of agglomeration during the high-temperature pyrolysis. In detail, manganese carbide peaks (DB card number: 01-080-1701) at 44.2°, 51.4° and 75.8° respectively due to the (511), (600) and (660) diffraction planes are visible for the Mn-N-C^{AF} powder. Ni-N-C^{AF} sample shows narrow diffraction peaks at 44.5°, 51.8° and 76.4° which can be ascribed respectively to the (111), (200) and (220) planes of nickel (DB card number: 00-004-0850) and nickel carbide (DB card number: 01-074-5561) particles. It is evident from the sharpness of the reflections that Ni has a higher tendency to form bigger clusters and it is not homogeneously dispersed in the carbonaceous matrix. AD-Fe-N-C^{AF} peaks at 44.7° and 50.8° correspond to the (111) and (200) planes respectively of both iron (DB card number: 01-071-3739) and iron nitride (DB card number: 01-075-2127) clusters. However, the intensity associated to them is relatively lower demonstrating a more uniform dispersion of Fe in the tridimensional structure of the material. Co-N-C^{AF} pattern presents a variety of different peaks which qualitatively put under evidence different species such as cobalt carbide, cobalt nitride, cobalt oxide and cobalt particles. No signals related to silicon dioxide are present, demonstrating a successful removal of the silica templates.

To elucidate the transformations between the first and the second pyrolysis steps, XRD analysis was conducted also for Fe-N-C-Postpyr1. Analyzing the XRD spectrum of Fe-N-C-Postpyr1 and comparing it with that of Fe_{AD}-N-C^{AF} after the first and the second pyrolysis respectively, it is evident that the graphitic reflection at about 26° is less sharp after a single heat treatment highlighting that an additional pyrolysis step leads to enhanced graphitization. Iron/iron carbide clusters are visible at about 44.5° and 49°. The XRD pattern of Fe-N-C-AW still shows the presence of metallic nanoparticles after acid washing already observed for Fe_{AD}-N-C^{AF}, leading to the conclusion that graphitic carbon layers were able to protect those clusters from the dissolution in acid by encasing them. [162] The porous structure of Fe_{AD}-N-C^{AF} is confirmed by the low magnification aberration corrected high angle annular dark field (AC-HAADF) image in **Fig. 1 b**, which is in accord with SEM analysis in **Fig. S2**. The high mag AC-HAADF shown in **Fig. 1 c** demonstrates the presence of single bright points, which are atomically dispersed iron sites; however, some nanoparticles were observed as evident in **Fig. S1 c-d** and those results are in perfect agreement with the XRD pattern. EDS further confirms the homogeneous dispersion of Fe atoms in the material and the effective doping of the carbonaceous structure with nitrogen moieties, as observed from elemental mapping in **Fig. 1 d**. Raman spectra of Fe_{AD}-N-C^{AF} in **Fig. 1 e** is useful to evaluate the degree of disorder of carbon; the deconvolution is based on previous works present in literature[163], with the D1-band peak at 1360 cm^{-1} associated to defects in the graphene layers, the D3-band peak at about 1500 cm^{-1} related to amorphous carbon and its long-range disorder, the D4-band peak at about 1230 cm^{-1} assigned to the simultaneous presence of sp^2-sp^3 structures and finally the G-band peak at about 1580 cm^{-1} ascribed to

sp^2 graphitic carbon. All the materials show similar trends as evident from **Fig. S3**, with values of intensity ratio I_D/I_G in the range of 1.05 to 1.09. This ratio is calculated based on the maximum values of the G and D bands and it is often reported in literature to quantify the relative amounts of ordered and disordered carbon. However, this value can lead to inaccurate conclusions when the broadening of the peaks is large as in this case and, as consequence, using the peak area is preferable. Based on this, all the samples show approximately two-thirds of carbon as disordered, demonstrating the presence of a large number of defects and a successful doping of the graphitic structure with nitrogen moieties already confirmed through EDS, which is beneficial for ORR. The BET analysis was conducted on Fe_{AD}-N-C^{AF} and Ni-N-C^{AF} samples and the results are presented in **Fig. 1 f-g** and **Fig. S4** respectively. Both the materials have almost the same specific surface area (482.9 $m^2\ g^{-1}$ and 477.2 $m^2\ g^{-1}$, Ni and Fe electrocatalysts respectively) and pore size distribution, highlighting that the morphology of the material is dependent only on the choice of the silica templates. The hierarchical porous structure with mesopores and micropores is evident respectively from the distribution of the pore dimensions, with a broad peak centered at about 19 nm, and the adsorption isotherm, with a non-negligible uptake at the lowest values of relative pressure. XPS spectra were used to analyze the surface chemical environment of the materials. High-resolution N1s, C1s and F1s spectra where deconvoluted based on previous studies[122]. All the materials after the second pyrolysis have similar atomic composition as summarized in **Tab. 2**, with Fe_{AD}-N-C^{AF} showing the largest amount of nitrogen.

Atomic %	**Fe-N-C-Postpyr1**	**Fe_{AD}-N-C^{AF}**	**Mn-N-C^{AF}**	**Ni-N-C^{AF}**	**Co-N-C^{AF}**
C 1s	90.47±0.35	94.86±0.47	94.39±1.53	93.54±1.55	96.19±0.49
N 1s	4.01±0.34	2.47±0.18	1.82±0.03	2.06±0.57	1.50±0.72
O 1s	4.58±0.52	2.58±0.28	3.65±1.44	4.20±2.04	2.01±0.98
Si 2p	0.30±0.03	0.07±0.01	0.09±0.06	0.04±0.01	0.11±0.06
Me 2p	0.04±0.04	0.01±0.00	0.02±0.02	0.10±0.01	0.03±0.03
F 1s	0.60±0.08	0.01±0.00	0.03±0.03	0.06±0.06	0.16±0.11

Table 13: Table 2. X-Ray photoelectron spectroscopy %at. concentration of FeAD-N-CAF, Mn-N-CAF, Co-N-CAF, Ni-N-CAF and Fe-N-C-Postpyr1.

About nitrogen moieties in **Fig. 1 h**, the presence of N pyridinic at 398.2 eV, metal-nitrogen coordination at 399.4 eV, N pyrrolic at 400.8 eV, N graphitic at 401.8 eV, bulk N-H at 402.9 eV and NO_x species respectively at 404.2 eV, 405.6 eV and 407.2 eV are observed. It is evident from **Tab. 3** that all the samples show a low ratio N pyridinic/N pyrrolic but a relatively high content of graphitic nitrogen.

N moiety	**Fe-N-C-Postpyr1**	**Fe_{AD}-N-C^{AF}**	**Mn-N-C^{AF}**	**Ni-N-C^{AF}**	**Co-N-C^{AF}**
N pyridinic	24.88±0.29	14.91±0.96	12.87±0.70	14.63±0.28	15.87±0.43
N-Me	13.78±0.81	6.62±2.45	6.45±0.36	7.57±0.35	6.36±0.57
N pyrrolic	31.65±2.83	35.71±0.24	38.99±1.31	33.78±2.35	36.27±0.86
N_{gr} / N^+	11.89±1.59	19.19±0.91	14.78±0.36	18.24±1.42	17.20±1.11
Bulk N – H	6.95±0.46	7.17±0.82	9.89±1.29	9.52±0.68	9.25±1.57
NO_x	4.80±0.43	6.04±1.75	6.75±0.27	6.21±0.41	6.52±0.53

NO_x	3.90±0.16	5.29±1.01	5.08±0.89	4.76±0.74	4.24±0.68
NO_x	2.15±0.40	5.09±0.71	5.19±0.29	5.30±0.61	4.28±0.59

Table 14: Table 3. X-Ray photoelectron spectroscopy high-resolution N 1s rel. %at. concentration for FeAD-N-CAF, Mn-N-CAF, Co-N-CAF, Ni-N-CAF and Fe-N-C-Postpyr1.

High-resolution carbon spectrum in **Fig. 1 i** shows graphitic carbon at 284.5 eV, disordered carbon at 285.1 eV, C-N bond at 286 eV, C-O at 287.1 eV, C=O at 288.3 eV, COOH at 289.7 eV, C-F2 at 291.3 eV and C-F3 at 293 eV. Graphitic carbon on the surface is predominant among carbon moieties as evident from **Tab. 4** and this is beneficial for corrosion resistance, while the presence of oxygenated species demonstrates an effective doping of graphene layers with defects. [164] C-F2 and C-F3 groups can be ascribed to the addition of Teflon to the precursors before the first pyrolysis step. High-resolution fluorine spectrum in **Fig. 1 l** obtained for the Fe_{AD}-N-C^{AF} sample show not only the presence of inorganic fluorine at binding energies greater than 686 eV but also the formation of metal fluoride species at 685 eV.

C moiety	**Fe-N-C-Postpyr1**	**Fe_{AD}-N-C^{AF}**	**Mn-N-C^{AF}**	**Ni-N-C^{AF}**	**Co-N-C^{AF}**
C graphitic	51.97±4.05	54.30±1.69	48.49±6.03	46.46±4.56	58.57±0.55
C disordered	14.45±4.36	9.31±1.48	14.63±5.07	15.52±4.23	5.62±0.34
C-N	10.55±1.34	10.54±0.42	11.59±2.08	13.57±2.12	9.59±0.47
C-O	6.87±0.43	6.36±0.23	6.35±0.82	5.86±0.76	6.04±0.48
C=O	4.30±0.76	4.64±0.01	4.13±0.68	4.11±0.94	4.64±0.19
COOH	6.03±0.40	7.18±0.22	7.78±1.37	8.24±1.22	7.08±0.19
C shake*	3.57±0.54	4.73±0.09	4.18±0.59	3.91±0.86	5.23±0.17
C shake*	2.26±0.52	2.96±0.10	2.44±0.47	2.31±0.67	3.24±0.08

Table 15: Table 4. X-Ray photoelectron spectroscopy high-resolution C 1s rel. %at. concentration for FeAD-N-CAF, Mn-N-CAF, Co-N-CAF, Ni-N-CAF and Fe-N-C-Postpyr1.

Tab. 1 also highlights how elemental composition significantly varies between Fe-N-C-Postpyr1 and Fe_{AD}-N-C^{AF}, with the former showing larger amounts of nitrogen and oxygen atoms that during the second pyrolysis were partially removed forming gaseous products. Interestingly, non-negligible amounts of silicon and fluorine are still present in the Fe-N-C-Posypyr1 sample and this is evidence of the fact that a second heat treatment is necessary to reduce their content to negligible values. The largest differences in the nitrogen moieties are a significantly greater ratio N pyridinic/N pyrrolic, a lower relative amount of graphitic nitrogen and approximately a double amount of nitrogen coordinated to iron in Fe-N-C-Postpyr1, while high-resolution carbon spectra demonstrate that a second heat treatment enhances graphitization by exposing carbon to high temperature for additional time and this is in line with XRD analysis. Additional XPS images for the other samples can be found in **Fig. S5**.

3.2 Electrochemical study on RRDE

The activity of the electrocatalysts toward ORR was evaluated through RRDE experiments by extracting from the anodic polarization curve the values of typical descriptors: the onset potential (E_{onset}) corresponding to a current density of 0.1 mA cm^{-2}, the halfwave potential ($E_{1/2}$) calculated through the

first-derivative method, the number of electrons transferred (n) and the hydrogen peroxide yield (%H_2O_2) evaluated respectively with the following equations. [165]

$$n = 4 * \frac{i_d}{i_d + \frac{i_r}{N}} \quad (2)$$

$$\%H_2O_2 = 2 * \frac{\frac{i_r}{N}}{i_d + \frac{i_r}{N}} \quad (3)$$

Where i_r and i_d are the absolute values of the ring current and the disk current respectively, while N is the collection efficiency of the ring which was empirically evaluated to be 0.5 through the reversible and single-electron ferrocyanide/ferricyanide half reaction. Higher values of E_{onset} and $E_{1/2}$ are indicators of enhanced electrocatalytic activity, since a lower overpotential to achieve a determined value of current density is necessary. %H_2O_2 and n are useful to understand the reaction mechanism and they are dependent on each other. In particular, a value of n equal to 4 means that $4e^-$ pathway is realized and this correspond to the absence of hydrogen peroxide generation which is beneficial for performances. Since they are dependent on the applied potential, their averages in the potential window from 0.25 V to E_{onset} are reported in this study.

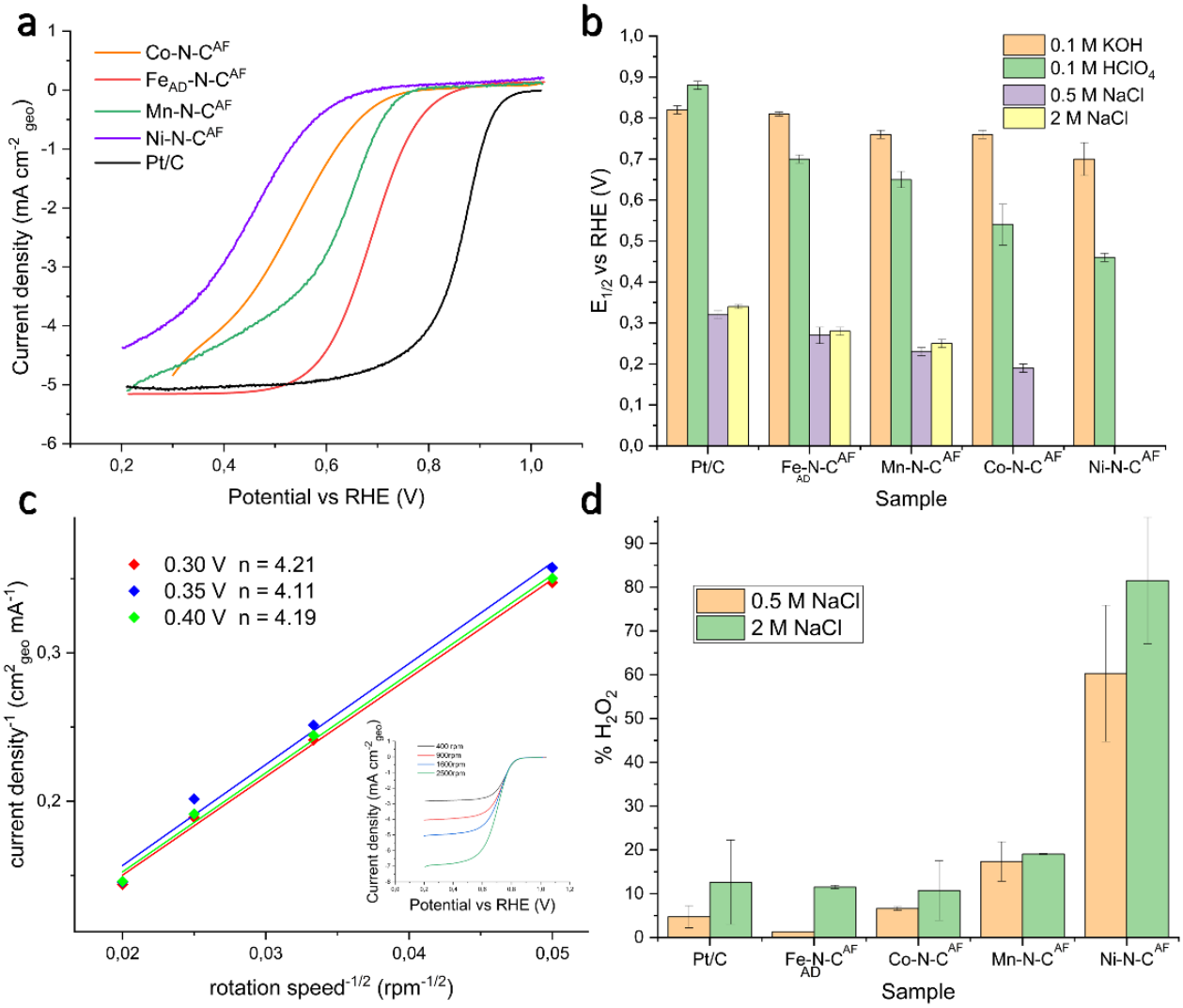

Figure 4.1. 2: Figure 2. Electrochemical performance on RRDE. (a) ORR polarization curve at 1600 rpm of M-N-C electrocatalysts and Pt/C in 0.1 M HClO4. (b) Comparison of E1/2 of M-N-C electrocatalysts and Pt/C in different electrolytes. (c) Koutecky-Levich plots of FeAD-N-CAF-BM in 0.1 M HClO4 at various potentials and ORR polarization curves at different rotation speeds. (d) %H2O2 produced by M-N-C electrocatalysts and Pt/C in 0.5 M NaCl and 2 M NaCl.

Fig. 2 a and **Fig. S6** show the ORR polarization curves of Fe_{AD}-N-C^{AF}, Mn-N-C^{AF}, Co-N-C^{AF} and Ni-N-C^{AF} electrocatalysts in 0.1 M $HClO_4$, 0.1 M KOH, 0.5 M NaCl and 2 M NaCl respectively with an electrocatalyst loading of 0.6 mg cm^{-2} at 1600 rpm, where commercial Pt/C is used as reference with a loading of 60 µg cm^{-2}. As expected from previous works [166], Fe_{AD}-N-C^{AF} electrocatalyst show better performances among PGM-free materials because of its intrinsic higher electrocatalytic property and the general trend of activity is Fe_{AD}-N-C^{AF} > Mn-N-C^{AF} > Co-N-C^{AF} > Ni-N-C^{AF} in every type of electrolyte, as demonstrated in **Fig. 2 b**. In detail, as shown in **Tab. S2**, halfwave potentials of 0.81 V in alkaline environment (0.82 V with Pt/C) and 0.70 V in acidic solution were achieved with Fe_{AD}-N-C^{AF} obtaining an average number of electrons transferred of 3.98 and 3.92 respectively. Higher activities are reached in alkaline electrolyte and this is in line with the fact that ORR is kinetically favored in this kind of medium

because of improved charge transfer. [167] The 4e$^-$ mechanism was also confirmed through Koutecky-Levich analysis as evident in **Fig. 2 c**. It was conducted by carrying out linear sweep voltammetry tests at four different rotation speeds in the range 400 – 2500 rpm with Fe_{AD}-N-C^{AF}-BM in 0.1 M $HClO_4$ and a loading of 700 µg cm^{-2}. The Koutecky-Levich equation was used as follows. [168]

$$\frac{1}{j} = \frac{1}{j_k} + \frac{1}{0.2nFC_bD^{2/3}\upsilon^{-1/6}}\omega^{-1/2} \quad (3)$$

Where j is the measured current density, j_k is the kinetic current density, ω is the rotation speed of the disk, n is the number of transferred electrons, F = 96485 C mol^{-1} is the Faraday constant, D = 1.93 x 10^{-5} cm^2 s^{-1} is the diffusion coefficient of O_2 in 0.1 M $HClO_4$, C_b = 1.22 x 10^{-3} mol L^{-1} is the bulk concentration of O_2 and v = 1.13 x 10^{-2} cm^2 s^{-1} is the kinetic viscosity of the electrolytic solution. [169] Poor performance is evident from **Tab. S3** in both neutral solutions since the scarcity of protons H^+ and hydroxyl ions OH^- is a limiting factor. **Fig. 2 d** demonstrates that when NaCl concentration increases from 0.5 M to 2 M, the number of electrons transferred significantly drops and this can be ascribed to the poisoning effect of chlorine ions that are easily adsorbed on the catalyst surface and act as site-blocking species, resulting in a reduction of active area available for ORR and an increased production of H_2O_2. [170]

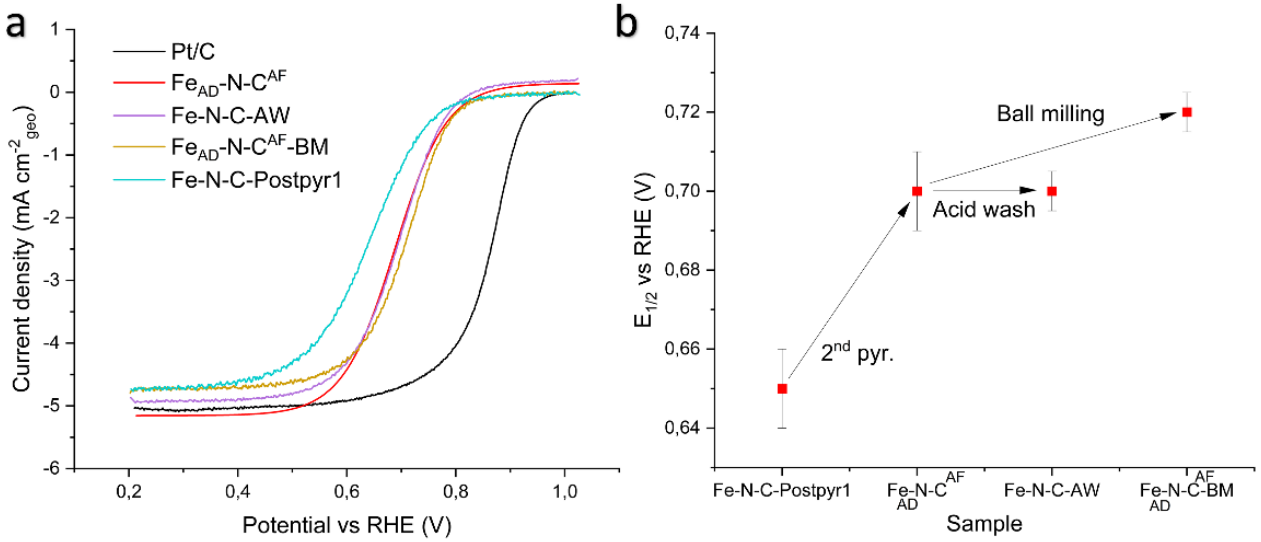

Figure 4.1. 3: Figure 3. (a) ORR polarization curves and (b) variation of E1/2 of the iron-based electrocatalyst at different synthetic steps in 0.1 M HClO4 at 1600 rpm with a loading of 600 µg cm-2.

Fe_{AD}-N-C^{AF} ORR activity was further compared in acid electrolyte with Fe-N-C-Postpyr1, Fe-N-C-AW, AD-Fe-N-C^{AF}-BM. As clear from **Fig. 3**, the second pyrolysis step leads to a strong enhancement of activity highlighting that after only a single heat treatment the configurations of carbon and nitrogen together with relatively high surface contents of silicon and fluorine result in a reasonably lower active site density. As expected, the acid-washing did not cause any change in the final performance since no phase transformations were observed while an additional ball-milling step led to a 20 mV positive shift of the halfwave potential, as result of greater homogeneity of particle size distribution. Those results

demonstrate that the acid-free method based on the use of Teflon can be a successful variation of the traditional SSM to synthesize materials for ORR electrocatalysis, with activity comparable to state-of-the-art non-precious electrocatalysts as shown in **table S5**. Additionally, a study on the electrocatalyst loading from 50 µg cm^{-2} to 900 µg cm^{-2} was conducted for the Fe_{AD}-N-C^{AF}-BM sample in acid medium.

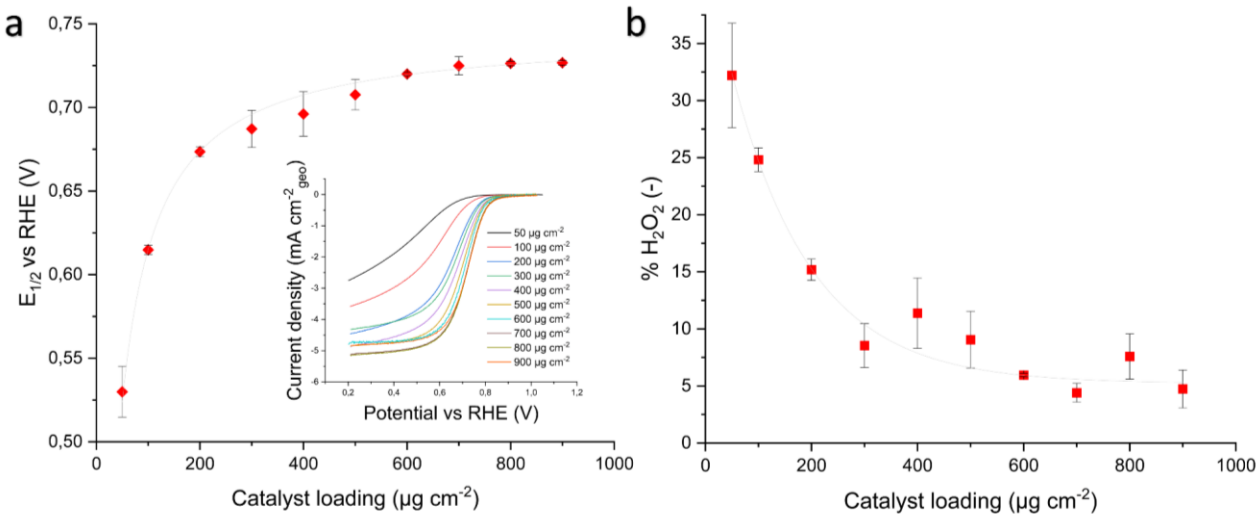

Figure 4.1. 4: Figure 4. (a) $E_{1/2}$ with corresponding polarization curves and (b) %H2O2 of FeAD-N-CAF-BM in 0.1 M HClO4 at 1600 rpm with electrocatalyst loading varying from 50 µg cm-2 to 900 µg cm-2.

Fig. 4 a-b show how halfwave potential and hydrogen peroxide yield respectively change by varying the electrocatalyst loading, pointing out that the performance reaches a plateau at 700 µg cm^{-2} with a value of $E_{1/2}$ of 0.73 V. Increasing the loading does not lead to a proportional increase of activity since, when the thickness of the electrocatalytic layer is relatively large on the disk, oxygen is not able to easily reach all the active sites of the material because of mass transfer limitations. In the range of 50 µg cm^{-2} to 300 µg cm^{-2}, hydrogen peroxide yield has a sharp reduction and this reveals a 2x2e^- pathway; in particular, when the loading increases, H_2O_2 has a greater probability of being further reduced to H_2O inside the material before reaching the ring and it is not detected as ring current. Accelerated durability testing was conducted on Fe_{AD}-N-C^{AF}-BM in acid medium through cycling in the typical potential window of operation in systems such as PEMFCs. It is well known that while the activity of PGM-free electrocatalysts has made promising improvements, the stability of those materials in acid medium is distant from technical requirements for their commercialization. Issues such as demetallation, flooding of micropores and carbon corrosion lead to a fast degradation of performances after few hours. [133]

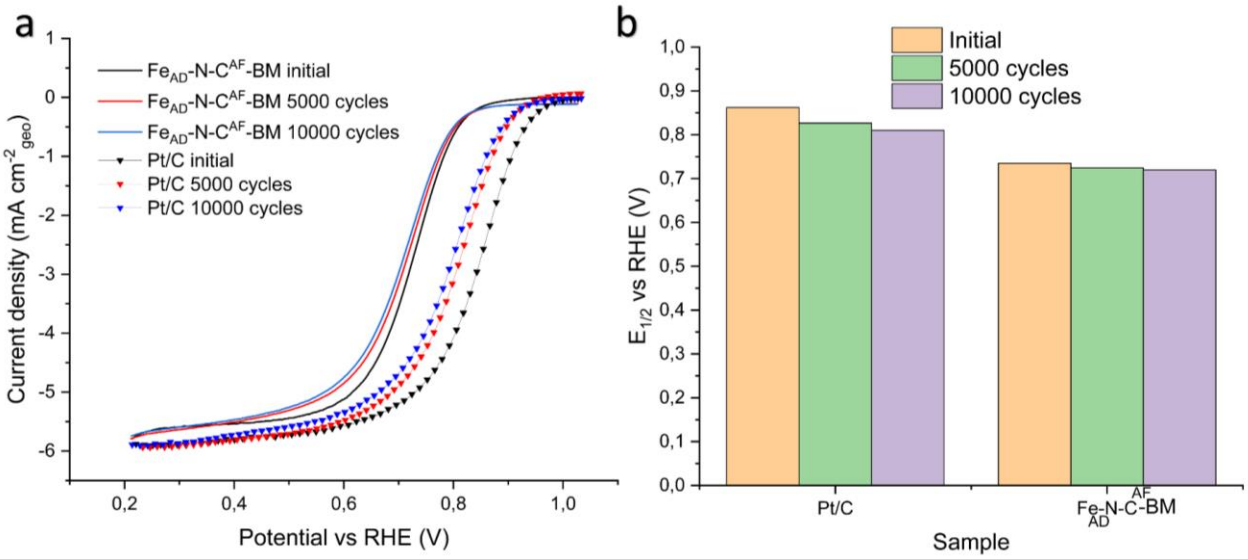

Figure 4.1. 5: Figure 5. Accelerated durability test on RRDE conducted on FeAD-N-CAF-BM with a loading of 700 µg cm-2 and Pt/C with a loading of 60 µg cm-2 in 0.1 M HClO4 at 1600 rpm. (a) ORR polarization curves and (b) E1/2 before and after potential cycling.

Fig. 5 a-b demonstrate excellent stability on RRDE of Fe_{AD}-N-C^{AF}-BM with a reduction of $E_{1/2}$ of 1.4% (4.1% for Pt/C) and 2.1% (6.0% for Pt/C) after 5000 and 10000 cycles respectively respect to the initial value, with negligible variation of the average number of transferred electrons. This result further confirms that this novel synthesis method could be a successful way to synthesize non-precious materials with enhanced electrocatalytic properties and stability, that can be reasonably ascribed to the presence of a hierarchical porous structure successfully doped with active sites and with a high degree of surface graphitization, as verified through physical-chemical characterization.

4. Conclusions and future perspectives

In summary, a novel and sustainable process for the synthesis of electrocatalysts with atomically dispersed active sites was presented in this study. It was demonstrated that the iron-based material shows activity towards ORR comparable to state-of-the-art PGM-free electrocatalysts with excellent stability in acid medium. This unique approach to synthesize non-precious materials is all to be explored also for different electrocatalytic processes, with the possibility to finely tune the tridimensional structure and porosity of the catalyst by varying synthesis conditions, precursors and mass ratios, silica templates and morphology of polytetrafluoroethylene powder.

5. Supporting Information

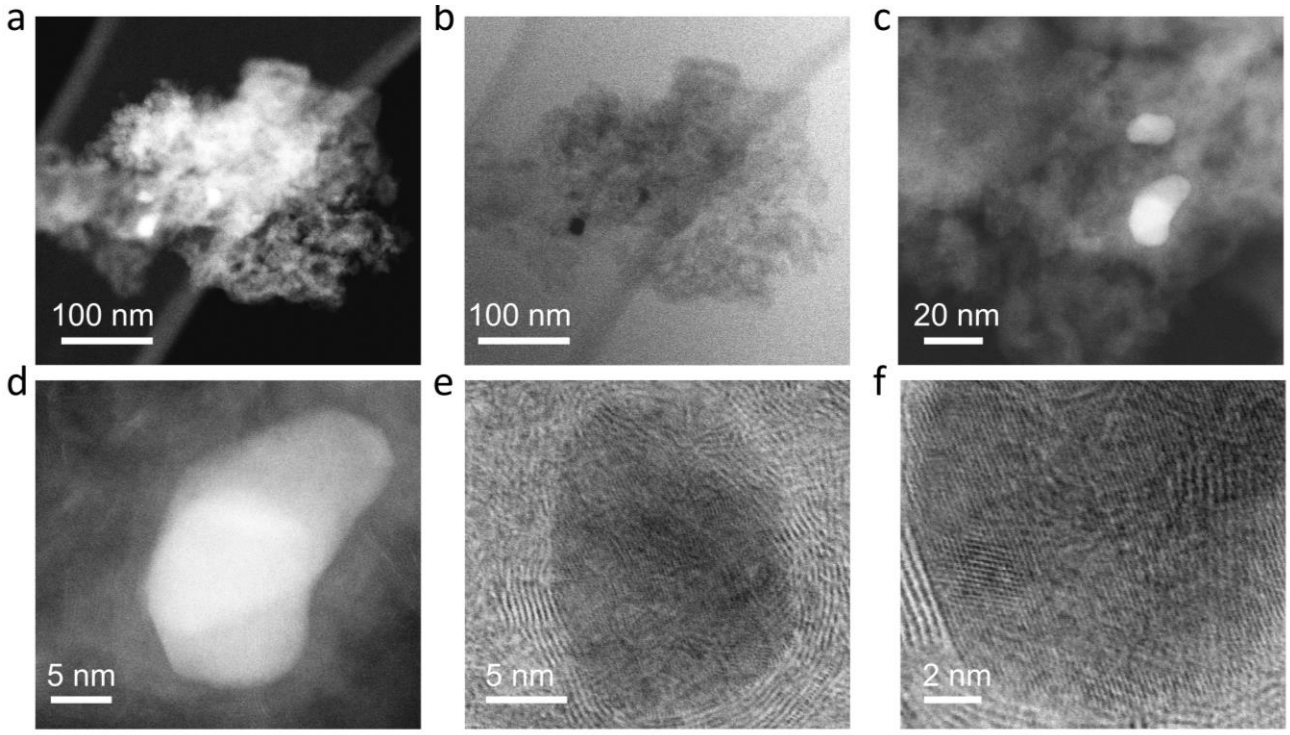

Figure 4.1. S 1: Figure S1. AC-HAADF/BF STEM images of the FeAD-N-CAF catalyst. (a-b) Low magnification darkfield and corresponding brightfield images showing the hierarchical porous structure and presence of Fe nanoparticles. (c-d) High magnification darkfield images of Fe nanoparticles contained within a graphitic shell, catalyzed by the Fe nanoparticle during pyrolysis. (e-f) High magnification brightfield images of the Fe nanoparticles, where the graphitic shell is clearly observed as well as the lattice of the Fe nanoparticle.

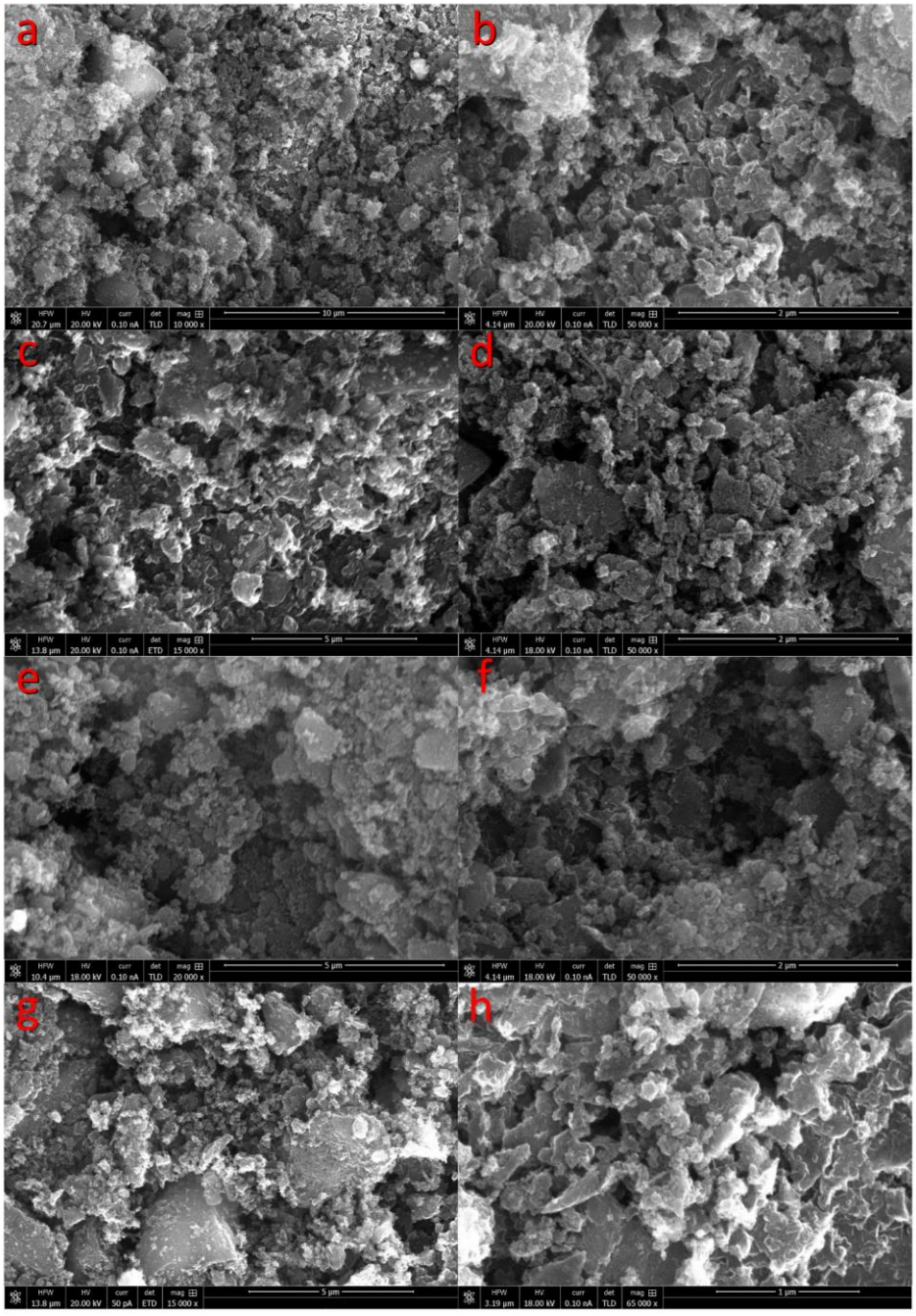

Figure 4.1. S 2: Figure S2. SEM images of (a-b) Co-N-CAF, (c-d) Mn-N-CAF, (e-f) Ni-N-CAF and (g-h) FeAD-N-CAF at different magnifications showing the hierarchical porous structure.

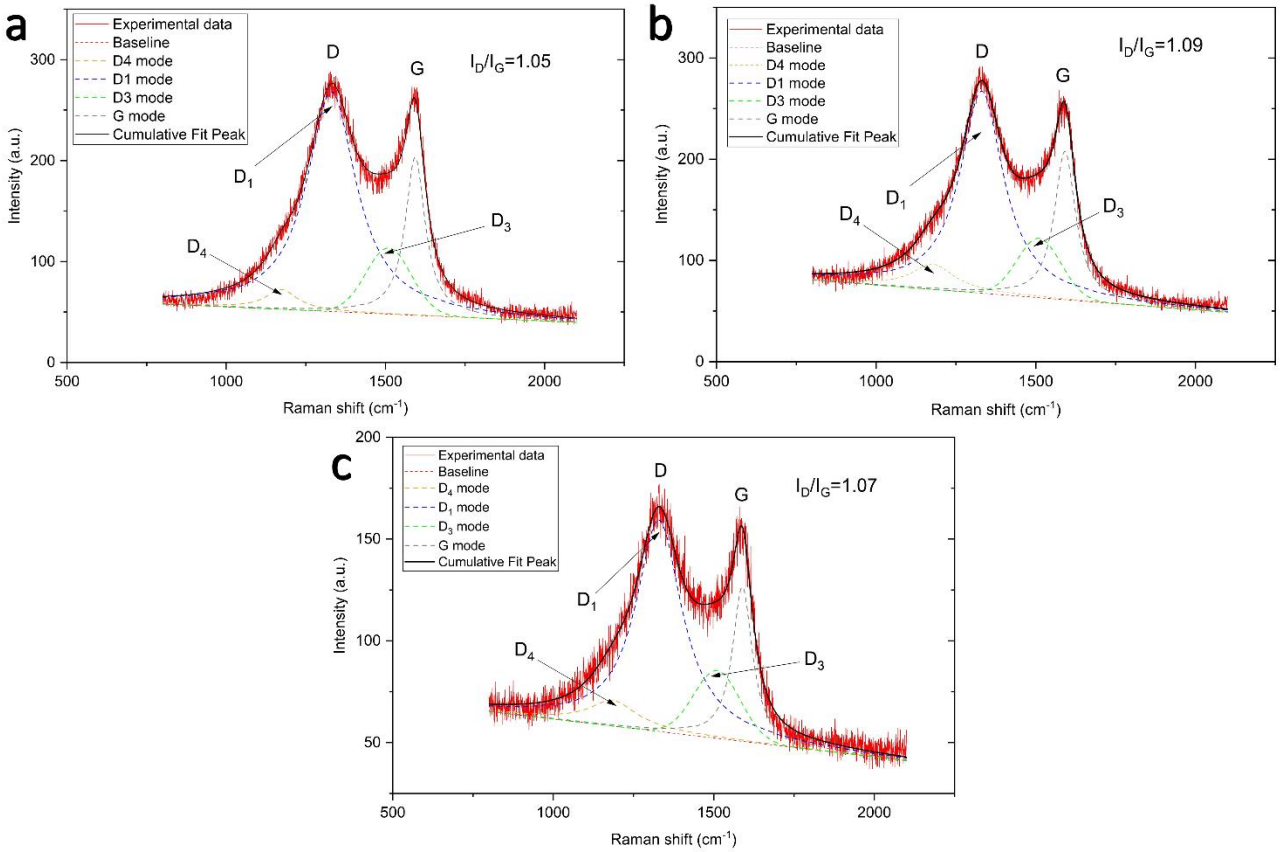

Figure 4.1. S 3: Figure S3. Raman spectra of (a) Co-N-CAF, (b) Mn-N-CAF and (c) Ni-N-CAF showing different vibrational modes of carbon.

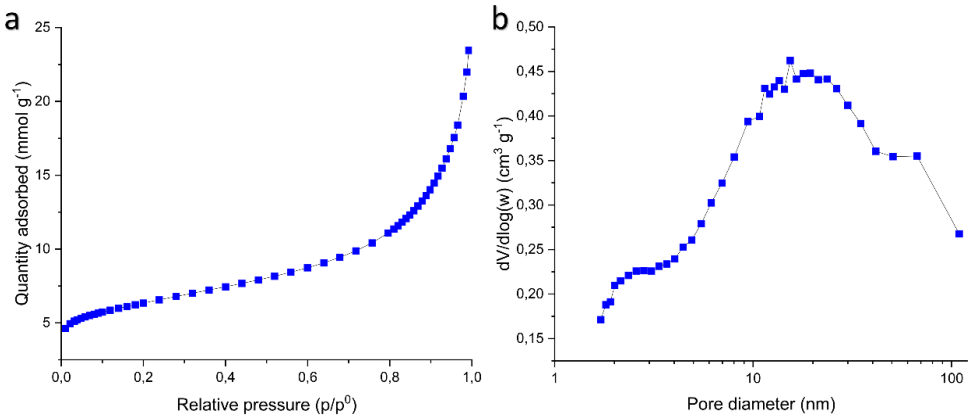

Figure 4.1. S 4: Figure S4. (a) N2 adsorption isotherm and (b) corresponding pore size distribution of Ni-N-CAF.

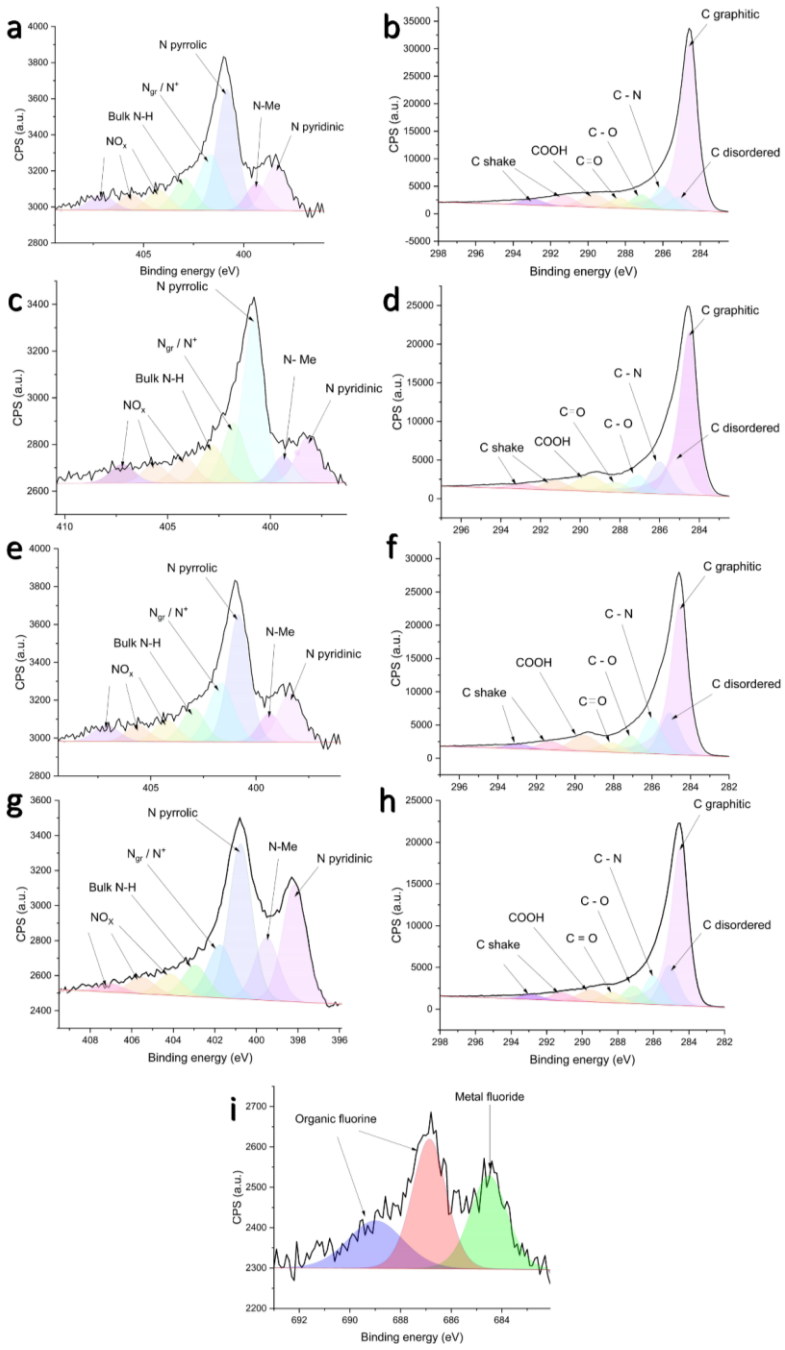

Figure 4.1. S 5: Figure S5. High-resolution N1s and C1s spectra respectively of (a-b) Co-N-CAF, (c-d) Mn-N-CAF, (e-f) Ni-N-CAF, high-resolution N1s, C1s and F1s spectra respectively of (g-i) Fe-N-C-Postpyr1.

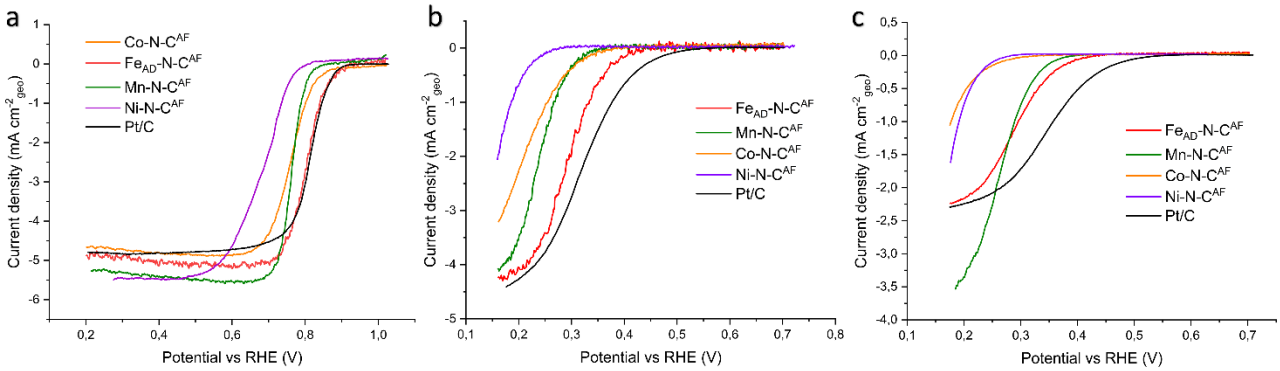

Figure 4.1. S 6: Figure S6. ORR polarization curves of M-N-C electrocatalysts and Pt/C at 1600 rpm in (a) 0.1 M KOH, (b) 0.5 M NaCl and (c) 2 M NaCl.

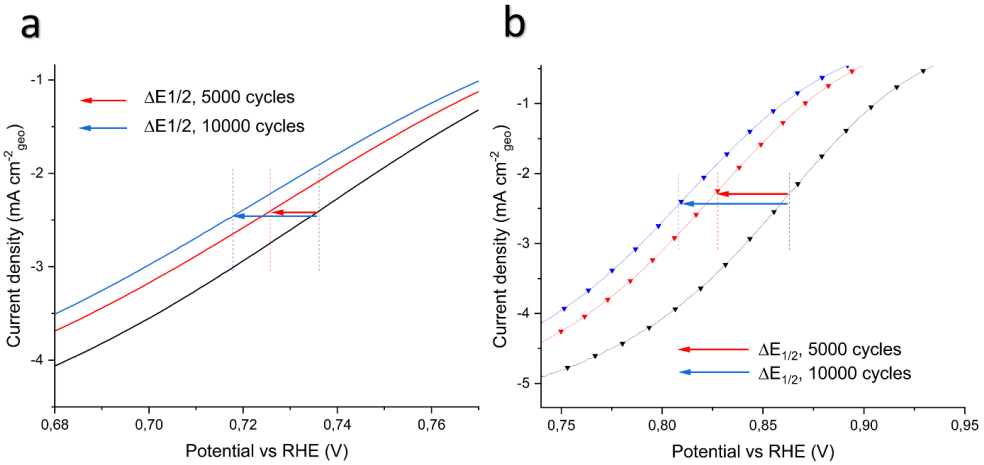

Figure 4.1. S 7: Figure S7. Results of the accelerated durability test on (a) FeAD-N-CAF-BM and (b) Pt/C: focus on the halfwave potential region.

F moiety	**Fe-N-C-Postpyr1**	**Fe$_{AD}$-N-C^{AF}**
F inorganic	67.03±1.00	61.00±6.22
Metal fluoride	32.97±1.00	39.00±6.22

Table 16: Table S1. X-Ray photoelectron spectroscopy high-resolution F1s rel. %at. concentration for AD-Fe-N-CAF, Fe-N-C-Postpyr1.

	E_{onset} (V vs. RHE)		$E_{1/2}$ (V vs. RHE)		$n_{average}$ (-)		$\%H_2O_{2,average}$ (-)	
	0.1 M KOH	0.1 M $HClO_4$	0.1 M KOH	0.1 M $HClO_4$	0.1 M KOH	0.1 M $HClO_4$	0.1 M KOH	0.1 M $HClO_4$
Fe_{AD}-N-C^{AF}	0.90 ± 0.01	0.82 ± 0.01	0.81 ± 0.00	0.70 ±0.01	3.98 ± 0.01	3.92 ±0.02	1.10 ± 0.22	3.87 ±1.00
Mn-N-C^{AF}	0.83 ± 0.01	0.75 ±0.01	0.76 ± 0.01	0.65 ±0.01	3.90 ± 0.02	3.30 ±0.05	5.09 ± 0.77	35.25 ±2.38
Co-N-C^{AF}	0.89 ± 0.00	0.73 ± 0.01	0.76 ± 0.01	0.54 ±0.05	3.94 ± 0.01	3.65 ±0.03	3.08 ± 0.69	17.55 ±1.53
Ni-N-C^{AF}	0.77 ± 0.03	0.65 ± 0.00	0.70 ± 0.04	0.46 ±0.01	3.72 ± 0.13	3.22 ±0.04	13.80 ±6.54	38.75 ±2.27
Pt/C	0.90 ± 0.00	0.96 ± 0.00	0.82 ± 0.01	0.88 ±0.01	3.99 ± 0.00	3.99 ±0.00	0.35 ± 0.10	0.49 ±0.13

Table 17: Table S2. ORR electrochemical performance of M-N-C electrocatalysts (600 µg cm-2) and Pt/C (60 µg cm-2) in 0.1 M KOH and 0.1 M HClO4 at 1600 rpm.

	E_{onset} (V vs. RHE)		$E_{1/2}$ (V vs. RHE)		$n_{average}$ (-)		$\%H_2O_{2,average}$ (-)	
	0.5 M NaCl	2 M NaCl	0.5 M NaCl	2 M NaCl	0.5 M NaCl	2 M NaCl	0.5 M NaCl	2 M NaCl
Fe_{AD}-N-C^{AF}	0.40±0.02	0.39±0.01	0.27±0.02	0.28±0.01	3.97±0.00	3.77±0.01	1.33±0.06	11.52±0.39
Mn-N-C^{AF}	0.33±0.01	0.35±0.01	0.23±0.01	0.25±0.01	3.65±0.09	3.62±0.00	17.34±4.51	19.06±0.10
Co-N-C^{AF}	0.34±0.01	0.26±0.00	0.19±0.01	-	3.89±0.01	3.79±0.14	6.61±0.42	10.72±6.79
Ni-N-C^{AF}	0.25±0.00	0.25±0.00	-	-	2.79±0.31	2.37±0.29	60.30±15.57	81.51±14.43
Pt/C	0.49±0.01	0.48±0.01	0.32±0.01	0.34±0.00	3.91±0.05	3.75±0.19	4.73±2.52	12.63±9.62

Table 18: Table S3. ORR electrochemical performance of M-N-C electrocatalysts (600 µg cm-2) and Pt/C (60 µg cm-2) in 0.5 M NaCl and 2 M NaCl at 1600 rpm.

	E_{onset} (V vs. RHE)	$E_{1/2}$ (V vs. RHE)	$n_{average}$ (-)	$\%H_2O_{2,average}$ (-)
Fe-N-C-Postpyr1	0.83±0.01	0.65±0.01	3.91±0.00	4.52±0.14
Fe_{AD}-N-C^{AF}	0.82±0.01	0.70±0.01	3.92±0.02	3.87±1.00
Fe-N-C-AW	0.80±0.01	0.70±0.00	3.88±0.00	5.95±0.11
AD-Fe-N-C^{AF}-BM	0.84±0.01	0.72±0.00	3.90±0.02	4.82±1.04
Pt/C	0.96±0.00	0.88±0.01	3.99±0.00	0.49±0.13

Table 19: Table S4. ORR electrochemical performance of Fe-N-C-Postpyr1, FeAD-N-CAF, Fe-N-C-AW, AD-Fe-N-CAF-BM (600 µg cm-2) and Pt/C (60 µg cm-2) in 0.1 M HClO4 at 1600 rpm.

Catalyst	Synthesis method and precursors	Acid washing	Electrolyte	E_{onset} vs RHE (V)	$E_{1/2}$ vs RHE (V)	Reference
Fe_{AD}-N-C^{AF}-BM	Acid-free sacrificial support method	-	0.1 M $HClO_4$	0.84	0.73	This work
Fe_{AD}-N-C^{AF}			0.1 M KOH	0.90	0.81	
NHMC (Fe-N-C)	Hybrid dual-templating: SiO_2 nanoparticles, F127 and iron-functionalized phenol-formaldehyde	15 wt % HF solution	0.5 M H_2SO_4	0.91	0.76	Deng et al. [171]
Fe-N/C-SAC	Molten salts mediated pyrolysis: nitrilotriacetic acid, iron acetylonate, KCl and $ZnCl_2$	-	0.1 M $HClO_4$	-	0.78	Xin et al. [172]
			0.1 M KOH	-	0.91	
Fe_3C/C-700	Fe3C nanoparticles encased by graphitic layers from ferrocene and cyanamide	-	0.1 M $HClO_4$	0.90	0.73	Hu et al. [162]
Fe_3C/C-800		-	0.1 M KOH	1.05	0.83	

FeNC-900	Sacrificial support method: SiO_2 nanospheres and Fe-doped ZIF-8 from MeIm, N,N-dimethylformamide, $Zn(NO_3)_2 \cdot 6H_2O$ and $FeSO_4 \cdot 7H_2O$	10 wt % HF solution	0.1 M $HClO_4$ 0.1 M KOH	0.84 0.96	0.71 0.85	Li et al. [173]
FeN/MPC2	Sacrificial support method for the synthesis of a carbon support (MPC) for Fe^{III}–1,10-phenanthroline complex	5 wt % HF solution	0.5 M H_2SO_4 0.1 M KOH	0.82 1.00	0.70 0.89	Osmieri et al. [174]
3DOM Fe–N–C-900	Iron doped ZIF-8 from MeIm, $Zn(NO_3)_2 \cdot 6H_2O$, ferrocene and methanol	-	0.1 M $HClO_4$ 0.1 M KOH	- -	0.88 0.78	Zhang et al. [175]
Fe_{SA}-N-C	Iron doped porphyrinic MOF (PCN-222)	-	0.1 M $HClO_4$ 0.1 M KOH	0.93 1.00	0.78 0.89	Jiao et al. [176]
Fe-NMP	Sacrificial support method: $Fe(NO_3)_3 \cdot 9H_2O$, pipemedic acid, nicarbazin, MeIm, urea, zinc, carbon nanotube and LM150 fumed silica	25 wt % HF solution	0.1 M KOH	0.97	0.84	Hossen et al. [164]
Fe-SAC/NC	Molten salt mediated pyrolysis: adenine, $ZnCl_2$, NaCl and Fe_2O_3	-	0.5 M H_2SO_4 0.1 M KOH	0.80 0.95	0.69 0.84	Hu et al. [177]

Co_{SA}-N-C	Cobalt doped ZIF-L and ZIF-8 from CTAB, $Co(NO_3)_2 \cdot 6H_2O$, $Zn(NO_3)_2 \cdot 6H_2O$ and MeIM	-	0.1 M $HClO_4$ 0.1 M KOH	- -	0.79 0.89	Zhou et al. [178]

Table 20: Table S5. Literature review of M-N-C electrocatalysts for oxygen reduction reaction.

Chapter 2: Metal-Nitrogen-Carbon Catalysts by Dynamic Template Removal for Highly Efficient and Selective Electroreduction of CO_2

Abstract

The renewable electroreduction of CO_2 to CO is a key component of future clean energy scenarios. These scenarios allow for the recycling of carbon emissions into value-added chemicals which achieves the joint goal of reducing greenhouse gase(s) while producing valuable chemical product(s). A catalyst which has a high activity and selectivity for the electroreduction of CO_2 to CO is highly desired for these applications. Non-precious metal catalysts (non-PGM) and specifically metal-nitrogen-carbon (M-N-C) catalysts are prime cathode candidates as they are selective for CO and H_2 formation with only trace amounts of other products such as CH_4. The traditional method of production of atomically dispersed M-N-C proceeds through either a sacrificial poymer approach or through hard-templating the catalyst with silica. The other is through the direct pyrolysis of non-abundant metal macrocycles such as MOF-based precursors via a soft-templating approach. These syntheses have substantial industrial limitations as they require harsh acid or basic solvents for post-pyrolytic removal of the support or they require rare chemical precursors. The method herein uses a novel mechanochemical mixing of a fluorine containing polymer with common pyrolytic precursors for the *in situ* removal of the template during the first pyrolysis. Further ball-milling and post-treatment in ammonia atmosphere yields a highly selective catalyst for CO_2 reduction. The role of the metal-center in these novel M-N-C catalysts in promoting CO_2 reduction is explored (M = Fe, Ni, Co, Mn) versus the performance of metal-free N-C. A mechanistic pathway for CO_2 reduction on the various novel M-N-C catalysts is suggested. The champion catalyst in terms of overall selectivity/activity (Ni-N-C) boasts a 98.9 +/- 0.2 % faradaic efficiency for CO formation (FE_{co}) at -1.1 V vs. RHE and an unmatched selectivity for CO_2 reduction (FE_{co} > 85 %) even at low overpotential (E = -0.3 V vs. RHE) compared to traditional Ni-N-C. The catalysts synthesized here present a promising class of new electrocatalysts which may be explored for a range of electrocatalytic applications.

Introduction

The ambient electrocatalytic CO_2 reduction reaction (CO_2RR) is a promising method for recycling CO_2 to value-added chemicals while mitigating the rising anthropogenic CO_2 emissions that are contributing to global warming.[36, 179] To that end, several companies have developed projects for the electroreduction of CO_2 to value-added chemicals including the Rheticus project in 2018 by Siemens and Evonik for the co-reduction of CO_2 and H_2O to syngas and Opus 12.[36, 180] The choice of cathode material in these systems is crucial as the CO_2RR usually requires a high-energy barrier and is more kinetically limited than the competing HER.[181, 182] Precious metals such as Ag and Au-based catalysts offer high activity and selectivity for CO_2 reduction but are prohibitively rare and expensive so the exploration of other metal and metal oxide catalysts is common such as Cu for the production of more highly reduced CO_2 reduction products and Sn-based catalysts for formate production.[183-185] Nonmetals (e.g., nitrogen-doped carbons) are a low-cost alternative to more expensive metal-based catalysts.[12, 125] Ultrathin 2D metal catalysts (e.g., monolayered Bi) are envisioned to offer higher surface areas and corresponding electrocatalytic activity compared to their bulk metallic counterparts but are often difficult to prepare.[186, 187] Among non-precious metal catalysts, metal-nitrogen-carbon (M-N-C) catalysts are prime candidates for cathode material(s) as they offer a high activity and selectivity for the targeted production of carbon monoxide. The mechanism for CO_2 reduction on M-N-C catalysts is generally assumed to proceed through M-N_x active sites or through metal-free N-C sites with the presence of separate metallic phases being more selective for the competing hydrogen evolution reaction (HER) and hence undesirable.[68, 70, 188, 189]

The M-N-C catalysts have several different types of active sites which are present as defects in layers of graphitic carbon. The elemental composition of M-N-C catalysts is predominantly carbon with a surface composition as measured by X-Ray Photoelectron Spectroscopy (XPS) to be *ca.* 85 – 95 % carbon, 1-4 % oxygen, 3-8 % nitrogen, with trace (< 0.5 %) surface metal content.[30, 190]. The primary active sites in M-N-C catalysts are atomically dispersed metal coordinated to nitrogen sites (M-N_x) and N-C sites where the nature of the nitrogen moiety (e.g., graphitic, pyridinic, pyrrolic N) may substantially influence the reactivity.[70, 190] Metal-free N-C catalysts also show substantial selectivity for CO_2 reduction with generally lower overall activity. [12] The nitrogen chemistry in M-N-C samples is a thoroughly researched topic as it has been found to have major electrochemical implications. For example, M-N-C catalysts for oxygen reduction reaction (ORR) have been found to benefit from an abundance of M-N_x active sites which have been shown to catalyze the reduction of oxygen to water while an abundance of hydrogenated and protonated nitrogen has been shown to catalyze parasitic peroxide formation. [134, 190, 191] The role of nitrogen functionalities was also shown to be vital for the CO_2R by the work of Leonard et al who prepared polyaniline-based Fe-N-C materials with different N precursors to examine its influence on CO_2R selectivity. The materials produced with melamine had the highest Fe-N_x moiety content and highest faradaic efficiency for CO formation. [192] Further experimental work and DFT simulations found that pyridinic N is a key moiety for CO_2 reduction due to having a low energy barrier for COOH* formation. Pyrrolic N as opposed to graphitic and pyridinic N was found to be the only nitrogen moiety where the initial formation of COOH* proceeded spontaneously. In this instance, the rate of CO desorption was proposed as the rate determining step (rds). [193, 194]. Along with alterations in the

nitrogen chemistry of M-N-C catalysts, the metal atom is a key determinant for altering the electrochemical performance. The nature of the metal atom has major implications in affecting the binding energies of key intermediates such as COOH*, CO*, H* and the resulting selectivity for CO_2R.

These binding energies can explain the selectivity for promoting either CO_2R or the hydrogen evolution reaction (HER) as well as the potential dependent selectivity for these catalysts. Generally, Fe-N-C and Ni-N-C have the highest selectivity for CO_2RR. Fe-N-C has a high selectivity for CO_2RR at low overpotential (E > -0.50 V vs. RHE) while Ni-N-C has increasing selectivity for CO_2RR at more cathodic potentials (E < -0.50 V vs. RHE) and correspondingly higher activity.[68, 70] These trends in activity based on the nature of the metallic substituent have been attributed to different CO_2 reduction mechanistic pathways via the rate-determining step (rds) being either CO_2 adsorption (CO_2*) or COOH* formation.[195] Generally, the M-N-C catalysts (e.g., M= Fe, Mn, Cr, Co, and Cu) have a potential-dependent faradaic efficiency for CO formation with Fe-N-C and Ni-N-C having the highest selectivity followed by Mn-N-C and Cr-N-C. Co-N-C and Cu-N-C have the lowest selectivity for CO_2RR and a much higher selectivity for the HER. [42] Fe, Mn, and Co-N-C offer strong binding to COOH* so have lower onset potentials for CO formation. However, the strong binding energy of H* for these catalysts explains the concurrent H_2 production which becomes more pronounced at higher overpotentials. By contrast, Ni-N-C usually offers a weak binding for COOH* and weak binding for H*. This explains the higher overpotential required for CO production on Ni-N-C and its high CO_2R selectivity at very cathodic potentials where the HER usually dominates. [44, 195, 196] It is helpful to organize these parameters into a few different categories to independently investigate how they influence CO_2R performance. The first category directing CO_2R performance in M-N-C catalysts is the nature of the metal atom while the next category is the metal atom coordination sphere. In parallel, the morphology and reaction parameters are key in altering the CO_2R selectivity.

This study aims to elucidate the structure/CO_2R activity relationships for a series of M-N-C and N-C catalysts synthesized by a novel method. The method is comprised of an initial wet impregnation step where the nitrogen/carbon source (nicarbazin) is mixed with the pore-forming mixture of silica and metal nitrate precursor. The dried sample is then combined with Teflon (Poly(tetrafluoroethylene) through high-energy ball-milling and carbonized during pyrolysis under inert atmosphere. Use of Teflon as a silica-removal agent was effectively used by the group of Singh et al for production of mesostructured carbon with higher surface areas and enhanced supercapacitor performance than those produced by the traditional HF treatment method.[156] The shortened synthesis presented herein yields a highly selective catalyst for CO_2 reduction even after a single ball-milling and pyrolysis step. For this reason, the process presents immediate advantages in terms of manufacturing scalability over the conventional sacrificial support method which utilizes on the order of 10 mL of concentrated hydrofluoric acid per gram of silica. [30] The use and disposal of $HF_{(liquid)}$ presents vastly increased operating expenses (OpEx) which the present synthesis completely avoids. The *in situ* generation of gas-phase HF and SiF_4 are, by comparison, much easier to process for environmental remediation than concentrated $HF_{(liq)}$. The gaseous products are sometimes fed through a granulated limestone-based sorbent and then scrubbed (hydrolyzed) with water to form fluorosilicic acid (H_2SiF_6 (FSA)). [197, 198]

The synthesis method, while analogous to the sacrificial support method (SSM), has several important differences which yield a morphologically and electrocatalytically unique material. The most pronounced of which is the temporal difference in the pore vs. active site formation. Conventionally, the SSM utilizes precursors which have low volatility and decompose at elevated temperatures greater than 700 ℃ so that the incorporation of nitrogen/carbon moieties may occur concurrently with active site formation.[30, 190] Hence, the active site formation occurs first followed by a post-pyrolytic treatment in HF or KOH to etch away metal-rich phases and form a hierarchically porous carbon framework that enhances the active site accessibility.[20] The present method intentionally introduces a volatile fluorine-containing polymer precursor (PTFE) which decomposes at a temperature (i.e., 450 – 560 ℃) lower than the proposed temperature for active site formation. In the conventional SSM, the silica nanospheres utilized in the synthesis for hard-templating are usually regarded as inactive during pyrolysis and are only observed to disperse at temperatures of 1180 ℃ or greater.[145] Here, however, the silica is removed as evidenced from EDS measurements through a reactive etching process with *in situ* generated gas-phase HF to generate SiF_4 in the gas-phase. PTFE carbonized in the absence of hydrogen is known to lead to tetrafluoroethylene (C_2H_4) instead of HF however in presence of partially polymerized H-containing carbon, the formation of hydrofluorocarbons such as PVDF are known to emit HF upon decomposition. [156, 199] Similarly, in presence of nicarbazin decomposition which begins before PTFE decomposition, the removal of silica is thought to occur through the *in situ* decomposition of hydrofluorocarbon intermediates yielding HF in the gas-phase (Figure S1). The variation in synthetic conditions yields a hierarchically porous catalyst with a continuous pore size distribution compared to the conventional M-N-C produced by hard-templating approach. The result is a highly active catalyst for CO_2 reduction which has higher selectivity and throughput (evaluated on a benchtop flow cell) than competing M-N-C catalysts.

Results and Discussion

Synthesis and Physical Characterization of M-N-C Catalysts

Catalysts with a high degree of atomically dispersed metal sites were synthesized using a novel synthesis method. The synthesis involves solution phase mixing of a carbon-nitrogen containing source (nicarbazin), a blend of silica templates, and a small fraction of metal nitrate precursor(s) (< 7 wt. %). The use of multiple silica sources is thought to create an internal network of hierarchically structured pores similar to the trademarked VariPore™ application of the sacrificial support method (SSM) utilized by Pajarito Powder, LLC.[200] The precursors are then mechanically integrated with polytetrafluoroethylene (PTFE) powder by ball-milling followed by pyrolysis in inert nitrogen atmosphere, and finally by a second ball-milling and pyrolysis under 10% NH_3 atmosphere. X-Ray Photoelectron Spectroscopy (XPS) survey and Energy Dispersive Spectroscopy (EDS) evidences the removal of silica by the first pyrolysis and the removal of additional fluorine content by the second pyrolysis. The removal of fluorinated species and additional creation of micropores during the second pyrolysis usually greatly benefits the overall electrochemical activity. The re-pyrolysis in the original SSM has been found to eliminate undesired metal nanoparticles and enhance their dispersion (through creation of additional M-N_x sites) without altering the total metal concentration on the catalyst surface or the morphology of the carbonaceous framework.[17]

The X-Ray Diffraction (XRD) spectra in Fig 1a shows two broad peaks for mixed graphitic/amorphous carbons at 26° and 44° for (002) and (100) graphitic planes, respectively. Additional peaks present in all samples indicate the formation of metal carbide, metal nitride, metal oxide, and metallic nanoparticle phases (Table S1). We may observe by High-Resolution Transmission Electron Microscopy (HRTEM) that there is a high degree of atomic dispersion (Fig 1d) maintained despite the presence of auxiliary metallic phases observed by XRD. The FWHM of the (002) peak of graphitic carbon was used as a measure of the defect density or locations where highly reactive catalyst sites may be located. The sharpness of the peak is inversely related to the defect density where a broader peak (higher FWHM) usually indicates a higher defect density.[201, 202] The defect density and FWHM trend seen in Fig 1b is Fe-N-C > Ni-N-C > Co-N-C > Mn-N-C. This trend indicates increased occurrence of long-range disorder and lattice defects for Fe-N-C and Ni-N-C as compared to Co-N-C and Mn-N-C samples. The FWHM for XRD peaks for representative metallic phases of each M-N-C shows the order of Fe-N-C > Ni-N-C > Mn-N-C > Co-N-C. The ICP-MS results present the same trend in total metallic loading (wt. %) as that observed in Fig1b (red curve) for the FWHM of representative metallic phases of the M-N-C catalysts (Figure S2). This agrees well with the Scherrer equation which predicts that an increase in crystallite size results in a decrease in FWHM of the observed XRD peak. This can be attributed to the increased tendency (at higher metal loading (e.g., for Co-N-C)) for metallic particles to migrate and aggregate into clusters/particles during high temperature pyrolysis. [203] The HRTEM data shows the samples show predominantly only atomically dispersed metal sites although some separate metallic nanoparticle phases are observable for Fe-N-C (Figure S3). Since, Ni is known to strongly catalyze the graphitization of carbon, we predict according to previous reports that at metal atom loadings beyond 2 wt.%, the nickel nanoparticles are encased in graphitic shells of carbon which may reduce the occurrence of HER. [204]

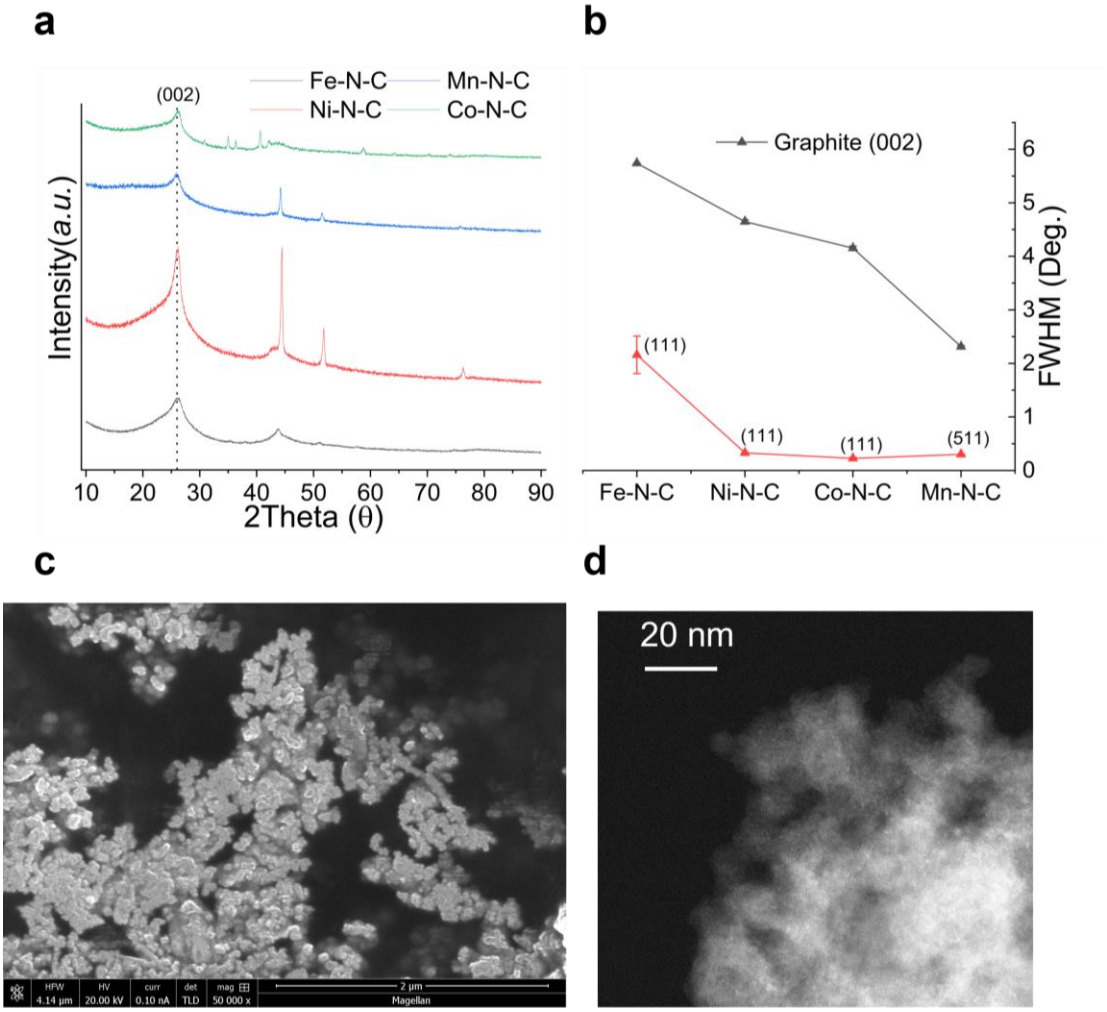

Figure 4.2. 1: Figure 1: XRD Patterns of M-N-C (M = Fe, Ni, Mn, Co) (a), FWHM(deg.) extracted from XRD spectra for (002) graphitic carbon and metallic phase(s) (b), SEM image of Ni-N-C catalyst (c), TEM image of Ni-N-C (d).

The SEM image in Figure 1 c shows that the the blend of silica in Ni-N-C bestows a hierarchical porosity. A similar hierarchical porosity can be observed for the other M-N-C catalysts (Figure S4) and the BET adsorption/desorption profile shows behavior characteristic of a Type 4B isotherm. The Barrett-Joyner-Halenda (BJH) pore size distribution shows a material with a high amount of microporosity and mesoporosity while the SEM data confirms the additional presence of macropores ranging up to 200-300 nm in diameter. The BJH pore size distribution presents a broad micro/mesoporous peak (depending on the blend of silica utilized) which is different from the multimodal or bimodal pore size distribution conventionally seen for M-N-C catalysts synthesized by SSM. [134] In order to study the influence of the silica template on the final catalyst structure and reactivity for CO_2 reduction, three different blends of silica template were used for Ni-N-C denoted as Ni-N-C, Ni-N-C (*), and Ni-N-C (**). The Ni-N-C (*) sample has the low surface area silica template replaced by a moderate and large surface area template while the Ni-N-C (**) sample has the larger surface area template removed. The compositions of the different silica blends can be found in supplementary information (Table S2).

A marked difference in the porosity and surface area is observed between Ni-N-C and Ni-N-C (*) samples which has a substantial impact on their CO_2 reduction performance. The wettability of the catalyst substrates were also investigated by measuring the dynamic advancing and receding contact angles and calculating the surface energies from the contact angle hysteresis. The surface energy of the catalysts is found to be *ca*. 2-4 mN/m independent of the pore size(s) of the samples (Figure S5). The BJH adsorption pore size distribution is shifted from a broad peak centered at a pore diameter of *ca.* 2-6 nm for Ni-N-C to a broad peak at *ca.* 12-26 nm for Ni-N-C (*) (Figure 2e). The resulting adsorption isotherm shows a decrease in the calculated BET surface area from 704.1 m^2g^{-1} to 462.9 m^2g^{-1} for Ni-N-C and Ni-N-C (*), respectively. Additionally, the % microporosity is increased in Ni-N-C vs. Ni-N-C (*) (44.2% vs. 40.6 %, respectively). A shift from a type 4B reversible isotherm for Ni-N-C to a type 4a irreversible isotherm with characteristic hysteresis for Ni-N-C (*) is observed. The adsorption profile and pore size distribution for Ni-N-C (**) can be found in supplementary (Figure S6). The samples were also screened by HRTEM/EDS in Figure 2a in order to ascertain the elemental distribution of the catalysts.

The EDS data evidences the complete removal of the silica template during pyrolysis as only trace silica remains (Figure S7). Figure 2a shows the HRTEM image of the sample with the red box indicating the analysis location utilized for EDS measurements. A large contribution from carbon is observed by EDS in agreement with the large percentage of surface carbon (85-95%) content detected by X-Ray Photoelectron Spectroscopy (XPS) (Table S3). The nitrogen content is dispersed throughout the carbon matrix while the Ni signal by EDS shows good mapping onto the nitrogen sites over the same area analyzed. This suggests the possible existence of metal-nitrogen coordination sites which are known to correlate with high electrochemical activity. [20, 190, 205, 206] Detailed XPS spectra were obtained for the N1s spectra to elucidate the nitrogen chemistry of the nitrogen atoms embedded in the carbon framework. The XPS spectra for the C1s region was also deconvoluted to better understand the surface carbon chemical composition. A series of fitting peaks were used to fit the N1s and C1s spectra (Figure 2 and Tables S4 and S5), respectively, according to previous publications. [190]

XPS analysis shows the evolution of the surface elemental composition during the synthesis process. The notation used here is M-N-C (x/y) where x = the initial temperature (℃) for pyrolysis under N_2 atmosphere and y = the second temperature (℃) for pyrolysis under NH_3 atmosphere while a dashed line denotes only one pyrolytic step (e.g., M-N-C (900/-) indicates only the first pyrolysis was performed). There is a marked decrease in the O 1s signal (% atomic concentration (%at.) of oxygen) after the second pyrolytic step which is accompanied by an increase in the %at. of carbon. The surface oxygen content decreases in the order of M-N-C (900/-) > Co-N-C > Mn-N-C > Ni-N-C ≅ Fe-N-C while the surface carbon content is more dependent on the number of pyrolytic steps than the metal substituent (i.e., M-N-C (900/-) has %at. carbon of *ca.* 90 % vs. *ca.* 95 % for M-N-C (900/950)). This decreased oxygen concentration is mostly likely due to removal of surface oxides including carbon oxides during repyrolysis. [17] The %at. of nitrogen is between 2-3 % for all samples and does not appear to depend on the metallic substituent or the number of pyrolysis steps. There is only trace amounts of fluorine (*ca.* 0.4 %) present after the first pyrolysis which disappears after the second pyrolysis which agrees with previous studies where volatile SiF_x species are removed upon repyrolysis.[191] There is only trace silica (< 0.20 at.%) observed for a few of the catalysts and fluorine for Co-N-C (0.22 at. %) while fluorine is completely absent from the other samples. Ni-N-C shows complete removal of both silicon and fluorine

from the final sample. Together, the data shows that the method of incorporation of PTFE powder completely removes the silica hard template and fluorine from the sample with the same effectiveness as leaching in KOH or HF does in the conventional SSM.[30, 190, 191] .

The N 1s XPS spectra was deconvoluted as shown in Figure 2b. All samples show substantial Metal-N_x coordination at a binding energy of 399.5 eV (8-17 % of total N 1s signal (at.%N)).This agrees well with EDS observation of metal sites mapping onto nitrogen sites. The predominant peak in the N 1s spectra for all samples is the pyrrolic nitrogen peak centered at 400.8 eV (26 – 45 at.%N). Both Fe-N-C and Ni-N-C show a reduction in Metal-N_x upon repyrolysis from *ca.* 17 % to *ca.* 13 % for Fe-N-C and from *ca.* 17 % to *ca.* 9 % for Ni-N-C. Additionally, the ratio of pyrrolic N to pyridinic N is unchanged between pyrolysis steps for Ni-N-C but is substantially reduced for Fe-N-C (Table S4). The increased pyrrolic N content in Ni-N-C agrees with previous reports that Ni doping causes the formation of pyrrole-type N species which act as anchoring sites. [207, 208] This explains the maintenance of a high ratio of pyrrolic N to pyridinic N between pyrolysis steps. However, no clear correlation is observable at present between the nitrogen moiety content and the resulting CO_2R performance (see electrochemical section for a more detailed discussion). For example, Ni-N-C has the highest CO_2 performance but has substantially lower Me-N_x content (8.83 +/- 0.47 %) than Co-N-C (16.25 +/- 0.86 %) which shows far less selectivity for CO_2R. This suggests that the nature of the metal atom in the catalysts is more impactful than the relative proportion of nitrogen moieties for influencing the selectivity for CO_2R. However, the nitrogen coordinative environment may allow for an alteration of the reaction pathway for CO_2 reduction on the M-N-C catalysts. For example, the rate-determining step for CO_2R on Ni-N-C catalysts is thought to be the formation of *COOH. [195] This process may be aided by a large proportion of pyrollic nitrogen in the vicinity which allows for the exergonic formation of *COOH.

The C 1s XPS spectra was deconvoluted into several peaks attributable to graphitized sp^2 hybridized carbon, amorphous sp^3 carbon, as well as carbon nitride and carbon oxide moieties (Table S5). As seen in figure 2c, the catalysts show a high proportion of graphitized carbon which together with reduced oxide content usually bestows increased electronic conductivity to the material. [209] The Raman Spectra also shows evidence of increased relative graphitization with lowered I_D/I_G ratios for all M-N-C catalysts (Figure S8). The graphitization of carbon is known to commence at a temperature of 900 °C in tandem with the formation of atomically dispersed metal-nitrogen moieties embedded in the carbon framework. [17, 145]. Increased graphitization may aid electron transport to and from the active site during electrocatalysis. The order of sp^2 graphite-like carbon content is M-N-C (M = Fe, Ni, or Co) > Mn-N-C (e.g., for Ni-N-C, % sp^2 carbon = 61.70 +/- 1.32 %, while for Mn-N-C, % sp^2 carbon = 40.00 +/- 1.98 %). This may be explained by the fact that Fe, Ni, and Co nanoparticles and their carbides, formed during pyrolysis, are known to catalyze the graphitization of carbon. [210] The degree of graphitization also increased upon re-pyrolysis. For example, sp^2 carbon content increased from 48.49 +/- 6.2 % for Fe-N-C (900/-) to 61.51 +/- 2.14 % for Fe-N-C (900/950). This observation is opposite to the decreased sp^2 carbon and increased sp^3 carbon upon re-pyrolysis of M-N-C materials obtained by SSM. [17] This may be due to trace metal nanoparticles remaining in the present method, that were removed by HF etching in the conventional SSM, which may further catalyze the graphitization of carbon in the second pyrolysis. The second pyrolysis may increase the degree of graphitization through (i). exposing a greater surface area of carbon since the silica template has left during the first pyrolysis, (ii). a “cleaning” of the surface

by re-pyrolysis in reductive atmosphere which may remove surface oxides and expose more of the carbon framework, or by (iii). re-pyrolysis under higher temperature (950 ℃) may allow for a higher degree of catalytic graphitization as observed during the first pyrolysis of SSM materials (when increasing from 870 ℃ to 1180 ℃). [145] In addition to increased catalytic stability (e.g., higher corrosion resistance for graphitized material) after the second pyrolysis, the M-N-C materials also present morphological stability which is crucial for reactant/product transport during catalysis. [136] SEM images before and after pyrolysis show that a hierarchical porosity is maintained after the second pyrolysis (Figure S9).

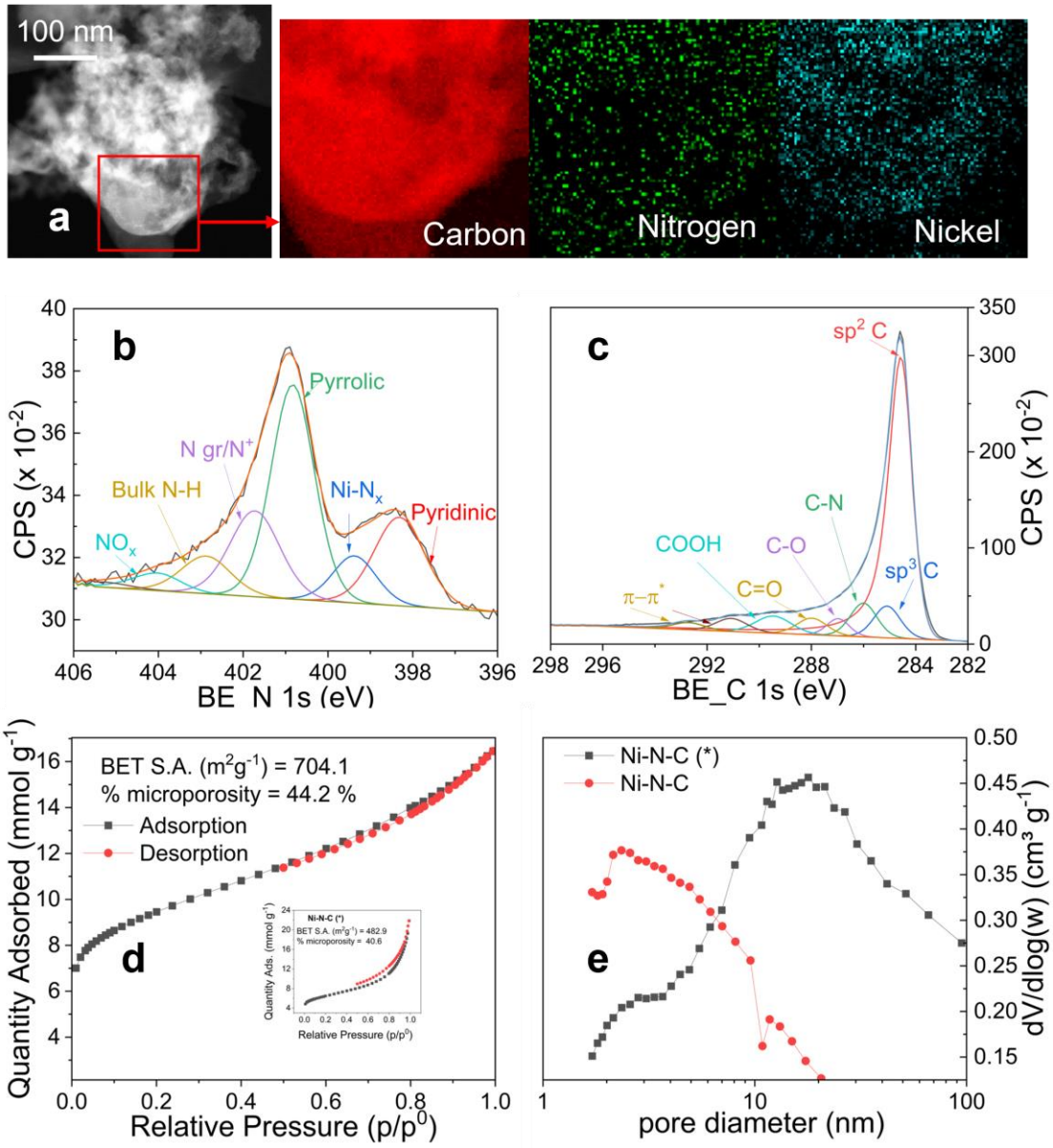

Figure 4.2. 2: Figure 2: TEM/EDS (a), N 1s XPS fitting (b), C 1s XPS fitting (c), BET adsorption/desorption isotherm (d), with Ni-N-C (*) isotherm inset. BJH Adsorption pore size distribution for Ni-N-C and Ni-N-C (*) (e).

Electrochemical Characterization of N-C and M-N-C Catalysts

The electrochemical performance of the M-N-C catalysts was studied and compared to the state-of-the-art M-N-C electrocatalysts selective for CO_2R and considered as benchmark non precious group metal (PGM) catalysts. The selectivity and activity of the catalysts towards either the CO_2 reduction reaction (CO_2R) or the hydrogen evolution reaction (HER) was studied as a function of the metal atom center where M-N-C (M = Fe, Ni, Co, Mn). This activity was evaluated and compared to an analogous metal-free N-C catalyst synthesized without a metal nitrate precursor.

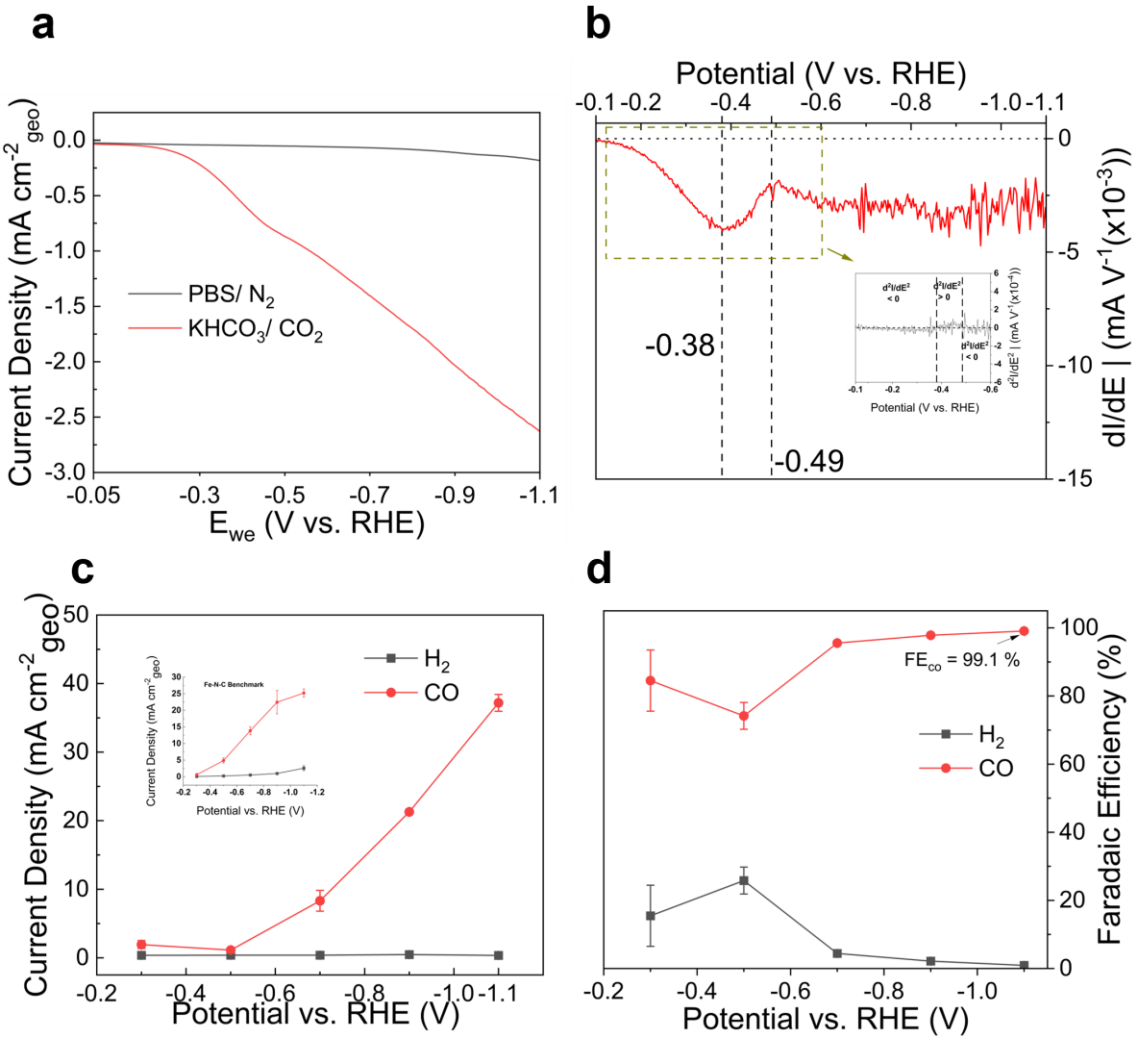

Figure 4.2. 3: Figure 3: LSV data obtained at 2 mV/s from 0.0 V to -1.1 V vs. RHE in the cathodic direction using N2-saturated phosphate buffer solution (PBS) or CO2-saturated KHCO3 for 0.1 mg/cm2 Ni-N-C (a), the first derivative and second derivative graph inset of the LSV data (b), current density magnitude (mA cm-2) for CO or H2 for 1.0 mg/cm2 Ni-N-C (c), faradaic efficiency (%) for CO or H2 production (d).

Firstly, the aqueous phase CO_2R performance was evaluated for Ni-N-C in a conventional H-cell arrangement with either N_2-saturated PBS or CO_2-saturated $KHCO_3$ buffer solution. There is a significant increase in the observed current density when utilizing CO_2-saturated $KHCO_3$ solution which indicates that Ni-N-C has a high selectivity for CO_2 reduction and a low selectivity for the HER. The onset potential for CO_2 reduction is easier to observe when the derivative of the current density with respect to the applied potential is plotted (Figure 3b). The onset potential for CO_2 reduction is very close to the thermodynamic minimum potential (e.g., E_{onset} is *ca.* -0.15 V vs. RHE which requires only *ca.* 40 mV overpotential). The second derivative is also plotted in the inset and we can see the value hovers around zero which indicates the linear portion of the red curve in Figure 3a may be well-approximated by a straight line. However, there is a slight curvature in the graph and a change in its concavity between *ca.* -0.38 V to -0.49 V marked by a change in sign of the second derivative from negative to positive and back to negative. This is an interesting observation as other studies have shown a continuously increasing FE_{co} for Ni-N-C at more cathodic potentials instead. [44, 211] It is well known that aqueous phase CO_2 reduction faces diffusion limitations due to the low solubility of CO_2 in aqueous electrolyte (e.g., D_{co2} = 0.0016 vs. D_{co2} = 16.0 $mm^2\ s^{-1}$ for CO_2 diffusion in aqueous electrolyte vs. humidified CO_2 gas).[212] Hence, in order to study the catalysts' performance/selectivity under higher current densities, the catalysts were evaluated in a benchtop gas diffusion electrode (GDE) flow cell.

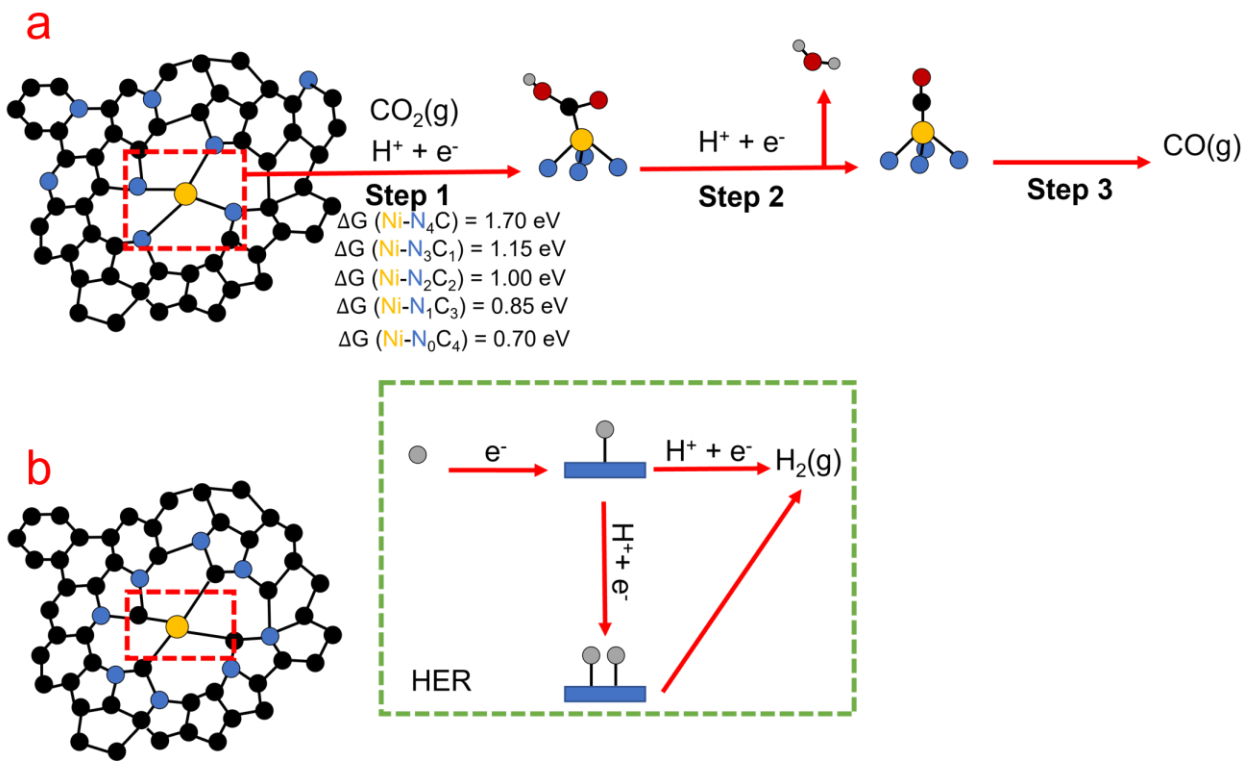

Figure 4.2. 4: Figure 4: Proposed mechanism for CO2R vs. HER on Ni-N-C catalyst. DFT calculated free energies for CO2→COOHads (step 1) for different M-Nx moieties are shown for step 1. [44, 62, 70]

By comparing Figure 3c and the inset graph, we can see the Ni-N-C catalyst produced using the present method outperforms the benchmark CO-selective Fe-N-C catalyst produced by the SSM in terms of overall activity (j_{co} = *ca.* -40 mA vs. j_{co} = *ca.* -25 mA for Ni-N-C and Fe-N-C, respectively, at -1.1 V vs.

RHE) and selectivity (FE_{co} = *ca.* 99 % vs. FE_{co} = *ca.* 90 % for Ni-N-C and Fe-N-C, respectively, at -1.1 V vs. RHE). Interestingly, the new Ni-N-C catalyst shows a considerable selectivity for CO_2 reduction even at a low overpotential of *ca.* 200 mV whereas conventional Ni-N-C catalysts usually require a higher overpotential to show similar CO_2R activity. [7, 44, 195] The high selectivity for CO_2R at both low and high overpotential for Ni-N-C may be due to having a multitude of active sites ranging from Ni-N_4C to Ni-N_0C_4 (Figure 4 a and b, respectively) with potential-dependent relative activities.[44, 62, 70, 195] DFT calculated binding energies from literature are shown in figure 4. [44, 62, 213] At low overpotential, the Ni-N_0C_4 site (site b) may dominate while at high overpotential, Ni-N_4C (site a) may provide the increased CO_2R activity. Additionally, both during the aqueous-phase CO_2 reduction reaction (Figure 3a) and the gas-phase CO_2 reduction reaction (Figure 3d), there is an observable decrease in CO_2R selectivity at -0.5 V and then a recovery at more cathodic potentials. This slight decrease in FE_{co} warrants further investigation and may be due to different factors including varied sensitivity to applied potential of *COOH and *H adsorption energies which affect the rate of CO_2R and HER, respectively. [195, 196] When the potential is made more cathodic than -0.5 V vs. RHE, Ni-N-C shows almost complete selectivity for CO_2R on the potential region up to -1.1 V vs. RHE as shown by a dramatic decrease in the percentage of H_2 detected and increase in percentage of CO detected by gas chromatography (Figure S10). We attribute this to the inaccessibility of liquid electrolyte to nickel nanoparticles encased in graphitic carbon which prevents the HER from occuring even at highly cathodic potentials. [204]

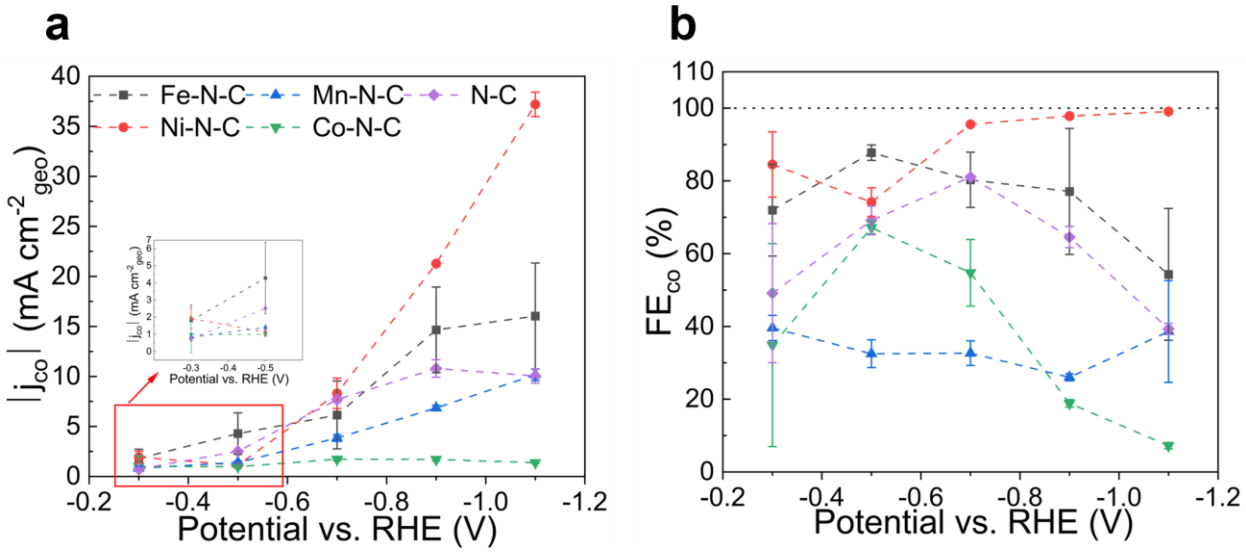

Figure 4.2. 5: Figure 5: CO partial current density magnitude plotted vs. applied potential (V) vs. RHE (a), FEco(%) for the M-N-C (M = Fe, Ni, Mn, Co) and N-C catalysts (b).

The performance of the M-N-C catalysts for CO_2R as a function of the metal atom is shown in Figure 5. The general trend in the selectivity of the catalysts synthesized by the present method agrees with previous studies on the role of the metal atom in steering CO_2R selectivity on M-N-C catalysts. [32, 214] The selectivity of the catalysts for CO_2 reduction is decreasing in the order of Ni-N-C > Fe-N-C > Mn-N-C ≅ N-C > Co-N-C. At high overpotential the difference is more pronounced with Ni-N-C far exceeding the activity and selectivity of the other catalysts. At low overpotential, Fe-N-C is highly selective for CO production in agreement with previous reports. Fe-N-C shows a similar volcano shaped FE_{co} potential

dependence and reaches a maximum at a lower overpotential than Fe-N-C synthesized by SSM, however it becomes more selective for HER at higher overpotential (Figure S11).It is interesting to note that the metal-free N-C catalyst also shows considerable CO_2R activity at moderate overpotential (e.g., N-C has CO_2R activity/selectivity at a potential of -0.7 V vs. RHE that is competitive with both Fe-N-C and Ni-N-C). The trend in the partial current density for H_2 (j_{H2}) shows the reverse trend as shown for j_{co}. Mn-N-C shows the highest HER activity followed by Co-N-C. Mn-N-C has a H_2 partial current density that increases until -0.9 V and then plateaus. The increased FE_{co} (between -0.5 and -0.7 V vs. RHE) afforded by Co-N-C is at the expense of a much lower overall current density (i.e., low j_{H2} and j_{co}). The other catalysts show monotonically increasing H_2 production at more cathodic potentials with the exception of Ni-N-C which shows negligible H_2 production across the whole potential region from -0.3 V to -1.1 V vs. RHE (Figure S12).

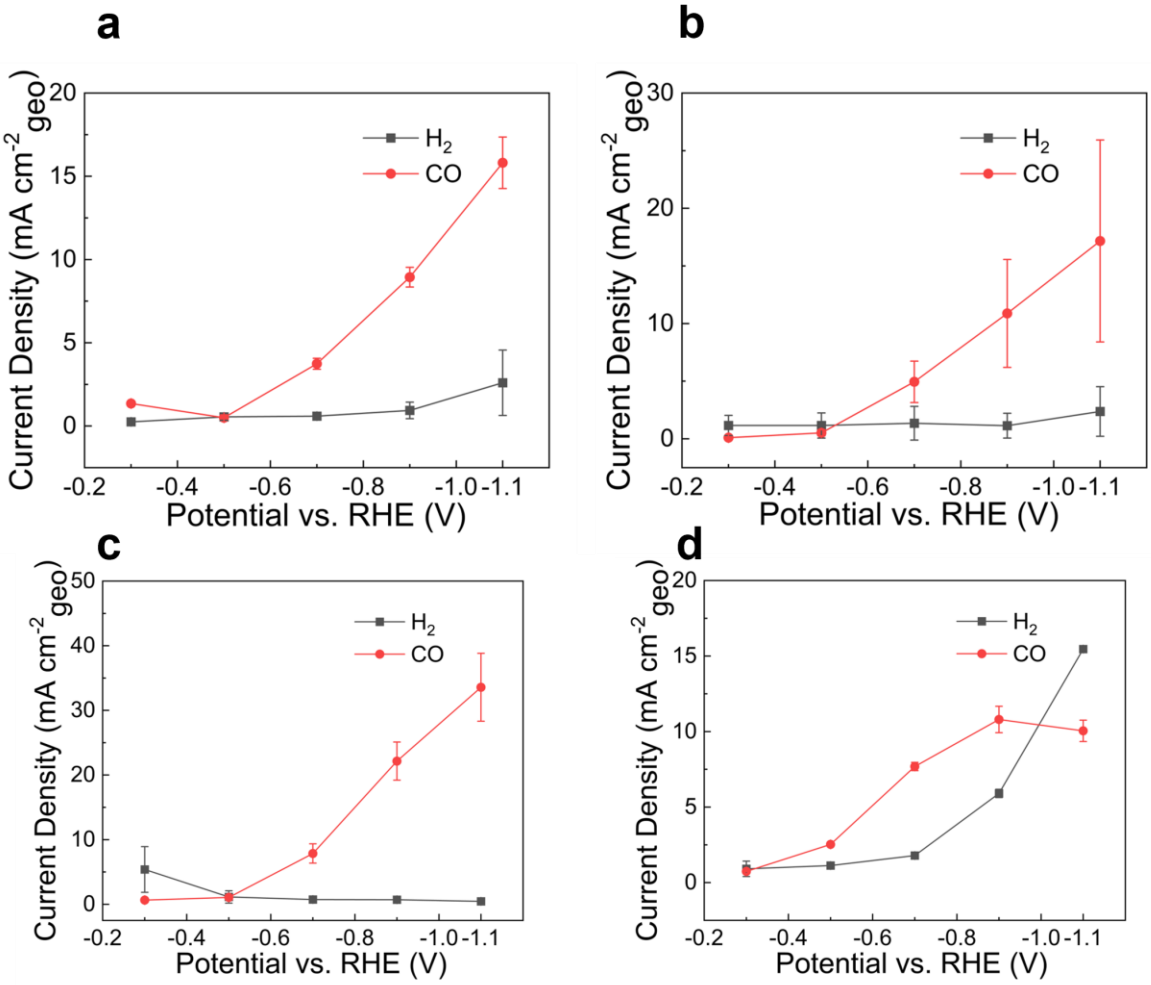

Figure 4.2. 6: Figure 6: Magnitude of partial current density for CO/H2 for Ni-N-C (900/-) (a), Ni-N-C (*) (b), Ni-N-C (**)(c), metal-free N-C (d).

In addition to the role of the metal subtituent on CO_2R performance, it was also desired to examine how factors such as the number of pyrolytic steps and the porosity influence CO_2R activity/selectivity. If the number of synthesis steps may be reduced with minimal effect on the CO_2R

performance, then the industrial viability of the process is immediately improved. Figure 6a shows the product distribution using a single pyrolytic step for Ni-N-C (900/-). The catalyst is still highly active for CO_2R as opposed to the HER across the whole potential range analyzed. Ni-N-C (900/-) reaches a j_{co} of *ca.* -16 mA cm^{-2} compared to a j_{co} of *ca.* -40 mA cm^{-2} for Ni-N-C (900/950). The selectivity after a single pyrolysis is very comparable to the final catalyst after two pyrolytic steps (e.g., at -1.1 V vs. RHE, FE_{co} = 86.1 +/- 10.4 % for Ni-N-C (900/-) and FE_{co} = 99.1 +/- 0.2 % for Ni-N-C (900/950)) (Figure S13). As well as the number of pyrolytic steps, the porosity of carbon-based catalysts is known to have a substantial impact on the electrocatalytic performance. These effects have been widely studied for the oxygen reduction reaction (ORR) on M-N-C catalysts such as by Liang et al who found increased reactant transport and ORR performance for macroporous vs. mesoporous material. [215] Introducing microporosity as well as meso- and macroporosity can offer the benefits of increased reactant transport in the macropores and increased surface area and active site utilization due to a higher microporosity and overall electrochemically active surface area (ECSA). [216, 217] However in reactions where a condensable product is produced (e.g., in oxygen reduction to water in ORR), excess microporosity can cause pores to be blocked by liquid formed at the active site which can drastically limit active site utilization.

Although the products of CO_2R are often gas-phase products, flooding may still occur due to condensate from humidified CO_2 or electrolyte flooding through the microporous layer (MPL). [57, 218] Hence, porosity is a key factor to vary in tailoring an electrocatalyst for a specific application. The porosity of metal-free nitrogen-doped carbons was previously investigated and found to be a controlling factor for influencing the CO_2R. Hursán et al studied four different N-C materials which differed only in pore size from nonporous N-C to NC-13, NC-27, and NC-90 (where the number represents the mean diameter (nm) of silica colloid precursor) and found that NC-27 offered the optimal pore size for CO_2R. [53] In an analogous study, we selected three different silica mixtures to impart different pore size distributions in the final catalysts (Ni-N-C, Ni-N-C (*), and Ni-N-C (**)). The composition of the silica mixtures can be found in supplementary information (Table S2). The performance of Ni-N-C is considerably improved compared to Ni-N-C (*) as a higher activity and selectivity for CO_2R is observed for Ni-N-C. By contrast, Ni-N-C (**) shows a performance very similar to Ni-N-C in terms of overall current density and faradaic efficiency for CO formation. The performance of Ni-N-C is enhanced compared to Ni-N-C (*) due to differences in the pore size distribution and surface area. The pore size is shifted towards micropores for Ni-N-C which enhances the overall ECSA and increases the active site exposure which results in a much higher CO_2R activity. By contrast the performance of Ni-N-C (**) is not affected so the combination of Aerosil OX 50 and Stöber spheres (D_{avg} = 320 nm) seems to provide for the optimum pore size distribution for CO_2R.

In addition to factors intrinsic to the catalyst morphology which may influence reactivity, the catalyst layer morphology on the gas diffusion electrode itself is also a critical parameter to control. It is also vital to establish that the reaction products (e.g., H_2 and CO) are emanating from the cathodic reaction. Since the counter electrode (anode) in this configuration is carbon-based, it may undergo a corrosion reaction given a sufficiently positive polarization which may give rise to the CO signal. In order to test this, several control experiments were performed to assess the influence of the electrolyte

type/concentration and inlet feed composition (Figure 7e).

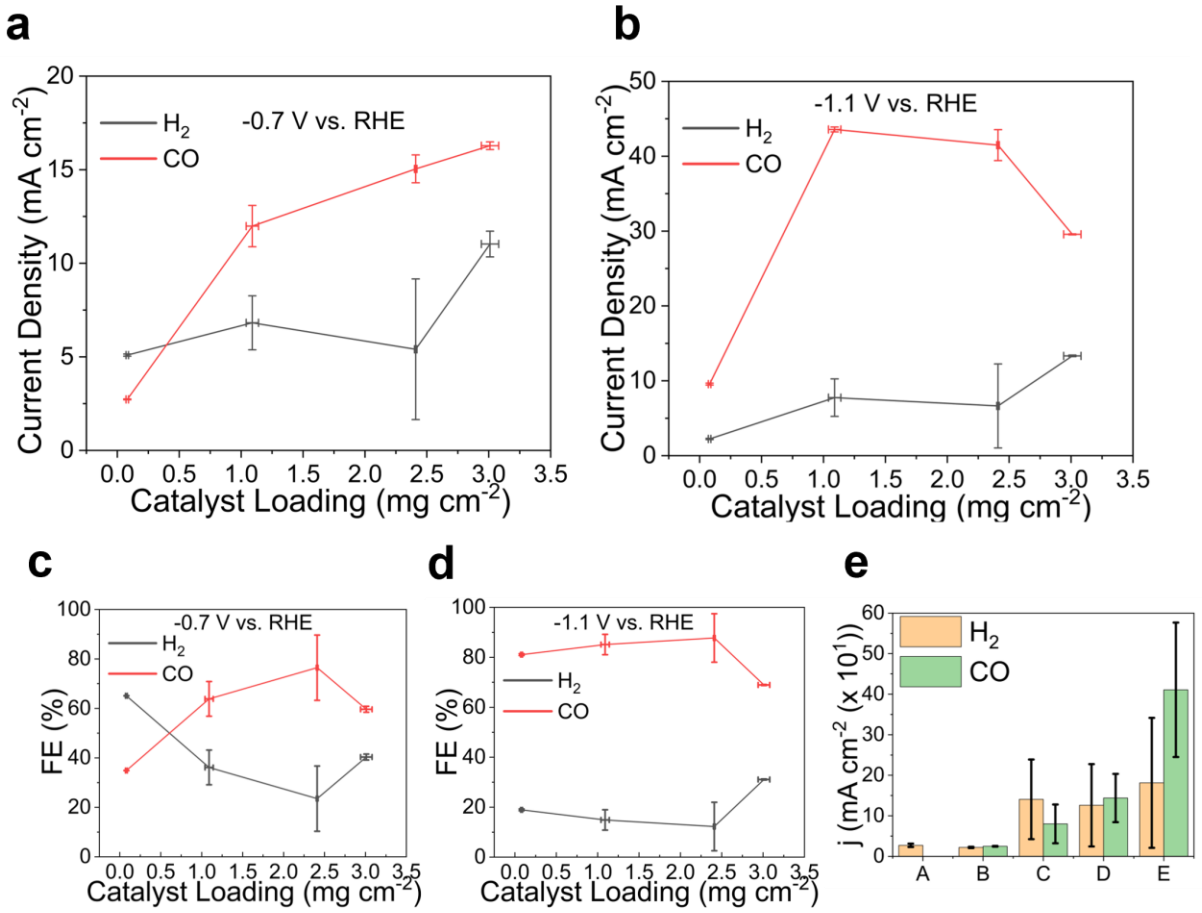

Figure 4.2. 7: Figure 7: H2 and CO partial current densities for Ni-N-C from 0.1 mg/cm2 to 3.0 mg/cm2 at (a) -0.7 V and (b) -1.1 V vs. RHE. The faradaic efficiency at (c) -0.7 V and (d) -1.1 V vs. RHE, for H2 and CO formation for Ni-N-C. Electrolyte/inlet feed controls (e) for Ni-N-C (*) at -0.7 V vs. RHE (A = 0.1 M PBS/N2, B = 0.176 M KHCO3/N2, C = 0.1 M KHCO3/CO2, D = 0.176 M KHCO3/CO2, E = 0.5 M KHCO3/CO2).

Control A shows that given a pure N_2 inlet and a non-carbon based electrolyte (phosphate buffer solution (PBS)), no CO is detected and only small amounts of H_2 is produced on Ni-N-C (*). Introducing potassium bicarbonate electrolyte and N_2 feed allows the production of a small amount of CO owing to CO_2 supplied by the electrolyte. The choice of concentration of the bicarbonate electrolyte was made to ensure the same electrolyte conductivity as the PBS electrolyte. Potassium bicarbonate is widely used for CO_2 reduction studies as it is an efficient pH buffer as well as acting as a reservoir of CO_2 so it may constantly be replenished to the active site. Some groups have taken advantage of this to avoid the need to produce a purified CO_2 stream, and instead to use highly concentrated bicarbonate electrolyte as the reactant for formate production. [64, 65] Finally, the selectivity for CO_2R vs. HER was studied as a function of the concentration of bicarbonate electrolyte. Increasing the bicarbonate electrolyte concentration results in an increase in the electrolyte buffering capacity as well as a decrease in the

ohmic resistance (i.e., decreased resistance for ionic transport away from the active site). As a result, the overall current density for both HER and CO_2R increases due to the enhanced ionic transport. In addition, the selectivity slowly increases towards favoring CO_2R over HER as the bicarbonate concentration increases. This is also seen by Li et al in their investigation of using bicarbonate feed for formate production (e.g., FE_{HCOO^-} *ca.* 45 % increases to *ca.* 60 % when [$KHCO_3$] increases from 1 M to 3 M). [64] In our case, it may be due to a pH effect from increased buffering capacity since for Ni-N-C, the rds is suggested to be the formation of *COOH and hence shows a pH-dependent activity. [195] In addition to reaction parameters such as electrolyte type/concentration and inlet feed composition, the cathodic loading is also important especially when considering industrial applications.

Because the catalyst loading largely dictates the resulting morphology, a catalyst loading study was performed to see the change in activity/selectivity for CO_2R. The modest current density shown here (j_{co} = *ca.* 40-45 mA) is substantially higher than the current densities obtained using commercial Ag nanoparticles and suggests the catalysts here are prime candidates for incorporating in a flow cell/electrolyzer configuration (e.g., a MEA-based electrolyzer) capable of producing higher current densities (2. S *14*: Figure S14: Comparison of geometric partial current densities with flow cell for Ag-based and Fe-N-C-based cathodes at 1.0 mg cm_{geo}^{-2} catalyst loading in 100 % CO_2 feed and 0.5 M $KHCO_3$ electrolyte.). The catalyst loading on the cathode and the ink composition (e.g., the ionomer to carbon ratio) are all vital components to optimize in improving the CO_2R performance. [219] The affect the loading may have on the catalyst layer (CL) is based on a change in either the morphology of the CL or changes in its wetting properties. As the loading increases, the CL thickness increases which can limit the ability for CO_2 to diffuse to the active site at very high loadings. Additionally, it will alter the potential drop across that layer and the resulting selectivity. The method of deposition of the CL (*e.g.*, automated spray coating, or drop casting), and the evaporation rate of the catalyst ink will also cause morphological changes in the CL. [66]

The catalyst loading was studied between 0.1 mg/cm^2 to 3.0 mg/cm^2 to observe differences in the resulting CO_2R vs. HER selectivity. At a low loading of 0.08 +/- 0.01 mg/cm^2, Ni-N-C shows a FE_{co} of *ca.* 34.9 +/- 0.06 % at -0.7 V vs. RHE which increases to 81.1 +/- 0.35 % at -1.1 V. It should also be noted the rate of HER is slightly increased in Figure 7 due to catalyst ageing of *ca.* 6 months which most likely led to nanoparticle agglomeration. Despite this, there is still considerable selectivity for CO_2R at low catalyst loading especially when you compare it to the original catalyst selectivity (e.g., FE_{co} = 99 % at -1.1 V vs. RHE at 1.0 mg/cm^2 which after 6 months of catalyst ageing decreases to *ca* 88 % FE_{co}). At -0.7 V vs. RHE, there is a steep increase in FE_{co} when the loading is increased from 0.08 mg/cm^2 to 1.09 +/- 0.05 mg/cm^2 followed by a more gradual increase in FE_{co} when the catalyst loading is increased to 2.41 +/- 0.01 mg/cm^2. This is followed by a decrease in FE_{co} from 76.5 +/- 13.2 % to 59.7 +/- 1.2 % FE_{co} at a loading of 3.01 +/- 0.07 mg/cm^2. Interestingly, at -1.1 V vs. RHE, the CO_2R selectivity is the same across the catalyst loading range studied from 0.08 to 2.41 mg/cm^2 but there is a steep drop in both the CO partial current density (j_{co}) and FE_{co} when the loading is increased further.

The trend in the partial current density follows a similar trend with some key differences. At -0.7 V, increasing the loading to 3.01 mg/cm^2 causes an increase in j_{co} along with a greater increase in j_{H2}. At -1.1 V, we see the steepest increase in j_{co} when the loading is increased from 0.08 to 1.09 mg/cm^2 (e.g.,

from 10 +/- 0.1 to 44 +/- 0.3 mA cm^{-2}). This may be explained by an increase in the number of active sites and triple phase boundaries which may catalyze the CO_2R. The CO partial current density then reaches a plateau and drops off as the loading is increased from 2.41 to 3.01 mg/cm^2. Similarly, Wu et al found the optimum CL thickness was *ca.* 9.2 μm for Sn-based GDEs, beyond which reactants experienced increased diffusion resistance. [220] This suggests the optimum loading for this arrangement is *ca.* 1.09 mg/cm^2 for achieving both high CO_2R activity and selectivity. The dropoff in current density at high loading may be attributed to an increase in the CL thickness to a point where the rate of CO_2 diffusion is hindered.

Conclusion

In summary, a novel synthesis method was developed for the acid-free synthesis of M-N-C catalysts with a high degree of graphitization, atomic dispersion, and catalytically active M-N_x moieties. The synthesis method provides a promising new route to M-N-C catalysts which may find application in many electrochemical reactions such as ORR, OER, NRR, and NO_3RR. The pore size distribution showed a large degree of microporosity optimized for CO_2 reduction compared to the catalysts presenting less microporosity and correspondingly lower CO_2RR activity. The M-N-C catalysts were examined for their metal-atom dependent selectivity for CO_2RR vs. HER for M-N-C (M = Fe, Ni, Mn, Co) vs. metal-free N-C. The metal-atom dependent selectivity for CO_2R proceeded according to Ni-N-C > Fe-N-C > Mn-N-C ≅ N-C > Co-N-C consistent with the observed metal-atom dependent selectivity of previous M-N-C catalysts. [7, 45] The metal-free N-C catalyst showed a comparable activity/selectivity at a potential of -0.7 V vs. RHE. The Ni-N-C (900/950) and Ni-N-C (900/-) both show a considerable activity for CO_2R reaching a FE_{co} of *ca.* 99.1 +/- 0.2 % and *ca.* 86.1 +/- 10.4 % at -1.1 V vs. RHE, respectively. This is encouranging from an industrial application point of view to reduce the number of pyrolysis steps. The structural and morphological evolution of the catalysts was shown as well as a potential mechanism for CO_2 reduction on the new catalysts. The structural and chemical level evolution of the catalysts before and after pyrolysis was compared to M-N-C catalysts made by the traditional sacrificial support method (SSM) which is a thoroughly researched topic. [17, 145, 190] The novel M-N-C catalysts show a large degree of CO_2R vs. HER activity at both low and high overpotential.

Methods

Synthesis of M-N-C and N-C Electrocatalysts

The series of Ni, Fe, Mn, Co, and metal-free M-N-C catalysts were synthesized according to a novel method. In a given synthesis (e.g., for Fe-N-C), 6.25 g nicarbazin, 0.6 g iron nitrate nonahydrate, and 3 g silica (composed of 1.25 g LM-150 fumed silica, 1.25 g OX-50, and 0.5 g Stober spheres with average diameter of 320 nm prepared by Stober's Method[221] which involves base-catalyzed hydrolysis of tetraethyl orthosilicate (TEOS) in a water-ethanol mixture) are dispersed in deionized water, sonicated for 30 minutes or until homogeneous, and then dried at 45 ℃ overnight.

The metal nitrate precursor is chosen to ensure the total number of metal atoms in each catalyst is the same regardless of the metallic substituent according to table S2. The resulting powder is ball-milled at 10 Hz for 1 hour using a mixture of Agate balls and a calculated mass (m_t(mg)) of Teflon

(Poly(tetrafluoroethylene), powder (free-flowing), 1 μm particle size) based on the wt.% Silica in the powder above according to the following equation:

$$m_t(mg) = \frac{\left(mass\ of\ powder\ in\ step\ 1(mg)\right) * \frac{wt.\%\ SiO_2}{100}}{\frac{0.09\ mg\ silica}{mg\ Teflon}}$$

The powder is loaded into a weigh boat and subjected to a pyrolysis under 100 % N_2 atmosphere heating from room temperature to 900 ℃ with a ramp rate of 5 ℃/min, and a 180 min hold at 900 ℃. The powder is ball-milled again with Agate balls at 10 Hz for 1 hour. The resulting powder is placed back into a weigh boat and subjected to the 2nd pyrolysis under a reductive atmosphere of 10 % NH_3/ 90 % N_2, with a 10 ℃/min ramp rate, and a 30 min hold at 950 ℃ to obtain the final powder.

Physical Characterization

The structure and atomically dispersed sites of the catalyst was analyzed by aberration-corrected scanning transmission electron microscopy (AC-STEM) using a JOEL ARM-200F at an accelerating voltage of 200 kV. The elemental mapping of the catalyst was obtained by energy dispersive X-ray spectroscopy (EDS) on a FEI Talos F200X at an accelerating voltage of 200 kV, equipped with superX 4 SSD EDX detectors. The surface morphology and porosity of the catalysts was visualized by scanning electron microscopy using a FEI Magellan 400 XHR SEM. The surface chemical structure, valence state and composition was analyzed using X-ray photoelectron spectroscopy (XPS) performed on a Kratos AXIS Supra spectrometer with a monochromatic Al Kα source. A Rigaku Powder X-ray diffractometer was used to obtain X-Ray Diffraction (XRD) data for the electrocatalysts. Inductively coupled plasma mass spectrometry (ICP-MS) was used to quantify the metallic content of the catalysts and is plotted in Figure S2. N_2 physisorption was performed on a Micromeritics 3Flex Analyzer at 77K for BET and pore size distribution data. Pore size distributions were estimated by a Barret, Joyner, and Halenda (BJH) adsorption model from experimental isotherms using the Kelvin model of pore filling. Advancing and receding contact angles were measured in polar (ethylene glycol) and dispersive (diiodomethane) solvent and the contact angle hysteresis was used to calculate the surface free energy. [53] Raman spectra were collected by a InVia, Renishaw Corp., UK system.

Preparation of the working electrode

A GDE was fabricated by hot pressing a Sterlitech PTFE membrane filter (0.1 μm) to a Freudenberg H23C6 gas diffusion layer (GDL). For a 1.0 mg/cm^2 loading, the catalyst ink was made by sonicating 900 μL IPA, 100 μL DI water, 10 mg catalyst powder, and 60 μL 5 wt. % nafion ionmor solution (in lower aliphatic alcohols). The ink was spray-coated onto the GDE and the loading was obtained from the change in mass after spraying. Unsupported Ag nanoparticles (particle size < 100 nm) were

purchased from Sigma-Aldrich which have a 99.5 % (trace metal basis) purity and were used for comparison.

Electrochemical CO_2 reduction

The electrocatalytic activity was evaluated using a custom-built gas diffusion electrode flow cell in a three-electrode configuration (2. S *12*: Figure S12: Flow Cell Diagram.). Connection to the counter/working electrode was made via alligator clips attached to conductive Cu tape. The interelectrode distance was 0.6 cm and was separated by a liquid electrolyte which was recirculated using an analog variable speed pump (Core Palmer Masterflex, Model No: SK-07555-00). The liquid electrolyte flow rate was measured to be 26.1 +/- 1.1 mL min^{-1}. The CO_2 was Research grade 4.8 purchased from Praxair (99.998%) with < 0.1 ppm CO and < 2 ppm THC (as CH_4). Pure CO_2 was fed to the gas chamber by an Alicat 0-50 sccm mass flow controller (MFC). A 5-channel EC-Lab VSP-300 potentiostat was used for LSV/CA data. The reference electrode was a Gaskatel™ reversible hydrogen electrode (RHE) and the electrolyte was either potassium bicarbonate or phospate buffer solution (PBS) electrolyte The electronic conductivity was measured by a Surpass 3.0 conductivity probe to standardize between PBS/$KHCO_3$ measurements. The faradaic efficiency for the product(s) detected was calculated based on the charge transferred to obtain the product (CO, H_2, or CH_4) over the total charge transferred to obtain all products.

$$FE_i = \frac{N_i n_i F}{\sum N_i n_i F}$$

Where, N_i represents the number of moles of product detected by either GC or ^{1}H NMR, n_i represents the number of moles of e^- transferred per mole of product produced (*e.g.*, 2 for CO and H_2), and F is Faraday's contant (F = 96485 C mol^{-1} of electrons).

Product detection

The gaseous products generated during CO_2 reduction electrolysis were sampled by PTFE/rubber septa thermo fischer gas vials and injected into a dual-column gas chromatograph to detect CO/H_2 along with any possible CH_4/hydrocarbons. An Agilent 7890B Gas Chromatography unit was used with parallel columns. Each gas sampling vial was purged with the flow cell effluent by means of an exit needle inserted into the vial to allow the composition of the gas vial to equilibrate with the gas chamber composition for 30 minutes. An Agilent HP-MOLESIEVE column connected to a thermal conductivity detector (TCD) using Helium carrier gas was used to quantify CO while the carrier gas was N_2 using the same HP-MOLESIEVE column and TCD detector for H_2 detection. A GS-CarbonPlot column connected to a flame ionization detector was used to screen for CH_4 or other hydrocarbons. ^{1}H NMR was performed to confirm the absence of any liquid products.

Supporting Information

Fe-N-C

No.	2theta(deg)	FWHM (deg)	d-spacing (nm)
1	26.1	5.739	0.348
2	44.1	2.387	0.207
3	44.7	2.16	0.196
4	50.8	0.39	0.179

Ni-N-C

No.	2theta(deg)	FWHM (deg)	d-spacing (nm)
1	26.0	4.647	0.349
2	44.1	2.547	0.206
3	44.5	0.329	0.204
4	51.8	0.411	0.176
5	76.4	0.518	0.125

Mn-N-C

No.	2theta(deg)	FWHM (deg)	d-spacing (nm)
1	26.1	2.313	0.345
2	44.1	2.669	0.207

3	44.2	0.302	0.205
4	51.4	0.432	0.177
5	75.8	0.410	0.125

Co-N-C

No.	2theta(deg)	FWHM (deg)	d-spacing (nm)
1	26.0	4.154	0.349
2	35.0	0.258	0.256
3	36.3	0.227	0.247
4	40.6	0.272	0.222
5	44.0	3.637	0.208
6	58.7	0.437	0.157

Table 21: Table S1: XRD peak assignment for M-N-C (M = Fe, Ni, Mn, Co) samples where Fe-N-C shows peaks at 44.7, and 50.8 for (111), (200), respectively, for both iron and iron nitride phases; Ni-N-C shows peaks at (44.5, 51.8, 76.4) for (111), (200), (220) peaks respectively, for nickel and nickel carbide; Mn-N-C shows manganese carbide peaks at 44.2, 51.4, 75.8 deg for (511), (600), (660), respectively; and Co-N-C shows auxiliary peaks for Cobalt carbide, cobalt nitride, cobalt oxide and cobalt nanoparticles.

Metallic Substituent	Metallic Precursor	Mass of Catalyst	# Metal Atoms * 10^{20}
Fe	Iron (III) nitrate nonahydrate	0.600	8.944
Ni	Nickel (II) nitrate hexahydrate	0.432	8.944
Mn	Manganese (II) nitrate hexahydrate	0.426	8.944
Co	Cobalt (II) nitrate hexahydrate	0.432	8.944

Sample	Nicarbazin (g)	Stöber Sphere (D_{avg} = 320 nm) (g)	Aerosil OX 50 (g)	Aerosil 90 (g)	Cab-0-Sil LM-150 (g)	Aerosil 200 (g)
M-N-C (M = Fe, Ni, Mn, Co)	6.25	0.5	1.25	--	1.25	--
Ni-N-C (*)	6.25	0.5	--	0.9375	1.25	0.3125
Ni-N-C (**)	6.25	0.5	2.5	--	--	--

Table 22: Table S2: Precursor composition for the M-N-C catalysts.

Sample	Fe-N-C	Ni-N-C	Mn-N-C	Co-N-C	FeNCpyr1	NiNCpyr1
O	2.73+/-0.42	2.23+/-0.10	4.22+/-0.70	6.76+/-0.49	6.02+/-0.87	5.57+/-0.42
C	93.87+/-0.32	95.48+/-0.12	93.91+/-0.78	90.03+/-0.35	90.25+/-0.40	91.38+/-0.10
N	3.19+/-0.11	2.26+/-0.07	1.86+/-0.16	2.98+/-0.20	3.32+/-0.45	2.64+/-0.40
Si	0.20+/-0.03	--	--	--	--	--
F	--	--	--	0.22+/-0.05	0.42+/-0.06	0.38+/-0.01
Me	0.03+/-0.02	0.03+/-0.00	--	--	--	0.03+/-0.01

Table 23: Table S3: Surface elemental composition as detected by XPS in % atomic concentration.

Sample	Fe-N-C	Ni-N-C	Mn-N-C	Co-N-C	FeNCpyr1	NiNCpyr1
1	29.18+/-1.29	19.39+/-0.94	14.68+/-0.49	23.77+/-2.06	24.01+/-1.12	17.12+/-2.03
2	13.14+/-1.14	8.83+/-0.47	9.38+/-0.66	16.25+/-0.86	17.23+/-0.91	17.07+/-0.9
3	26.50+/-0.92	40.32+/-1.67	45.12+/-0.47	35.64+/-3.89	39.55+/-1.88	40.51+/-1.91
4	14.63+/-1.17	18.62+/-0.97	16.90+/-0.38	12.38+/-0.46	9.37+/-0.55	12.31+/-0.57
5	8.03+/-0.19	8.03+/-0.86	8.41+/-1.25	7.12+/-1.02	6.93+/-1.94	6.37+/-0.99

6	4.24+/-1.00	3.72+/-0.50	3.86+/-0.16	3.19+/-0.48	2.25+/-0.11	3.48+/-0.54
7	4.28+/-1.45	1.08+/-1.07	1.66+/-0.03	1.65+/-1.65	0.67+/-1.22	3.14+/-1.9

Table 24: Table S4: Nitrogen component fitting for M-N-C samples. % Atomic concentration of N 1s signal for 1: pyridinic N (398.2 eV), 2: N-Mex (399.5 eV), 3: pyrrolic N (400.8 eV), 4: graphitic N/ protonated N (401.6 eV), 5: bulk N-H (402.8 eV), 6, 7: NOx species (404.1 eV and 405.6 eV).

Sample	Fe-N-C	Ni-N-C	Mn-N-C	Co-N-C	FeNCpyr1	NiNCpyr1
1	61.51+/-2.14	61.70+/-1.32	40.00+/-1.98	46.94+/-6.59	48.49+/-6.2	58.19+/-2.01
2	5.74+/-1.04	8.36+/-1.61	26.17+/-1.63	21.62+/-5.29	20.1+/-1.33	13.07+/-2.84
3	10.26+/-1.24	8.88+/-0.35	15.08+/-0.49	13.21+/-1.64	12.19+/-0.58	9.66+/-1.73
4	5.28+/-0.31	3.79+/-0.40	5.09+/-0.42	4.65+/-0.45	4.57+/-0.39	3.51+/-0.49
5	4.67+/-0.32	4.88+/-0.15	3.33+/-0.58	4.26+/-0.36	4.68+/-0.33	4.77+/-0.17
6	6.25+/-0.21	6.08+/-0.14	6.93+/-0.17	6.32+/-0.20	6.32+/-0.21	6.13+/-0.29
7	4.01+/-0.21	4.06+/-0.10	2.28+/-0.05	2.14+/-0.35	2.35+/-0.06	2.81+/-0.38
8	2.27+/-0.16	2.25+/-0.07	1.15+/-0.10	0.88+/-0.28	1.31+/-0.2	1.86+/-0.08

Table 25: Table S5: Carbon component fitting. % Atomic concentration of C 1s signal for 1: sp2 carbon (284.6 eV), 2: sp3 carbon (285.1 eV), 3: C-N (286.0 eV), 4: C-O (287.1 eV), 5: C=O (288.3 eV), 6: COOH (289.7 eV), 7,8: π- π* shake up (291.3 eV, and 292.9 eV).

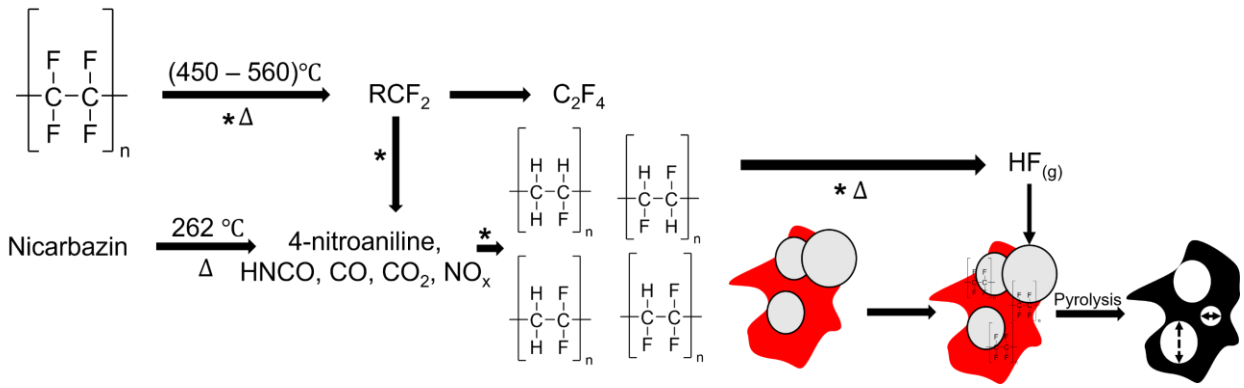

Figure 4.2. S 1: Figure S1: Proposed mechanism for in situ silica removal (* route) during pyrolysis for one-pot M-N-C synthesis.

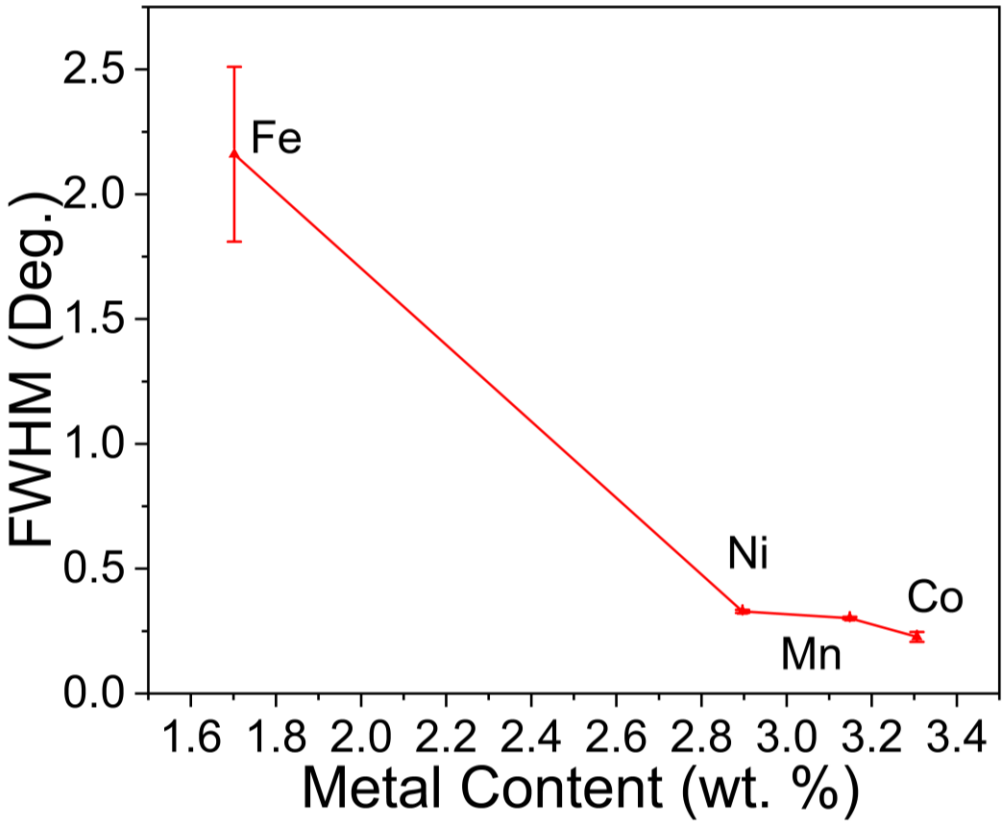

Figure 4.2. S 2: Figure S2: The FWHM (deg.) of representative metallic XRD peak shown in Fig 1b plotted vs. the total metallic content in weight percentage as measured by inductively coupled plasma mass spectrometry (ICP-MS).

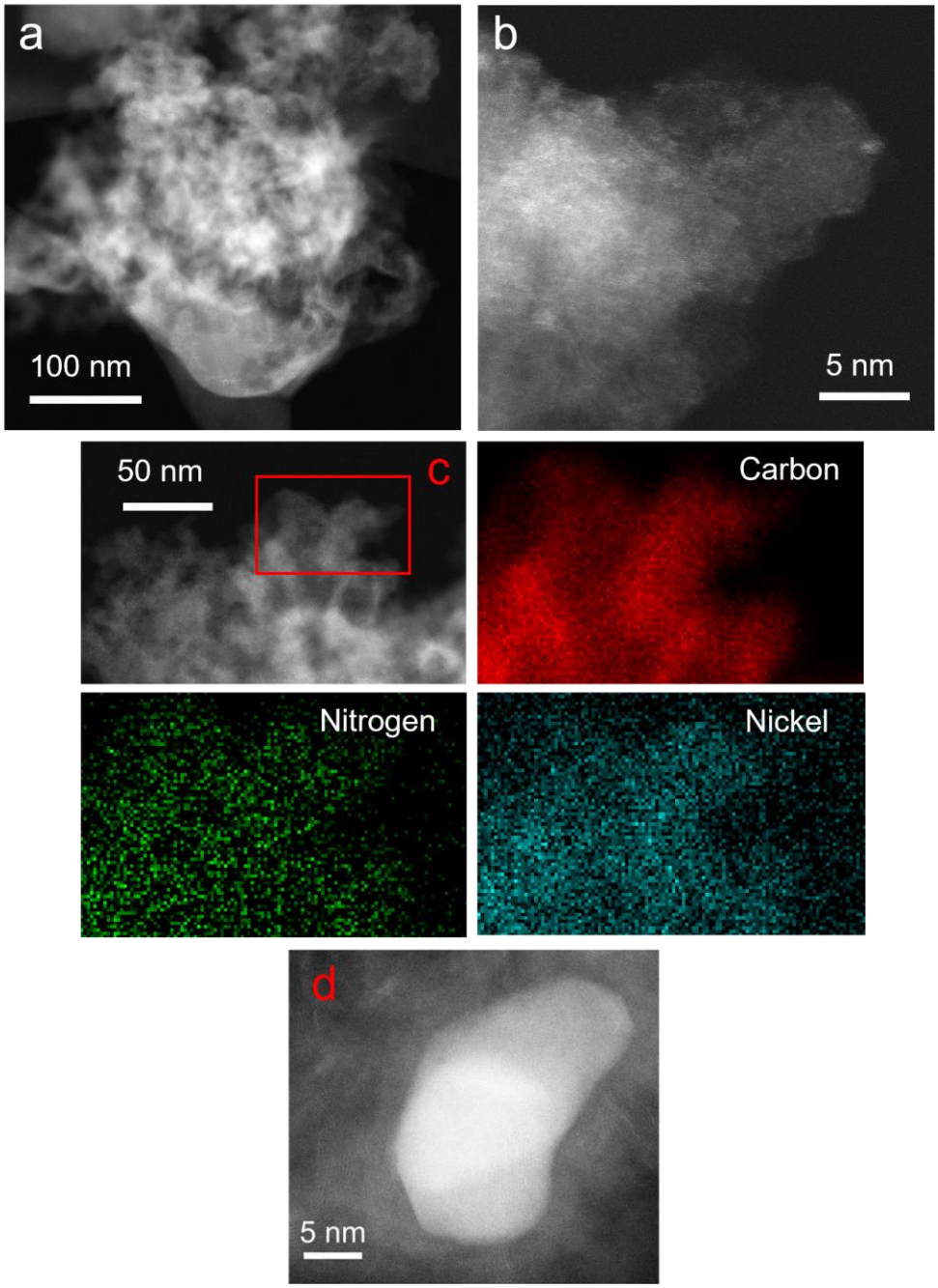

Figure 4.2. S 3: Figure S3: (A, B, and C) HRTEM and EDS spectra (red inset) for Ni-N-C. (D). HRTEM image of Fe-N-C nanoparticle.

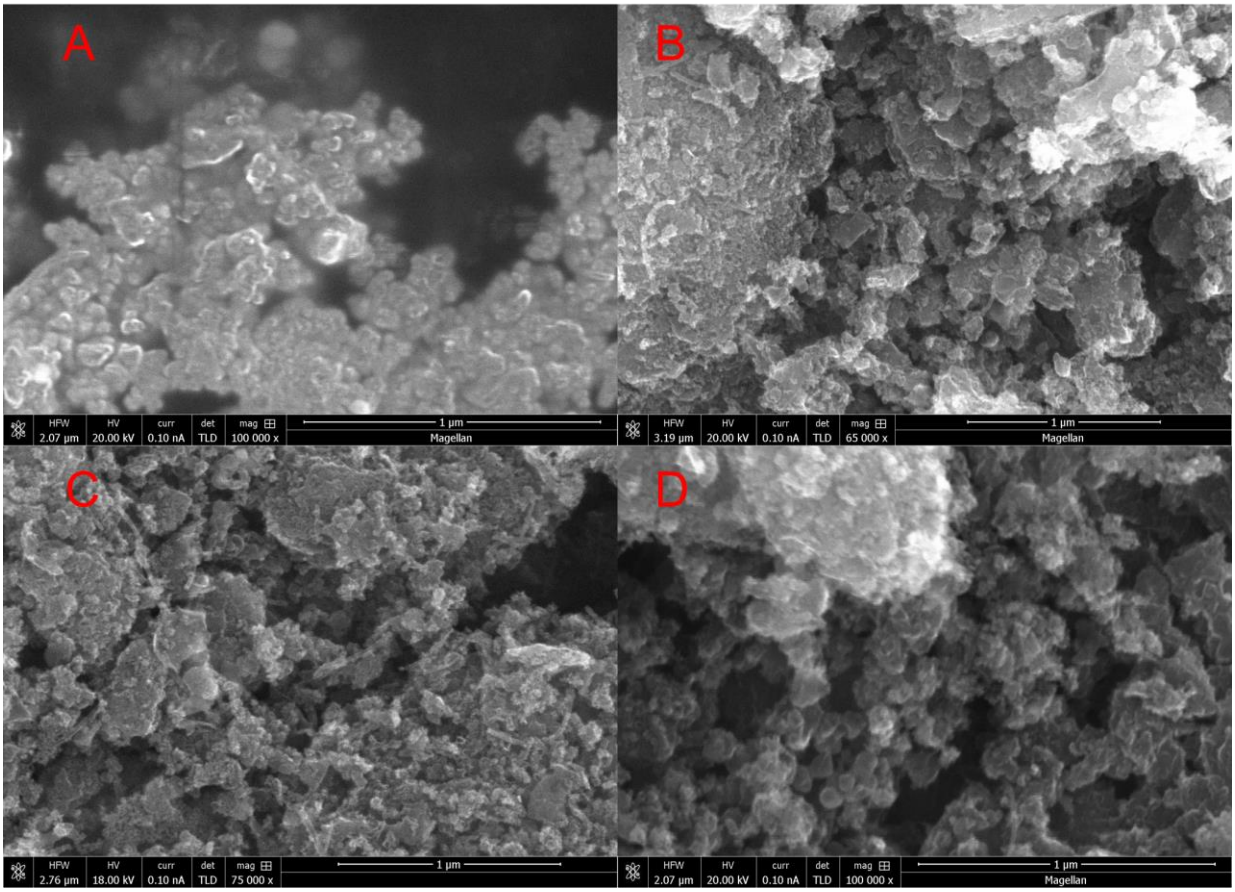

Figure 4.2. S 4: Figure S4: SEM of Ni-N-C (A), Fe-N-C (B), Mn-N-C (C), Co-N-C (D).

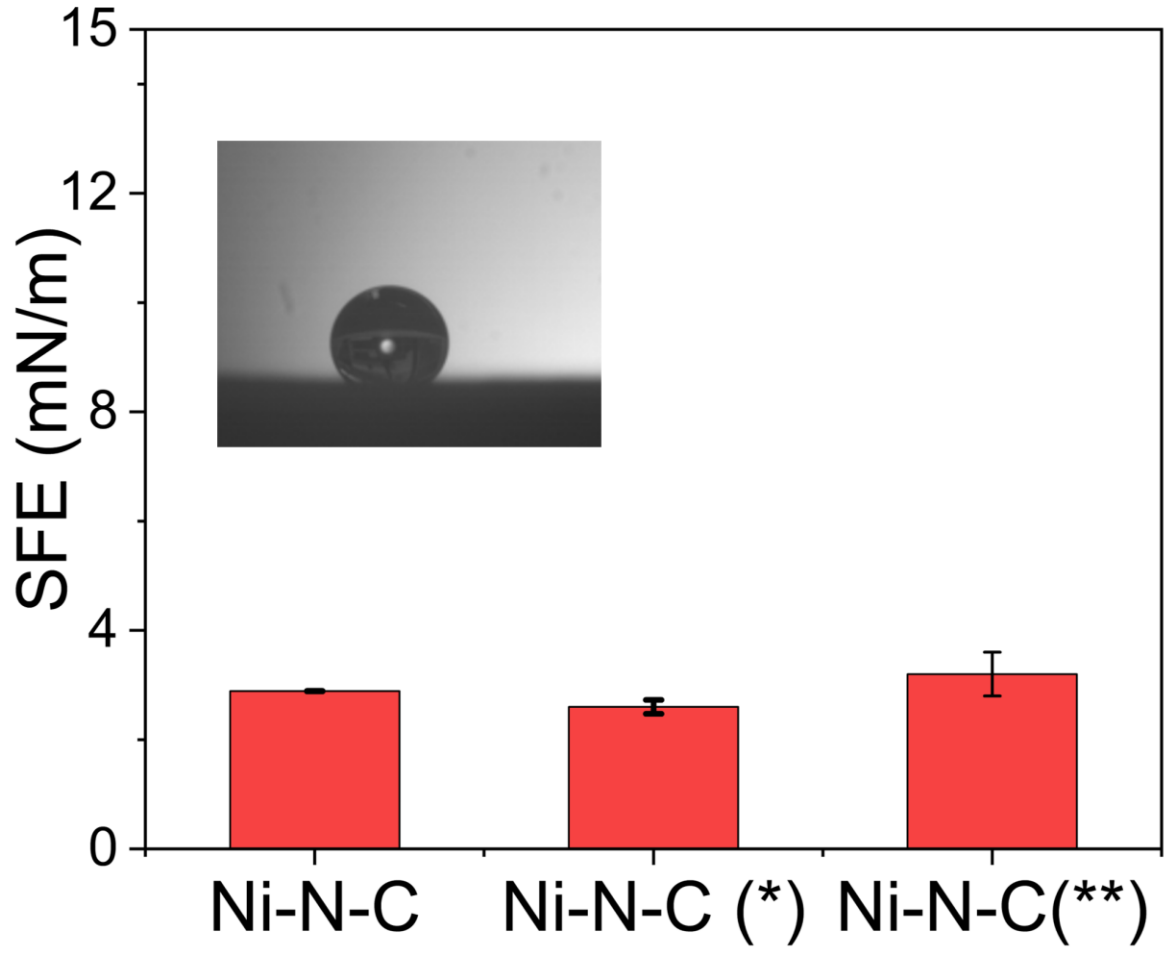

Figure 4.2. S 5: Figure S5: Surface free energy of Ni-N-C catalysts using three different pore-forming silica mixtures shown in Table S2.

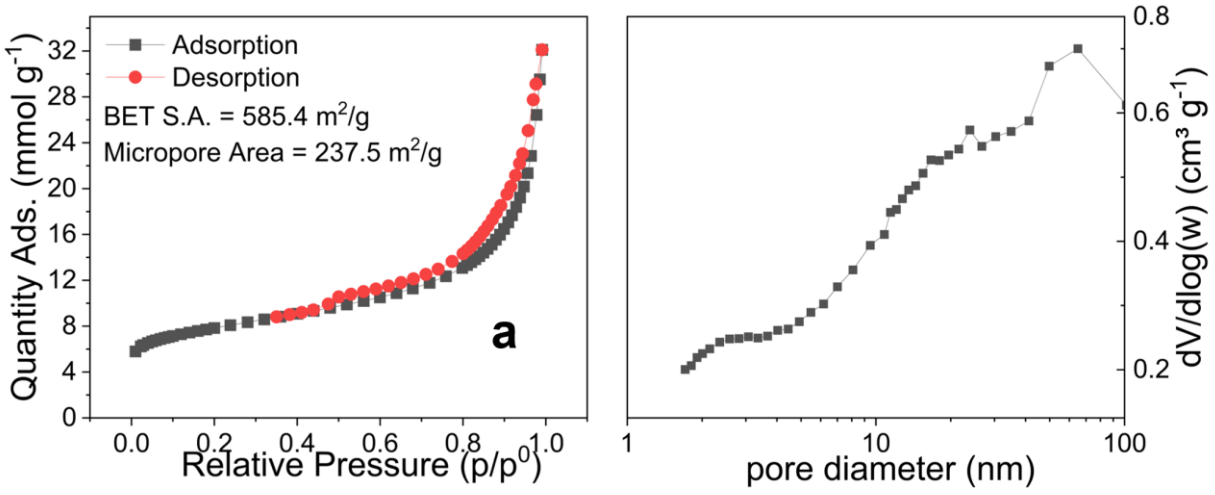

Figure 4.2. S 6: Figure S6: BET Adsorption isotherm and BJH pore size distribution for Ni-N-C(**).

Element	Atomic Fraction (%)	Mass Fraction (%)	Fit Error (%)
C	91.49	88.75	0.48
N	3.25	3.68	0.02
O	4.54	5.87	0.15
Na	0.10	0.19	0.24
Si	0.56	1.26	0.08
Fe	0.06	0.25	0.37

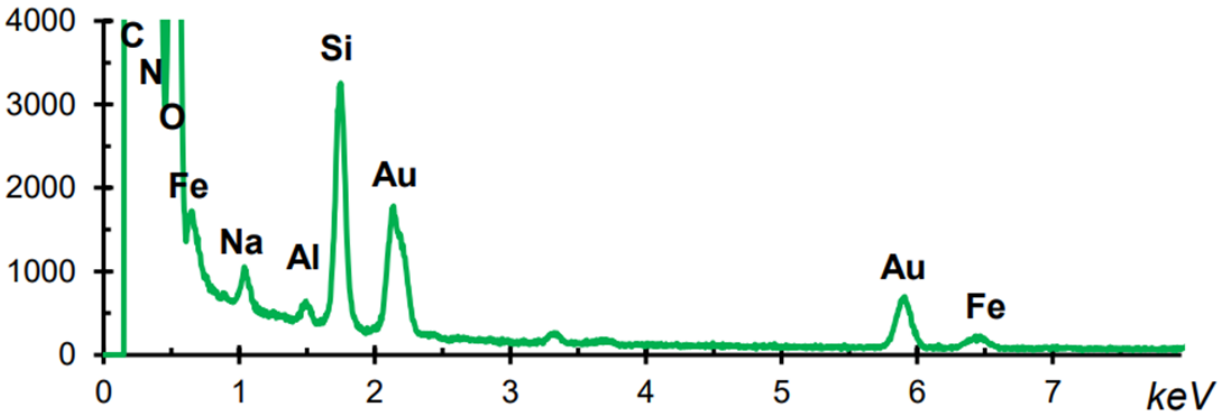

Figure 4.2. S 7: Figure S7: EDS Quantification for Fe-N-C.

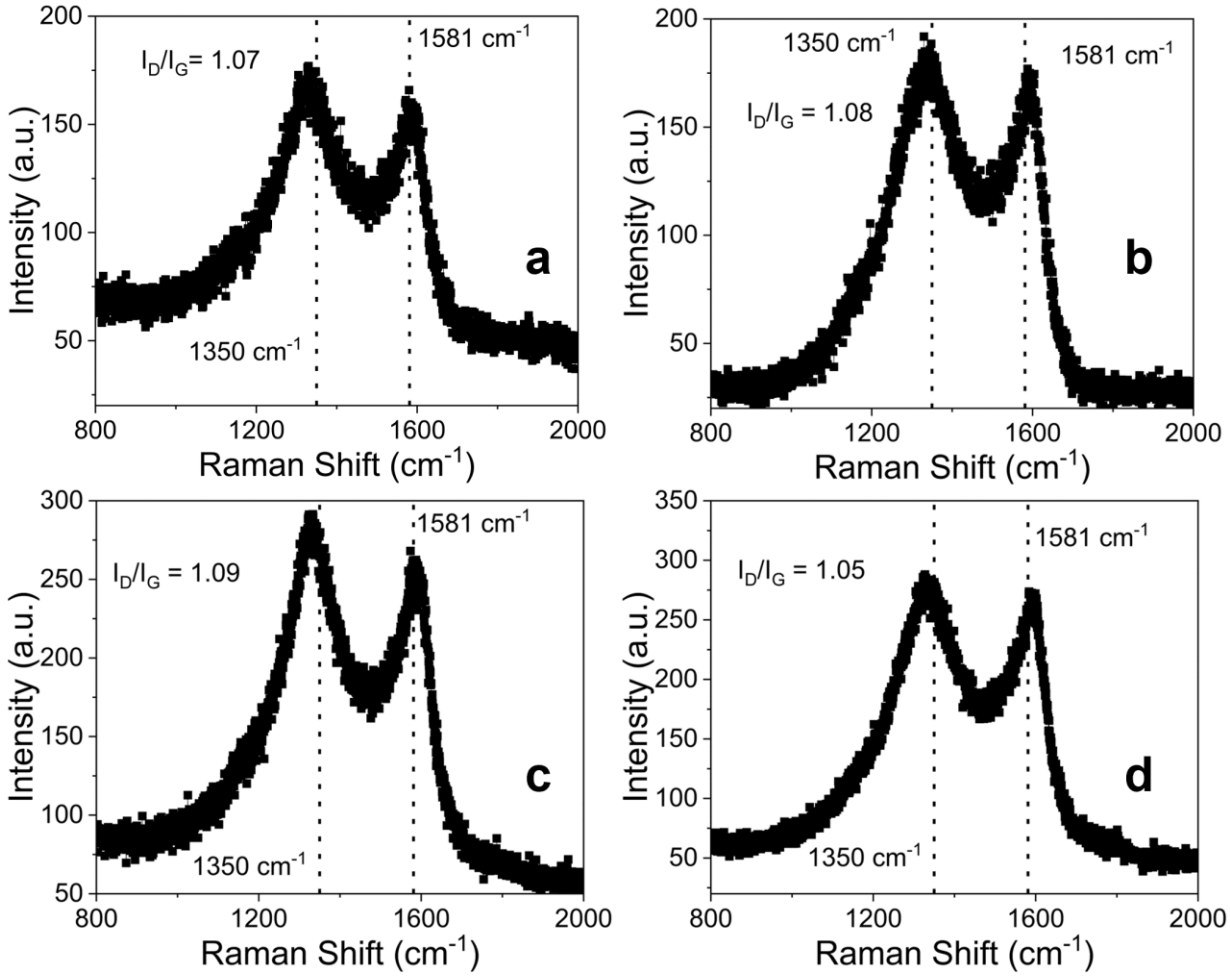

Figure 4.2. S 8: Figure S8: Raman spectra for M-N-C catalysts (A = Ni-N-C, B = Fe-N-C, C = Mn-N-C, D = Co-N-C) with characteristic E2g vibrational mode at ~1581 cm-1(G-band) while disordered carbon shows a peak at ~1350 cm-1(D1-band) fitted according to previous publications. [163, 222]

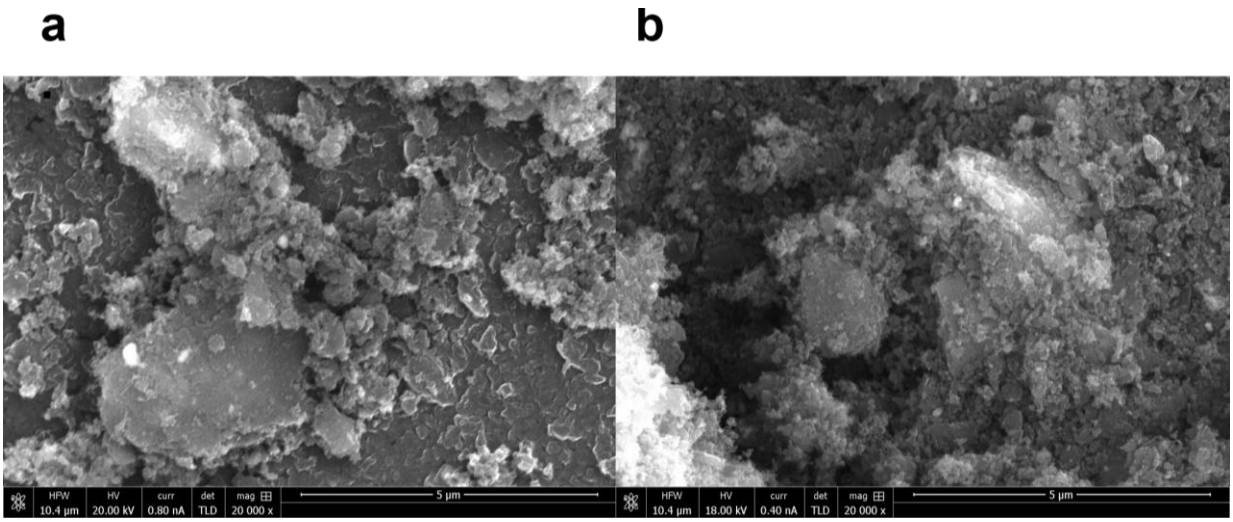

Figure 4.2. S 9: Figure S9: SEM image of Ni-N-C (900/-) (a) and SEM image of Ni-N-C (900/950) (b).

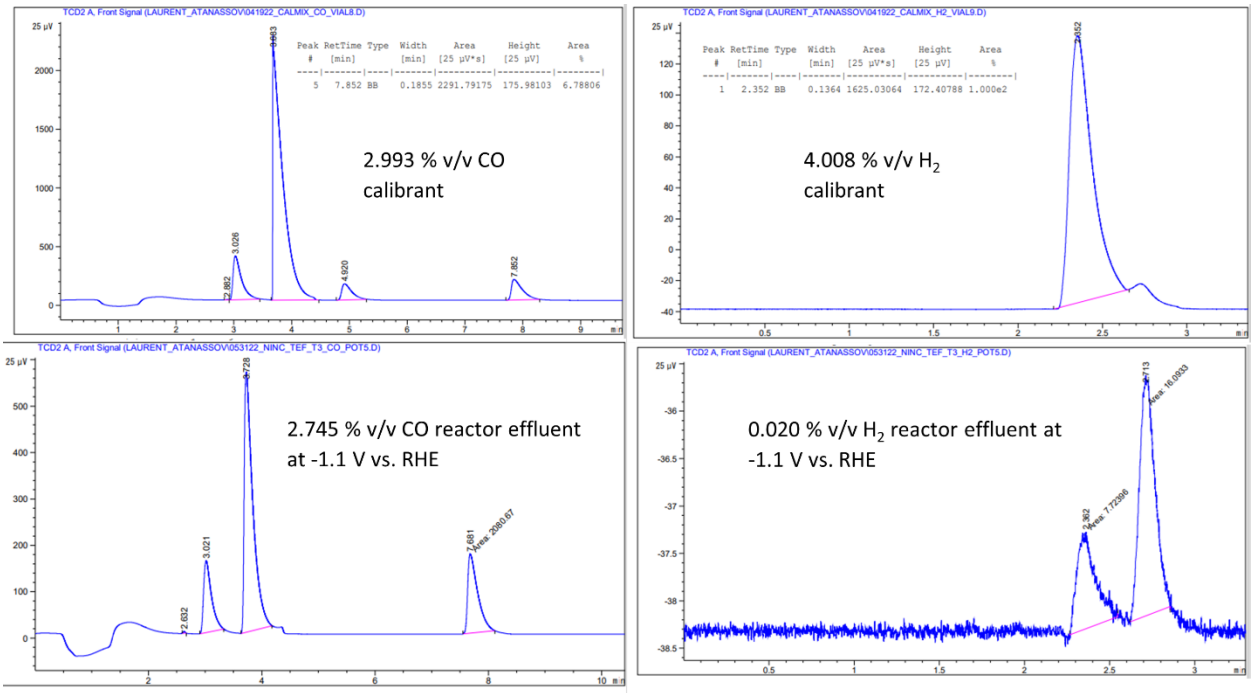

Figure 4.2. S 10: Figure S10: (a) Sample CO calibrant gas with CO elution (7.75 min +/- 0.1 min) peak area. (b) Sample H2 calibrant gas with H2 elution (2.35 min +/- 0.1 min) peak area. (c, d) Reactor effluent at -1.1 V vs. RHE cathodic potential for novel Ni-N-C at 1.06 mg/cm¬2 catalyst loading. This corresponds to 36.1 mA cm-2 CO partial current density and 0.3 mA cm-2 H2 partial current density or FEco = 99.3 % , and FEH2 = 0.7 %.

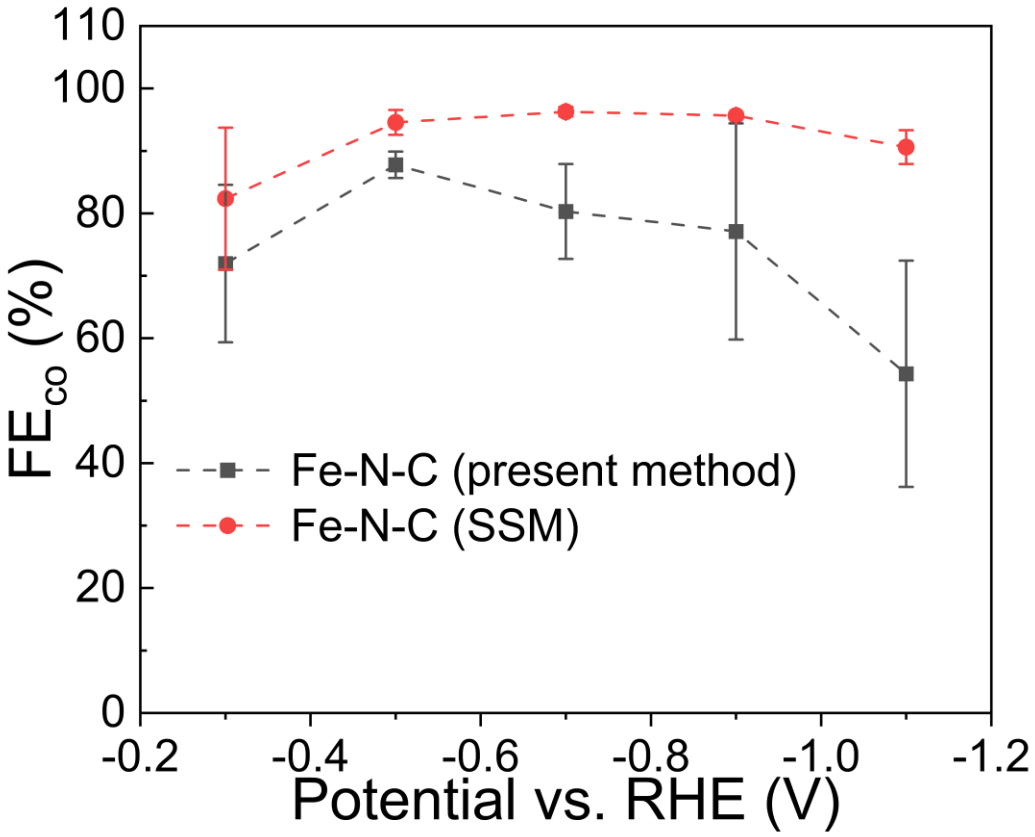

Figure 4.2. S 11: Figure S11: Comparison of faradaic efficiency for CO formation for Fe-N-C synthesized by the present method vs. the sacrificial support method (SSM).

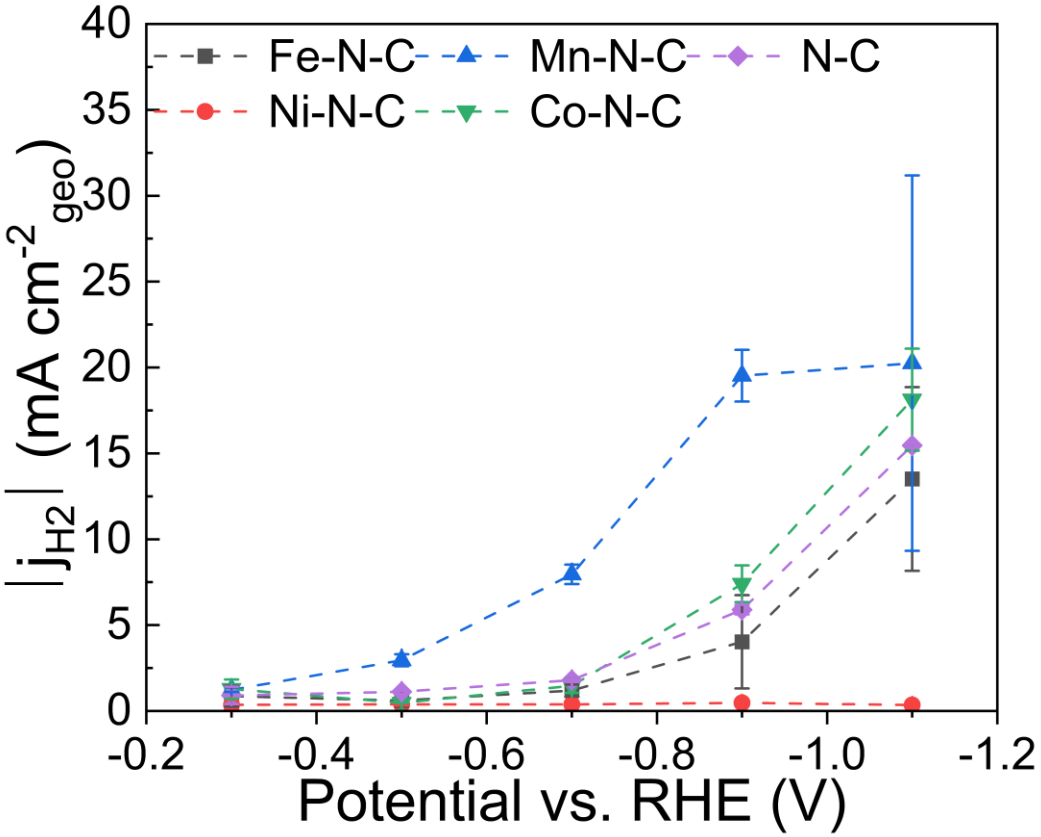

Figure 4.2. S 12: Figure S12: Partial current density magnitude for H2 for the M-N-C catalysts and N-C catalyst.

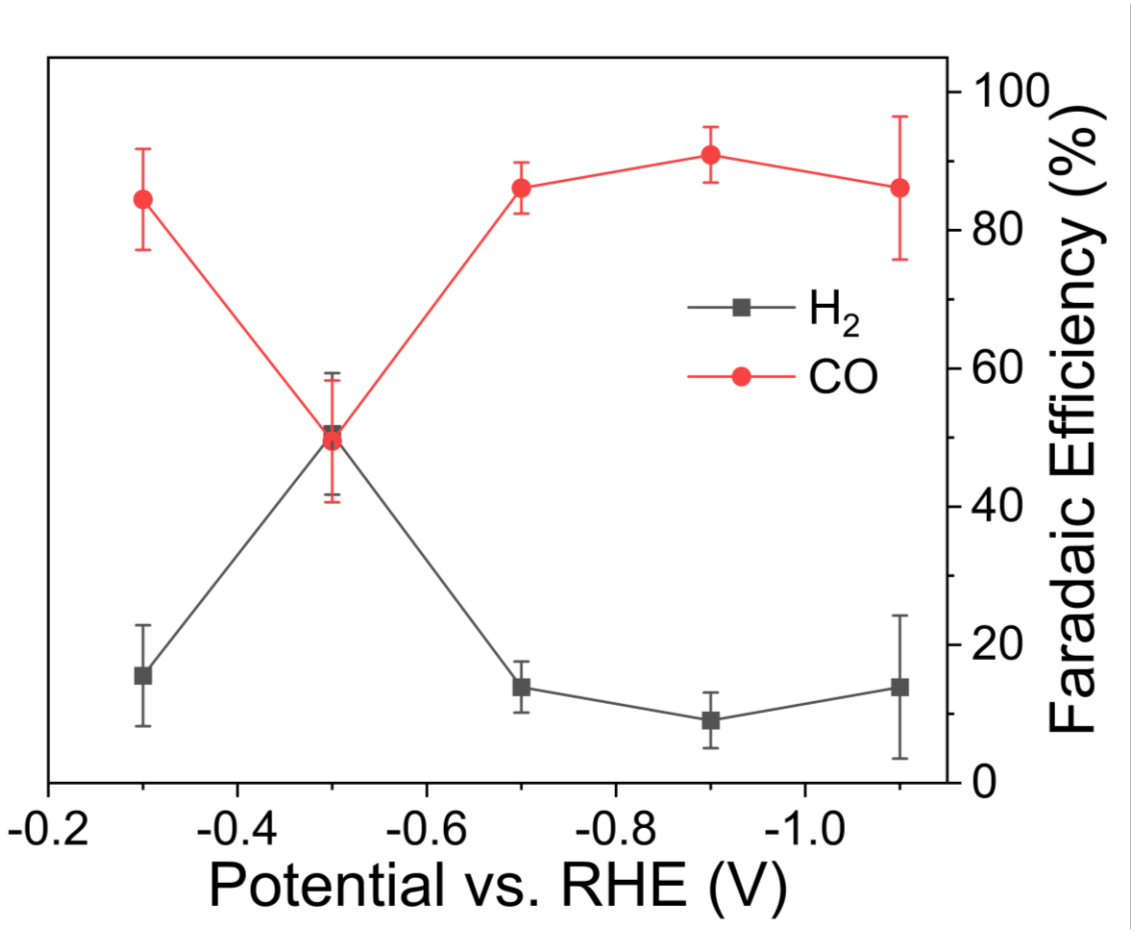

Figure 4.2. S 13: Figure S13: Faradaic efficiency for CO and H2 formation for Ni-N-C (900/-).

Chapter 3: Outlook/Perspective on the Dynamic Template Removal Synthesis

The emerging Dynamic Template Removal synthesis technique as a route towards metal-nitrogen-carbon catalysts holds promise in the context of non-PGM carbon-based catalysts for ORR/fuel cell as well as CO_2R applications. The ability to arrive at a metal-nitrogen-carbon catalyst with similar electrocatalytic characteristics via a new route further bolsters their status as benchmark non-PGM candidates. As mentioned in part 2 of the introduction (p.12), the synthesis route towards a metal-nitrogen-carbon catalyst with a high degree of atomic dispersion, graphitization, and favorable chemical motifs for CO_2 reduction is important from an industrial point of view of scaling up the proposed synthesis (Table 12).

Catalyst	*Synthesis Method*	*Performance*	*Abundance/scale-up/harsh solvent*	Reference
Fe/Phen/Z8-derived Fe-N-C	Soft-template; ZIF-8; 1,10 Phenanthroline (Phen), iron acetate; solvothermal EtOH/water, ball mill, flash pyrolysis 1050/950 °C Ar/NH_3	0.91 W cm^{-2} at 2.0 A cm^{-2} (plateau) compared to 1.14 W cm^{-2} for Pt at 2.0 A cm^{-2} (continuously increasing)	Generally abundant precursors, ZIF-8 is commercially available but most expensive component (47.5 \$ g^{-1})	Jaouen et al. [222]
Ni-N-C	Sacrificial polymer; aniline, metal chloride, APS, HCl, Ketjen Black; solvothermal; ball mill, pyrolysis (HT) 900 °C N_2, acid-wash (AW) in 2 M sulfate acid	High Throughput CO production: jco >200 mA cm^{-2} in CO_2 electrolyzer at high FE_{co} (85%)	Abundant precursors, synthesis: HT-AW-HT-AW-HT requires 2X acid wash steps requiring large acid disposal	Möller et al. [44]

M-N-C (M = Fe, Ni, Mn, Cr, Co)	Space-confinement-assisted molecular-level complexing; urea, citric acid, metal nitrate, pyrolysis 900 °C Ar	Fe-N-C: FE_{co} = 55, 86, 19 % at -0.3, -0.5, -0.9 V vs. RHE (max FE_{co} = 86 %); Ni-N-C: FE_{co}= 89, 96, 81 % at -0.6, -0.75, -0.97 V (max FE_{co} = 96 %)	Abundant precursors, no acid-wash step mentioned	Pan et al. [62]
M-N-C (M = Mn, Fe, Co, Ni)	Sacrificial polymer; 4,4'-Dipyridyl hydrate, metal chloride, carbonized 500 °C in Ar HNO_3 leach for N-C; Metal introduced through wet-impregnation, pyrolysis 900 °C in Ar, acid reflux wash	Fe-N-C: FE_{co}= 20, 65, 19 % at -0.38, -0.52, -0.78 V vs. RHE (max FE_{co}= 65%); Ni-N-C: FE_{co}= 6.9, 84, 69 % at -0.41, -0.76, -0.83 V vs. RHE (max FE_{co}= 84%)	Abundant polymer and precursor(s), necessitates two acid wash step(s) and heating under reflux	Ju et al. [213]
Ni-N-GS (graphene spheres)	Electrospinning of polymer solution followed by carbonization; polyacrylonitrile, polypyrrolidone, DCDA, Nickel nitrate, DMF heated under stirring, electrospun to produce nanofibers (NF), NF pyrolysis 750 °C in H_2, acid wash HCl (37 wt.%)(2X)	FE_{co}= 8, 93, 39 % at -0.44, -0.82, -0.98 V vs. RHE (max FE_{co} = 93.4 +/- 2 % at -0.82 V vs. RHE)	Abundant precursors, electrospinning increases process complexity, requires atleast 2 acid-wash steps in concentrated HCl	Jiang et al. [61]

Ni-N-C	PANI fiber grown on carbon paper (CP) in acidic electrolyte, cathodic reduction, immersed in $Ni(CN)_4^{2-}$ to tether Ni^{2+} ions by anion exchange rxn., carbonized btw. 700-1200 °C in N_2 followed by AW	For the champion Ni-N-C carbonized at 1100 °C: FE_{co}= 57, 86, 89, 11 % at -0.6, -0.7, -0.8, -1.1 V vs. RHE (max FE_{co}= 89 % at -0.8 V vs. RHE)	Abundant precursors, complexity of aqueous-based cathodic reduction, requires acid-wash step	Wang et al. [223]
Fe phthalocyanine-doped carbon nanotubes (CNT) Co phtalocyanine-doped CNT	Low-temperature hydrothermal synthesis (250 °C) for CNT, Ph/CNT, Fe/Ph/CNT, Co/Ph/CNT	For Fe-based catalyst: $E_{1/2}$ in 1 M KOH of -0.210 V vs. Hg\HgO compared to -0.197 V for Pt For Co-based catalyst: $E_{1/2}$ = -0.050 V	Abundant precursors, mild hydrothermal synthesis conditions, requires several acid-wash steps using 1:1 HNO_3 / HCl (aqua regia)	Arechederra et al. [224]
Fe-N-C	Low-temperature hydrothermal synthesis; Glucose, 2-methyl imidazole, zinc nitrate, iron nitrate at 200 °C for 24h, pyrolysis X2 (950 °C) in H_2 then NH_3 , AW	GLU-IMID-C-5 has $E_{1/2}$ ~ 0.7 V in O_2-satd. 0.5 M H_2SO_4	Abundant precursors, mild hydrothermal conditions, pyrolysis (X2), Requires acid-wash in dilute nitric acid	Gokhale et al. [225]
Atomically Ni-N single sites on carbon nanosheets (NiSAs/FN-CNSs)	NiSAs/FN-CNSs synthesis mixes PTFE, melamine, nickel acetate, pyrolysis(X2), 600 °C followed by 900 °C	FE_{co} = 6.9, 99.8, 83.4, 68.4 % at -0.3, -0.8, -1.1, -1.2 V vs. RHE (max FE_{co} = 99.8 %)	Abundant precursors, using no PTFE, leads to NP/nanotube, increasing PTFE/melamine reduces NP and forms CNS	Wang et al. [226]

Fe-N-C	Sacrificial support method; optimized blend of silica (Stöber spheres, Aerosil OX50, Cab-O-Sil LM150), nicarbazin, metal nitrate; wet chemistry/solvothermal mixing, ball mill (BM), pyrolysis (pyr) (7% H_2), 975 °C, pyr 10% NH_3, 950 °C	FE_{co} = 82.4, 94.6, 96.3, 95.7, 90.6 % at -0.3, -0.5, -0.7, -0.9, -1.1 V vs. RHE	Abundant precursors, process: BM/Pyr/BM/Pyr, Requires acid leaching step in concentrated HF	Delafontaine et al. chemelectro-chem
Fe-N-C, Ni-N-C	Novel dynamic template removal method, optimized blend of silica, nicarbazin, metal nitrate, wet chemistry/solvothermal, ball mill with PTFE, pyr1 (100 % N_2), 900 °C, pyr2 (10% NH_3)	Fe-N-C: FE_{co}= 72, 87.8, 80.4, 77.1, 54.3 % ; Ni-N-C: FE_{co}= 84.5, 74.2, 95.6, 97.8, 99.1 %; At -0.3, -0.5, -0.7, -0.9, -1.1 V vs. RHE	Abundant precursors, process: BM/Pyr/BM/Pyr No acid leaching	This Work

Table 26: Comparison of different synthesis methods in literature for M-N-C catalysts to the novel method presented in this section with an emphasis on their performance for CO_2R and/or ORR and the ease in industrially scaling up the synthesis.

In terms of the performance of the catalysts for CO_2 reduction, the Ni-N-C synthesized by the novel process presented here shows higher selectivity and activity for CO_2 reduction to CO than the competing catalysts in the literature without the use of any harsh solvents. The synthesis of Wang et al is similar and leads to single atom Ni sites dispersed on carbon nanosheets but has a lower selectivity at low overpotential for CO_2R (e.g., 7 % FE_{co} vs. 85 % FE_{co} for the present method). [226] Additionally, it shows the same high maximum CO_2R selectivity of *ca.* 99% FE_{co} but decreasing CO_2R selectivity at more cathodic potentials. Further, the ability to tailor the pore size distribution (PZD) through varying the precursor silica blend offers a tunable parameter for influencing the final catalyst porosity in the same way which materials synthesized by the SSM have variable PZD.

It is interesting to note that, while the metal atom substituent is a key factor influencing the M-N-C catalyst selectivity (thought to be through variations in the metal d-band center) and yields a selectivity consistent with literature : Ni-N-C > Fe-N-C > Mn-N-C ≅ N-C > Co-N-C, the porosity is a key factor influencing the CO_2R as well as ORR activity. For instance, in Figure 4.2. 6: Figure 6: Magnitude of partial current density for CO/H2 for Ni-N-C (900/-) (a), Ni-N-C (*) (b), Ni-N-C (**)(c), metal-free N-C

(d).(-0.3 V vs. RHE), both Ni-N-C (*) and Ni-N-C (**) have less CO_2R selectivity than when the optimized silica blend is used in Ni-N-C. One reason may be that the active sites available in Ni-N-C (*)/Ni-N-C (**) are more kinetically limited and hence require higher overpotentials. Additionally, the CO_2R activity order of Ni-N-C ~ Ni-N-C (**) >> Ni-N-C (*) at high overpotential (-1.1 V vs. RHE), seems to point to the fact that Stöber spheres and Aerosil OX-50 are the key pore-forming agents for enhancing CO_2R activity/selectivity (Table 22: Table S2: Precursor composition for the M-N-C catalysts. Additionally, we can see how the morphology affects the ORR activity. The trend in % peroxide formation as detected by RRDE for the novel M-N-C catalysts as a function of catalyst loading seems to point to a two-step ORR mechanism. At low catalyst loading of 50 µg cm^{-2}, we see a high 30-35 % H_2O_2 formation which drops to 5 % H_2O_2 at high catalyst loading of 600-700 µg cm^{-2} (Figure 4.1. 5: Figure 5. Accelerated durability test on RRDE conducted on FeAD-N-CAF-BM with a loading of 700 µg cm-2 and Pt/C with a loading of 60 µg cm-2 in 0.1 M HClO4 at 1600 rpm. (a) ORR polarization curves and (b) E1/2 before and after potential cycling. The catalyst loading trend suggests that a 2e- reduction of O_2 to H_2O_2 followed by a subsequent 2e- reduction to H_2O mechanism is occurring. This is because at low loading, the peroxide formation is high but as the loading is increased, the peroxide residence time is increased as the catalyst layer thickness is increased so that it may react further to completely reduce to H_2O. As peroxide formation can have a negative impact on catalyst stability[191], this is an interesting observation which warrants further investigation. The half-wave potential indicates favorable ORR activity in alkaline (0.1 M KOH, $E_{1/2}$= 0.81 V vs. RHE) and acidic media (0.1 M $HClO_4$, $E_{1/2}$= 0.73 V). Despite this sequential ORR mechanism, the catalyst stability as measured by RRDE remains exceptional. A reduction in $E_{1/2}$ of only 1.4 % (4.1 % for Pt/C) and 2.1 % (6.0 % for Pt/C) is observed for Fe-N-C (loading = 700 µg cm^{-2}) at 5000 and 10000 RRDE cycles, respectively.

The high catalytic stability may be attributed partly to the high level of bulk graphitization as measured by Raman (Figure 4.2. S 8: Figure S8: Raman spectra for M-N-C catalysts (A = Ni-N-C, B = Fe-N-C, C = Mn-N-C, D = Co-N-C) with characteristic E2g vibrational mode at ~1581 cm-1(G-band) while disordered carbon shows a peak at ~1350 cm-1(D1-band) fitted according to previous publications. [163, 222] as well as surface graphitization as measured by C1s XPS analysis (Table 25: Table S5: Carbon component fitting. % Atomic concentration of C 1s signal for 1: sp2 carbon (284.6 eV), 2: sp3 carbon (285.1 eV), 3: C-N (286.0 eV), 4: C-O (287.1 eV), 5: C=O (288.3 eV), 6: COOH (289.7 eV), 7,8: π- π* shake up (291.3 eV, and 292.9 eV). The catalysts show a high proportion of pyrrolic N which is observed to preferentially anchor Ni atoms (to a greater degree than Fe atoms), and thereby maintain high pyrrolic N content between pyrolysis steps (Table 24: Table S4: Nitrogen component fitting for M-N-C samples. % Atomic concentration of N 1s signal for 1: pyridinic N (398.2 eV), 2: N-Mex (399.5 eV), 3: pyrrolic N (400.8 eV), 4: graphitic N/ protonated N (401.6 eV), 5: bulk N-H (402.8 eV), 6, 7: NOx species (404.1 eV and 405.6 eV). In an analogous study to Artyushkova et al[190], the N-moiety content remains a point for future optimization to change the Me-N_x, and N-moiety content by utilizing alternative N, C sources to observe the influence on the electrocatalytic activity. The pyrolysis conditions remain a point of further optimization too, as the ramp rate, pyrolysis atmosphere, and total mass loss during pyrolysis have major implications on the final catalyst performance. [17, 146, 147]

As an additional variable to optimize, the Teflon/silica weight ratio has major implications on the final surface area, pore size distribution, and resulting performance. With increasing Teflon/silica weight

ratio and increased carbonization duration, Liang et al found increased surface area (through increased microporosity) for hierarchical porous carbons (HPC) derived from Indicalamus leaves. [157] Teng et al took advantage of Teflon's insolubility in water and ethanol to form mesostructured silica-resin composites via evaporation-induced self-assembly and subsequent pyrolysis. They utilized both a soft template (Pluronic F127), and hard template (silica (TEOS)) which upon mixing with Teflon and carbonizing, lead to ordered mesoporous carbons by removal of soft/hard template simultaneously. Importantly, the F127 soft template imparts larger mesopores (4.5 nm) while the silica template imparts smaller mesopores (2.4 nm) for formation of a bimodal mesoporous carbon with high microporosity and overall surface area. [158] This presents an opportunity to be applied for M-N-C syntheses for combined soft-template and hard-template M-N-C synthesis by the dynamic template removal process. Additionally, other routes could be adapted to this new synthesis such as that explored by Shui et al for combined sacrificial polymer and sacrificial MOF M-N-C synthesis. [26] The dynamic template removal synthesis presents opportunities for integration into existing M-N-C synthesis as well as further optimization for the development of advanced non-PGM based catalysts The manufacturing scalability of the synthesis is immediately improved compared to the competing syntheses as the precursor components are readily available, low-cost, and may be integrated via solvent-free mechanochemical mixing. The new catalysts present excellent CO_2R performance and ORR performance/stability compared to the state-of-the-art non-PGM M-N-C catalysts. The next step in evaluating the newly synthesized catalysts for industrial applications is to evaluate them under more realistic MEA-based fuel cell/electrolyzer vs. RDE/flow-cell environments. Fortunately, the synthesis presents the opportunity for fast and efficient iteration through different synthesis conditions for the production of a highly efficient and selective M-N-C catalyst tailored for a specific electrochemical reaction.

References

1. Lacis, A.A., et al., *Atmospheric CO2: Principal control knob governing Earth's temperature.* Science, 2010. **330**(6002): p. 356-359.
2. Esposito, R., et al. *Improving the Business Case for CCS in the Electric Power Generation Industry*. in *Proceedings of the 15th Greenhouse Gas Control Technologies Conference*. 2021.
3. Lee, M.-Y., et al., *Current achievements and the future direction of electrochemical CO2 reduction: A short review.* Critical Reviews in Environmental Science and Technology, 2020. **50**(8): p. 769-815.
4. Martín, A.J., G.O. Larrazábal, and J. Pérez-Ramírez, *Towards sustainable fuels and chemicals through the electrochemical reduction of CO 2: lessons from water electrolysis.* Green Chemistry, 2015. **17**(12): p. 5114-5130.
5. Delafontaine, L., T. Asset, and P. Atanassov, *Metal–Nitrogen–Carbon Electrocatalysts for CO2 Reduction towards Syngas Generation.* ChemSusChem, 2020. **13**(7): p. 1688-1698.
6. Eren, E.O. and S. Özkar, *Recent advances in heterogeneous catalysts for the effective electroreduction of carbon dioxide to carbon monoxide.* Journal of Power Sources, 2021. **506**: p. 230215.
7. Varela, A.S., et al., *Metal-doped nitrogenated carbon as an efficient catalyst for direct CO2 electroreduction to CO and hydrocarbons.* Angewandte Chemie International Edition, 2015. **54**(37): p. 10758-10762.
8. Miao, M., et al., *Recent Progress and Prospect of Electrodeposition-type Catalysts in Carbon Dioxide Reduction Utilizations.* Materials Advances, 2022.
9. Ozden, S., et al., *Graphene-based catalyst for CO2 reduction: The critical role of solvents in materials design.* Journal of Catalysis, 2021. **404**: p. 512-517.
10. Ferri, M., et al., *Steering Cu-Based CO2RR Electrocatalysts' Selectivity: Effect of Hydroxyapatite Acid/Base Moieties in Promoting Formate Production.* ACS Energy Letters, 2022. **7**(7): p. 2304-2310.
11. Luo, F., et al., *Kinetic Diagnostics and Synthetic Design of Platinum Group Metal-Free Electrocatalysts for the Oxygen Reduction Reaction Using Reactivity Maps and Site Utilization Descriptors.* Journal of the American Chemical Society, 2022.
12. Asset, T., et al., *Investigating the nature of the active sites for the CO2 reduction reaction on carbon-based electrocatalysts.* ACS Catalysis, 2019. **9**(9): p. 7668-7678.
13. Barkholtz, H.M. and D.-J. Liu, *Advancements in rationally designed PGM-free fuel cell catalysts derived from metal–organic frameworks.* Materials Horizons, 2017. **4**(1): p. 20-37.
14. Ma, S., et al., *Cobalt imidazolate framework as precursor for oxygen reduction reaction electrocatalysts.* Chemistry–A European Journal, 2011. **17**(7): p. 2063-2067.
15. Morozan, A. and F. Jaouen, *Metal organic frameworks for electrochemical applications.* Energy & environmental science, 2012. **5**(11): p. 9269-9290.
16. Armel, V., J. Hannauer, and F. Jaouen, *Effect of zif-8 crystal size on the O2 electro-reduction performance of pyrolyzed Fe–N–C catalysts.* Catalysts, 2015. **5**(3): p. 1333-1351.
17. Chen, Y., et al., *Catalysts by pyrolysis: Direct observation of transformations during re-pyrolysis of transition metal-nitrogen-carbon materials leading to state-of-the-art platinum group metal-free electrocatalyst.* Materials Today, 2022.
18. Gokhale, R., et al., *Novel dual templating approach for preparation of highly active Fe-NC electrocatalyst for oxygen reduction.* Electrochimica Acta, 2017. **224**: p. 49-55.
19. Serov, A., et al., *Nano-structured non-platinum catalysts for automotive fuel cell application.* Nano Energy, 2015. **16**: p. 293-300.

20. Serov, A., et al., *Highly active and durable templated non-PGM cathode catalysts derived from iron and aminoantipyrine.* Electrochemistry Communications, 2012. **22**: p. 53-56.
21. Liu, G., et al., *Development of non-precious metal oxygen-reduction catalysts for PEM fuel cells based on N-doped ordered porous carbon.* Applied Catalysis B: Environmental, 2009. **93**(1-2): p. 156-165.
22. Videla, A.H.M., et al., *Varying the morphology of Fe-NC electrocatalysts by templating Iron Phthalocyanine precursor with different porous SiO2 to promote the Oxygen Reduction Reaction.* Electrochimica Acta, 2015. **177**: p. 43-50.
23. Sa, Y.J., et al., *A general approach to preferential formation of active Fe–N x sites in Fe–N/C electrocatalysts for efficient oxygen reduction reaction.* Journal of the American Chemical Society, 2016. **138**(45): p. 15046-15056.
24. Chung, H.T., et al., *Direct atomic-level insight into the active sites of a high-performance PGM-free ORR catalyst.* Science, 2017. **357**(6350): p. 479-484.
25. Yin, X., et al., *PGM-free ORR catalysts designed by templating PANI-type polymers containing functional groups with high affinity to iron.* Journal of The Electrochemical Society, 2019. **166**(7): p. F3240.
26. Shui, J., et al., *Highly efficient nonprecious metal catalyst prepared with metal–organic framework in a continuous carbon nanofibrous network.* Proceedings of the National Academy of Sciences, 2015. **112**(34): p. 10629-10634.
27. Proietti, E., et al., *Iron-based cathode catalyst with enhanced power density in polymer electrolyte membrane fuel cells.* Nature communications, 2011. **2**(1): p. 1-9.
28. Primbs, M., et al., *Establishing reactivity descriptors for platinum group metal (PGM)-free Fe–N–C catalysts for PEM fuel cells.* Energy & Environmental Science, 2020. **13**(8): p. 2480-2500.
29. Pylypenko, S., et al., *Non-platinum oxygen reduction electrocatalysts based on pyrolyzed transition metal macrocycles.* Electrochimica Acta, 2008. **53**(27): p. 7875-7883.
30. Serov, A., et al., *Original mechanochemical synthesis of non-platinum group metals oxygen reduction reaction catalysts assisted by sacrificial support method.* Electrochimica Acta, 2015. **179**: p. 154-160.
31. Workman, M.J., et al., *Fe–N–C catalyst graphitic layer structure and fuel cell performance.* ACS Energy Letters, 2017. **2**(7): p. 1489-1493.
32. Hu, X.-M., et al., *Selective CO2 reduction to CO in water using earth-abundant metal and nitrogen-doped carbon electrocatalysts.* ACS catalysis, 2018. **8**(7): p. 6255-6264.
33. Huan, T.N., et al., *Electrochemical reduction of CO2 catalyzed by Fe-NC materials: A structure–selectivity study.* ACS catalysis, 2017. **7**(3): p. 1520-1525.
34. Lu, S., et al., *Electrosynthesis of Syngas via the Co-Reduction of CO2 and H2O.* Cell Reports Physical Science, 2020: p. 100237.
35. Jouny, M., W. Luc, and F. Jiao, *General techno-economic analysis of CO2 electrolysis systems.* Industrial & Engineering Chemistry Research, 2018. **57**(6): p. 2165-2177.
36. Sánchez, O.G., et al., *Recent advances in industrial CO2 electroreduction.* Current Opinion in Green and Sustainable Chemistry, 2019. **16**: p. 47-56.
37. Tackett, B.M., E. Gomez, and J.G. Chen, *Net reduction of CO 2 via its thermocatalytic and electrocatalytic transformation reactions in standard and hybrid processes.* Nature Catalysis, 2019. **2**(5): p. 381-386.
38. Verma, S., S. Lu, and P.J. Kenis, *Co-electrolysis of CO 2 and glycerol as a pathway to carbon chemicals with improved technoeconomics due to low electricity consumption.* Nature Energy, 2019. **4**(6): p. 466-474.

39. Kim, C., et al., *Achieving selective and efficient electrocatalytic activity for CO2 reduction using immobilized silver nanoparticles.* Journal of the American Chemical Society, 2015. **137**(43): p. 13844-13850.
40. Jiang, K., et al., *Silver nanoparticles with surface-bonded oxygen for highly selective CO2 reduction.* ACS Sustainable Chemistry & Engineering, 2017. **5**(10): p. 8529-8534.
41. Lu, Q. and F. Jiao, *Electrochemical CO2 reduction: Electrocatalyst, reaction mechanism, and process engineering.* Nano Energy, 2016. **29**: p. 439-456.
42. Huang, L., et al., *Metal-Nitrogen-doped carbon single-atom electrocatalysts for CO2 electroreduction.* Composites Part B: Engineering, 2021: p. 108986.
43. Amiinu, I.S., et al., *Multifunctional Mo–N/C@ MoS2 electrocatalysts for HER, OER, ORR, and Zn–air batteries.* Advanced Functional Materials, 2017. **27**(44): p. 1702300.
44. Möller, T., et al., *Efficient CO 2 to CO electrolysis on solid Ni–N–C catalysts at industrial current densities.* Energy & Environmental Science, 2019. **12**(2): p. 640-647.
45. Varela, A.S., et al., *Electrochemical reduction of CO2 on metal-nitrogen-doped carbon catalysts.* ACS Catalysis, 2019. **9**(8): p. 7270-7284.
46. Chen, Y., et al., *Single-atom catalysts: synthetic strategies and electrochemical applications.* Joule, 2018. **2**(7): p. 1242-1264.
47. Lee, S.-M., S.-H. Lee, and J.-S. Roh, *Analysis of Activation Process of Carbon Black Based on Structural Parameters Obtained by XRD Analysis.* Crystals, 2021. **11**(2): p. 153.
48. Artyushkova, K., *Misconceptions in interpretation of nitrogen chemistry from x-ray photoelectron spectra.* Journal of Vacuum Science & Technology A: Vacuum, Surfaces, and Films, 2020. **38**(3): p. 031002.
49. Luo, X., et al., *Significant improvements in CO2 capture by pyridine-containing anion-functionalized ionic liquids through multiple-site cooperative interactions.* Angewandte Chemie, 2014. **126**(27): p. 7173-7177.
50. Wang, C., et al., *Typical transition metal single-atom catalysts with a metal-pyridine N structure for efficient CO2 electroreduction.* Applied Catalysis B: Environmental, 2021. **296**: p. 120331.
51. Tang, Y., et al., *Single rhodium atoms anchored in micropores for efficient transformation of methane under mild conditions.* Nature communications, 2018. **9**(1): p. 1-11.
52. Lefèvre, M., et al., *Iron-based catalysts with improved oxygen reduction activity in polymer electrolyte fuel cells.* science, 2009. **324**(5923): p. 71-74.
53. Hursán, D., et al., *Morphological attributes govern carbon dioxide reduction on N-doped carbon electrodes.* Joule, 2019. **3**(7): p. 1719-1733.
54. Liang, H.-W., et al., *Hierarchically porous carbons with optimized nitrogen doping as highly active electrocatalysts for oxygen reduction.* Nature communications, 2014. **5**(1): p. 1-7.
55. Li, M., et al., *Heterogeneous single-atom catalysts for electrochemical CO2 reduction reaction.* Advanced Materials, 2020. **32**(34): p. 2001848.
56. Bohra, D., et al., *Mass Transport in Catalytic Pores of GDE-Based CO2 Electroreduction Systems.* 2020.
57. Krause, R., et al., *Industrial application aspects of the electrochemical reduction of CO2 to CO in aqueous electrolyte.* Chemie Ingenieur Technik, 2020. **92**(1-2): p. 53-61.
58. Cofell, E.R., et al., *Investigation of electrolyte-dependent carbonate formation on gas diffusion electrodes for CO2 electrolysis.* ACS applied materials & interfaces, 2021. **13**(13): p. 15132-15142.
59. Jing, X., F. Li, and Y. Wang, *Assessing the economic potential of large-scale carbonate-formation-free CO 2 electrolysis.* Catalysis Science & Technology, 2022.

60. Baumgartner, L.M., et al., *Narrow Pressure Stability Window of Gas Diffusion Electrodes Limits the Scale-Up of CO2 Electrolyzers.* ACS sustainable chemistry & engineering, 2022. **10**(14): p. 4683-4693.
61. Jiang, K., et al., *Transition-metal single atoms in a graphene shell as active centers for highly efficient artificial photosynthesis.* Chem, 2017. **3**(6): p. 950-960.
62. Pan, F., et al., *Identification of champion transition metals centers in metal and nitrogen-codoped carbon catalysts for CO2 reduction.* Applied Catalysis B: Environmental, 2018. **226**: p. 463-472.
63. Dunwell, M., et al., *The central role of bicarbonate in the electrochemical reduction of carbon dioxide on gold.* Journal of the American Chemical Society, 2017. **139**(10): p. 3774-3783.
64. Li, T., et al., *Conversion of bicarbonate to formate in an electrochemical flow reactor.* ACS Energy Letters, 2020. **5**(8): p. 2624-2630.
65. Larrea, C., et al., *Multi-parameter study of CO2 electrochemical reduction from concentrated bicarbonate feed.* Journal of CO2 Utilization, 2022. **57**: p. 101878.
66. Jhong, H.R.M., F.R. Brushett, and P.J. Kenis, *The effects of catalyst layer deposition methodology on electrode performance.* Advanced Energy Materials, 2013. **3**(5): p. 589-599.
67. Monteiro, M.C., et al., *Efficiency and selectivity of CO2 reduction to CO on gold gas diffusion electrodes in acidic media.* Nature communications, 2021. **12**(1): p. 1-7.
68. Varela, A.S., W. Ju, and P. Strasser, *Molecular nitrogen–carbon catalysts, solid metal organic framework catalysts, and solid metal/nitrogen-doped carbon (MNC) catalysts for the electrochemical CO2 reduction.* Advanced Energy Materials, 2018. **8**(30): p. 1703614.
69. Ravel, B. and M. Newville, *J. Synchrotron Radiat*. 2005.
70. Ju, W., et al., *Understanding activity and selectivity of metal-nitrogen-doped carbon catalysts for electrochemical reduction of CO 2.* Nature communications, 2017. **8**(1): p. 1-9.
71. Pan, F., et al., *Unveiling active sites of CO2 reduction on nitrogen-coordinated and atomically dispersed iron and cobalt catalysts.* Acs Catalysis, 2018. **8**(4): p. 3116-3122.
72. Zhao, J., et al., *Effective tunable syngas generation via CO2 reduction reaction by non-precious Fe-NC electrocatalyst.* Chemical Engineering Journal, 2020. **389**: p. 124323.
73. Wang, Z.-L., et al., *Optimizing electron densities of Ni-NC complexes by hybrid coordination for efficient electrocatalytic CO2 reduction.* ChemSusChem, 2020. **13**(5): p. 929-937.
74. Li, C.W. and M.W. Kanan, *CO2 reduction at low overpotential on Cu electrodes resulting from the reduction of thick Cu2O films.* Journal of the American Chemical Society, 2012. **134**(17): p. 7231-7234.
75. Zhong, D., et al., *Coupling of Cu (100) and (110) facets promotes carbon dioxide conversion to hydrocarbons and alcohols.* Angewandte Chemie International Edition, 2021. **60**(9): p. 4879-4885.
76. Hori, Y., et al., *Selective formation of C2 compounds from electrochemical reduction of CO2 at a series of copper single crystal electrodes.* The Journal of Physical Chemistry B, 2002. **106**(1): p. 15-17.
77. Raciti, D. and C. Wang, *Recent advances in CO2 reduction electrocatalysis on copper.* ACS Energy Letters, 2018. **3**(7): p. 1545-1556.
78. Sun, Z., et al., *Factors Influencing the Performance of Copper-Bearing Catalysts in the CO2 Reduction System.* ACS Energy Letters, 2021. **6**(11): p. 3992-4022.
79. Li, C.W., J. Ciston, and M.W. Kanan, *Electroreduction of carbon monoxide to liquid fuel on oxide-derived nanocrystalline copper.* Nature, 2014. **508**(7497): p. 504-507.
80. Verdaguer-Casadevall, A., et al., *Probing the active surface sites for CO reduction on oxide-derived copper electrocatalysts.* Journal of the American Chemical Society, 2015. **137**(31): p. 9808-9811.

81. Raciti, D., K.J. Livi, and C. Wang, *Highly dense Cu nanowires for low-overpotential CO2 reduction.* Nano letters, 2015. **15**(10): p. 6829-6835.
82. Ma, M., K. Djanashvili, and W.A. Smith, *Selective electrochemical reduction of CO 2 to CO on CuO-derived Cu nanowires.* Physical Chemistry Chemical Physics, 2015. **17**(32): p. 20861-20867.
83. Schouten, K., et al., *A new mechanism for the selectivity to C 1 and C 2 species in the electrochemical reduction of carbon dioxide on copper electrodes.* Chemical Science, 2011. **2**(10): p. 1902-1909.
84. Ren, D., B.S.-H. Ang, and B.S. Yeo, *Tuning the selectivity of carbon dioxide electroreduction toward ethanol on oxide-derived Cu x Zn catalysts.* Acs Catalysis, 2016. **6**(12): p. 8239-8247.
85. Hoang, T.T., et al., *Nanoporous copper films by additive-controlled electrodeposition: CO2 reduction catalysis.* ACS catalysis, 2017. **7**(5): p. 3313-3321.
86. Qin, T., et al., *Enhanced Electrochemical Reduction of CO2 to Ethylene on Electrodeposited Copper in 0.1 M KHCO3.* Int. J. Electrochem. Sci, 2018. **13**(11): p. 10101-10112.
87. Wang, H., et al., *Self-selective catalyst synthesis for CO2 reduction.* Joule, 2019. **3**(8): p. 1927-1936.
88. Ye, W., X. Guo, and T. Ma, *A review on electrochemical synthesized copper-based catalysts for electrochemical reduction of CO2 to C2+ products.* Chemical Engineering Journal, 2021. **414**: p. 128825.
89. Kitchens, C.L., M.C. McLeod, and C.B. Roberts, *Solvent effects on the growth and steric stabilization of copper metallic nanoparticles in AOT reverse micelle systems.* The Journal of Physical Chemistry B, 2003. **107**(41): p. 11331-11338.
90. Rana, S., et al., *Spontaneous reduction of copper (ii) to copper (i) at solid–liquid interface.* The Journal of Physical Chemistry Letters, 2018. **9**(21): p. 6364-6371.
91. Dang, T.M.D., et al., *The influence of solvents and surfactants on the preparation of copper nanoparticles by a chemical reduction method.* Advances in Natural Sciences: Nanoscience and Nanotechnology, 2011. **2**(2): p. 025004.
92. Bacon, G., *The interlayer spacing of graphite.* Acta crystallographica, 1951. **4**(6): p. 558-561.
93. Liu, L., et al., *Effects of Solvent Molecules on the Interlayer Spacing of Graphene Oxide.* Transactions of Tianjin University, 2018. **24**(6): p. 555-562.
94. Zheng, S., et al., *Correlating interlayer spacing and separation capability of graphene oxide membranes in organic solvents.* ACS nano, 2020. **14**(5): p. 6013-6023.
95. Ozden, S., et al., *Interface and defect engineering of hybrid nanostructures toward an efficient HER catalyst.* Nanoscale, 2019. **11**(26): p. 12489-12496.
96. Joyner, J., et al., *Graphene supported MoS2 structures with high defect density for an efficient HER electrocatalysts.* ACS applied materials & interfaces, 2020. **12**(11): p. 12629-12638.
97. Lee, J., et al., *Stabilization of graphene nanopore.* Proceedings of the National Academy of Sciences, 2014. **111**(21): p. 7522-7526.
98. Pan, F. and Y. Yang, *Designing CO 2 reduction electrode materials by morphology and interface engineering.* Energy & Environmental Science, 2020. **13**(8): p. 2275-2309.
99. Xue, D., et al., *Defect engineering on carbon-based catalysts for electrocatalytic CO2 reduction.* Nano-Micro Letters, 2021. **13**(1): p. 1-23.
100. Vasilyev, D.V. and P.J. Dyson, *The role of organic promoters in the electroreduction of carbon dioxide.* Acs Catalysis, 2021. **11**(3): p. 1392-1405.
101. Ghobadi, K., et al., *Electrochemical activation of CO2 by a di-Schiff base of N, N'-bis (2-hydroxy-1-naphthaldehyde)-m-phenylenediimine.* Polyhedron, 2018. **155**: p. 13-19.
102. Von Wolff, N., et al., *Implications of CO2 activation by frustrated Lewis pairs in the catalytic hydroboration of CO2: a view using N/Si+ frustrated Lewis pairs.* ACS Catalysis, 2016. **6**(7): p. 4526-4535.

103. Knopf, I. and C.C. Cummins, *Revisiting CO2 reduction with NaBH4 under aprotic conditions: synthesis and characterization of sodium triformatoborohydride.* Organometallics, 2015. **34**(9): p. 1601-1603.
104. Reske, R., et al., *Particle size effects in the catalytic electroreduction of CO2 on Cu nanoparticles.* Journal of the American Chemical Society, 2014. **136**(19): p. 6978-6986.
105. Liu, S. and S. Huang, *Size effects and active sites of Cu nanoparticle catalysts for CO2 electroreduction.* Applied Surface Science, 2019. **475**: p. 20-27.
106. Alexey Serov, P.B.A., *Non-PGM catalysts for ORR based on charge transfer organic complexes*, USPTO, Editor. 2014, UNM Rainforest Innovations: USA.
107. Chong, R., et al., *Hydroxyapatite decorated TiO2 as efficient photocatalyst for selective reduction of CO2 with H2O into CH4.* International Journal of Hydrogen Energy, 2018. **43**(49): p. 22329-22339.
108. Wang, X., et al., *Photocatalytic Reduction of CO2 Using Titanium-Substituted and Fluorine-Doped Titanium-Substituted Hydroxyapatite as Photocatalysts.* Catalysis Letters, 2017. **147**(11): p. 2706-2713.
109. Loiudice, A., et al., *Tailoring copper nanocrystals towards C2 products in electrochemical CO2 reduction.* Angewandte Chemie International Edition, 2016. **55**(19): p. 5789-5792.
110. Mistry, H., et al., *Highly selective plasma-activated copper catalysts for carbon dioxide reduction to ethylene.* Nature communications, 2016. **7**(1): p. 1-9.
111. Baturina, O.A., et al., *CO2 electroreduction to hydrocarbons on carbon-supported Cu nanoparticles.* Acs Catalysis, 2014. **4**(10): p. 3682-3695.
112. Li, Q., et al., *Controlled assembly of Cu nanoparticles on pyridinic-N rich graphene for electrochemical reduction of CO2 to ethylene.* Nano Energy, 2016. **24**: p. 1-9.
113. Song, Y., et al., *High-selectivity electrochemical conversion of CO2 to ethanol using a copper nanoparticle/N-doped graphene electrode.* ChemistrySelect, 2016. **1**(19): p. 6055-6061.
114. Zhao, J., et al., *Phosphate tuned copper electrodeposition and promoted formic acid selectivity for carbon dioxide reduction.* Journal of Materials Chemistry A, 2017. **5**(23): p. 11905-11916.
115. Recillas, S., et al., *Studies on the precipitation behaviour of calcium phosphate solutions.* Journal of Ceramic Processing Research, 2012. **13**(1): p. 5-10.
116. Ferri, M., et al., *In-depth study of the mechanism of heavy metal trapping on the surface of hydroxyapatite.* Applied Surface Science, 2019. **475**: p. 397-409.
117. Diallo-Garcia, S., et al., *Identification of surface basic sites and acid–base pairs of hydroxyapatite.* The Journal of Physical Chemistry C, 2014. **118**(24): p. 12744-12757.
118. Souza, F., et al., *Adsorption of CO2 on biphasic and amorphous calcium phosphates: An experimental and theoretical analysis.* Chemical Physics Letters, 2019. **714**: p. 143-148.
119. Cheng, Z.H., et al., *FTIR study of adsorption of CO2 on nonstoichiometric calcium hydroxyapatite.* Langmuir, 1998. **14**(23): p. 6681-6686.
120. Wai, M.H., et al., *Influence of surface formate species on methane selectivity for carbon dioxide methanation over nickel hydroxyapatite catalyst.* ChemCatChem, 2020. **12**(24): p. 6410-6419.
121. Serov, A., et al., *Palladium supported on 3D graphene as an active catalyst for alcohols electrooxidation.* Journal of The Electrochemical Society, 2015. **162**(12): p. F1305.
122. Kabir, S., et al., *Role of nitrogen moieties in N-doped 3D-graphene nanosheets for oxygen electroreduction in acidic and alkaline media.* ACS applied materials & interfaces, 2018. **10**(14): p. 11623-11632.
123. Hori, Y., et al., *Electrochemical reduction of CO at a copper electrode.* The Journal of Physical Chemistry B, 1997. **101**(36): p. 7075-7081.
124. Ross, M.B., et al., *Designing materials for electrochemical carbon dioxide recycling.* Nature Catalysis, 2019. **2**(8): p. 648-658.

125. Wang, H., et al., *Efficient electrocatalytic reduction of CO2 by Nitrogen-doped nanoporous carbon/carbon nanotube membranes: a step towards the electrochemical CO2 refinery.* Angewandte Chemie, 2017. **129**(27): p. 7955-7960.
126. Hummers Jr, W.S. and R.E. Offeman, *Preparation of graphitic oxide.* Journal of the american chemical society, 1958. **80**(6): p. 1339-1339.
127. Kuhl, K.P., et al., *New insights into the electrochemical reduction of carbon dioxide on metallic copper surfaces.* Energy & Environmental Science, 2012. **5**(5): p. 7050-7059.
128. Asset, T., F. Maillard, and F. Jaouen, *Electrocatalysis with Single-Metal Atom Sites in Doped Carbon Matrices.* Supported Metal Single Atom Catalysis, 2022: p. 531-582.
129. Serov, A., et al., *Anode catalysts for direct hydrazine fuel cells: from laboratory test to an electric vehicle.* Angewandte Chemie, 2014. **126**(39): p. 10504-10507.
130. Wang, Y., et al., *Hollow Carbon Sphere and Polyhedral Carbon Composites Supported Iron Nanoparticles as Excellent Bifunctional Electrocatalysts of Zn–Air Battery.* Energy Technology, 2022. **10**(5): p. 2200057.
131. Xing, L., et al., *Membrane electrode assemblies for PEM fuel cells: A review of functional graded design and optimization.* Energy, 2019. **177**: p. 445-464.
132. Shen, P.K., *PEM fuel cell catalyst layers and MEAs*, in *PEM fuel cell electrocatalysts and catalyst layers*. 2008, Springer. p. 355-380.
133. Ding, L., T. Tang, and J.-S. Hu, *Recent progress in proton-exchange membrane fuel cells based on metal-nitrogen-carbon catalysts.* Acta Phys. Chim. Sin, 2020. **37**: p. 2010048.
134. Stariha, S., et al., *PGM-free Fe-NC catalysts for oxygen reduction reaction: Catalyst layer design.* Journal of Power Sources, 2016. **326**: p. 43-49.
135. Jasinski, R., *A new fuel cell cathode catalyst.* Nature, 1964. **201**(4925): p. 1212-1213.
136. He, Y., et al., *Metal-nitrogen-carbon catalysts for oxygen reduction in PEM fuel cells: self-template synthesis approach to enhancing catalytic activity and stability.* Electrochemical Energy Reviews, 2019. **2**(2): p. 231-251.
137. Zagal, J.H., S. Specchia, and P. Atanassov, *Mapping transition metal-MN4 macrocyclic complex catalysts performance for the critical reactivity descriptors.* Current Opinion in Electrochemistry, 2021. **27**: p. 100683.
138. Asset, T. and P. Atanassov, *Iron-nitrogen-carbon catalysts for proton exchange membrane fuel cells.* Joule, 2020. **4**(1): p. 33-44.
139. Liu, J., et al., *Recent advances in active sites identification and regulation of MN/C electro-catalysts towards ORR.* Science China Chemistry, 2019. **62**(6): p. 669-683.
140. Specchia, S., P. Atanassov, and J.H. Zagal, *Mapping transition metal–nitrogen–carbon catalyst performance on the critical descriptor diagram.* Current Opinion in Electrochemistry, 2021. **27**: p. 100687.
141. Rauf, M., et al., *Insight into the different ORR catalytic activity of Fe/N/C between acidic and alkaline media: protonation of pyridinic nitrogen.* Electrochemistry Communications, 2016. **73**: p. 71-74.
142. Lim, K.H. and H. Kim, *Nitrogen-doped carbon catalysts derived from ionic liquids in the presence of transition metals for the oxygen reduction reaction.* Applied Catalysis B: Environmental, 2014. **158**: p. 355-360.
143. Osmieri, L., *Transition metal–nitrogen–carbon (M–N–C) catalysts for oxygen reduction reaction. Insights on synthesis and performance in polymer electrolyte fuel cells.* ChemEngineering, 2019. **3**(1): p. 16.
144. Osmieri, L., L. Pezzolato, and S. Specchia, *Recent trends on the application of PGM-free catalysts at the cathode of anion exchange membrane fuel cells.* Current Opinion in Electrochemistry, 2018. **9**: p. 240-256.

145. Huang, Y., et al., *Catalysts by pyrolysis: Direct observation of chemical and morphological transformations leading to transition metal-nitrogen-carbon materials.* Materials Today, 2021.
146. Long, G., et al., *Effect of pyrolysis conditions on nitrogen-doped ordered mesoporous carbon electrocatalysts.* Chinese Journal of Catalysis, 2015. **36**(8): p. 1197-1204.
147. Domínguez, C., et al., *Effect of the pyrolysis atmosphere and nature of iron precursor on the structure and activity of Fe/N based electrocatalysts for the oxygen reduction reaction.* International Journal of Hydrogen Energy, 2016. **41**(47): p. 22560-22569.
148. Osmieri, L., A.H.M. Videla, and S. Specchia, *Activity of Co–N multi walled carbon nanotubes electrocatalysts for oxygen reduction reaction in acid conditions.* Journal of Power Sources, 2015. **278**: p. 296-307.
149. Pérez-Alonso, F., et al., *Effect of carbon nanotube diameter for the synthesis of Fe/N/multiwall carbon nanotubes and repercussions for the oxygen reduction reaction.* Journal of power sources, 2013. **240**: p. 494-502.
150. Wang, N., et al., *Space-confined pyrolysis for fabrication of peacods-like Fe3O4@ C-Ni nanostructures for catalysis and protein adsorption.* Nanotechnology, 2019. **30**(41): p. 415602.
151. Serov, A., K. Artyushkova, and P. Atanassov, *Fe-N-C oxygen reduction fuel cell catalyst derived from carbendazim: synthesis, structure, and reactivity.* Advanced Energy Materials, 2014. **4**(10): p. 1301735.
152. Ziegelbauer, J.M., et al., *Direct spectroscopic observation of the structural origin of peroxide generation from Co-based pyrolyzed porphyrins for ORR applications.* The Journal of Physical Chemistry C, 2008. **112**(24): p. 8839-8849.
153. Osmieri, L., et al., *Influence of different transition metals on the properties of Me–N–C (Me= Fe, Co, Cu, Zn) catalysts synthesized using SBA-15 as tubular nano-silica reactor for oxygen reduction reaction.* international journal of hydrogen energy, 2016. **41**(47): p. 22570-22588.
154. Oh, H.-S., et al., *Development of highly active and stable non-precious oxygen reduction catalysts for PEM fuel cells using polypyrrole and a chelating agent.* Electrochemistry Communications, 2011. **13**(8): p. 879-881.
155. Wu, G., et al., *Synthesis–structure–performance correlation for polyaniline–Me–C non-precious metal cathode catalysts for oxygen reduction in fuel cells.* Journal of Materials Chemistry, 2011. **21**(30): p. 11392-11405.
156. Singh, D.K., et al., *No more HF: teflon-assisted ultrafast removal of silica to generate high-surface-area mesostructured carbon for enhanced CO2 capture and supercapacitor performance.* Angewandte Chemie International Edition, 2016. **55**(6): p. 2032-2036.
157. Liang, Y., et al., *Teflon: A decisive additive in directly fabricating hierarchical porous carbon with network structure from natural leaf.* ACS Sustainable Chemistry & Engineering, 2017. **5**(10): p. 9307-9312.
158. Teng, W., Y. Zhong, and R. Liu, *Synthesis of ordered mesoporous carbons by Teflon-assisted removal of silica template in tri-constituent co-assembly for supercapacitors.* Emergent Materials, 2020. **3**(3): p. 339-346.
159. Stankiewicz, A.I. and P. Yan, *110th anniversary: the missing link unearthed: materials and process intensification.* Industrial & Engineering Chemistry Research, 2019. **58**(22): p. 9212-9222.
160. Van Gerven, T. and A. Stankiewicz, *Structure, energy, synergy, time・The fundamentals of process intensification.* Industrial & engineering chemistry research, 2009. **48**(5): p. 2465-2474.
161. Thompson, E., et al., *Iron-catalyzed graphitization of biomass.* Green Chemistry, 2015. **17**(1): p. 551-556.
162. Hu, Y., et al., *Hollow spheres of iron carbide nanoparticles encased in graphitic layers as oxygen reduction catalysts.* Angewandte Chemie, 2014. **126**(14): p. 3749-3753.

163. Ramya, A., A.N. Mohan, and B. Manoj, *Wrinkled graphene: synthesis and characterization of few layer graphene-like nanocarbons from kerosene.* Materials Science-Poland, 2016. **34**(2): p. 330-336.
164. Hossen, M.M., et al., *Synthesis and characterization of high performing Fe-NC catalyst for oxygen reduction reaction (ORR) in Alkaline Exchange Membrane Fuel Cells.* Journal of Power Sources, 2018. **375**: p. 214-221.
165. Zhou, R., et al., *Determination of the electron transfer number for the oxygen reduction reaction: from theory to experiment.* Acs Catalysis, 2016. **6**(7): p. 4720-4728.
166. Xu, H., et al., *Atomically dispersed M–N–C catalysts for the oxygen reduction reaction.* Journal of Materials Chemistry A, 2020. **8**(44): p. 23187-23201.
167. Ozoemena, K.I., *Nanostructured platinum-free electrocatalysts in alkaline direct alcohol fuel cells: catalyst design, principles and applications.* RSC advances, 2016. **6**(92): p. 89523-89550.
168. Jiang, T., W. Luan, and S. Wu, *Co-based fuel cell cathode electrocatalyst for both acid and alkaline environment.* Energy Procedia, 2019. **158**: p. 2372-2377.
169. Zhu, J., et al., *Self-assembled nanofiber networks of well-separated B and N codoped carbon as Pt supports for highly efficient and stable oxygen reduction electrocatalysis.* ACS Sustainable Chemistry & Engineering, 2018. **7**(1): p. 660-668.
170. Mikkola, M.S., et al., *The effect of NaCl in the cathode air stream on PEMFC performance.* Fuel cells, 2007. **7**(2): p. 153-158.
171. Deng, C., et al., *Hybrid dual-template induced nitrogen-doped hierarchically porous carbon as highly efficient oxygen reduction electrocatalyst.* International Journal of Hydrogen Energy, 2021. **46**(73): p. 36167-36175.
172. Xin, C., et al., *Integration of Morphology and Electronic Structure Modulation on Atomic Iron-Nitrogen-Carbon Catalysts for Highly Efficient Oxygen Reduction.* Advanced Functional Materials, 2022. **32**(2): p. 2108345.
173. Li, Z., et al., *Fe, N co-doped carbonaceous hollow spheres with self-grown carbon nanotubes as a high performance binary electrocatalyst.* Carbon, 2019. **154**: p. 466-477.
174. Osmieri, L., et al., *Fe-N/C catalysts for oxygen reduction reaction supported on different carbonaceous materials. Performance in acidic and alkaline direct alcohol fuel cells.* Applied catalysis b: environmental, 2017. **205**: p. 637-653.
175. Zhang, X., et al., *Atomically dispersed hierarchically ordered porous Fe–N–C electrocatalyst for high performance electrocatalytic oxygen reduction in Zn-Air battery.* Nano Energy, 2020. **71**: p. 104547.
176. Jiao, L., et al., *From metal–organic frameworks to single-atom Fe implanted N-doped porous carbons: efficient oxygen reduction in both alkaline and acidic media.* Angewandte Chemie International Edition, 2018. **57**(28): p. 8525-8529.
177. Hu, J., et al., *Melt-salt-assisted direct transformation of solid oxide into atomically dispersed FeN4 sites on nitrogen-doped porous carbon.* Nano Energy, 2020. **72**: p. 104670.
178. Zhou, L., et al., *3D star-like atypical hybrid MOF derived single-atom catalyst boosts oxygen reduction catalysis.* Journal of Energy Chemistry, 2021. **55**: p. 355-360.
179. Zhu, D.D., J.L. Liu, and S.Z. Qiao, *Recent advances in inorganic heterogeneous electrocatalysts for reduction of carbon dioxide.* Advanced materials, 2016. **28**(18): p. 3423-3452.
180. Lim, H., *Opus 12's CO2 transformation and the importance of collaboration.* Iscience, 2021. **24**(6).
181. Appel, A.M., et al., *Frontiers, opportunities, and challenges in biochemical and chemical catalysis of CO2 fixation.* Chemical reviews, 2013. **113**(8): p. 6621-6658.

182. Vasileff, A., Y. Zheng, and S.Z. Qiao, *Carbon solving carbon's problems: recent progress of nanostructured carbon-based catalysts for the electrochemical reduction of CO2.* Advanced Energy Materials, 2017. **7**(21): p. 1700759.
183. Chen, Z., et al., *Grain-boundary-rich copper for efficient solar-driven electrochemical CO2 reduction to ethylene and ethanol.* Journal of the American Chemical Society, 2020. **142**(15): p. 6878-6883.
184. Luc, W., et al., *Two-dimensional copper nanosheets for electrochemical reduction of carbon monoxide to acetate.* Nature Catalysis, 2019. **2**(5): p. 423-430.
185. Liu, S., et al., *Efficient electrochemical reduction of CO2 to HCOOH over sub-2 nm SnO2 quantum wires with exposed grain boundaries.* Angewandte Chemie International Edition, 2019. **58**(25): p. 8499-8503.
186. Gao, S., et al., *Partially oxidized atomic cobalt layers for carbon dioxide electroreduction to liquid fuel.* Nature, 2016. **529**(7584): p. 68-71.
187. Han, N., et al., *Ultrathin bismuth nanosheets from in situ topotactic transformation for selective electrocatalytic CO2 reduction to formate.* Nature communications, 2018. **9**(1): p. 1-8.
188. Chen, B., et al., *Enhancement of Mass Transfer for Facilitating Industrial-Level CO2 Electroreduction on Atomic Ni□ N4 Sites.* Advanced Energy Materials, 2021. **11**(40): p. 2102152.
189. Fan, Q., et al., *Activation of Ni particles into single Ni–N atoms for efficient electrochemical reduction of CO2.* Advanced Energy Materials, 2020. **10**(5): p. 1903068.
190. Artyushkova, K., et al., *Chemistry of multitudinous active sites for oxygen reduction reaction in transition metal–nitrogen–carbon electrocatalysts.* The Journal of Physical Chemistry C, 2015. **119**(46): p. 25917-25928.
191. Artyushkova, K., et al., *Correlations between synthesis and performance of Fe-based PGM-free catalysts in acidic and alkaline media: evolution of surface chemistry and morphology.* ACS Applied Energy Materials, 2019. **2**(8): p. 5406-5418.
192. Leonard, N., et al., *The chemical identity, state and structure of catalytically active centers during the electrochemical CO 2 reduction on porous Fe–nitrogen–carbon (Fe–N–C) materials.* Chemical science, 2018. **9**(22): p. 5064-5073.
193. Liu, Y., J. Zhao, and Q. Cai, *Pyrrolic-nitrogen doped graphene: a metal-free electrocatalyst with high.*
194. Sharma, P.P., et al., *Nitrogen-doped carbon nanotube arrays for high-efficiency electrochemical reduction of CO2: on the understanding of defects, defect density, and selectivity.* Angewandte Chemie, 2015. **127**(46): p. 13905-13909.
195. Vijay, S., et al., *Unified mechanistic understanding of CO2 reduction to CO on transition metal and single atom catalysts.* Nature Catalysis, 2021. **4**(12): p. 1024-1031.
196. Liang, S., et al., *Electrochemical Reduction of CO2 to CO over Transition Metal/N-Doped Carbon Catalysts: The Active Sites and Reaction Mechanism.* Advanced Science, 2021. **8**(24): p. 2102886.
197. Dahlke, T., O. Ruffiner, and R. Cant, *Production of HF from H2SiF6.* Procedia Engineering, 2016. **138**: p. 231-239.
198. Sindram, M., X. Pettiau, and O. Barthe. *Flue gas treatment in the ceramic industry*. in *10 th World Congress on Ceramic Tile Quality QualiCer, Castèllon (Spain)*. 2008.
199. Conesa, J. and R. Font, *Polytetrafluoroethylene decomposition in air and nitrogen.* Polymer Engineering & Science, 2001. **41**(12): p. 2137-2147.
200. Kishi, H., et al., *Structure of active sites of Fe-NC nano-catalysts for alkaline exchange membrane fuel cells.* Nanomaterials, 2018. **8**(12): p. 965.
201. Maslova, O., et al., *Determination of crystallite size in polished graphitized carbon by Raman spectroscopy.* Physical review B, 2012. **86**(13): p. 134205.

202. Morozan, A., et al., *Effect of the transition metal on metal–nitrogen–carbon catalysts for the hydrogen evolution reaction.* Journal of The Electrochemical Society, 2015. **162**(9): p. H719.
203. Wang, D., et al., *Atomically dispersed metal-nitrogen-carbon electrocatalysts for oxygen reduction reaction: from synthesis strategies to activity engineering.* Materials Today Energy, 2022. **26**: p. 101017.
204. Koshy, D.M., et al., *Understanding the origin of highly selective CO2 electroreduction to CO on Ni, N-doped carbon catalysts.* Angewandte Chemie International Edition, 2020. **59**(10): p. 4043-4050.
205. Sgarbi, R., et al., *Oxygen reduction reaction mechanism and kinetics on M-NxCy and M@ NC active sites present in model MNC catalysts under alkaline and acidic conditions.* Journal of Solid State Electrochemistry, 2021. **25**(1): p. 45-56.
206. Gokhale, R., et al., *Direct synthesis of platinum group metal-free Fe-NC catalyst for oxygen reduction reaction in alkaline media.* Electrochemistry communications, 2016. **72**: p. 140-143.
207. Mei, B., et al., *Unraveling the Potential-Dependent Volcanic Selectivity Changes of an Atomically Dispersed Ni Catalyst During CO2 Reduction.* ACS Catalysis, 2022. **12**: p. 8676-8686.
208. Zhang, N., et al., *High-purity pyrrole-type FeN 4 sites as a superior oxygen reduction electrocatalyst.* Energy & Environmental Science, 2020. **13**(1): p. 111-118.
209. Liu, Y., et al., *Structural evolution of porous graphitic carbon nanosheets based on quinonyl decomposition for supercapacitor electrodes.* Applied Surface Science, 2021. **537**: p. 147824.
210. Hoekstra, J., et al., *Base metal catalyzed graphitization of cellulose: A combined Raman spectroscopy, temperature-dependent X-ray diffraction and high-resolution transmission electron microscopy study.* The Journal of Physical Chemistry C, 2015. **119**(19): p. 10653-10661.
211. Li, J., et al., *Volcano trend in electrocatalytic CO2 reduction activity over atomically dispersed metal sites on nitrogen-doped carbon.* ACS Catalysis, 2019. **9**(11): p. 10426-10439.
212. Weekes, D.M., et al., *Electrolytic CO2 reduction in a flow cell.* Accounts of chemical research, 2018. **51**(4): p. 910-918.
213. Ju, W., et al., *Understanding activity and selectivity of metal-nitrogen-doped carbon catalysts for electrochemical reduction of CO2.* Nature communications, 2017. **8**(1): p. 1-9.
214. Jiang, K., et al., *Isolated Ni single atoms in graphene nanosheets for high-performance CO 2 reduction.* Energy & Environmental Science, 2018. **11**(4): p. 893-903.
215. Liang, J., et al., *Facile oxygen reduction on a three-dimensionally ordered macroporous graphitic C3N4/carbon composite electrocatalyst.* Angewandte Chemie International Edition, 2012. **51**(16): p. 3892-3896.
216. Lee, S., et al., *Designing a highly active metal-free oxygen reduction catalyst in membrane electrode assemblies for alkaline fuel cells: effects of pore size and doping-site position.* Angewandte Chemie International Edition, 2015. **54**(32): p. 9230-9234.
217. Wang, Y.-C., et al., *Constructing a triple-phase interface in micropores to boost performance of Fe/N/C catalysts for direct methanol fuel cells.* ACS Energy Letters, 2017. **2**(3): p. 645-650.
218. Wu, Y., et al., *Effects of microporous layer on electrolyte flooding in gas diffusion electrodes and selectivity of CO2 electrolysis to CO.* Journal of Power Sources, 2022. **522**: p. 230998.
219. Artyushkova, K., et al., *Role of surface chemistry on catalyst/ionomer interactions for transition metal–nitrogen–carbon electrocatalysts.* ACS Applied Energy Materials, 2017. **1**(1): p. 68-77.
220. Wu, J., et al., *Electrochemical reduction of carbon dioxide: IV dependence of the Faradaic efficiency and current density on the microstructure and thickness of tin electrode.* Journal of Power Sources, 2014. **258**: p. 189-194.
221. Stöber, W., A. Fink, and E. Bohn, *Controlled growth of monodisperse silica spheres in the micron size range.* Journal of colloid and interface science, 1968. **26**(1): p. 62-69.

222. Jaouen, F., et al., *Heat-treated Fe/N/C catalysts for O2 electroreduction: are active sites hosted in micropores?* The Journal of Physical Chemistry B, 2006. **110**(11): p. 5553-5558.
223. Wang, Z.L., et al., *Optimizing Electron Densities of Ni-N-C Complexes by Hybrid Coordination for Efficient Electrocatalytic CO2 Reduction.* ChemSusChem, 2020. **13**(5): p. 929-937.
224. Arechederra, R.L., et al., *Growth of phthalocyanine doped and undoped nanotubes using mild synthesis conditions for development of novel oxygen reduction catalysts.* ACS applied materials & interfaces, 2010. **2**(11): p. 3295-3302.
225. Gokhale, R., et al., *Hydrothermal synthesis of platinum-group-metal-free catalysts: structural elucidation and oxygen reduction catalysis.* ChemElectroChem, 2017. **5**(SAND-2017-8565J).
226. Wang, G., et al., *Cost-effective and durable electrocatalysts for Co-electrolysis of CO2 conversion and glycerol upgrading.* Nano Energy, 2022. **92**: p. 106751.